Tesi di Perfezionamento in Fisica

SCUOLA
NORMALE
SUPERIORE

Dynamical Properties and Assembly of Galaxies in the Epoch of Reionization

Supervisor: Prof. Andrea Ferrara

Co-supervisor: Dr. Andrea Pallottini

Candidate: Mahsa Kohandel

Declaration

I hereby declare that this Thesis is my own original work and it is based on the following peer-reviewed papers:

[1] **Kohandel, M.**; Pallottini, A.; Ferrara, A.; Zanella, A.; Behrens, C.; Carniani, S.; Gallerani, S.; Vallini, L., *Kinematics of galaxies from line emission*, Mon.Not.Roy.Astron.Soc. 487 (2019) no.3, 3007-3020

[2] **Kohandel, M.**; Pallottini, A.; Ferrara, A.; Carniani, S.; Gallerani, S.; Vallini, L. ; Zanella, A.; Behrens, C., *Velocity dispersion in the interstellar medium of early galaxies*, Mon.Not.Roy.Astron.Soc. 499 (2020) no.1, 1250-1265

[3] Pallottini, A.; Ferrara, A.; Decataldo, D.; Gallerani, S.; Vallini, L.; Carniani, S.; Behrens, C.; **Kohandel, M.**; Salvadori, S, *Deep into the structure of the first galaxies: SERRA views*, Mon.Not.Roy.Astron.Soc. 487 (2019) no.2, 1689-1708

[4] Ferrara, A.; Vallini, L.; Pallottini, A.; Gallerani, S.; Carniani, S.; **Kohandel, M.**; Decataldo, D.; Behrens, C., *A physical model for line emission from galaxies*, Mon.Not.Roy.Astron.Soc. 489 (2019) no.1, 1-12

[5] Zanella, A.; Pallottini, A.; Ferrara, A.; Gallerani, S.; Carniani, S.; **Kohandel, M.**; Behrens, C., *Early galaxy growth: mergers or gravitational instability?*, Mon.Not.Roy.Astron.Soc. 500 (2020) no.1, 118-137

[6] Carniani, S.; Ferrara, A.; Maiolino, R.; Castellano, M.; Gallerani, S.; Fontana, A.; **Kohandel, M.**; Lupi, A.; Pallottini, A.; Pentericci, L.; Vallini, L.; Vanzella, E., *Missing [C II] emission from early galaxies*, Mon.Not.Roy.Astron.Soc. 499 (2020) no.4, 5136-5150

[7] Zanella, A.; Le Floc'h, E.; Harrison, C. M.; Daddi, E.; Bernhard, E.; Gobat, R.; Strazzullo, V.; Valentino, F.; Cibinel, A.; Sánchez Almeida, J.; **Kohandel, M.**; Fensch, J.; Behrendt, M.; Burkert, A.; Onodera, M.; Bournaud, F.; Scholtz, J., *A contribution of star-forming clumps and accreting satellites to the mass assembly of galaxies* Mon.Not.Roy.Astron.Soc. 489 (2019) no.2, 2792-2818

Contents

Abstract

In a quest for understanding the nature of the furthest galaxies in the Universe, a large amount of effort has been expended to build large telescopes as well as to perform sophisticated cosmological simulations. Despite these achievements, we still know little about the structural and dynamical properties of star-forming galaxies belonging to the epoch when the age of the Universe was less than a Giga year i.e. the Epoch of Reionization (EoR). Indeed, galaxy dynamics in such a distant universe is an uncharted field and we do not have solid answers to several fundamental questions about the structure of EoR galaxies:

1- What are the dynamical and morphological properties of EoR galaxies?

2- Do we expect galaxies to form their disk structure as early as the EoR?

3- Are there any signatures of galaxy-galaxy mergers in such early epochs?

4- Are EoR galaxies rotationally supported or dispersion-dominated systems?

5- What is the energy source powering the gas velocity dispersion in EoR galaxies?

Atacama Large Millimeter/submillimeter Array (ALMA), being the most powerful millimeter/sub-millimeter interferometer on Earth, has been playing a revolutionary role in the field of high-z galaxy dynamics by providing spatially-resolved emission-line observations. However, as we aim at studying the first galaxies that appeared in the Universe, the limiting angular resolutions and signal-to-noise ratio of the observations significantly limit such studies. These limitations can be overcome either by performing deeper observations or targeting lensed galaxies. While waiting for such high-quality data to be available for EoR galaxies, we can address the problem theoretically.

This Thesis focuses on the study of structural and dynamical properties of EoR galaxies by utilizing analytical modelings (when possible) as well as state-of-the-art hydrodynamical simulations of galaxies. Since our aim is to provide a solid comparison and/or prediction for the upcoming observations, we develop a framework in which a common cross-talk among observations and pure theoretical works becomes possible. The Thesis is structured as follows:

1- In Chapter 1, we give the reader the necessary theoretical and observational background information to follow the whole Thesis. A brief review of the conventional galaxy formation

in the context of the standard model of cosmology is followed by explaining the current status of observations of distant galaxies with particular attention to the EoR.

2- In Chapter 2, we introduce the ISM physics including far-infrared (FIR) line emissions, then we introduce semi-analytical models of galaxies that we have developed to get the first insights on the properties of [C II] emission line coming from high-z galaxies either as the kinematics or star formation tracer. We end this Chapter by explaining the modeling features of a suite of hydrodynamical simulations used in the rest of the Thesis.

3- In Chapter 3, we explore different kinematical features of EoR galaxies and their connection with the assembly process as imprinted in the FIR line emission profiles. This is achieved by tracing the evolution of a simulated galaxy from $z = 7$ to $z = 6$ through the FIR [C II] emission.

4- In Chapter 4, we study the structure of spatially resolved, line-of-sight velocity dispersion in EoR galaxies traced by [C II] line emission in the redshift range of $6 < z < 8$. We also quantify the contribution of the different energy sources powering such velocity dispersions in EoR galaxies.

5- In Chapter 5, we address one of the recent puzzling issues in high-z galaxy dynamics studies, which is related to the observations of surprisingly cold galactic disks at high redshift universe. This problem is addressed by studying the dynamical properties of a large sample of simulated EoR galaxies in the redshift range of $6 \leq z < 9$ probed by [C II] and nebular Hα emission.

6- Finally in Chapter 6, we present the conclusions and the future prospects.

Chapter 1

Introduction

We give the reader the necessary theoretical and observational background information to follow the whole Thesis. A brief review of the conventional galaxy formation in the context of the standard model of cosmology is given in Sec. 1.1. Then a review of the current status of observations of distant galaxies especially the ones in the EoR is given in Sec. 1.2 which summarizes our knowledge of the global properties of distant galaxies. In Sec. 1.3, we review the status of observational studies which deal with kinematics and dynamics of galaxies with a focus on distant ones.

1.1 Galaxy formation in a ΛCDM Universe

1.1.1 ΛCDM cosmology

Cosmology provides the space-time framework within which galaxies should be described and also initial conditions from which first structures in the Universe start forming. The modern era of cosmology started with Einstein's formulation of General Relativity (GR; Einstein, 1915). In this theory, every interval of the space-time between two events, ds, is measured using the metric of the space-time $g_{\mu\nu}$ which is governed by GR field equations

$$R_{\mu\nu} - \frac{1}{2} g_{\mu\nu} R + \Lambda g_{\mu\nu} = \frac{8\pi G}{c^4} T_{\mu\nu} \,. \tag{1.1}$$

Here $R_{\mu\nu}$ is the Ricci tensor, describing the local curvature of the space-time, c is the speed of light, R is the Ricci scalar, $T_{\mu\nu} = (\rho c^2 + P) U^\mu U^\nu - g^{\mu\nu} P$ (valid for a uniform ideal fluid with ρc^2 the energy density, P the pressure, and $U^\mu = c dx^\mu / ds$ the four-velocity of the fluid) is the energy-momentum tensor of the matter content of the Universe, Λ is the cosmological constant and G is the gravitational constant. Cosmological models built on GR (Friedmann, 1922, 1924) are based on a very simple but crucial principle; i.e. the "Cosmological Principle". According to this principle, the geometrical properties of a 3−dimensional space are identical at all spatial locations (i.e. the homogeneity of the Universe) and at all directions (i.e. the isotropy of the Universe).

This assumption is acceptable only if we consider sufficiently large scales. The appropriate metric of the space-time for such a Universe is the Friedman-Robertson-Walker (FRW) metric

$$ds^2 = c^2dt^2 - a^2[\frac{1}{1-kr^2}dr^2 + r^2d\Omega^2]\,, \tag{1.2}$$

where $a = a(t)$ is the cosmic scale factor and k stands for the spatial curvature of the space-time which can be $\pm 1, 0$. Substituting FRW metric (eq.1.2) into GR field equations (eq.1.1) and using the energy–momentum tensor of a perfect fluid results in Friedman equations

$$\frac{\dot{a}^2 + kc^2}{a^2} = \frac{8\pi G\rho}{3} + \frac{\Lambda c^2}{3}\,, \tag{1.3a}$$

$$\frac{\ddot{a}}{a} = -\frac{4\pi G}{3}\left(\rho + \frac{3p}{c^2}\right) + \frac{\Lambda c^2}{3}\,, \tag{1.3b}$$

which govern the expansion of the space in a homogeneous and isotropic Universe. Observations have helped in developing the preferred cosmological theory. Hubble 1929 observed that galaxies outside of our Local Group are moving away from us with velocities, v, proportional to their distances, R, according to $v = \dot{a}/aR \equiv H(t)R$ where $H(t)$ is the Hubble parameter; This suggests an expanding Universe. The Hubble parameter at the present time is denoted by H_0. Quantities that depend on the value of H_0 are expressed in terms of $h \equiv H_0/100\mathrm{km\,s^{-1}Mpc^{-1}}$. Using the definition of $H(t)$ and eq. 1.3, one can relate the expansion of the Universe indicated by $H(t)$ to the matter-energy density ρ

$$H(t)^2 = \frac{8\pi G}{3}\rho - \frac{kc^2}{a^2} + \frac{\Lambda c^2}{3}\,, \tag{1.4}$$

in which $\rho = \rho_m + \rho_r$ with ρ_m being the non-relativistic matter energy density, Dark Matter (DM) and baryonic matter, while ρ_r being the radiation energy density. One can define a critical density as $\rho_{\mathrm{crit}} = 3H(t)^2/8\pi G$. This quantity is useful to define a density parameter Ω_i for each type of energy density $\Omega_i = \rho_i/\rho_{\mathrm{crit}}$. Using these parameters, eq. 1.4 becomes

$$H(t) = H_0\left[\frac{\Omega_m}{a^3} + \frac{\Omega_r}{a^4} + \frac{\Omega_k}{a^2} + \Omega_\Lambda\right]\,. \tag{1.5}$$

So by knowing the values of density parameters as well as H_0, the standard cosmological model, i.e. ΛCDM, is completely defined. Recent observations (Planck Collaboration et al., 2016) constrain these parameters in a narrow range; $\Omega_m = 0.3089 \pm 0.0062$, $\Omega_\Lambda = 0.6911 \pm 0.0062$, $\Omega_k = 0.000 \pm 0.005$,$H_0 = 100h\,\mathrm{km\,s^{-1}Mpc^{-1}}$ with $h = 0.6774 \pm 0.0046$. We will adopt these parameters in the rest of the Thesis.

One of the important parameters needed when studying distant galaxies is the "redshift". Because of the expansion of the Universe, waves propagating in the Universe are stretched. Thus, photons with a wavelength λ_{em} emitted at an earlier time t will be observed at the present time t_0 with a wavelength $\lambda_{\mathrm{obs}} = \lambda_{\mathrm{em}}a_0/a(t)$. Since $a_0 > a(t)$ in an expanding Universe, $\lambda_{\mathrm{obs}} > \lambda_{\mathrm{em}}$, and

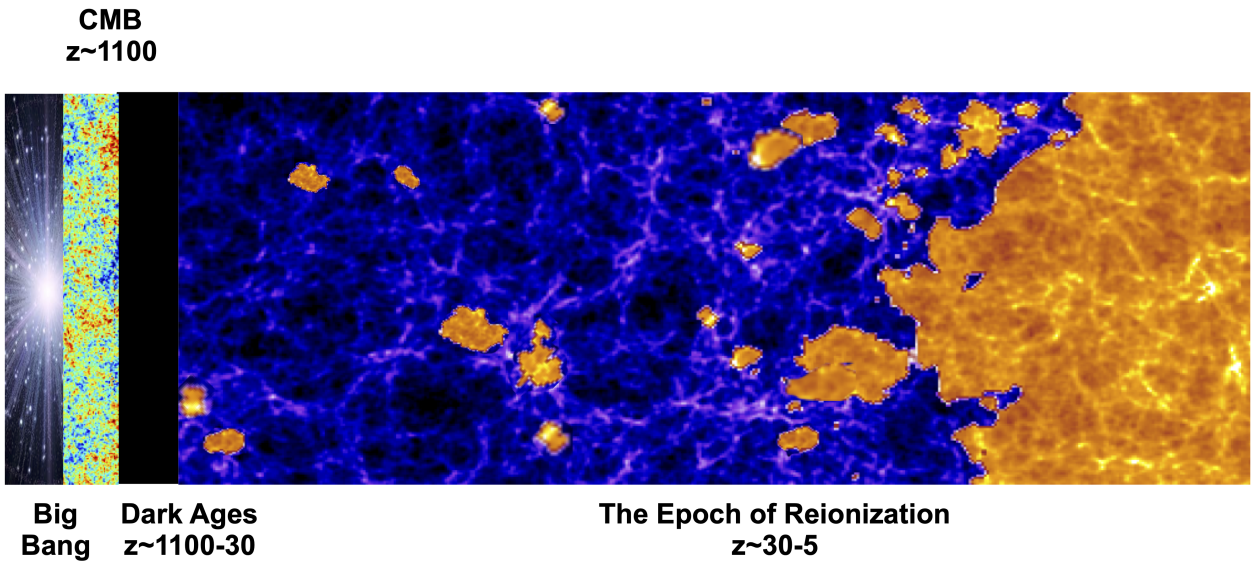

Figure 1.1: Schematic view of cosmic epochs in the first billion years of the Universe (Figure 1 in Dayal & Ferrara 2018)

so the wavelength of the photons is redshifted. The amount of redshift z between time t and t_0 is given by

$$z \equiv \frac{\lambda_{\rm obs}}{\lambda_{\rm em}} - 1 = \frac{a_0}{a(t)} - 1\,. \tag{1.6}$$

If an object has redshift z means that its observed spectrum is shifted to the red relative to its rest-frame (intrinsic) spectrum by $\Delta\lambda = \lambda_{\rm obs} - \lambda_{\rm em} = z\lambda_{\rm em}$. Because of the constancy of the speed of light, an object's redshift can also be used to infer its distance.

1.1.2 Cosmic epochs in ΛCDM cosmology

In the standard model of cosmology, the Universe has started about 13.7 billion years ago from an initial singularity, called the "Big Bang" (BB) where all the fundamental interactions of the Universe (Gravity, Electromagnetic, Weak and Strong interactions) were unified. By then, the temperature of the Universe and its density was extremely high. Since our understanding of particle physics is only robust below energies of $\sim 1\,\mathrm{GeV}(\sim 10^{13}\,\mathrm{K})$, the physics of the very early Universe (earlier than $10^{-6}\,\mathrm{s}$) is still uncertain. The extensions of the standard model of particle physics characterize this very early stage of the Universe by a number of symmetry-breaking phase transitions. The first 10^{-43} seconds after the BB, called the "Planck era", has remained unknown since we lack a full quantum theory of gravity to describe it. Among the fundamental interactions, gravity is known

to be the first interaction to decouple from the others just after the Planck era. The period from 10^{-43} to 10^{-36} seconds after the BB, known as the "GUT" epoch (Georgi & Glashow, 1974), is when all the other electronuclear forces were still unified. One of the most important phenomena related to the formation of the first structures in the Universe is cosmological Inflation which is believed to happen in the very early Universe when the Universe has gone through a phase of a rapid, exponential expansion driven by the vacuum energy quantum fields (Linde, 1982). Inflation has sourced the nearly scale-invariant primordial density perturbations that have resulted in the large-scale structure we observe today. Thus, it offers a promising explanation for the physical origin of the initial perturbations. The next epoch is called the "Electroweak" era, in which the strong interaction got decoupled from the weak interaction. Finally, at the end of this era, due to the "Higgs mechanism", the electroweak symmetry got broken and the Universe ended up recovering all its fundamental forces uncoupled from each other.

After these very early stages of the Universe, several subatomic particles are formed. Later on, when the temperature of the Universe had dropped to $\sim 10^9\,\mathrm{K}$ (a few minutes after the BB), the primordial nucleosynthesis started to take place, which eventually led to the creation of atomic nuclei (like Deuterium, Helium and a few other elements) in the Universe. Since then, the Universe was still very hot, it remains in a plasma state until about $2 \times 10^5\,\mathrm{yrs}$ after the BB that it becomes cool enough (the temperature of the Universe drops below $13.6\,\mathrm{eV}$) for the formation of neutral atoms like Hydrogen. This epoch is known as the "Recombination" epoch. At this time ($z \sim 1100$), because of the resulting drop in the number density of free electrons, the Universe becomes transparent to photons. As a consequence, photons are decoupled from atoms and form what is known as cosmic background radiation (CMB). This radiation has been observed by several satellites such as COBE, WMAP, and Planck. It has a black body spectrum with a mean temperature $T = 2.72548 \pm 0.00057\,\mathrm{K}$ (Fixsen, 2009) and fluctuations of the order of $\sim 10^{-5}$ (Planck Collaboration et al., 2016) which reflects the density inhomogeneities caused by the quantum fluctuations not erased at the end of Inflation. The CMB radiation is the furthest picture of the Universe that we have so far and it dates back to when the Universe was about ~ 380000 yrs old.

Immediately after the recombination epoch, the Universe entered a phase called the Dark Ages, where no significant radiation sources existed. This epoch ranges from $z \sim 1100$ to $z \sim 30$. The small inhomogeneities in the dark matter density field present during the recombination epoch started growing via gravitational instability giving rise to highly nonlinear structures, i.e., collapsed haloes (see Sec. 1.1.3 for the details). These collapsed haloes formed potential wells, whose depth depends on their mass and, within which baryons could fall. If the potential well of the halo was deep enough, the gas would be able to dissipate its energy, cool via atomic or molecular transitions and fragment within the halo. This produced conditions appropriate for the condensation of gas and the formation of stars in galaxies. Once these luminous objects started forming, the Dark Ages were over. The first population of luminous stars and galaxies generated ultraviolet (UV) radiation

through nuclear reactions. In addition to galaxies, perhaps an early population of accreting black holes (quasars) and the decay or annihilation of dark matter particles also generated some amount of UV light. The UV photons with energies > 13.6eV were then able to ionize hydrogen atoms in the surrounding intergalactic medium, a process known as the cosmic reionization (Madau et al., 1999; Gnedin, 2000; Barkana & Loeb, 2001). Reionization is thus the second major change in the ionization state of hydrogen in the Universe (the first one being recombination). In Fig. 1.1, a schematic view of cosmic epochs in the first billion years of the Universe is shown.

1.1.3 From initial density perturbations to first galaxies in the Universe

The structures observed today, such as galaxies and the clusters of galaxies have grown from small initial density perturbations (relic fluctuations from the cosmological inflation) due to gravitational instability. The growth of small perturbations under the action of gravity was first studied by Jeans (Jeans, 1902) and Lifshitz (Lifshitz, 1946). Detailed calculations can be found in Mo et al. 2010 (see also Dayal & Ferrara, 2018, for a review). In the following, the formation of the first galaxies is described in some detail.

If we consider the Universe as a fluid with an average density $\bar{\rho}(t)$ with a slightly overdense region, we can study the growth of such density perturbations within the framework of the linear perturbation theory by the linearized form of the hydrodynamical equations (mass and momentum conservation plus the Poisson equation) for a fluid in a gravitational field

$$\frac{D\rho}{Dt} + \rho\nabla_r.\mathbf{u} = 0\,, \tag{1.7a}$$

$$\frac{D\mathbf{u}}{Dt} = -\frac{\nabla_r P}{\rho} - \nabla_r\Phi\,, \tag{1.7b}$$

$$\nabla_r^2\Phi = 4\pi G\rho\,, \tag{1.7c}$$

where $\mathbf{r}$ is the proper coordinate, $\partial/\partial t$ is the partial derivative for fixed $\mathbf{r}$ and $\frac{D}{Dt} \equiv \frac{\partial}{\partial t} + \mathbf{u}$. ∇_r is the convective time derivative that describes the time derivative as a quantity moves with the fluid. The combined form of the above equations in comoving coordinates (i.e. $\mathbf{r} = a(t)\mathbf{x}$) yields to the time-evolution of the density contrast $\delta(\mathbf{x}, t) = \rho(\mathbf{x}, t)/\bar{\rho}(t) \ll 1$, in comoving co-ordinates, as

$$\frac{\partial^2\delta(\mathbf{x},t)}{\partial t^2} + 2\frac{\dot{a}(t)}{a(t)}\frac{\partial\delta(\mathbf{x},t)}{\partial t} = \frac{c_s^2}{a(t)^2}\nabla^2\delta(\mathbf{x},t) + 4\pi G\bar{\rho}(t)\delta(\mathbf{x},t), \tag{1.8}$$

where c_s is the sound speed. According to Eqn. 1.8, the gravitationally-driven perturbation growth (second term on the RHS) is opposed by the pressure term (first term on RHS) as well as cosmological expansion (second term on LHS). It is convenient to represent perturbation fields by

their Fourier transforms

$$\delta(\mathbf{x},\mathbf{t}) = \mathbf{\Sigma_k}\delta_\mathbf{k}(\mathbf{t})\exp(\mathbf{ik}.\mathbf{x}) \quad , \quad \delta_\mathbf{k}(\mathbf{t}) = \frac{\mathbf{1}}{\mathbf{V_u}}\int \delta(\mathbf{x},\mathbf{t})\exp(-\mathbf{ik}.\mathbf{x}), \tag{1.9}$$

where V_u is the volume of a large box on which the perturbations are assumed to be periodic and $\mathbf{k}$ is the wave-vector. In the Fouries space, eq. 1.8 can be written as

$$\frac{\partial^2\delta_\mathbf{k}}{\partial t^2} + 2H(t)\frac{\partial\delta_\mathbf{k}}{\partial t} = \delta_\mathbf{k}\left(4\pi G\bar{\rho}(t) - \frac{k^2c_s^2}{a(t)^2}\right). \tag{1.10}$$

The source term (RHS) vanishes at a scale where the pressure gradient balances gravity resulting in the *Jeans wavelength*, the scale that is just stable against collapse, expressed as

$$\lambda_J = \frac{2\pi a(t)}{k_J} = c_s\left(\frac{\pi}{G\bar{\rho}}\right)^{1/2}. \tag{1.11}$$

The mass enclosed within the cosmic Jeans length $\lambda_J/2$ is defined as

$$M_J \equiv \frac{4\pi}{3}\rho\left(\frac{\lambda_J}{2}\right)^3. \tag{1.12}$$

which is referred to as the Jeans mass. Density perturbations with wavelengths of $\lambda \gtrsim \lambda_J$ start to collapse due to gravity, while those with $\lambda \lesssim \lambda_J$ are pressure supported against gravitational collapse. By substituting the Jeans length into eq. 1.12, the Jeans mass becomes proportional to $M_J \propto (c_s^2 a)^{3/2}$. So, having the information on the sound speed of different mass components of the Universe at various epochs, we can specify which perturbations are unstable at a given time and therefore start to collapse. Before recombination ($z \gtrsim 1100$), baryons are a relativistic fluid with a constant sound speed and the corresponding Jeans mass is larger than a super-cluster ($M_J \sim 10^{18} M_\odot$). Therefore, baryons are pressure supported at this epoch. While immediately after recombination and before thermal decoupling from the CMB ($200 \lesssim z \lesssim 1100$), the sound speed can be approximated assuming a non-relativistic monoatomic gas such that

$$c_s^2 = \left(\frac{5k_BT_\gamma}{3m_p}\right), \tag{1.13}$$

where k_B is the Boltzmann constant, m_p is the proton mass and T_γ is the CMB temperature. This results in a co-moving Jeans length (Mo et al., 2010):

$$\lambda_J \approx 0.01(\Omega_b h^2)^{-1/2}\,\mathrm{Mpc}, \tag{1.14}$$

where Ω_b is the baryonic density parameter at $z = 0$, yielding a constant Jeans mass

$$M_J \approx 1.5 \times 10^5 (\Omega_b h^2)^{-1/2} \, M_\odot \,, \tag{1.15}$$

a value comparable to that of present-day globular clusters. Thus, the first baryonic perturbations to start gravitational collapse were on the scale of globular clusters after recombination.

Inflation theory predicts that primordial perturbations have a scale-invariant power spectrum $P(k) \propto k^{n_s}$ where the spectral index has been measured to have a value $n_s = 0.9645 \pm 0.0049$ (Planck Collaboration et al., 2016). The gravitational growth of perturbations modifies the primordial spectrum by depressing its amplitude on scales smaller than the horizon at the matter-radiation equality. The result is that, on small scales, $P(k) \propto k^{n_s - 4}$, while the largest scales retain the original quasi-linear spectrum $\propto k^{n_s}$ (e.g. Bardeen et al., 1986). Given that most of the power in the ΛCDM model is concentrated on small scales, these are the first to go nonlinear, resulting in the formation of bound halos.

Once density perturbations grow beyond the linear regime, i.e. $\delta(\mathbf{x}, t) \sim 1$, the full non-linear collapse must be followed. It should be noted that dark matter has a head start with respect to baryons in graviational collapse, so baryons end up accreting onto already formed dark matter structures. The dynamical collapse of a dark matter halo can be solved exactly in case of specific symmetries, the simplest of which is the collapse of a top-hat spherically symmetric density perturbation. In a ΛCDM Universe, the motion of a mass shell in a spherically symmetric perturbation is given by (Mo et al., 2010)

$$\frac{d^2 r}{dt^2} = -\frac{GM}{r^2} + \frac{\Lambda c^2}{3} r \,, \tag{1.16}$$

with Λ contributing to the gravitational acceleration. Integrating this equation yields

$$\frac{1}{2}\left(\frac{dr}{dt}\right)^2 - \frac{GM}{r} - \frac{\Lambda c^2}{6} r^2 = \mathcal{E} \,, \tag{1.17}$$

where $\mathcal{E}$ is the specific energy of the mass shell. The shell reaches a maximum radius r_{max} at time t_{max} before the perturbation detaches from the Hubble flow at

$$t_{max} = \frac{1}{H_0}\left(\frac{\zeta}{\Omega_\Lambda}\right)^{1/2} \int_0^1 dx \left[\frac{1}{x} - 1 + \zeta(x^2 - 1)\right] , \tag{1.18}$$

where $\zeta = (\Lambda c^2 r_{max}^3 / 6GM)$. The initial radius of the shell r_i can be linked to r_{max} as

$$\frac{r_i}{r_{max}} \approx \left(\frac{w_i}{\zeta}\right)^{1/3} \left[1 - \frac{1}{5}(1 + \zeta)\left(\frac{w_i}{\zeta}\right)^{1/3}\right] , \tag{1.19}$$

where $w_i = \Omega_\Lambda(t_i)/\Omega_m(t_i) = (\Omega_\Lambda/\Omega_m)(1 + z_i)^{-3}$. Combining this with the fact that the enclosed

mass is $M = (1+\delta_i)\Omega_{m,i}\bar{\rho}(t_i)(4\pi r_i^3/3)$ yields

$$\delta_i = \frac{3}{5}(1+\zeta)\left(\frac{w_i}{\zeta}\right)^{1/3}. \tag{1.20}$$

This can be linearly evolved till the present time to obtain δ_0 as

$$\delta_0 = \frac{a_0 g_0}{a_i g_i}\delta_i = \frac{3}{5}g_0(1+\zeta)\left(\frac{w_i}{\zeta}\right)^{1/3}, \tag{1.21}$$

where $w_i = w_0/(1+z_i)^3$ and g is the linear growth factor. We can derive the linear overdensity at the collapse time as

$$\delta_c(t_{col}) = \frac{3}{5}g(t_{col})(1+\zeta)\left(\frac{w(t_{col})}{\zeta}\right)^{1/3} \approx 1.686[\Omega_m(t_{col})]^{0.0055}, \tag{1.22}$$

i.e. the linear over-density at collapse time t_{col} is weakly dependent on the density parameter with $\delta_{crit} \simeq 1.686$ (Mo et al., 2010).

According to the simple assumptions above, the structure should collapse to a point. In reality, since dark matter shells lack pressure, they would go through the center in a sort of damped harmonic oscillator which is called "virialization". Accurate modeling of the non-linear regime collapse (Barkana & Loeb, 2001) leads to the following expressions for the virial radius R_{vir}, the circular velocity V_{vir}, and the virial temperature T_{vir} of the halo of mass M_h which collapses at redshift z

$$R_{vir} = 0.784\left(\frac{M_h}{10^8 h^{-1}M_\odot}\right)^{1/3}\left[\frac{\Omega_m\Delta_c}{\Omega_m^z 18\pi^2}\right]\left(\frac{1+z}{10}\right)^{-1} h^{-1}\mathrm{kpc}, \tag{1.23}$$

$$V_{vir} = 23.4\left(\frac{M_h}{10^8 h^{-1}M_\odot}\right)^{1/3}\left[\frac{\Omega_m\Delta_c}{\Omega_m^z 18\pi^2}\right]^{1/6}\left(\frac{1+z}{10}\right)^{1/2}\mathrm{km\,s^{-1}}, \tag{1.24}$$

$$T_{vir} = 1.98\times10^4\left(\frac{\mu}{0.6}\right)\left(\frac{M_h}{10^8 h^{-1}M_\odot}\right)^{2/3}\left[\frac{\Omega_m\Delta_c}{\Omega_m^z 18\pi^2}\right]^{1/3}\left(\frac{1+z}{10}\right)\mathrm{K}, \tag{1.25}$$

where (Bryan & Norman, 1998)

$$\Delta_c = 18\pi^2 + 82(\Omega_m^z - 1) - 39(\Omega_m^z - 1)^2, \tag{1.26}$$

$$\Omega_m^z = \frac{\Omega_m(1+z)^3}{\Omega_m(1+z)^3 + \Omega_\Lambda}, \tag{1.27}$$

and μ is the mean molecular weight.

This method predicts the main physical quantities of the halo. To determine the evolution of the number density of dark matter halos (i.e. the Halo Mass Function HMF), Press & Schechter 1974 have provided an analytical formalism. In this formalism, the probability that the density, at

a given spatial position and time, exceeds the critical density δ_{crit} collapsing into a bound object, is given by

$$p[> \delta_{crit}] = \frac{1}{\sqrt{2\pi}\sigma(M)} \int_{\delta_{crit}}^{\infty} e^{-\frac{\delta_s^2}{2\sigma^2(M)}} d\delta_s = \frac{1}{2}\mathrm{erfc}\left[\delta_{crit}/\sqrt{2}\sigma(M)\right], \tag{1.28}$$

where δ_s represents the smoothed density field and $\sigma(M)$ represents its mass variance, obtained by convolving the initial power spectrum $P(k)$ with a window function. Expressing the number density of halos between mass M_h and $M_h + dM_h$ at redshift z, can be written as

$$n(M_h, z)dM_h = \sqrt{\frac{2}{\pi}} \frac{\bar{\rho}}{M_h^2} \nu e^{-\nu^2/2} \left| \frac{d\ln\nu}{d\ln M_h} \right| dM_h \,, \tag{1.29}$$

where $\nu = \delta_{crit}(z)/\sigma(M)$. Further, $\delta_{crit}(z)$ is related to its value at $z = 0$ such that $\delta_{crit}(z) = \delta_{crit}(0)D(z)$, where $D(z)$ is the linear growth rate normalised to the present day value so that $D(z = 0) = 1$ and $D(z)$ can be written as (Carroll et al., 1992):

$$D(z) = \frac{g(z)}{g(0)(1+z)} \,, \tag{1.30}$$

where

$$g(z) = 2.5\Omega_m[\Omega_m^{4/7} - \Omega_\Lambda + (1 + \Omega_m/2)(1 + \Omega_\Lambda/70)]^{-1} \,. \tag{1.31}$$

This implies that the Press-Schechter HMF is fully defined once the initial conditions ($P(k)$, $\sigma(M)$) are specified.

Once we have nonlinear dark matter structures as the birthplace of the first galaxies, the next step is to describe the fate of baryons. This step is very crucial since the majority of the information that we have about galaxies through observations is carried by electromagnetic signals from baryonic components of galaxies. Once a dark matter halo forms a potential well, it accretes gas from the intergalactic medium (IGM) to form its ISM and circum-galactic medium (CGM). The virial temperature of the DM halo is very important for this step. In order to continue collapsing inside the DM halo, the gas must be able to cool to compensate for the gravitational heating. The associated loss of pressure causes the gas to collapse towards the center, likely forming a rotationally supported disk-like structure. Cooling processes largely involve collisionally-excited line emission from atoms and continuum radiation (e.g. bremsstrahlung, recombination, and collisional ionizations) with heavy elements (including C, N, and O) being the most efficient radiators.

The gas in the first galaxies would have been metal-free, being composed of a primordial mixture of ($\sim 75\%$) hydrogen and ($\sim 25\%$) helium. Radiative dissipation in such systems had to rely essentially on either molecular hydrogen or collisional excitation of hydrogen and He atoms. The efficiency of the cooling radiation as a function of the gas temperature can be seen in Fig. 1.2 for gas with primordial composition. The two peaks of the solid red curve correspond to cooling

by H and He (at $\sim 10^4$ and $\sim 10^5$ K respectively). Indeed, most galaxies obtain their gas from the recombination and collisional excitation cooling of hydrogen. However, hydrogen cooling becomes very inefficient below $\sim 10^4$ K. Since structure formation is hierarchical, smaller DM halos formed earlier. Thus the first galaxies in the Universe likely accreted their gas through the rotational-vibrational transitions of the H_2 molecule. Molecular hydrogen allowed gas to condense onto even smaller halos, with virial temperatures of order $\sim 10^3$ K (Haiman et al., 1996; Bromm et al., 2002). However, H_2 can be directly dissociated once the first galaxies form by radiation in the so-called Lyman-Werner band ($\sim 10.2 - 13.6$ eV). Later on, with the formation of heavy elements, the cooling rates increase, and the gas can collapse and form a disk on the cooling timescale that is typically shorter than the free-fall time of the system (Ferrara, 2008).

As a result of gas collapse into the potential well of DM halos, Giant Molecular Clouds (GMC) form which are the birthplaces of the first generation of stars (PopIII) in the Universe which is believed to be formed at around $z \sim 20 - 30$ (Ciardi & Ferrara, 2005). The process of star formation and fragmentation of collapsing gas clouds into a protostar in the primordial Universe is a highly complicated problem (see Milosavljević & Safranek-Shrader 2016 for a review). The UV light produced by these first stars and galaxies spread out throughout the Universe, ionizing and heating the IGM resulting in the EoR epoch. The EoR physics involves a huge range of scales from the small-scale physics of star formation to very large cosmological scales (see the review by Mesinger 2016). This epoch is believed to be completed around $z \sim 6$ (Fan et al., 2006; McGreer et al., 2011). After the formation of the first sources, as time progressed, those objects gradually evolved, merging with their neighbors and accreting large quantities of gaseous fuel from a filamentary IGM. Then, through a combination of galaxy-galaxy mergers, rapid star formation, and secular evolution, the morphology of those galaxies transformed into what is observed locally.

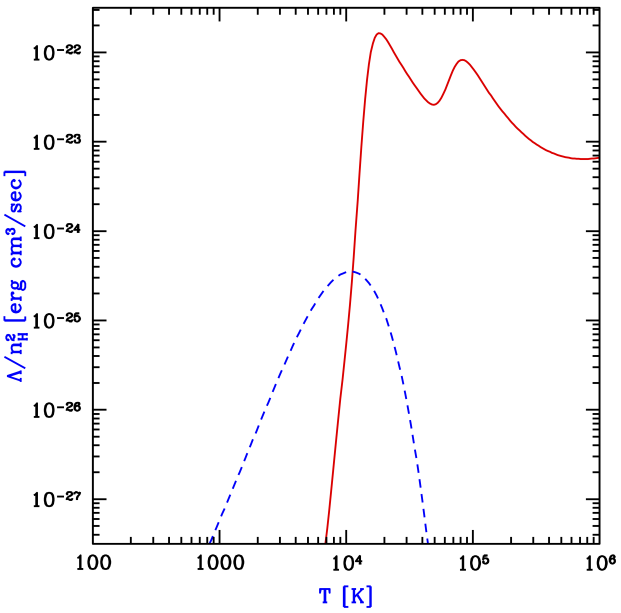

Figure 1.2: The cooling function, taken from Barkana & Loeb 2001, computed using Abel online calculator (http://logy.harvard.edu/tabel/PGas/cool.html), assuming primordial abundances. The solid red curve corresponds to atomic gas (H and He), while the dashed blue curve corresponds to molecular hydrogen.

1.2 Observations of high-z galaxies

Now that we know what theory predicts regarding the formation of first galaxies, the next question is whether we are able to detect such distant objects. Indeed, we are living in the golden age in a hunt for high redshift galaxies. Detection of such galaxies has been possible thanks to observatories such as the Hubble Space Telescope (HST), the 8.2m Very Large Telescope (VLT), the 85cm Spitzer and the 10m Keck telescope. By covering from the optical through to mid-infrared wavelengths, these facilities have put outstanding constraints on the physical properties of early galaxy populations.

In this section, we first explain how the detection of such far-away galaxies is possible and what we have learned about EoR galaxies thanks to such observations.

1.2.1 Detection techniques

There are different ways to attempt to pinpoint high redshift galaxies. The two methods that have proved most effective in recent years both involve optical to near-infrared observations of rest-frame UV light, and both rely on neutral Hydrogen. The bulk of detected high-z galaxies can be categorized into two main groups; I) Lyman Break Galaxies (LBGs) and II) Lyman Alpha Emitters (LAEs).

The Lyman break technique to identify LBGs

This technique which was first proposed by Meier 1976 relies on identifying the 912Å Lyman break caused by the absorption of Lyman continuum photons by neutral ISM gas. At $z \gtrsim 5$, the Lyman Break shifts to 1216Å, with photons of lower wavelengths being absorbed by neutral hydrogen in both the ISM and the intervening IGM. This absorption is called “Gunn-Peterson" trough (Gunn & Peterson, 1965). In Fig. 1.3, the illustration of the redshifted form of the rest-frame ultraviolet spectral energy distribution SED from a galaxy at $z \simeq 7$ is shown. The spectrum shows the sharp drop at $\lambda_{\rm rest} = 1216$Å due to the strong "Gunn-Peterson" absorption by intervening neutral hydrogen. LBG selections have yielded thousands of candidates with redshifts as high as $z \sim 12$ thanks to two key instruments - the Advanced Camera for Surveys (ACS) and the Wide Field Camera3 (WFC3) on board the *HST* (Bouwens et al., 2007, 2010, 2011; Ellis et al., 2013; Oesch et al., 2013; Bowler et al., 2014; Bouwens et al., 2015; Atek et al., 2015; Bowler et al., 2015; Oesch et al., 2016; Livermore et al., 2017) , shedding light on the juvenile galaxies that had formed in the first billion years of the Universe.

The Lyα line to identify LAEs

The second technique to identify high-z galaxies is through the detection of Lyα recombination line at 1216 Å(rest-frame of the galaxy) in their spectra. This technique, which is also called the

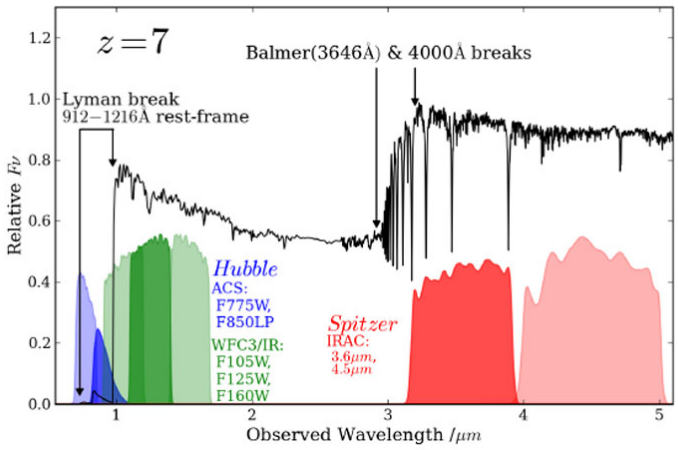

Figure 1.3: An illustration of the redshifted form of the rest-frame ultraviolet spectral energy distribution anticipated from a young galaxy at $z \simeq 7$, showing how the ultraviolet light is sampled by the key red optical(i_{775}, z_{850}) and near-infrared ($Y_{105}, J_{125}, H_{160}$) filters on-board HST (in the ACS and WFC3/IR cameras respectively), while the longer-wavelength rest-frame optical light is probed by the 3.6 μm and 4.5μm IRAC channels on-board Spitzer. The spectrum shows the sharp drop at $\lambda_{\rm rest} = 1216$Å due to the strong "Gunn-Peterson" absorption by intervening neutral hydrogen. (Figure 1 in Dunlop 2013).

narrowband technique, has identified hundreds of galaxies up to redshift $z \simeq 8$ (Ouchi et al., 2005; Taniguchi et al., 2005; Kashikawa et al., 2006; Ouchi et al., 2008, 2010; Kashikawa et al., 2011; Matthee et al., 2014, 2015, 2017; Ouchi et al., 2018). However, this technique is very limited for redshifts $z \geq 7$. The reason is that Lyα has an extremely high optical depth against neutral hydrogen; this line is significantly attenuated by the IGM. So as we go further in the EoR and as the fraction of neutral hydrogen increases in the IGM, the number of star-forming galaxies detected in Lyα emission decreases.

1.2.2 Spectroscopic confirmation

The spectroscopic confirmation of the detected galaxies is crucial. Moreover, it is inevitable when studying the ISM properties of galaxies. This task becomes progressively difficult as we aim at understanding the ISM of $z > 5$ galaxies because commonly-used rest-frame optical emission lines at lower z observations, such as Hα, Hβ, [O III]$\lambda\lambda$4959, 5007, and [O II]$\lambda\lambda$3726, 3729 are redshifted out from the atmospheric window in the near-infrared, and ground-based telescopes cannot observe these lines. In this regard, astronomers have been searching for other emission lines in the spectra of high-z star forming galaxies (SFGs). These alternatives include both nebular emission lines (such as CIII]$\lambda\lambda$1907 , 1909 rest-frame ultraviolet emission doublet(Stark et al., 2015a), [OIII]+Hβ (Smit et al., 2014) and CIV]λ1548 Å(Stark et al., 2015b)) and far-infrared fine structure lines (such as [C II] 158μm (Maiolino et al., 2015; Willott et al., 2015; Capak et al., 2015; Pentericci et al., 2016;

Knudsen et al., 2016; Bradač et al., 2017; Matthee et al., 2017; Carniani et al., 2018b,a; Matthee et al., 2017; Smit et al., 2018; Harikane et al., 2019) and [O III] 88μm(Inoue et al., 2016a; Carniani et al., 2017; Laporte et al., 2017; Marrone et al., 2018; Hashimoto et al., 2018; Tamura et al., 2019)).

Although detection of rest-frame optical lines from $z > 5$ galaxies has to wait for the launch of the James Webb Space Telescope (JWST), the list of observed FIR line emissions at such redshifts is already extensive. The Atacama Large Millimeter/Submillimeter Array (ALMA) has been playing a revolutionizing role in this regard, both for galaxies at intermediate (see Hodge et al. 2014 for a recent review) and high redshifts.

Among the FIR emission lines (which are known to be the main coolants of the ISM (Dalgarno & McCray, 1972a; Wolfire et al., 2003)), [C II] at 158μm, being typically the strongest FIR line (Stacey et al., 1991) and carrying 1% of the total infrared luminosity (De Looze et al., 2014), is now routinely observed at $z \geq 5$ both in individual systems (e.g. Jones et al. 2017; Smit et al. 2018) and large galaxy samples. The ALMA Large Program to INvestigate [C II] at Early times (ALPINE) survey has provided the first large sample of star-forming galaxies at $4 < z < 6$ (Le Fèvre et al., 2020) which includes 122 galaxies with $SFR > 10\,\mathrm{M_\odot yr^{-1}}$ and stellar mass $10^9 < M_\star < 10^{10.5}\mathrm{M_\odot}$ among which for 2/3 of the sample the [C II] line has been detected. The Reionization Era Bright Emission Line Survey (REBELS) is the most recent ALMA Large Program (Bouwens et al., 2021) in which the [C II] line, as well as the [O III] line, are detected for nearly 40 bight UV-selected galaxies at $z > 6.5$. In Tab. 1.1 a list of individual high-z galaxies probed by [C II] line is tabulated.

Table 1.1: Sample of high-z galaxies probed by [C II] line.

Target Name	ID	z	$\log(L_{[\mathrm{C\ II}]}/\mathrm{L}_\odot)$	FWHM/km s^{-1}	Reference
UDS16291	U16	6.64	7.9	50	Pentericci et al. 2016
RXJ1347:1216	RXJ	6.77	7	75	Bradač et al. 2017
COSMOS13679	C13	7.15	7.9	90	Pentericci et al. 2016
WMH5b	WMH5b	6.07	8.4	94	Jones et al. 2017; Willott et al. 2015
A385-5.1	A38	6.03	6.9	100	Knudsen et al. 2016
BDF3299	B32	7.15	7.8	102	Maiolino et al. 2015; Carniani et al. 2017
COS-2987030247	C29	6.81	8.6	124	Smit et al. 2018
HZ8w	HZ8W	5.15	8.3	136	Capak et al. 2015
COSMOS24108a	C24a	6.63	7.9	150	Pentericci et al. 2016
COSMOS24108	C24	6.63	8.1	150	Pentericci et al. 2016
BDF2203	B22	6.12	8.1	150	Carniani et al. 2018a
CLM1	CLM1	6.17	8.4	162	Willott et al. 2015
HZ1	HZ1	5.69	8.4	165	Capak et al. 2015
HIMIKO	HIMIKO	6.60	8.1	180	Ouchi et al. 2013; Carniani et al. 2018b
HZ6	HZ6	5.29	9.2	188	Capak et al. 2015
HZ3	HZ3	5.54	8.7	200	Capak et al. 2015
COS-3018555981	C30	6.85	8.7	230	Smit et al. 2018
NTTDF6345	N63	6.70	8.2	250	Pentericci et al. 2016
WMH5	WMH5	6.07	8.7	251	Jones et al. 2017; Willott et al. 2015
HZ8	HZ8	5.15	8.7	254	Capak et al. 2015
WMH5a	WMH5a	6.07	8.5	270	Jones et al. 2017; Willott et al. 2015
HZ4	HZ4	5.54	9.0	297	Capak et al. 2015
B14-65666	B14	7.15	9.1	349	Hashimoto et al. 2018
HZ9	HZ9	5.54	9.2	351	Capak et al. 2015
HZ2	HZ2	5.66	9.0	377	Capak et al. 2015
HZ7	HZ7	5.25	8.7	483	Capak et al. 2015

1.2.3 FIR lines to probe high-z galaxy properties

In the past decade, detection of FIR emission lines have revealed both global and spatially resolved properties of high-z galaxies. In the following, we briefly introduce and discuss these properties.

[C II] line as a tracer of star formation

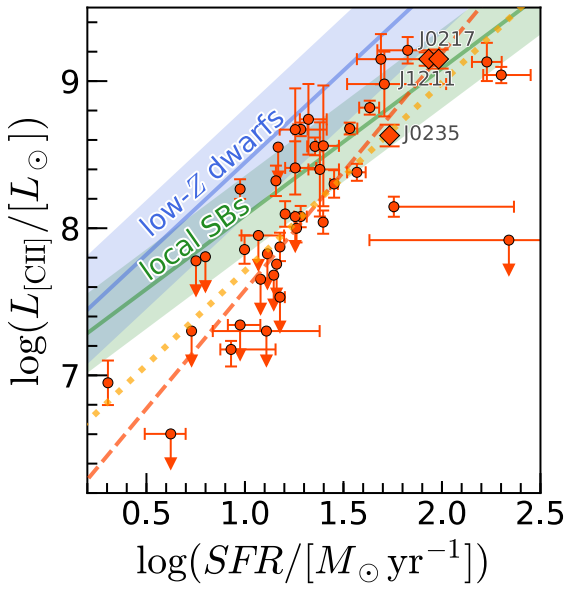

Figure 1.4: $L_{\rm CII}$-SFR relation of $5 < z < 9$ galaxies. The red diamonds and circles represent $z = 5-9$ LBGs and LAEs in the literature. The red dashed line is the fitting function for the $z = 5-9$ galaxies. The orange dotted line is a fitting function in Schaerer et al. 2020 for ALPINE sample. The blue and green lines denote relations $z \sim 0$ low-metallicity dwarf galaxies ("low-Z dwarfs") and starburst galaxies ("local SBs") from De Looze et al. 2014. (Figure 4 in Harikane et al. 2019)

In an attempt to analyze the application of FIR fine-structure lines in tracing the star formation rate of galaxies, a very tight relation between [C II] line luminosity and global star formation rate is found in the local Universe (De Looze et al., 2014; Kapala et al., 2015; Herrera-Camus et al., 2015). This finding makes the [C II] line a promising tool to investigate the properties of early galaxies and to trace their star formation. It is currently debated whether the same relation also holds at high redshifts. However, the behavior of the [C II] line emission at $z > 5$ appears much more complex than observed locally. ALMA observations have shown that only a sub-sample of the available [C II] detections in early galaxies follows the De Looze et al. 2014 relation, finding several [C II] - under luminous galaxies at high-z and suggesting a large scatter in $L_{\rm CII}$-SFR (Carniani et al., 2018a; Harikane et al., 2019). In Fig. 1.4, the [C II] luminosities as a function of SFR for the sample of galaxies at $z \geq 5$ is shown. This plot which is taken from Harikane et al. 2019 includes the relation for $z \sim 0$ starburst and dwarf galaxies as well. The majority of high$-z$ sources presents a large scatter around the local relation, with a considerable (15–20%) fraction of the outliers being "[C II]-deficient" with respect to their SFR (Carniani et al., 2018a; Harikane et al., 2019).

In the past few years, both observational (Maiolino et al., 2015; Capak et al., 2015; Knudsen et al., 2016; Matthee et al., 2017) and theoretical studies (Vallini et al., 2015; Olsen et al., 2017; Pallottini et al., 2017b; Lagache et al., 2018; Popping et al., 2016, 2019) have concentrated on this issue. Vallini et al. 2015 suggested that the fainter [C II] line luminosity can be explained if these sources deviate from the Kennicutt–Schmidt (KS) relation (Kennicutt, 1998; Schmidt, 1959)

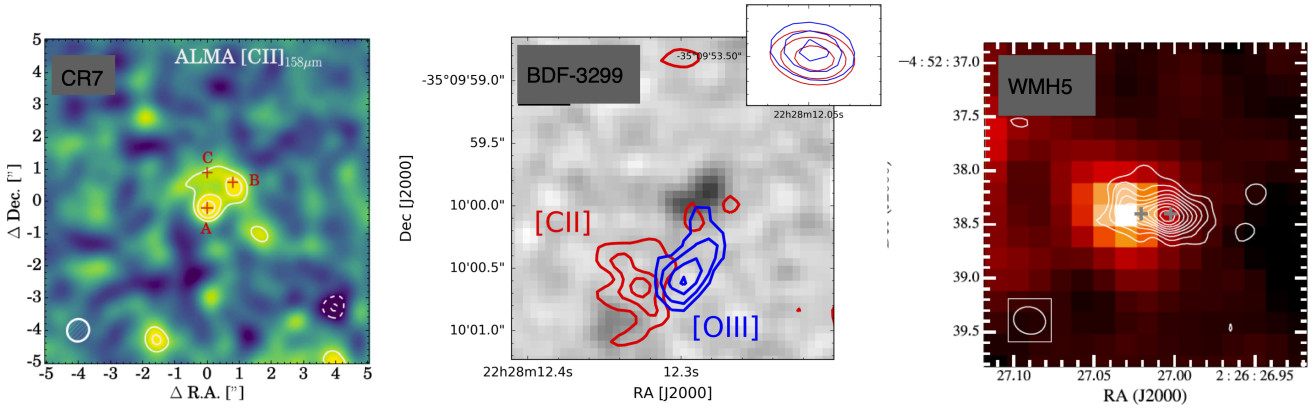

Figure 1.5: Examples of spatially resolved [C II] line observations of galaxies in the EoR; *Upper left: ALMA [C II] narrowband image of CR7- The red crosses mark the positions of the UV clumps of CR7. Upper right:*The HST Y band image of the BDF3299 field is shown in the background in greyscale. The blue contours show the [O III] map while the red contours show the [C II] emission. *Lower:* Contours of [C II] moment zero map of WMH5 overlaid on top of the near-IR image which is an average of the Z- and Y-band images. (Figures from Carniani et al. 2017, Matthee et al. 2017 and Jones et al. 2017)

and/or if they have a low metallicity. These authors found that [C II] emission substantially drops for metallicities $Z < 0.2Z_{\odot}$, a result later confirmed by Olsen et al. 2017 and Lagache et al. 2018.

Beside low metallicities, high-z galaxies also show evidence for peculiarly intense radiation fields (e.g. Stark et al. 2017), and compact sizes (Shibuya et al., 2019a). In this situation, radiative feedback (e.g. due to radiation from massive stars) can be more effective, causing for instance the photo-evaporation of molecular clouds (Gorti & Hollenbach, 2002; Decataldo et al., 2017, 2019). This process indirectly regulates the line luminosity resulting from the associated PDRs (Vallini et al., 2017). Similar arguments have also been invoked to explain the [C II] deficit in some local galaxies (Herrera-Camus et al., 2018). Stronger/harder radiation fields may also alter the ionization state of carbon atoms. Despite these findings, no consensus has yet been reached on whether the [C II] 158 μm line remains a good tracer of star formation at high redshifts. We will get back to this relation in Sec. 2.2.2 and 2.3.5 by investigating the physics of the [C II] line emission and its relation with global galaxy properties.

Spatially resolved galaxy properties

Millimetre-interferometer observations done by ALMA have enabled us to not just study the global properties of high-z galaxies, but also to start spatially resolving their internal structures. Fig. 1.5 presents three examples of galaxies with $z > 6$ which have been observed with ALMA; "CR7" is a luminous LAE at $z = 6.6$ (Matthee et al., 2017), "BDF3299" is an LBG at $z = 7.15$ (Maiolino et al., 2015; Carniani et al., 2017) and "WMH5" is an LBG at $z = 6$ (Willott et al., 2015; Jones et al., 2017). The typical angular resolution ($\theta_{\rm beam}$) in these observations is ~ 0.3", which

corresponds to 2kpc at $z = 6$. Compared to local observations, those have a very low resolution which makes it challenging to study the detailed structure and morphology of high-z galaxies systems. However, one should note that the typical integration time of these observations is $\sim$ one hour. So, deeper observations are required for detailed studies of such systems. Despite the limitations, these observations have revealed some properties of EoR galaxies and at the same time have raised a couple of baffling questions.

A large fraction of the galaxies observed in [C II] emission is characterized by a multi-component morphology (Matthee et al., 2017; Carniani et al., 2018a; Jones et al., 2017, 2020). In some cases, surprisingly, the [C II] emission coming from the galaxy does not coincide with the star-forming regions traced by the rest-frame UV light (Matthee et al., 2017; Carniani et al., 2017, 2018b). Moreover, for a small fraction of $z > 6$ galaxies, [O III] 88 μm line is also detected (Inoue et al., 2016a; Laporte et al., 2017; Carniani et al., 2017; Tamura et al., 2019; Hashimoto et al., 2018; Harikane et al., 2019). In some cases like BDF3299 (see Fig. 1.5), there are spatial (order of few kpcs) as well as spectral offsets between the [C II] emitting gas and other tracers such as FIR [O III] emission and optical/UV emissions. Some of the observed spatial offsets and spectral offsets can be ascribed to uncertainties between different observations. However, some of the observed offsets might be due to physically distinct regions of a galaxy, characterized by different physical conditions, or accretion events (minor merging) or major merging (Carniani et al., 2017).

Both from theoretical and observational sides, people have tried to understand the origin of the observed offsets. For example, these spatial offsets might be ascribed to strong feedback that cleans the most vigorous star-forming regions (or even the entire galaxy). In this case, the UV-stellar emission would be detected, while little or no [C II] emission would be observed (Vallini et al., 2017; Maiolino et al., 2015). Low metallicity, chemical inhomogeneity, and variations in the ionization parameter could also explain the faintness of [C II] emission in UV-bright regions (Vallini et al., 2015; Pallottini et al., 2017b; Carniani et al., 2017). Dust extinction, on the contrary, could explain the lack of UV detection in [C II] bright galaxies (Katz et al., 2017; Carniani et al., 2017).

1.3 High-z galaxy dynamics

As we stated at the beginning of this chapter, our aim is to study the dynamical properties of EoR galaxies. Before diving into the status of dynamics studies at such high redshifts, we want to explain why we do care about galaxy dynamics by touching upon the kinematics properties of local as well as intermediate redshift galaxies.

Galaxies are gravitationally bound objects and their internal motions relate to fundamental questions about their masses and assembly history. Thanks to the advent of large telescopes coupled with technologies like Integral Field Unit (IFU) spectroscopy, the topic of high-z galaxy dynamics has flourished in the past decade (see: Glazebrook, 2013, for a review).

Galaxies in the local Universe range a variety of structures, from galaxies with smooth light

profiles to structures with spiral arms. These galaxies can be classified based on their morphology into four broad classes (Mo et al., 2010), i.e. Elliptical galaxies, Spiral galaxies, Lenticular galaxies, and Irregular galaxies. Extending galaxy kinematics observations to intermediate redshifts (i.e. $1 < z < 3$ the so-called *cosmic noon* epoch:) Genzel et al. 2006; Genzel et al. 2013; Förster Schreiber et al. 2009b; Law et al. 2009; Epinat et al. 2010, 2012; Jones et al. 2010; Wisnioski et al. 2015; Stott et al. 2016; Burkert et al. 2016; Harrison et al. 2017; Swinbank et al. 2017; Wisnioski et al. 2019; Loiacono et al. 2019 have revealed galaxies with variety of kinematic types (i.e., disks, mergers, dispersion- dominated sources), as well as signatures of inflows and outflows. However, disk galaxies make up a substantial fraction of the observed SFG population both in the local Universe (Blanton & Moustakas, 2009) and the cosmic noon epoch.

1.3.1 Rotation curves

Local SFGs typically consist of a thin, rotationally supported disk with spiral arms and often a bar, plus a central bulge component. The stellar surface brightness profile of disk galaxies $I(R)$ is roughly exponential in radius R, following the distribution of the form

$$I(R) = I_0 \exp\left(-R/R_d\right), \quad I_0 = \frac{L}{2\pi R_d^2}, \tag{1.32}$$

with R being the cylindrical radius, R_d being the exponential scale-length, I_0 being the central luminosity surface density and L the total luminosity. One way to specify the kinematics of a disk is by its rotation curve $V_{\rm rot}(R)$ which expresses the rotation velocity as a function of galactocentric distance.

Most of the galaxy studies in the nearby universe have used the 21 cm emission line from the atomic hydrogen (HI) as the tracer of dynamics. The HI gas often extends beyond the stellar component of the galaxy making it ideal for probing the flattening of rotation curves due to the presence of DM (Rubin et al., 1970, 1978). In Fig. 1.6, the optical and HI maps along with the rotation curve (taken from Kleiner et al., 2019) of a nearby spiral galaxy (IC 5201) are shown. In this spiral galaxy, the cold gas is extended to scales $> 20\,$kpc and the rotation curve derived from the HI emission-line exhibits the dominance of DM at large radii.

At higher redshifts and in particular for intermediate redshifts ($1 < z < 3$), galaxy kinematics becomes very challenging with the HI gas because of the limited sensitivity of current radio telescopes. For this reason, there are very few intermediate redshift galaxies (Übler et al., 2018; Girard et al., 2018) for which the quality of observations is good enough to assess the kinematics of cold gas using CO line emission. Thus, the majority of intermediate redshift kinematics studies are based on ionized gas tracers such as Hα and [O III] lines. Although a few hundreds of intermediate redshift galaxies (e.g Förster Schreiber et al., 2018) are observed with the latest IFU instruments, high-quality galaxy kinematics analysis have been performed only for a small fraction of them.

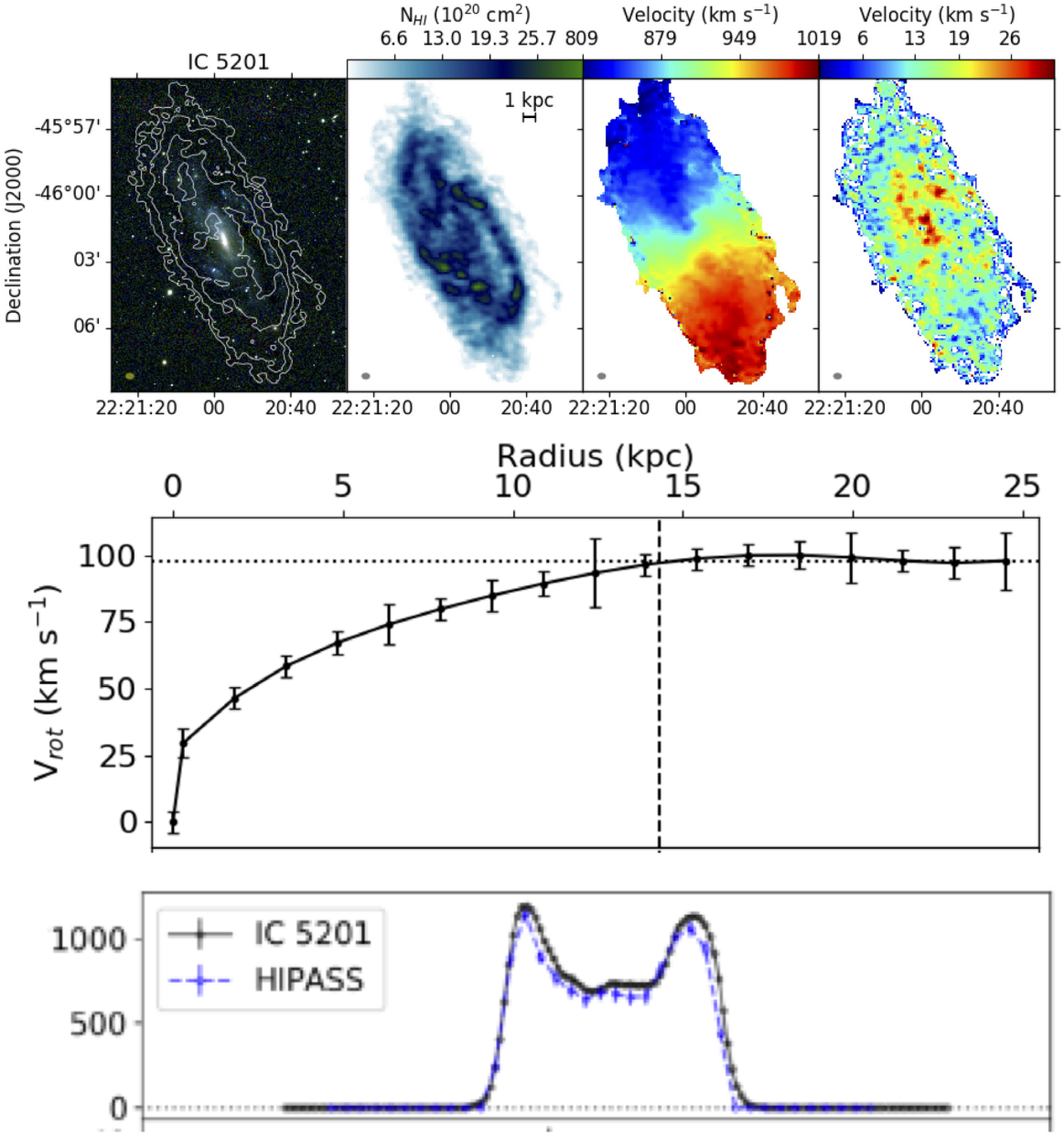

Figure 1.6: Kinematics of IC 5201 (a local spiral galaxy) observed in HI emission. *Upper panel from left to right:* The optical map, the HI map along with the mean velocity and dispersion maps derived from HI line. *Middle panel:* The rotation curve derived from HI maps. *Lower panel:* The HI integrated spectrum. (Figures from Kleiner et al. 2019)

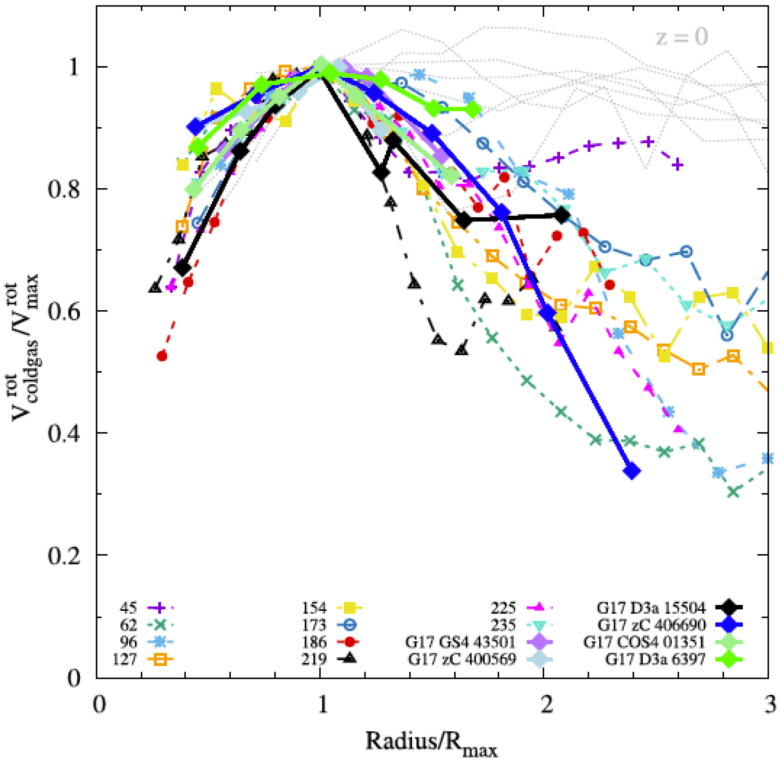

Figure 1.7: Rotation curves of intermediate redshift galaxies with respect to $z = 0$ local ones.

Therefore, the question about the shape of rotation curves of these galaxies is still a matter of debate. For example, Genzel et al. 2017 and Lang et al. 2017 found that the rotation curves of intermediate redshift SFGs are falling at outer radii suggesting that this population of galaxies are strongly baryon dominated. However, other works (e.g. Di Teodoro et al., 2018; Übler et al., 2018) have found that DM is dominating the rotation curve at outer radii similarly to local galaxies. In Fig. 1.7, rotation curves of some intermediate redshift galaxies are plotted.

The studies of galaxy dynamics do not stop at intermediate redshifts. With the improvement of the quality of the view that ALMA is giving us from the high-z universe, the [C II] line is starting to be considered as a suitable tracer of galaxy kinematics (from $z \sim 4$ galaxies to the ones in the EoR: De Breuck et al., 2014; Jones et al., 2017; Smit et al., 2018; Rizzo et al., 2020, 2021; Fraternali et al., 2021). Regarding the EoR galaxies, although the resolution of observations is not still optimal to properly model the gas kinematics, there have been pieces of evidence for ordered rotation of galaxies at $z > 6$ (Smit et al., 2018; Bakx et al., 2020) as well as early signatures of galaxy mergers (Jones et al., 2017). In the upper panel of Fig. 1.8a, the velocity fields of three galaxies in the EoR are shown which are detected in [C II] line. Data with high angular resolution and high S/N are crucial for performing robust kinematics analysis. With the help of gravitational lensing Rizzo et al. 2021 have got access to such high-quality data suitable for not only spatially resolving the ISM of galaxies at redshifts as high as $z \sim 4.5$, but also constructing their rotation curves. In the bottom panel of Fig. 1.8a, an example of such observations is shown.

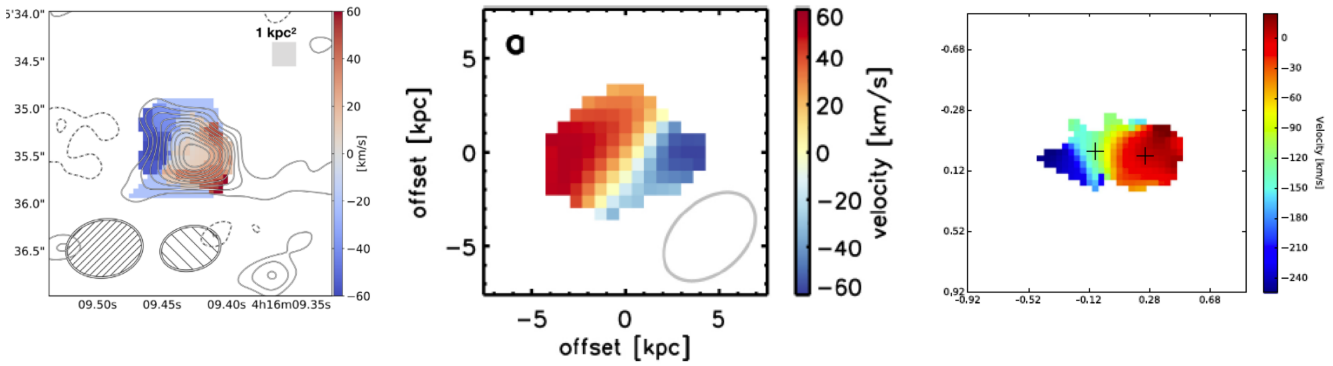

(a) Spatially resolved velocity field measured in three galaxies in the EoR detected in [C II] line. *Left panel:* MACS0416 Y1; a rotation-dominated system at $z = 8.3$ (Bakx et al., 2020), *center panel:* COS-3018555981; an undisturbed rotating gas disk at $z = 6.9$ (Smit et al., 2018) and *right panel:* WMH5; early formation of a galaxy through the accretion of smaller satellite galaxies along a filamentary structure at $z = 6.1$ (Jones et al., 2017)

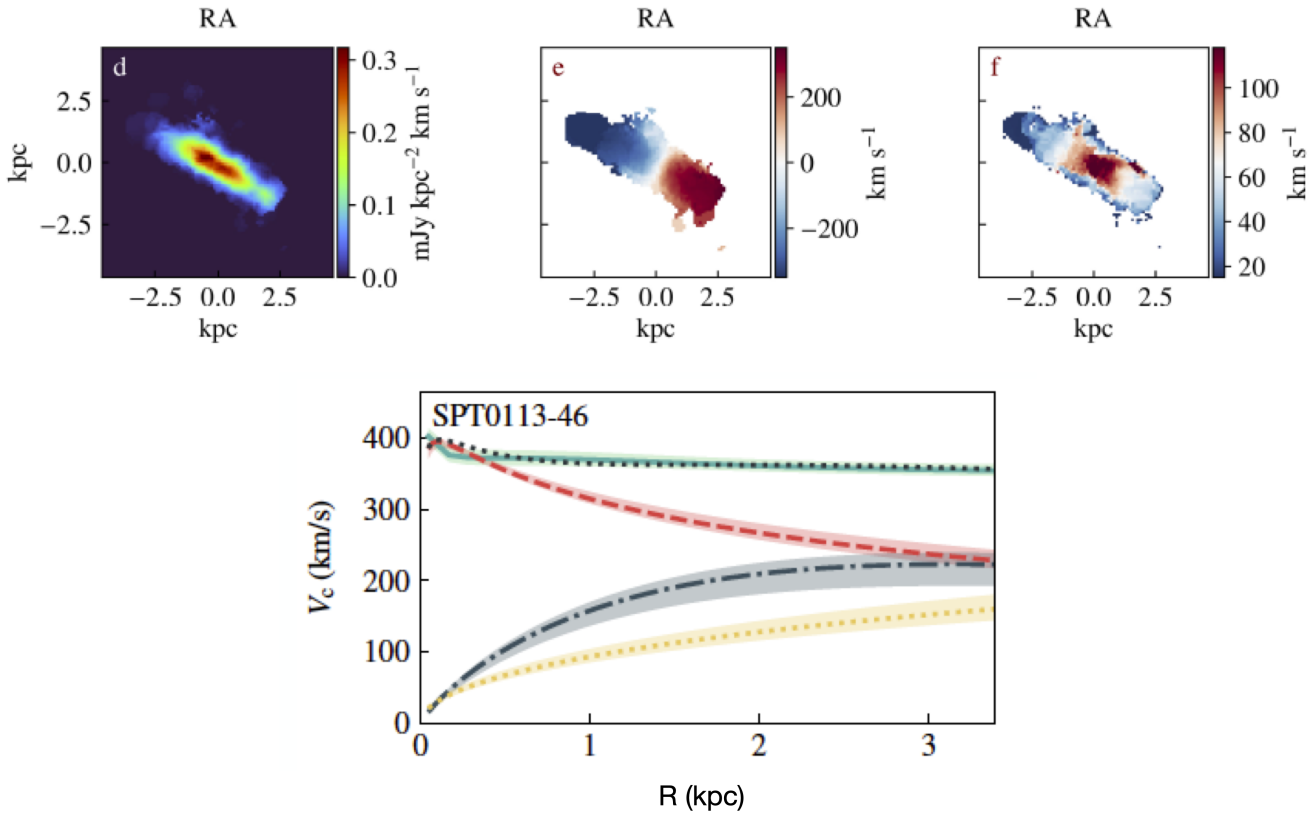

(b) SPT from Rizzo et al. 2021

Figure 1.8: Spatially resolved kinematics of high-z galaxies.

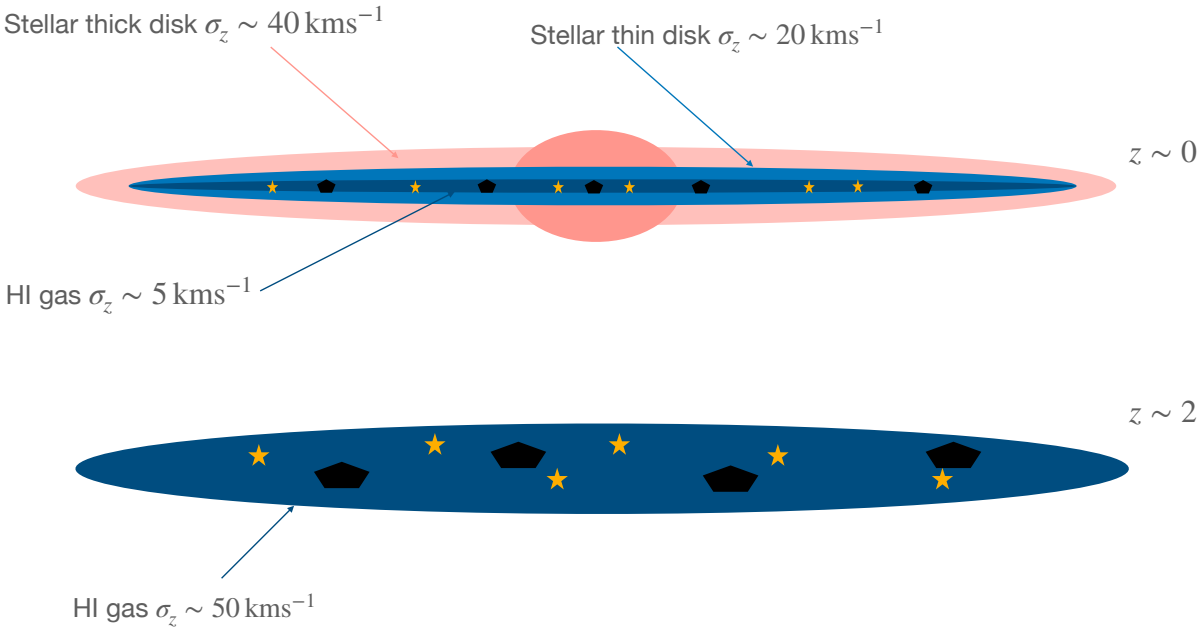

Figure 1.9: Schematic illustration of local vs. high-z galactic disks in an edge-on view. *Top:* components of the Milky Way and similar local spirals containing stellar thin/thick discs and a very thin gas disk in the center. The latter contains all the Giant Molecular Clouds, HII regions, molecular and neutral gas, and young stars. *Bottom:* a clumpy high-redshift disc. This contains a thick ($\sim$ 1 kpc scale height) and highly turbulent discs of molecular gas, young stars, super-giant HII regions (kpc scale star-forming clumps), and super-Giant Molecular Clouds (Figure 2 in Glazebrook 2013).

These results are very promising and it is worth the effort to push galaxy dynamics studies to even higher redshifts both from the observational and theoretical point of view (see Chap. 3 and 4).

1.3.2 Vertical structure of galactic disks

Another important property of galactic disks is their velocity dispersion which is related to their vertical structure and pressure support. Thanks to high-resolution observations, we have been able to study this quantity quite well in the Milky Way (MW) and nearby galaxies. In the case of local spiral galaxies, the young stellar populations reside on the so-called thin disk structure (see Fig. 1.9 for a schematic illustration), in which the velocity dispersion, σ_z, is related to the vertical mass distribution, Σ, by a gravitational equilibrium i.e. $\sigma_z \sim G\Sigma h_z$ where h_z is the vertical exponential scale height. According to van der Kruit & Freeman 2011, the stellar thin disk of local spirals has an exponential height of $200 - 300\,\mathrm{pc}$ and a vertical velocity dispersion of $\sigma_z \sim 20\,\mathrm{km\,s}^{-1}$. In the middle of this stellar thin disk, there is an even thinner layer where the gas collects the neutral hydrogen, molecular clouds, dust, HII regions, and young OB and A stars all sit in this thinner

layer which has a dispersion of only $\sim 5-10\,\mathrm{km\,s^{-1}}$ (Bolatto et al., 2008). MW has another component which is called the thick disk which contains the older population of stars. It has a scale height of $\sim 1500\,\mathrm{pc}$ (Gilmore & Reid, 1983) and vertical dispersion of $\sim 40\,\mathrm{km\,s^{-1}}$ (Pasetto et al., 2012).

As we go to higher redshifts, obtaining the detailed kinematics of galaxies becomes more challenging. However, the kpc-scale gas kinematics studies of the intermediate SFGs (Genzel et al., 2006; Förster Schreiber et al., 2009b; Law et al., 2009; Stott et al., 2016; Förster Schreiber et al., 2018; Mieda et al., 2016; Mason et al., 2017) have surprisingly shown that although a remarkable number of galaxies around the cosmic noon resemble ordered, disk-like structures, they show significantly higher velocity dispersions ($\sim 50-100\,\mathrm{km\,s^{-1}}$) compared to local star-forming galaxies ($\sim 20-25\,\mathrm{km\,s^{-1}}$, Andersen et al. 2006; Epinat et al. 2010) (see Fig. 1.9 for the schematic comparison). This elevated gas velocity dispersion of $z\sim 2$ disks is usually attributed to the geometrically thick disks which have been observed in some cases in HST images (Elmegreen & Elmegreen, 2005; Elmegreen & Elmegreen, 2017). The ratio of circular rotation velocity to dispersion V_{rot}/σ_z for $z\sim 2$ disks typically ranges from $1-10$ (Law et al., 2009; Förster Schreiber et al., 2009b; Gnerucci et al., 2011; Genzel et al., 2011) which compares with a value of $10-20$ for MW and other local spiral disks (Epinat et al., 2010). So the intermediate-redshift disks seem to be dynamically hot structures. To explain the evolution of σ_z, a framework of marginally-stable gas-rich disks is suggested (Dekel et al., 2009; Genzel et al., 2011; Wisnioski et al., 2015) where $V_{rot}/\sigma_z \propto f_{\rm gas}^{-1}$ in which $f_{\rm gas}$ is the fraction of gas in the galactic disk. Therefore, it is believed that it is a high gas fraction of high-z disks that results in a high velocity dispersion. However, Rizzo et al. 2021 have shown that for high-z dusty SFGs like SPT0113-46 (see Fig. 1.8b), the observed velocity dispersion is not as high as suggested by previous theoretical works and the galactic disks are surprisingly cold at redshifts as high as $z\sim 4.5$ i.e. $V_{rot}/\sigma_z\sim 10$. In Fig. 1.10, the positions of recently observed high-z galaxies in $\sigma-z$ plane are shown. We will explore this feature in EoR galaxies in Chap. 5.

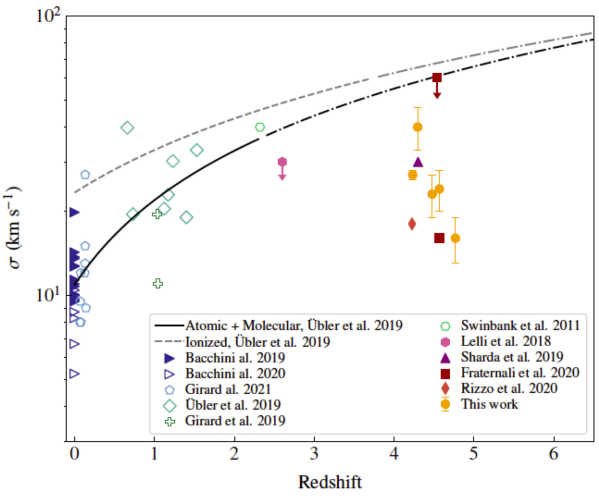

Figure 1.10: The average velocity dispersion for high-z galaxies. (Fig. 9 in Rizzo et al., 2021)

The driving mechanism of the observed gas velocity dispersion is a very important and debated issue as it carries key information on energy deposition and dissipation processes in galaxies. Feedback from star formation activity, including supernovae (SN) and radiation pressure, is one of the extensively studied mechanisms (e.g. Thompson et al. 2005; Lehnert et al. 2013; Dib et al. 2006; Ostriker & Shetty 2011; Le Tiran & Lehnert 2011; Shetty & Ostriker 2012; Green et al. 2014;

Martizzi et al. 2015; Moiseev et al. 2015; Pallottini et al. 2017a; Hayward & Hopkins 2017; Lupi 2019).

Green et al. 2014, using Hα observations of nearby ($z \sim 0.1$) and intermediate ($1 < z < 3$) redshift galaxies, have shown that the gas velocity dispersion in a galaxy is correlated with its total star formation rate suggesting that star formation itself is the main driver at all epochs. However, except for some analytical works like Hayward & Hopkins 2017, most theoretical works have struggled to produce velocity dispersions $\gtrsim 10\,\mathrm{km\,s^{-1}}$ purely as a result of stellar feedback (e.g. Dib et al. 2006; Joung et al. 2009; Shetty & Ostriker 2012). Although some models invoke very high momentum input rates to boost the resulting velocity dispersion (Hopkins et al., 2011), it is not yet clear whether such high momentum inputs are physically plausible (Krumholz & Thompson, 2012; Rosdahl & Teyssier, 2015).

Alternatives to stellar feedback are different kinds of instabilities occurring on sub-kpc scales. Kim et al. 2003; Piontek & Ostriker 2004; Yang & Krumholz 2012 have shown that both magneto-rotational and thermal instabilities only produce velocity dispersions of a few $\mathrm{km\,s^{-1}}$. Velocity dispersion sourced by the gravitational energy of galaxy-scale accretion flows has also been proposed (Genzel et al., 2011); at present, though, it is unclear whether this mechanism provides enough energy to support the observed velocity dispersion (e.g. Elmegreen & Burkert, 2010; Hopkins et al., 2013; Klessen & Hennebelle, 2010; Krumholz & Burkhart, 2016). Despite these efforts, whether observed gas dynamics in local and intermediate-redshift ($z \sim 2$) galaxies is driven by gravitational processes (e.g. Orr et al., 2019a) or stellar feedback (Genzel et al., 2011) is still debated.

Pushing the galaxy kinematics studies to high-z and obtaining the pressure support of EoR galaxies have not yet been possible in observations due to the poor quality of observations at those redshifts. While waiting for the next generation observations to get there, theoretical models can help us predict the dynamical status of such faraway galaxies and guide the future observations (see Chap. 4).

1.3.3 Tully–Fisher relation

Despite the diverse formation histories of individual galaxies, local disk galaxies obey a tight relation which exists between their luminosity L (or the corresponding mass) and rotation velocity (usually taken as the maximum of the rotation curve well away from the center, V_{max} or the width of an emission line). This relation is called the Tully-Fisher relation (TF) (Tully & Fisher, 1977) which in observation is expressed as $L = AV_{\mathrm{max}}^{\alpha}$ (or $log(L) = \alpha log(V_{\mathrm{max}}) + A$) where A is the zero-point and α is the slope.

The origin of TF relation and its evolution is tied to basic relations governing the structural assembly of dark matter halos. In the framework of hierarchical galaxy formation, considering a spherical dark matter halo of mass M_h and virial velocity V_h, a simple theoretical expression can

be derived for the evolution of TF relation (Mo et al., 2010)

$$M_h = \frac{V_h^3}{10GH(z)} \,. \tag{1.33}$$

If one assumes a constant baryonic disk mass fraction and constant galactic DM fraction, the redshift evolution of the TF relation for the galactic disk will be governed by $H(z)$

$$M_{\rm disk} \propto \frac{V_{\rm rot}(R_e)^3}{H(z)} \,, \tag{1.34}$$

where $M_{\rm disk}$ is the total baryonic mass of the disk and R_e is the effective radius. So, the theoretical TF relation has a constant slope and an evolving zero-point due to the increasing $H(z)$ factor which means that disks at fixed rotation velocity are less massive (luminous) at higher redshifts. For the local galaxies, the slope of the TF relation varies between $2.5 \leq z \leq 4.5$ (Pierce & Tully, 1992; McGaugh et al., 2000; Bell & de Jong, 2001; Pizagno et al., 2005; Avila-Reese et al., 2008; Trachternach et al., 2009; Williams et al., 2010; Reyes et al., 2011; Zaritsky et al., 2014; Lelli et al., 2016). The scatter observed in TF relation for local galaxies is usually attributed to different sample size, various methods to convert luminosity to mass or to the choice of velocity parameter. As we go to higher redshifts, the situation regarding the scatter in the TF relation gets worse. While some find very weak zero-point evolution of the TF relation for galaxies at $1 < z < 2$ (Conselice et al., 2005; Kassin et al., 2007; Di Teodoro et al., 2016; Molina et al., 2017; Pelliccia et al., 2017), other works find a negative zero-point evolution up to redshifts of $z \sim 3$ (Puech et al., 2008; Cresci et al., 2009; Gnerucci et al., 2011; Swinbank et al., 2012; Price et al., 2016; Straatman et al., 2017).

Comparing these observational findings with theoretical modelings have challenged the standard model of cosmology (McGaugh, 2012; Dutton, 2012) so it is worth the effort to push the challenge to even higher redshifts when the galaxies are still in their juvenile phase (see Sec. 3.3.2).

Chapter 2

Modelling the ISM of high-z galaxies

This chapter starts with a brief introduction to the ISM physics including the FIR line emissions (Sec. 2.1). Then in Sec. 2.2, we explain semi-analytical models of galaxies that we have developed in Kohandel et al. 2019 and Ferrara et al. 2019 with the aim of getting first insights on the properties of [C II] emission line coming from high-z galaxies either as the kinematics or star formation tracer. Finally, in Sec. 2.3, we explain the modeling features of SERRA suite of simulations (Pallottini et al., 2017b, 2019) which is used in next chapters as a laboratory to study the dynamics of EoR galaxies.

2.1 Physics of the ISM

Understanding the complex environment of the ISM of galaxies requires deep knowledge of the physics of a wide range of spatial scales, from the extent of the galaxy as a whole down to the local blobs of gas that collapse to form individual stars. We saw in the previous chapter that FIR emission lines (such as [C II] and [O III]) from the ISM of galaxies carry crucial information about their internal structure. In this section, we explain the general structure of the ISM of galaxies and the physics behind the FIR emission lines.

2.1.1 Gas phases in the ISM

Gas as the main component (accounting for up to 99%) of the ISM is composed of mostly hydrogen and helium, with hydrogen accounting for $\sim 70\%$ of the total mass, helium for 28% and all other elements for the remaining 2%. The interstellar gas can be found in a wide range of density ($10^{-3} - 10^{6}\,\mathrm{cm}^{-3}$). Since hydrogen is the most abundant element, it is common to differentiate different phases of the ISM based on its chemical state. It is conventional to describe the ISM in different phases; Molecular gas, Cold Neutral Medium (CNM), Warm Neutral Medium (WNM), Warm Ionized Medium (WIM), H II ionized regions and Hot Ionized Medium (HIM). The physical

Table 2.1: Physical properties of different ISM phases; temperature (T), number density (n) and fractional ionization (n_e/n_H)

ISM Phase	T(K)	n(cm^{-3})	n_e/n_H
Molecular Gas	$10-100$	$>10^2$	$<10^{-6}$
Cold Neutral Medium (CNM)	$50-100$	$\sim 20-50$	$\sim 10^{-4}$
Warm Neutral Medium (WNM)	$6000-10000$	$0.2-0.5$	~ 0.1
Warm Ionized Medium (WIM)	~ 8000	$0.2-0.5$	0.7
H II regions	10^{4-5}	$\sim 10^{2-3}$	1.0
Hot Ionized Medium (HIM)	10^{5-6}	$\sim 10^{-3}-10^{-1}$	1.0

properties like temperature (T), number density (n) and fractional ionization (n_e/n_H) of these phases are listed in Tab. 2.1.

Molecular Gas

The most interesting phase of the ISM is the one organized in molecular clouds (MCs) since they are the birthplace of stars. The massive clouds in the ISM which are sufficiently dense ($n > 10^2\,\mathrm{cm}^{-3}$) provide the suitable situation for H atoms to bind together and form molecules such H_2, CO, HCN. Although H_2 molecule is the most abundant molecule, unfortunately, it is very challenging to directly detect it. As suitable alternatives, it is common to study the molecular gas in the ISM through indirect tracers, such as the continuum far-infrared/sub-mm emission by cold dust, submillimetre CO rotational lines, or some submillimetre fine structure lines (such as [CI]). These observations have revealed that most of the molecular gas in the MW is located in discrete GMCs (Tielens, 2010) with typical sizes of 40 pc, masses of $4\times10^5 M_\odot$, densities of $\sim 200\,\mathrm{cm}^{-3}$ and temperature of 10 K. Although the molecular gas occupies a very small volume of the ISM ($\sim 0.05\%$), it accounts for $\sim 30\%$ of its mass (Wolfire et al., 2010).

Neutral Medium

The neutral gas in the ISM is divided into two phases CNM and WNM. This two-phase structure of the neutral gas was first suggested theoretically by Field et al. 1969. The CNM occupies $\sim 1\%$ of the ISM volume while WNM accounts of $\sim 30\%$ (Draine, 2011). The CNM contains mainly HI clouds which have densities $50-100\,\mathrm{cm}^{-3}$ and temperatures $\sim 20-50$ K. In these HI clouds starlight can barely ionize H or He resulting in a very low ionization faction ($\sim 10^{-4}$). Only sufficiently energetic x-rays can penetrate these clouds and affect their ionization fraction (Draine, 2011). However, the WNM contains the more diffuse HI gas ($n \sim 0.2-0.5\,\mathrm{cm}^{-3}$) with relatively higher temperatures ($\sim 6000-10000$ K). Most of the WNM is located in the Photodissociation regions (PDRs) (Sec. 2.1.1). HI gas is best studied by 21cm hyperfine structure line of atomic hydrogen.

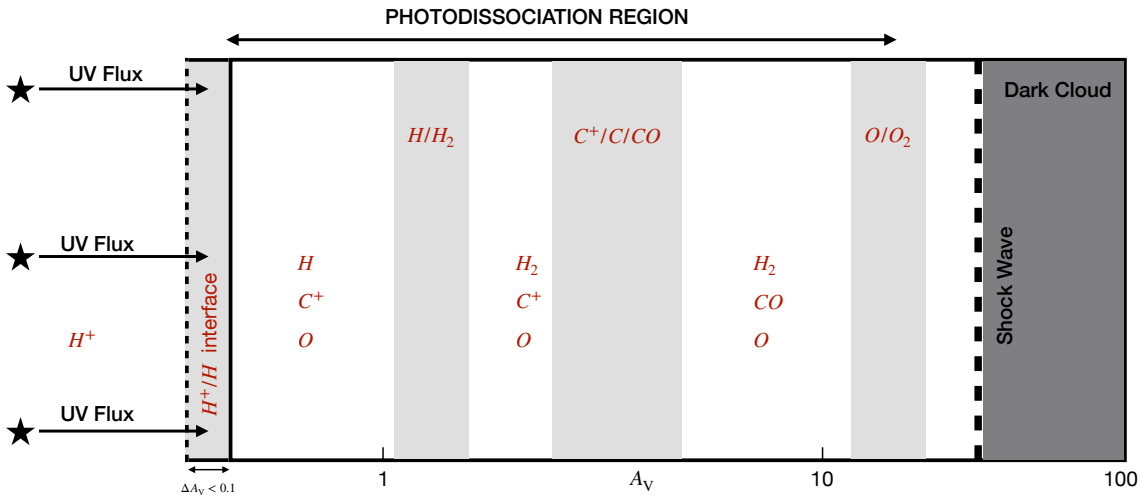

Figure 2.1: Schematic diagram of a PDR diagram of the structure of a PDR based on the model of Hollenbach & Tielens 1999

Ionized gas

The ionized gas is categorized into three phases, i.e. H II regions, HIM and WIM. The photoionized gas surrounding a hot, luminous star is referred to as a H II region. The density of a H II region is about $10^{2-3}\,\mathrm{cm}^{-3}$ and its temperature ranges in $10^{4-5}\,\mathrm{K}$. H II region is commonly studied through recombination lines of H (and He) and forbidden metal lines such as [O III](1660.81, 1666.15 Å) and [N II](6548.05, 6583.45 Å). HIM refers to the lowest density gas ($\sim 10^{-3} - 10^{-1}\,\mathrm{cm}^{-3}$) in the ISM. This is the gas that has been shock-heated to temperatures $\geq 10^4\,\mathrm{K}$ usually by blastwaves from supernova explosions (Draine, 2011). The most common ionized species in the HIM phase of the ISM are CIV, NV and OVI. Most of the ionized gas in the ISM is in the diffuse WIM (Haffner et al., 2009) which has a temperature $T \sim 8000\,\mathrm{K}$ with number densities $n \sim 0.2 - 0.5\,\mathrm{cm}^{-3}$. The main tracer of the WIM phase is Hα emission.

Photodissociation regions

The interface between the H II region and the dense molecular cloud is called a PDR. Far-ultraviolet (FUV $6 < h\nu < 13.6\,\mathrm{eV}$) photons produced mainly by O and B stars impinging on a nearby molecular could produce PDRs. In Fig. 2.1, a schematic diagram of the structure of a PDR is shown which is based on the classical model of Hollenbach & Tielens 1999. This picture is a simplified version of a PDR on which the molecular cloud is illuminated from one side by a unidirectional interstellar radiation field. As the radiation penetrates from one side, it gets attenuated by dust grains and gas which causes the transition from WNM to CNM inside the PDR. In this model (Draine, 2011), the PDR is bounded by an ionization front (the surface where hydrogen is half ionized and half atomic) and contains a photodissociation front (where hydrogen

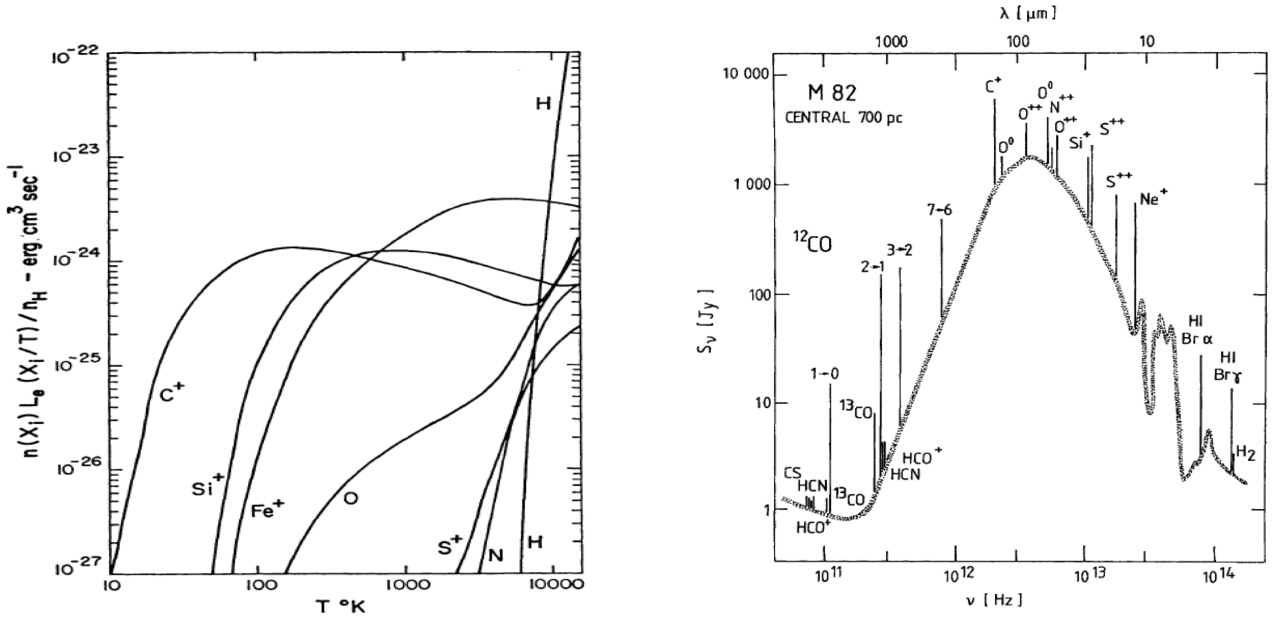

Figure 2.2: [C II] as one of the major coolants of the ISM *Left:* the contribution of [C II] to the ISM cooling (Figure 1 in Dalgarno & McCray, 1972b), *Right:* Spectral Energy Distribution of a nearby starburst galaxy, M82 (from Burton, 1992) featuring the [C II] line as one of the strongest emission lines.

is half atomic and half molecular). The depth at which these fronts take place depends on the intensity of the radiation field, the gas density and dust properties. The depth into the PDR is usually measured by the amount of visual extinction ($A_V = A_{5500A}$) of the incident radiation field caused by the dust column to this depth. For instance, $A_V = 1$ corresponds to a reduction by a factor of 2.5 in the incident visual flux and, by assuming a constant ratio of gas to dust, corresponds to a hydrogen column density of about $2 \times 10^{21}\,\mathrm{cm}^{-2}$. The penetrating FUV photons dictate the chemistry through photoionization and photodissociation processes. The main chemical reactions that happen in a PDR include the formation and the photodissociation of H_2, the formation and the photodissociation of CO, and the photoionization of C into C II. PDRs are very important in galaxy studies since they dominate the infrared and sub-millimetre emission spectra. For instance, [C II] , as the brightest FIR line, emerges from PDRs as well as molecular gas (see Sec. 2.1.2).

2.1.2 ISM cooling through fine structure lines

The multi-phase gas in the ISM of galaxies cools through the conversion of kinetic energy into luminosity by collision processes. Depending on the phase of the gas, the cooling mechanism is different. Both atoms and molecules can contribute to the cooling process.

Coolings through atomic transitions can be divided into two groups; the permitted transitions and forbidden ones. In the first group, the term permitted means that these transitions are allowed by usual quantum mechanics selection rules in a certain atom or ion. Lyman series of

atomic hydrogen is one of the dominant coolants through permitted transitions in the ISM with $T \sim 10^4\,\mathrm{K}$. Specifically, the Lyman-α emission line is produced by the electron transition from $n = 2$ orbital to $n = 1$ orbital of atomic hydrogen with a wavelength of $\lambda_{\mathrm{rest}} = 1216\text{Å}$. Such radiation has been detected in both local and far away star-forming galaxies.

The second group is cooling through atomic fine-structure emission lines which are also called forbidden lines. When the temperature of the ISM is below $10^4\,\mathrm{K}$, it is quite difficult for gas to cool through permitted transitions since the number of electrons with enough energy to excite such transitions is very limited. While permitted transitions occur between energy levels with different principal quantum numbers, the forbidden transitions occur between fine-structure energy levels which are caused by the interaction between orbital and spin angular momenta of electrons. An atom or ion shows a fine-structure level when their electrons in the outermost shell have both non-zero total orbital angular momentum and non-zero spin angular momentum. Since H and He do not have such a property, fine-structure cooling in the ISM is dominated by carbon and oxygen (Wolfire et al., 1995).

Carbon in both atomic and ion forms has fine structure levels. Since the atomic carbon can be photoionized by photons with energies $E > 11.26\,\mathrm{eV}$ which is below the Lyman limit, carbon can be found mainly in the form of C II in the diffuse ISM. Singly ionized carbon has two fine structure levels on its ground state, an upper level with total angular momentum $J = 3/2$ and a lower level with $J = 1/2$. The transition between these two levels at $\lambda = 158\mu\mathrm{m}$ is very easy to excite since the energy separation between them is $\Delta E/k_{\mathrm{B}} \sim 92\,\mathrm{K}$. These properties are such that the line can arise from nearly every phase in the ISM except WIM and HIM. It can emerge from diffuse HI clouds, diffuse ionized gas, molecular gas, and PDRs. Indeed, [C II] at $158\mu\mathrm{m}$ is typically considered as the strongest FIR line (Stacey et al., 1991) which carries typically 1% of the total infrared luminosity (De Looze et al., 2014), therefore it is one of the most efficient coolants of the ISM (Malhotra et al., 1997; Luhman et al., 1998, 2003) (see Fig. 2.2).

The mechanism to produce transitions in any two-level system like C II fine structure levels can be explained with a general formalism.

Optically-thin two-level system

Imagine an atomic system with two bound states, a lower level l and an upper level u, with statistical weights g_l and g_u, separated by an energy E_{ul}. If we assume that the number density of the atoms in the lower level is n_l and the number density in the upper level as n_u, the total number density of the atoms then follows is $n = n_l + n_u$. For simplicity, we assume a static ($dn/dt = 0$), monoatomic (H) system without additional chemical reactions. The level population of this system can be altered either by upwards ($l \rightarrow u$) or downwards ($u \rightarrow l$) transitions. The upwards transition can be triggered by collisional excitation (with electrons, protons and other species such as He atoms and molecules) or the absorption of a photon from the interstellar

radiation field. The downwards transition, in turn, can occur due to collisional de-excitation or the emission of a photon. The rates of change of n_l and n_u can be written as

$$\frac{dn_u}{dt} = C_{lu}n_l - C_{ul}n_u - A_{ul}n_u - B_{ul}I_\nu n_u + B_{lu}I_\nu n_l \,, \tag{2.1}$$

$$\frac{dn_l}{dt} = -C_{lu}n_l + C_{ul}n_u + A_{ul}n_u + B_{ul}I_\nu n_u - B_{lu}I_\nu n_l \,, \tag{2.2}$$

where C_{lu} and C_{ul} are the collisional excitation and de-excitation rates, A_{ul}, B_{ul} and B_{lu} are the three Einstein coefficients for the transition, describing spontaneous emission, stimulated emission and absorption, respectively. I_ν is the specific intensity of the local radiation field at a frequency $\nu_{ul} = E_{ul}/h$.

We assume that there are more than one colliding species in the system with number densities n_i. We also consider that the level populations of the system have reached a statistical equilibrium (i.e. $dn_u/dt = dn_l/dt$). Therefore, n_l and n_u will be linked with an algebraic equation

$$(\Sigma_i n_i C^i_{lu} + B_{lu}I_\nu)n_l = (\Sigma_i n_i C^i_{ul} + A_{ul} + B_{ul}I_{ul})n_u \,. \tag{2.3}$$

If the gas is optically thin (i.e. the emitted photon can leave the system without being absorbed) and if the intensity of radiation field at frequency ν_{ul} is small, one can ignore the contribution of incident ratiation fiels I_ν in eq. 2.3

$$\frac{n_u}{n_l} = \frac{\Sigma_i n_i C^i_{lu}}{\Sigma_i n_i C^i_{ul} + A_{ul}} \,. \tag{2.4}$$

The principle of detailed balance states that in local thermal equilibrium (LTE), the rate at which collisions cause transitions from level l to level u must be the same as the rate at which they cause transitions from level u to level l

$$n_l n_i C^i_{lu} = n_u n_i C^i_{ul} \,. \tag{2.5}$$

In LTE the ratio between n_l and n_u is given by the Boltzmann distribution

$$\frac{n_u}{n_l} = \frac{g_u}{g_l} e^{-E_{ul}/k_B T} \,. \tag{2.6}$$

Therefore, we have

$$\frac{n_u}{n_l} = \frac{g_u}{g_l} \frac{e^{-E_{ul}/k_B T}}{1 + A_{ul}/\Sigma_i C^i_{ul} n_i} \,. \tag{2.7}$$

It is convenient to define a critical density $n^{\rm cr}_i$ for each colliding species as

$$n^{\rm cr}_i \equiv \frac{A_{ul}}{C^i_{ul}} \,, \tag{2.8}$$

which determines whether de-excitation due to collisions with that species dominates spontaneous radiative decays. When $n_i \gg n_i^{cr}$, collisions dominate and level population tends to its LTE values. While if $n_i \ll n_i^{cr}$, radiative decay dominates. In this regime we have

$$\frac{n_u}{n_l} \simeq \frac{\Sigma_i n_i C_{lu}^i}{A_{ul}}\,, \tag{2.9}$$

and hence the emissivity of the transition $\varepsilon \equiv A_{ul} n_u$ becomes

$$\varepsilon \simeq n_i n_l C_{lu}^i\,. \tag{2.10}$$

If one considers the total density of atoms as $n = n_l + n_u$, the radiative cooling rate (Λ_{ul}^i) of the collection of atoms (i.e. the rate at which the atoms emit photons multiplied by the energy of the photons) becomes

$$\Lambda_{ul}^i(T) = n_i n E_{ul} C_{lu}^i(T)\,. \tag{2.11}$$

In the high-density regime, where $A_{ul} \ll n_i C_{ul}^i$, we have

$$n_u \simeq \frac{g_u}{g_l} e^{-E_{ul}/k_B T} n_l\,. \tag{2.12}$$

Therefore the cooling rate becomes

$$\Lambda_{ul}^i(T) = n A_{ul} \frac{(g_u/g_l) e^{-E_{ul}/k_B T}}{1 + (g_u/g_l) e^{-E_{ul}/k_B T}} E_{ul}\,. \tag{2.13}$$

Based on these analyses, the cooling rate scales with the density squared in the low- density regime ($\Lambda_{ul}^i \propto n^2$) while in the high-density regime the scaling relation is linear ($\Lambda_{ul}^i \propto n$).

2.2 Semi-analytical insights into EoR galaxies

2.2.1 Kinematics of ideal disk galaxies probed by [CII] line

In this section, we study the possibility of using [C II] line emission as a tracer of gas kinematics in the EoR. The kinematics observable that we model in this section is the line profile. We develop a simple analytical model of a disc galaxy to elucidate the physics involved in shaping the line profile, and build a controlled environment for the analysis of [C II] emission from high-z galaxies.

Analytical model for the [C II] emission from EoR galaxies

The [C II] transition can be excited via collisions of C II atoms with other species present in the gas. Following Dalgarno & McCray 1972a, we consider a partially ionised volume of gas in which carbon atoms are maintained in C II stage by far UV radiation in the Habing band ($6 < h\nu/\mathrm{eV} < 13.6$,

Habing 1968). The [C II] emissivity (ε), excited by collisions with free electrons and hydrogen atoms, is written as a function of the gas (n), electron (n_e) and neutral hydrogen (n_H) number densities as follows (see Sec. 2.1.2)

$$\varepsilon(n,T) = n\,(\frac{Z}{Z_\odot})\,A_C\left[\frac{n_H}{1+n_H/n_H^{\rm cr}}\Lambda^H + \frac{n_e}{1+n_e/n_e^{\rm cr}}\Lambda^e\right], \tag{2.14}$$

where Λ^H and Λ^e are the specific cooling rates due to collision with H atoms and free electrons at temperature T. Z is the metallicity of the gas, $Z_\odot = 0.0134$ is the solar metallicity (Asplund et al., 2009), and $A_C = 2.69\times10^{-4}$ is the adopted solar ratio of carbon to hydrogen number densities (Asplund et al., 2009). Note that we have included in an approximate manner the effects of the critical densities $n_H^{cr} = 3000\,{\rm cm}^{-3}$ and $n_e^{cr} = 8\,{\rm cm}^{-3}$ (Goldsmith et al., 2012) for hydrogen and electron collisions to ensure the validity of eq. 2.14 in high density regimes.

In our model, we require ε to vanish in highly ionised regions ($T > 10^4\,{\rm K}$) where our assumption that all the carbon is singly ionised would not be valid anymore. In this treatment, we also assume that the [C II] line is optically thin (see discussion in Goldsmith et al., 2012), which means that the integrated intensity is proportional to the C II column density along the l.o.s., irrespective of the optical depth of the medium. In this approximation, for each gas parcel of volume V, we then compute the [C II] luminosity as $L = \varepsilon V$.

CMB effects

The CMB has a thermal black body spectrum at a local temperature of $T^0_{\rm CMB} = 2.725$ K, increasing with redshift as $T_{\rm CMB}(z) = (1+z)\,T^0_{\rm CMB}$. Assuming LTE, this sets the minimum temperature of the ISM, which at high redshift becomes non-negligible. Any emission coming from the ISM will be seen against the CMB background. As discussed in Da Cunha et al. 2013, the contrast of the emission against the CMB radiation in the rest-frame is given by

$$\Delta I_\nu = [B_\nu(T_s) - B_\nu(T_{\rm CMB})]\left(1-e^{-\tau}\right), \tag{2.15}$$

where $B(\nu)$ is the Planck function and T_s is the spin temperature of the FIR line. Assuming the [C II] line to be optically thin in the sub-mm band, i.e. $e^{-\tau_\nu} \approx 1-\tau_\nu$, the ratio between the

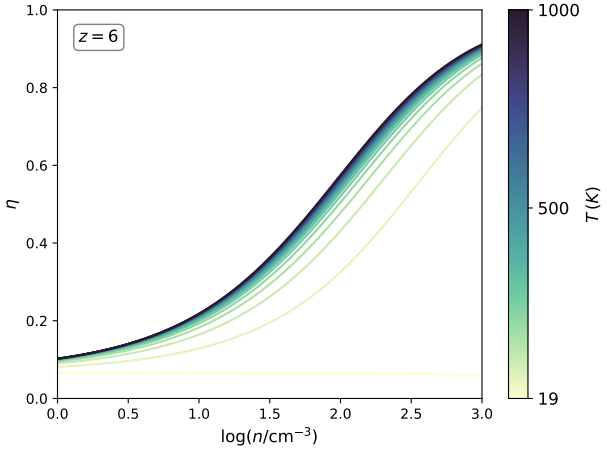

Figure 2.3: CMB suppression of [C II] emission (η) as a function of gas number density (n). Different lines indicate different gas temperature (T). The suppression is calculated at redshift $z = 6$ via eq. 2.16; see the text for the details of the calculation (Figure 1 in Kohandel et al. 2019).

flux observed against the CMB and the intrinsic flux emitted is[1]:

$$\eta \equiv \frac{F^{\rm obs}_{\nu/(1+z)}}{F^{\rm int}_{\nu/(1+z)}} = 1 - \frac{B_\nu(T_{\rm CMB})}{B_\nu(T_s)}\,. \tag{2.16}$$

As T_s approaches $T_{\rm CMB}$, $\eta \to 0$; in this case the CMB completely suppresses the line flux. For [C II], the spin temperature is defined using the ratio of the thermal equilibrium population of the upper (u: $2_{P_{3/2}}$), and lower (l: $2_{P_{1/2}}$) level of fine structure transition

$$\frac{n_u}{n_l} = \frac{g_u}{g_l} e^{-T_*/T_s}\,, \tag{2.17}$$

where $T_* = 91.7\,{\rm K}$ is the equivalent temperature of the level transition, and $g_u = 4$, $g_l = 2$ are the statistical weights. Following the procedure used in Vallini et al. 2015 (see also Pallottini et al., 2015), T_s is defined as

$$\frac{T_*}{T_s} = \ln \frac{A_{ul}(1 + \frac{c^2 I_\nu}{2h\nu}) + n_e C^e_{ul} + n_H C^H_{ul}}{A_{ul}(\frac{c^2 I_\nu}{2h\nu^3}) + n_e C^e_{ul} e^{-T_*/T} + n_H C^H_{ul} e^{-T_*/T}}\,, \tag{2.18}$$

where A_{ul} is the Einstein coefficient for spontaneous emission and C^e_{ul} (C^H_{ul}) is the collisional de-excitation rate for collisions with e (H-atoms). For the [C II] line emission $A_{ul} = 2.36 \times 10^{-6}\,{\rm s}^{-1}$ (Suginohara et al., 1999) and $C^e_{lu}(T) = (8.63 \times 10^{-6}/g_l\sqrt{T})\gamma_{lu}(T)e^{-T_*/T}$ with $\gamma_{lu}(T)$ being the effective collision strength computed based on Keenan et al. 1986. $C^H_{lu}(T)$ is tabulated in Dalgarno & McCray 1972a.

As discussed in Gong et al. 2012, at high redshifts the soft UV background at 1330 Å produced by the first galaxies and quasars can pump the C II ions from the energy level $2s^2 2p\ 2P_{1/2}$ to $2s2p^2\ 2D_{3/2}$ ($\lambda = 1334.53$ Å), and $2s^2 2p\ 2P_{3/2}$ to $2s^2 2p^2\ 2D_{3/2}$ ($\lambda = 1335.66$ Å). This pumping effect can lead to the [C II] transition $2D_{3/2} \to 2P_{3/2} \to 2P_{1/2}$ which would mix the levels of the [C II] line. Similarly to Vallini et al. 2015, we add this UV pumping effect in eq. 2.18.

In summary, with n_e, n_H and T we can compute the spin temperature of the [C II] line using eq. (2.18) and the CMB suppression using eq. (2.16). In Fig. 2.3, the CMB suppression factor, η, is shown as a function of gas density for different temperatures and for $z = 6$. We fix the metallicity to be $Z = 0.5\,{\rm Z}_\odot$ and vary the temperature. [2] The cooler the gas, the more the [C II] emission is suppressed. Note that, independently of T, the emission is suppressed by about 90% for low-density gas ($n \lesssim 1\,{\rm cm}^{-3}$), because collisions are not efficient enough to decouple T_s from the temperature of the CMB, in agreement with results in the literature (Gong et al., 2012;

[1] FIR flux observed against CMB is defined as $F^{\rm obs}_{\nu/(1+z)} = (1+z)A\Delta I_\nu/d_L^2$, where A is the physical area of the galaxy and d_L is the luminosity distance.

[2] In this case the ionisation fraction of the gas is computed by solving the equilibrium between collisional ionisation, ionisation due to cosmic rays and X-rays and recombination rates for H and He (Wolfire et al., 1995). It depends on the hydrogen number density, temperature, and metallicity of the gas.

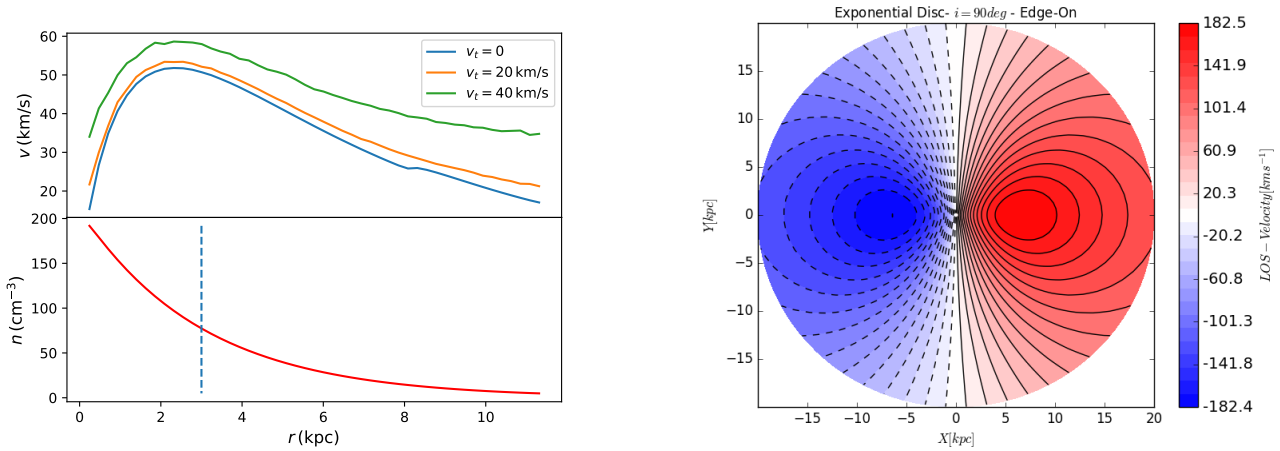

Figure 2.4: Semi-analytical model of an exponential disk for kinematics analysis

Vallini et al., 2015; Pallottini et al., 2015).

This general formalism for modeling the [C II] emission for EoR galaxies can be applied to either semi-analytical models of galaxies or to zoom-in simulations of galaxies (see Chapter 3).

Galaxy spectra

We consider a geometrically-thin disk and assume that the surface-brightness profile of the disk has an exponential form

$$I(r) \propto \exp(-r/r_d)\,, \tag{2.19}$$

where r_d is the disk scale length. If the mass surface density is also exponential with the same scale length, i.e.

$$\Sigma(r) = \Sigma_0 \exp\left(-r/r_d\right), \tag{2.20}$$

the potential that such a disk generates at the equatorial plane is (Binney & Tremaine, 2008):

$$\Phi(r,0) = -\pi G \Sigma_0 r [I_0(y)K_1(y) - I_1(y)K_0(y)]\,, \tag{2.21}$$

where $y = r/2r_d$ and I_n, K_n are the modified Bessel functions of first and second kind, respectively. If we differentiate this potential with respect to r, we obtain the circular speed of the exponential disk (Freeman, 1970)

$$v_c^2(r) = 4\pi G \Sigma_0 r_d y^2 [I_0(y)K_0(y) - I_1(y)K_1(y)]\,. \tag{2.22}$$

Using the circular velocity v_c, we can define the velocity along the l.o.s. as follows

$$v(r,\theta,\phi)^2 = 4\pi G \Sigma_0 r_d y^2 [I_0(y)K_0(y) - I_1(y)K_1(y)] \cos^2\phi \sin^2\theta\,, \tag{2.23}$$

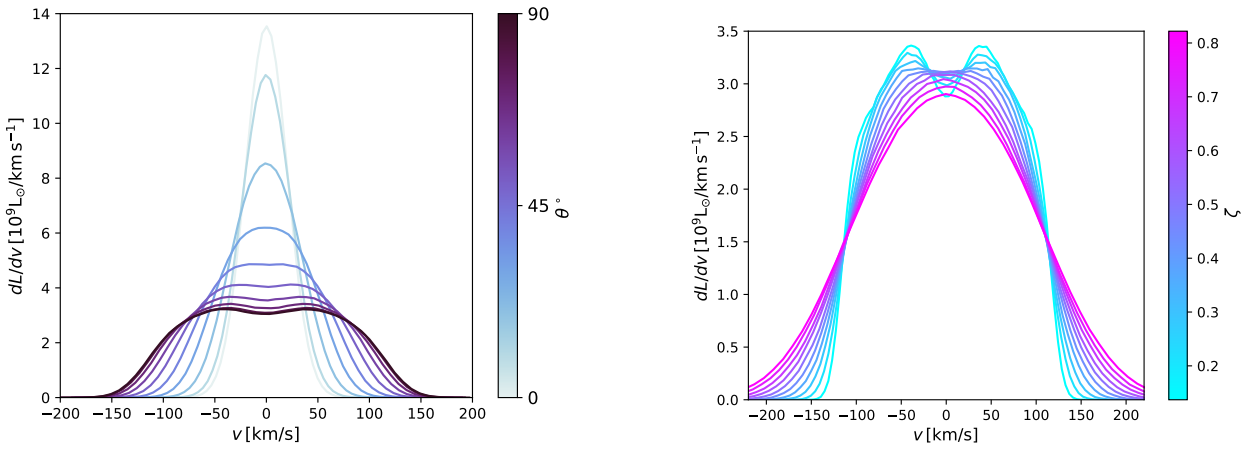

Figure 2.5: Spectral profile of a geometrically thin disk with an exponential profile (Figure 2 in Kohandel et al. 2019). *Left panel*: Disk inclination is between $\theta = 0°$(face-on) and $\theta = 90°$ (edge-on). In addition to rotational velocities, isotropic turbulent motions extracted from a Gaussian distribution having an r.m.s. amplitude of $20\,\mathrm{km\,s^{-1}}$ are added to the disk. *Right panel*: The inclination of the disk is fixed to be edge-on and we vary the amplitude of turbulent motions. Both inclination and large turbulent motions broaden the wings of the line and lower the amplitude by a factor of ~ 4 and ~ 1.2 respectively.

where θ is the angle between the l.o.s axis and the normal to the disk plane and ϕ is the polar angle on the plane of the face-on disk. We assume a thin disk with $\Sigma_0 = 1000\,\mathrm{M_\odot/pc^2}$, $r_d = 3\,\mathrm{kpc}$, and a thickness of 100 pc.

For our kinematic analysis, it is useful to define a 2D Cartesian grid centred on the galaxy centre. We choose a grid of size $(24\,\mathrm{kpc})^2$ divided into a total of $(4 \times 10^3)^2$ cells, i.e. each cell has a linear resolution of 6 pc. In each cell, surface density and velocities are computed using eqs. 2.20 and 2.23, respectively. We also account for random turbulent motions (i.e. deviations from perfect circular orbits) by adding in each cell a random velocity, the components (t) of which are extracted from a Gaussian distribution

$$p(t) = \frac{1}{\sqrt{2\pi {v_t}^2}} e^{-t^2/2v_t^2}\,, \tag{2.24}$$

where v_t is the standard deviation of the distribution. We assume isotropic turbulence so the three added components have the same magnitude.

Assuming a uniform temperature of 100 K for the disk[3], an ionisation fraction of $x_e = 0.2$, and a metallicity of $Z = \mathrm{Z_\odot}$, we compute the [C II] luminosity using the model described in Sec. 2.2.1. Having the l.o.s velocity and luminosity for each cell, we extract the integrated spectral profile by computing the histogram of velocities weighted by the corresponding value of [C II] luminosity.

[3]The reference temperature $T = 100\,K$ is the mean temperature found for molecular gas in our high-z galaxies simulations, see Fig. 8 in Pallottini et al. 2017b.

First, we explore the effect of the inclination of the disk by focusing on the spectral profile of the emission. In the left panel of Fig. 2.5, we show the [C II] spectra from our disk galaxies including turbulent velocities with $v_t = 20\,\mathrm{km\,s^{-1}}$. Different lines correspond to a different inclination of the disk. As discussed by Elitzur et al. 2012, the spectral profile of such a disk in the edge-on view ($\theta = 90°$) should show a double peak structure. We see in Fig. 2.5 that inclining the disk from face-on view ($\theta = 0$) to the edge-on case smoothly changes the spectral profile from having a Gaussian shape to the double peak structure. Also inclining the disk towards edge-on produces broader wings compared to the face-on case. In addition, the peak amplitude of the line decreases by a factor of ~ 4 in the edge-on case. These effects happen because by inclining the disk towards the edge-on view, $\sin(\theta) \to 1$ (see eq. 2.23) allows for stronger contributions from high l.o.s. velocities. Consequently, the peak amplitude of the line decreases to keep the total [C II] luminosity, given by the integral below the curve, constant.

Random motions also change the spectral profile. In the right panel of Fig. 2.5, we set the inclination of the disk to be edge-on (double peak profile) and then vary v_t. For each of the cases with different turbulence velocities, we calculate $\zeta = v_t/\bar{v}_c$ in which $\bar{v}_c \simeq 75\,\mathrm{km\,s^{-1}}$ is the mass-weighted average circular velocity of the exponential disk. We find (Fig. 2.5, right panel) that if $\zeta > 0.5$ the double peak profile is erased, which means that turbulent motions can mask the presence of the disk in the spectrum. Furthermore, and similarly to the effect of inclination discussed above, turbulence broadens the line wings and decreases the line intensity at the peak by a factor of ~ 1.2.

With these controlled case examples, we conclude that depending on the inclination of the disk and the amount of turbulent motions, emission from a rotating disk might produce quite a range of different line profiles. In particular, inclination and turbulence have a degenerate effect in changing the spectral shape of emission. The double peak signature of our rotating edge-on disk is erased either by changing the inclination ($\theta < 70°$) or significant turbulent velocities ($\zeta > 0.5$). Similarly, the single Gaussian shape can be the signature of a highly turbulent disk or simply a face-on view of a disk with moderate turbulent motions.

In Chapter 3, the kinematics of [C II] line emission for a more realistic galaxy is discussed in detail. For a better comparison with the analysis of the simulation, it is convenient to define two cases of our analytical model; Smooth Disk: a smooth disk with $\zeta < 0.5$ featuring a symmetric double-peak profile in the edge-on view and a single Gaussian profile in the face-on view and Turbulent dominated Disk: a Disturbed Disk with $\zeta > 0.5$, which has a smooth single Gaussian spectral profile both in the face-on and edge-on view.

2.2.2 Physics of [CII]-SFR relation

We saw in Sec. 1.2.3 that it is still debated if there is a relation between the [C II] lunimosity and the star formation rate of the galaxy. To address this question, an analytical model developed in

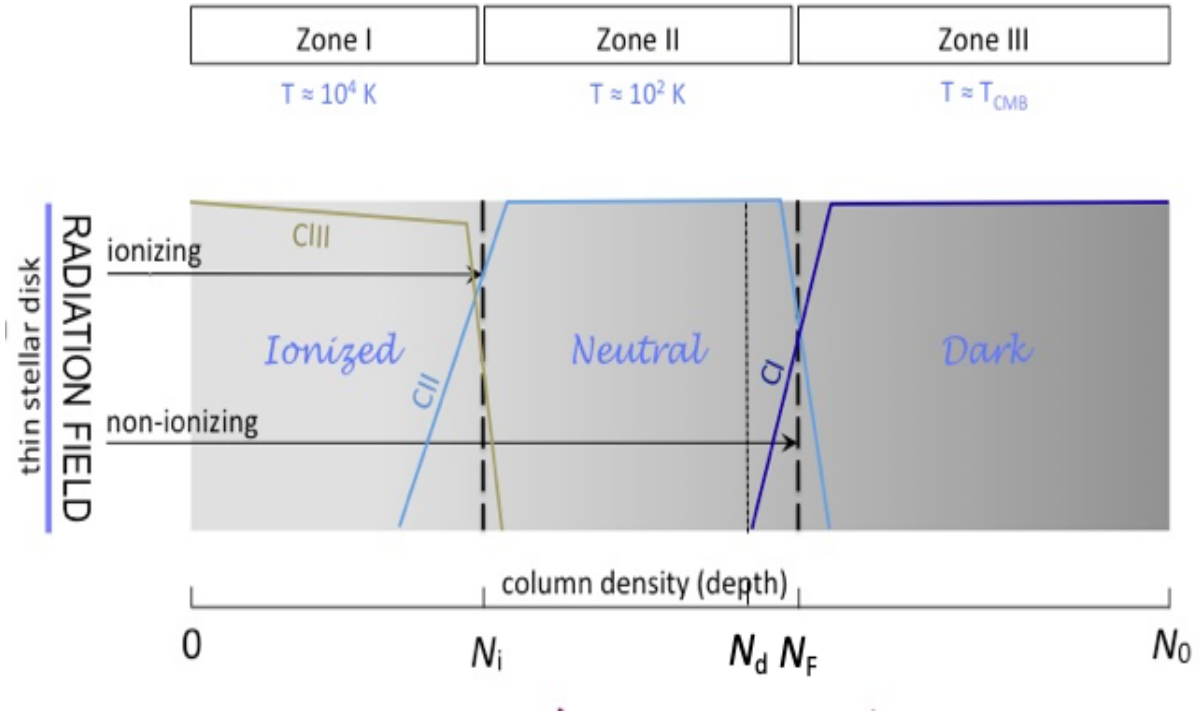

Figure 2.6: Schematic ionisation structure of slab in our galaxy model. The radiation field produced by the thin layer of stars located at the galaxy mid-plane illuminates the overlying gas slab of total column density N_0. Zone I, extending up to N_i, is ionised and C is mostly in C III form. In Zone II only non-ionising ($h\nu < 1Ryd$) FUV photons penetrate; nevertheless these can keep carbon in C IIform. We also highlight the column density N_d at which the dust optical depth to non-ionising UV photons becomes equal to unity. Finally, beyond N_F even FUV radiation is totally absorbed and carbon is neutral. (Figure 1 in Ferrara et al. 2019)

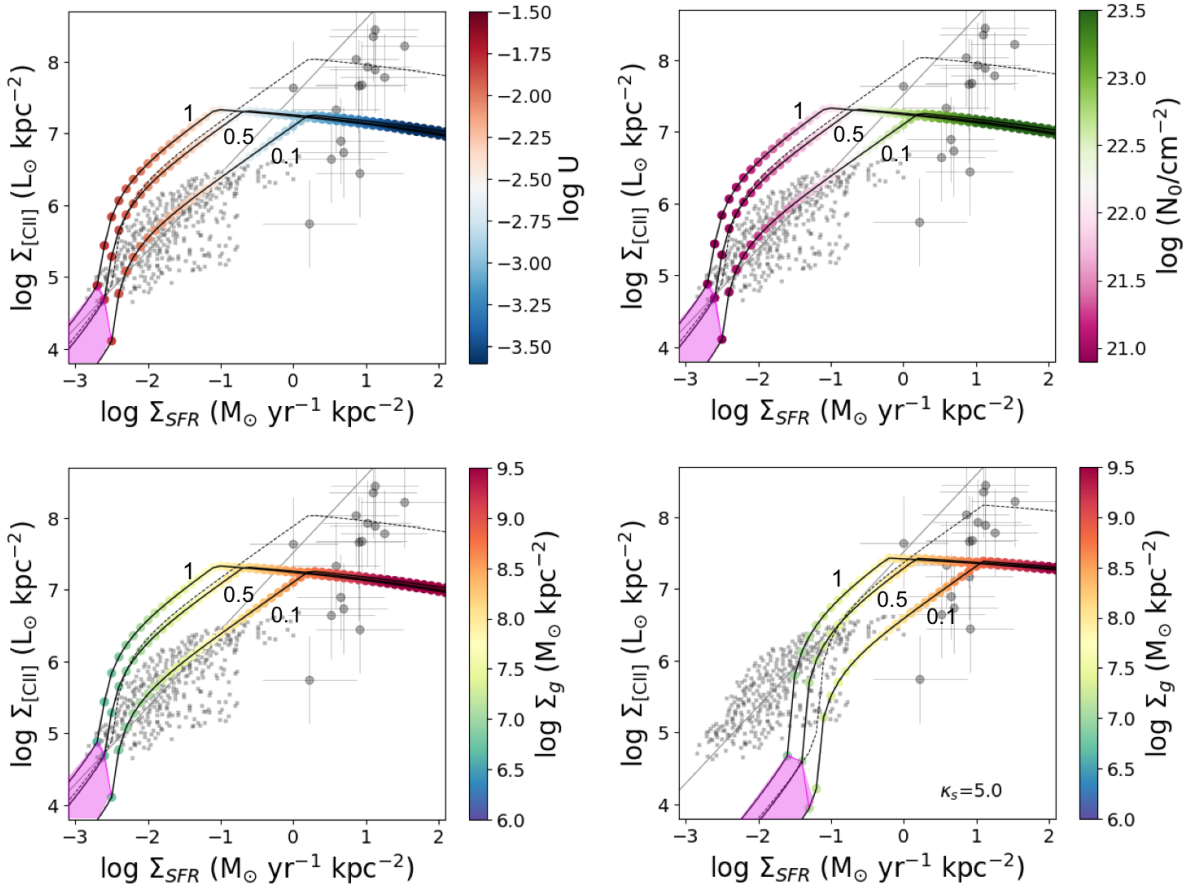

Figure 2.7: Predicted $\Sigma_{\rm CII}$ - $\Sigma_{\rm SFR}$ relation for three metallicities $Z = 0.1, 0.5, 1$ (indicated by the labels), and gas density $n = 500\,{\rm cm}^{-3}$. For reference, the thin dashed line shows the case $Z = 0.1$ and $n = n_{\rm crit} = 3027\,{\rm cm}^{-3}$. Model points are colour-coded according to values of ionisation parameter in panel (a), column density (b), and Σ_g (c-d). In panel (d) we set $\kappa_{\rm s} = 5$ (see eq. 2.27); this value is typical of starburst galaxies (e.g. Daddi et al., 2010). Gray small crosses are the De Looze et al. 2014 data for a sample of spatially resolved local dwarf galaxies; the best fit to the data is shown by the thin solid line. Points with errors are either single galaxies without any sub-component, and data for individual components within galaxies taken from the sample of $z > 5$ sources analized by Carniani et al. 2018a (Figure 5 in Ferrara et al. 2019)

Ferrara et al. 2019 aims to understand what determines the [C II] luminosity of a galaxy and what is the physical reason for the L_{CII}-SFR relation.

The galaxy is modelled as a plane parallel slab of gas with uniform number density n, metallicity Z, total gas column density N_0, illuminated by a source emitting both ionising (photon energy $h_P\nu > h_P\nu_L = 13.6$ eV) and non-ionising radiation with specific energy flux (erg cm^{-2}s^{-1}Hz^{-1})

$$F_\nu = F_L \left(\frac{\nu}{\nu_L}\right)^{-\beta} , \tag{2.25}$$

where F_L is the flux at the Lyman limit $\nu_L = 3.2 \times 10^{15}$ Hz, $\beta = 4 - 5$ for normal Pop II stars, and $\beta \simeq 1.5$ for AGN-like sources. N_0 is considered as a parameter of the model. Fig. 2.6 portraits a sketch of the ionisation structure of the slab. Three different zones are characterized by column densities. The ionising photons create a H II region (Zone I) in which carbon is mostly in C III form, extending up to a column density N_i, which is smaller than Stromgren length since we assume that there is also dust. Beyond N_i the gas becomes neutral (Zone II), but non-ionising UV photons maintain carbon in a singly ionised state. The neutral layer extends up the point at which UV photons are absorbed by dust and H_2 molecules, at a column density N_F which slightly exceeds N_d, where the optical depth due to dust reaches unity. At even larger depths (Zone III) the gas is UV dark, and the only heating is provided by cosmic rays (and CMB at high redshift). In this region, gas is mostly in molecular form and carbon is found in a neutral state.

The [C II] line flux emitted by a slab with total gas column density N_0 depends on whether the H II region is ionisation- or density-bounded. We assume that the H II layer (Zone I) has a temperature $T = 10^4$ K, whereas in Zone II we set $T = 10^2$ K. The abundance of carbon is taken to be $\mathcal{A}_\mathcal{C} = 2.7 \times 10^{-4}$ (Asplund et al., 2009), and we linearly scale it with $\mathcal{D}$, or equivalently, given our assumption of a constant dust-to-metal ratio, with Z. The [C II] line flux (erg cm^{-2}s^{-1}) emerging from the slab is given by

$$F_{[\rm CII]} = n\mathcal{A}_C\mathcal{D}\left\{\Lambda^{(4)}_{[\rm CII]} N_{\rm HI}(y_i) + \Lambda^{(2)}_{[\rm CII]}\left[\min(N_F, N_0) - N_i\right]\right\} , \tag{2.26}$$

where n is the total gas density and cooling functions $\Lambda^{(n)} = \Lambda(T = 10^n\text{K})$. It turns out that the ionized part is always sub-dominant and the dominant term in eq. 2.26, depends on the balance between three column densities in galaxies. To predict from model the observed $\Sigma_{\rm CII} - \Sigma_{\rm SFR}$ relation, we use the empirical Kennicutt-Schmidt (KS) average relation, as given, e.g. by Heiderman et al. 2010,

$$\Sigma_{\rm SFR} = 10^{-12}\kappa_{\rm s}{\Sigma_g}^m \qquad (m = 1.4) , \tag{2.27}$$

where we have allowed for deviations from the relation through the "burstiness" parameter $\kappa_{\rm s}$. Values of up to $\kappa_{\rm s} = 100$ have been measured for sub-millimeter galaxies (see e.g. Hodge et al., 2014). Galaxies with $\kappa_{\rm s} > 1$ show a larger SFR per unit area with respect to those located on

the KS relation having the same value of Σ_g (Hodge et al., 2014). Fig. 2.7 shows the Predicted $\Sigma_{\rm CII}$ - $\Sigma_{\rm SFR}$ relation along with local De Looze et al. 2014 data points as well as Carniani et al. 2018a $z > 5$ sample of galaxies. From these plots, we see that high-z galaxies are totally disjoint from the local galaxies. High-z galaxies are characterized by low ionization parameter. The model predicts there is a flattening/saturation of the $\Sigma_{\rm CII}$; when SFR increases above some threshold, the curve does not continue to grow. This is the point that the galaxy has limited amount of gas that can be shinned by UV photons (N_F). For starburst galaxies ($\kappa_{\rm s} = 5$), all curves are shifted to the right. The reason is that the galaxy has less gas to shine and count in [C II] emission. So starburst galaxies have lower [C II] emission in comparison to the stars they have.

We study this relation in a more realistic model of an EoR galaxy in the next section (see Fig. 2.11).

2.3 SERRA: a suite of zoom-in simulations of EoR galaxies

The SERRA[4] suite of simulations focuses on zooming-in on the formation and evolution of galaxies in the EoR starting from cosmological initial conditions. In particular, SERRA targets $M_\star \sim 10^8 - 10^{10} M_\odot$ galaxies at $z = 6$. The details of the models adopted in these simulations can be found in Pallottini et al. 2017a,b, 2019. Each simulation contains 10-30 galaxies. Since most of our dynamics analysis (see Chap. 3 and 4) is based on two particular galaxies (called Althæa and Freesia) in SERRA suit, we explain their modeling schemes and main properties in the following.

Althæa and Freesia are two prototypical LBG galaxies that are hosted by a $M_{\rm h} \simeq 10^{11} {\rm M}_\odot$ DM halo at $z = 6$. The simulation setup for Althæa and Freesia is almost identical with just one important difference. In the case of Freesia, a self-consistent on-the-fly radiative transfer is coupled to the hydrodynamical simulations while in the case of Althæa interstellar radiation field (ISRF) is treated approximately. In Pallottini et al. 2019, the relevance of coupling self-consistently radiative transfer to the simulations is thoroughly discussed.

2.3.1 Simulation set-up and modeling schemes

Both simulations are carried out using a customised version of the Adaptive Mesh Refinement (AMR) code RAMSES[5](Teyssier, 2002). They both start from cosmological initial conditions [6] at $z = 100$ generated with MUSIC (Hahn & Abel, 2011). Then at $z \simeq 6$ the simulations zoom in the DM halo which is hosting the targeted galaxy. The total simulation volume is $(20\,{\rm Mpc/h})^3$ that is evolved with a base grid with 8 levels (gas mass $6 \times 10^6 {\rm M}_\odot$); the zoom-in region has a volume

[4] Greenhouse in Italian.

[5] `https://bitbucket.org/rteyssie/ramses`

[6] We assume cosmological parameters compatible with *Planck* results: ΛCDM model with total matter, vacuum and baryonic densities in units of the critical density $\Omega_\Lambda = 0.692$, $\Omega_m = 0.308$, $\Omega_b = 0.0481$, Hubble constant $\rm H_0 = 100\,h\,km\,s^{-1}\,Mpc^{-1}$ with $\rm h = 0.678$, spectral index $n = 0.967$, $\sigma_8 = 0.826$ (Planck Collaboration et al., 2014).

of $(2.1\,\mathrm{Mpc/h})^3$ and is resolved with 3 additional levels of refinement, thus yielding a gas mass resolution of $m_b = 1.2 \times 10^4 \mathrm{M}_\odot$. In this zoom-in region, it is allowed for 6 additional levels of refinement by adopting a Lagrangian-like criterion. This enables us to reach scales of $l_{\rm res} \simeq 30\,\mathrm{pc}$ at $z = 6$ in the densest regions, i.e. the most refined cells have mass and size typical of Galactic MCs (e.g. Federrath & Klessen, 2013).

Gravity

In RAMSES, the evolution of DM particles is computed with a particle-mesh solver. Gravity is accounted for by solving the Poisson equation on the AMR grid via a multi-grid scheme with Dirichlet boundary conditions on arbitrary domains (Guillet & Teyssier, 2011).

Hydrodynamics

Euler equations govern gas evolution that in RAMSES are numerically solved by adopting a Monotone Upstream-centered Scheme for Conservation Laws (MUSCL, e.g. Toro 2009), a second-order extension of the Godunov method (Godunov 1959).

Chemical network In SERRA, a non-equilibrium chemical network is implemented by using KROME[7] (Grassi et al., 2014). The selected network includes H, H^+, H^-, He, He^+, He^{++}, H_2, H_2^+ and electrons. The network follows a total of 48 reactions[8], including photo-chemistry, dust processes and cosmic ray-induced reactions (Bovino et al., 2016). Individual initial conditions for various species and ions are computed accounting for the chemistry in a primordial Universe (Galli & Palla, 1998).

Metals and dust Metallicity (Z) is tracked as the sum of heavy elements, and we assume solar abundance ratios of different metal species (Asplund et al., 2009). Dust evolution is not explicitly tracked during the simulation. We make the assumption that the dust-to-gas mass ratio scales with metallicity, i.e. $\mathcal{D} = \mathcal{D}_\odot(Z/\mathrm{Z}_\odot)$, where $\mathcal{D}_\odot/\mathrm{Z}_\odot = 0.3$ for MW (e.g. Hirashita & Ferrara, 2002).

Dust provides a formation channel for molecular hydrogen: the formation rate of H_2 on dust grains is approximated following Jura 1975:

$$R_{\rm H2-dust} = 3 \times 10^{-17} n\, n_{\rm H} (\mathcal{D}/\mathcal{D}_\odot)\,\mathrm{cm^{-3}\,s^{-1}}\,, \tag{2.28}$$

where n and $n_{\rm H}$ are the total and Hydrogen gas densities, respectively. We note that for $\mathcal{D} \geq 10^{-2}\mathcal{D}_\odot$ the dust channel is dominant with respect to gas-phase formation.

[7] `https://bitbucket.org/tgrassi/krome`

[8] The reactions, their rates, and corresponding references are listed in App. B of (Bovino et al., 2016): we use reactions from 1 to 31 and 53, 54, from 58 to 61, and from P1 to P9; the rates are reported in Tab. B.1, Tab. B.2, and Tab. 2 of Bovino et al. 2016, respectively.

We adopt an initial metallicity floor $Z_{\rm floor} = 10^{-3}{\rm Z}_{\odot}$ since at $z \geq 40$ our resolution does not allow us to reach a density high enough for efficient H_2 formation in the pristine gas of mini-halos and consequently recover the formation of first stars (e.g. O'Shea et al., 2015; Smith et al., 2018). Such floor only marginally affects the gas cooling time and it is compatible with the metallicity of diffuse enriched IGM in cosmological metal enrichment simulations (e.g. Pallottini et al., 2014).

To summarise, metals and dust are treated as passive scalars and we allow for metal enrichment by SN explosions and by winds from massive stars.

Gas thermodynamics In SERRA, the evolution of thermal and turbulent energy content of the gas is modeled. The thermal energy is evolved by the thermo-chemical framework set with KROME (see Pallottini et al., 2017b, for details). The turbulent energy content of the gas similarly to Agertz & Kravtsov 2015: turbulent (or non-thermal) energy density $e_{\rm nt}$ is injected in gas by SN, winds and radiation pressure, and it is dissipated as (Teyssier et al., 2013, see eq. 2)

$$\dot{e}_{\rm nt} = -\frac{e_{\rm nt}}{t_{\rm diss}}\,, \tag{2.29}$$

where $t_{\rm diss}$ is the dissipation time scale, which can be written as in Mac Low 1999

$$t_{\rm diss} = 9.785 \left(\frac{l_{\rm cell}}{100\,{\rm pc}}\right)\left(\frac{\sigma_{\rm nt}}{10\,{\rm km\,s^{-1}}}\right)^{-1} {\rm Myr}\,, \tag{2.30}$$

where $\sigma_{\rm nt} = \sqrt{e_{\rm nt}}$ is the turbulent velocity dispersion.

Radiation

Althæa In the case of Althæa (Pallottini et al., 2017b), ISRF is not evolved in a self-consistent manner and it is treated approximately. For the spectral energy density (SED), a MW like spectrum (Draine, 1978) is assumed. SED is specified using 10 energy bins from 0.75 eV to 14.16 eV. Beyond 13.6 eV the flux drops to zero, i.e. the ionizing radiation is not included. A spatially uniform ISRF is considered whose intensity is rescaled with the SFR such that $G = G_0({\rm SFR/M_{\odot}/yr})$, where $G_0 = 1.6 \times 10^{-3}{\rm erg\,cm^{-2}\,s^{-1}}$ is the far UV (FUV) flux in the Habing band ($6 - 13.6\,{\rm eV}$) normalized to the average MW value (Habing, 1968). On top of the ISRF, the CMB is considered, that sets a temperature floor for the gas.

Freesia In Freesia, the radiative transfer is carried out on the fly. Radiation coupling to hydrodynamics is performed with RAMSES-RT (Rosdahl et al., 2013), that solves photons advection within a momentum-based framework with the closure given by setting an M1 condition for the Eddington tensor (Aubert & Teyssier, 2008). In RAMSES-RT, photons are treated as a fluid that is spatially tracked by sharing the same AMR structure of the gas. Photons are separated into different energy bins, each one tracking an independent "fluid". For Freesia, we select 5 photon bins

to cover both the energy range of the Galactic UV ISRF (Draine, 1978), the same range adopted for Althæa , and H ionising radiation. Fig. 2.8 shows the stellar energy distribution (SED) per unit mass and unit energy for a stellar population at different ages. The first two low energy bins cover the Habing (1968) band[9] $6.0-13.6\,\mathrm{eV}$, which is fundamental in regulating the temperature of the ISM and PDRs. The second bin included in the Habing band is specific for the Lyman-Werner radiation ($11.2-13.6\,\mathrm{eV}$), which photo-dissociates H_2 via the two-step Solomon process (Stecher & Williams, 1967). The last three bins cover the H-ionizing photons up to the first ionisation level of He ($13.6-24.59\,\mathrm{eV}$). For H-ionizing photons, the energy width is chosen such that the bins have the same number of photons when the SED is averaged on a fiducial stellar population. Our fiducial stellar population has an age 10 Myr and $Z_\star = \mathrm{Z}_\odot$: these stars are the main sources of the ISRF, since such young stars dominate the spectrum of a galaxy with an exponentially rising SFR, as expected for Freesia (Pallottini et al., 2017a,b). To calculate the SED-averaged quantities, we fix the SED to the fiducial one. Note that using three energy bins for H ionisation allows us to reasonably capture the temperature evolution of H^+ regions since photo-ionisation coupling with the gas is computed using the mean energy within each bin.

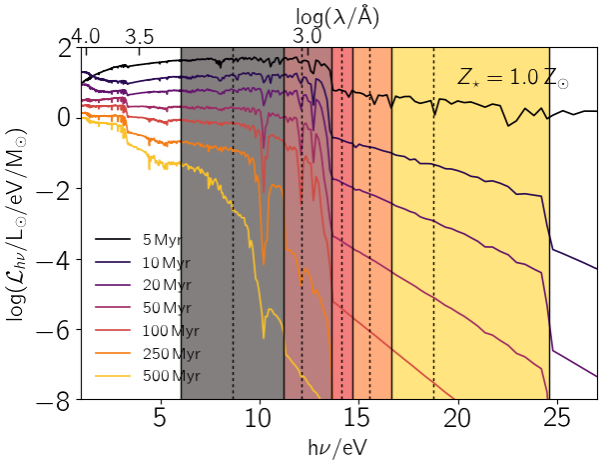

Figure 2.8: SED per stellar mass per unit energy ($h\nu$) as a function of $h\nu$ per a stellar population with solar metalicity. SEDs of different ages are plotted with different colours. With shaded regions we highlight the photon energy bins considered in this work; in each bin dashed vertical lines indicates the photon energy averaged by weighting on a $t = 10$Myr, SED, i.e. the one assumed in the simulation to precalculate photon average quantities. The wavelength (λ) corresponding to $h\nu$ is indicated in the upper axis (Figure 1 in Pallottini et al. 2019).

In RAMSES the time-step is determined by the Courant condition (Courant et al., 1928), i.e. $\delta t \sim l_{\rm cell}/v_g$, with v_g being the gas velocity; taking v_g of the order of the rotational velocity of the galaxy, this yields $\delta t \sim 30\,\mathrm{pc}/100\,\mathrm{km\,s^{-1}} \sim 0.3\,\mathrm{Myr}$. RAMSES-RT adopts an explicit scheme for the time evolution of radiation. Since hydrodynamics and radiation are coupled, it follows that the time-step of the simulation is determined by the minimum between the sound and light crossing time. To limit the computational load, we consider the reduced speed of light approximation to propagate wave-fronts (Gnedin & Abel, 2001), adopting $c_{red} = 10^{-2}c$. With such prescription, we expect $\delta t \sim l_{\rm cell}/c_{red} \sim 0.01\,\mathrm{Myr}$. Using a reduced speed of light approach yields artefacts when propagating light fronts very far from the sources, e.g. in IGM reionisation studies; however, it well captures the radiation transfer in the ISM/CGM of galaxies (see Deparis et al., 2019, for a detailed study of the impact of a

[9]The Habing flux G is indicated in unit of $G_0 = 1.6\times10^{-3}\mathrm{erg\,cm^{-2}\,s^{-1}}$, the MW value.

reduced speed of light), as such it is well suited for the present work.

Stars

Formation In SERRA, the star formation rate density ($\dot{\rho}_\star$) depends on the H_2 density (ρ_{H2}) via a Schmidt 1959; Kennicutt 1998-like relation:

$$\dot{\rho}_\star = \zeta_{sf} \frac{\mu m_p n_{H2}}{t_{ff}} , \tag{2.31}$$

where $\dot{\rho}_\star$ is the local star formation rate density, ζ_{sf} the star formation efficiency, m_p the proton mass, μ the mean molecular weight, and t_{ff} the free-fall time. The star formation efficiency is set to $\zeta_{sf} = 10\%$, by adopting the average value observed for MCs (Murray, 2011), while molecular hydrogen density n_{H2} computation is included in the non-equilibrium chemical network. It is shown in Pallottini et al. 2017a that the adopted SFR prescription gives similar results to other schemes in which the efficiency is derived from a turbulent virial theorem criterion (Semenov et al., 2016).

Stellar populations A single star particle in SERRA can be considered as a stellar cluster, with metallicity $Z_\star$ set equal to that of the parent cell. For the stellar cluster, a Kroupa 2001 initial mass function is assumed. By using STARBURST99 (Leitherer et al., 1999), single population stellar evolutionary tracks given by the `padova` (Bertelli et al., 1994) library are adopted, that covers the $0.02 \leq Z_\star/Z_\odot \leq 1$ metallicity range.

Star formation rate For the analysis of the simulation, it is convenient to define the star formation rate surface density (Σ_{SFR}) as

$$\Sigma_{SFR} = \frac{\Sigma_\star(t_\star < \Delta t)}{\Delta t} , \tag{2.32}$$

where we account for young star clusters i.e. setting $\Delta t = 30\,\mathrm{Myr}$.

Stellar feedback In SERRA, we account for stellar energy inputs and chemical yields that depend both on metallicity $Z_\star$ and age $t_\star$ of the stellar cluster. Stellar feedback includes SNe, winds from massive stars, and radiation pressure. Due to the stellar feedback, gas elements of the ISM perceive pressure in both thermal (P_{th}) and non-thermal (P_{nt}) forms. The detailed description of thermal and non-thermal pressure terms due to stellar feedback can be found in Pallottini et al. 2017a. The non-thermal pressure mimics the stellar feedback-driven turbulence (Agertz et al., 2013; Agertz & Kravtsov, 2015; Teyssier et al., 2013). So these pressure terms induce random gas motions that

we define as the thermal ($\sigma_{\rm th}$) and turbulent ($\sigma_{\rm nt}$) velocity dispersion:

$$\sigma_{\rm th} = \sqrt{\frac{P_{\rm th}}{\rho}}, \qquad \sigma_{\rm nt} = \sqrt{\frac{P_{\rm nt}}{\rho}}, \tag{2.33}$$

where ρ is the total gas density in the cell. The thermal component is affected by gas cooling processes, while the turbulent component dissipates with a time scale given by the eddy turn-over time (eq. 2.30).

Stellar feedback in SERRA incorporates Type II and Ia SNe, winds from OB and AGB stars, and radiation pressure. The energy dissipation in MCs for SN blastwaves (Ostriker & McKee, 1988) and OB/AGB stellar winds (Weaver et al., 1977) is also accounted (Pallottini et al., 2017a, see in particular Sec. 2.4 and App. A). Continuous mechanical energy deposition rate from winds and supernovae is derived from the stellar tracks and added in the cell where the star resides. The relative fraction of thermal and kinetic energy depends on the SN blast stage: energy conserving Sedov-Taylor stage (about 70% thermal, 30% kinetic), shell formation stage, and pressure-driven snowplough (about 15% thermal and 35% kinetic).

For radiation pressure, the kinetic energy is computed from the momentum injection rate, in turn, based on the luminosity of the source and the optical thickness of the gas to the radiation in various bands (e.g. Krumholz & Thompson, 2012). We use an energy-based implementation that mimics the one typically adopted in particle-based codes (Hopkins et al., 2011).

Stellar tracks are also used to calculate photon production. As shown in Pallottini et al. (2019, in particular see Fig. 1 therein) at each time step, stars dump photons in the hosting cell in each energy bin according to their stellar age and metallicity. Photons are then advected and absorbed in the radiation step, contributing at the same time to the photo-chemistry. Dust and gas account for the absorption of the radiation, consistently with the chemical reaction cross-sections and the Weingartner & Draine 2001 dust distribution (see Pallottini et al., 2019, in particular Fig. 2 therein). Note that, at a given halo mass, SERRA galaxies feature star formation and stellar mass histories that are consistent with Lupi et al. 2020, which uses a set of feedback prescriptions similar to FIRE2 (Hopkins et al., 2018).

2.3.2 Galaxy Identification

For object (i.e. DM halos and galaxies) identification we adopt ROCKSTAR-GALAXIES[10] (Behroozi et al., 2013), a clustering algorithm that performs a phase-space identification for multimass simulations, i.e. uses a friend-of-friend algorithm that adopts a metric accounting for both spatial and velocity separations. We treat separately DM and stellar particles and we allow ROCKSTAR-GALAXIES to identify groups with a minimum number of 100 (20) DM (stars) particles.

[10] `https://bitbucket.org/pbehroozi/rockstar-galaxies`

To identify progenitors/descendants through cosmic time, we use an algorithm similar to MERGERTREE (Knebe et al., 2013). First, we produce all the catalogues of the available simulation. For each couple of snapshots consecutive in time, we cross-match the galaxies/DM halos identified in the two catalogues.

Given two snaphots at redshift $z_1 < z_2$, the halo A at z_1 is flagged as the progenitor of the halo B at z_2 if their intersection has > 100 DM (20 stellar) particles. Using the progenitor list for each couple of consecutive snapshots, we can build the full progenitor/descendant graph for each galaxy and halo. In general, we indicate a galaxy by name of the simulation, number of the snapshot, and stellar halo-id. When a specific name is chosen for a galaxy, it is propagated through the main progenitor and descendant branch of its graph. For instance, Freesia is the most massive galaxy in serra00 has been identified at $z \simeq 8$ (see Pallottini et al., 2019, for the details).

2.3.3 modeling Line emissions

The chemical network used in SERRA includes H, He, H^+, H^-, He, He^+, He^{++}, H_2, H_2^+ and electrons. The abundance of other metals are calculated by assuming solar abundances. So to obtain the ion abundances (e.g. C^+) and line emissions, we need to do it in post-processing. We use the spectral synthesis code, CLOUDY (Ferland et al., 2017) to predict various line emission and the corresponding ion. However, there are some typical challenges and shortcomings to consider when combining emission-line codes with simulations (see Olsen et al. 2018 for an overview). Two of the main issues in this regard are the consistency of the post-processing and the limits given by the resolution. These two issues are addressed in detail in Pallottini et al. 2019. The limited resolution of a typical galaxy simulation ($\sim 10\,$pc) does not allow us to recover the physical ion structure/line emission even if we would run a single CLOUDY model per cell, which 1) is computationally very expensive and 2) the assumptions are not completely consistent with the one adopted in the run. To overcome these limitations, we have adopted a special post-processing model which is summarized below.

Emission coming from the small scale clumps inside MCs is accounted similarly to Vallini et al. 2017, 2018. We assume that a MC with mean density n_0 and volume V encompasses clumps with sizes of the Jeans length (l_J) and it is characterized by a differential number of clumps $\mathrm{d}N_{\rm clump}$:

$$\mathrm{d}N_{\rm clump} = (V/l_J^3)\mathrm{d}P\,, \tag{2.34a}$$

where $\mathrm{d}P$ is the distribution of density n inside a molecular cloud with mean density n_0; $\mathrm{d}P$ can be described via a log-normal function (Padoan & Nordlund, 2011)

$$\mathrm{d}P = \frac{1}{\sigma_s\sqrt{2\pi}} \exp - \left(\frac{s-s_0}{\sigma_s\sqrt{2}}\right)^2 \mathrm{d}s\,, \tag{2.34b}$$

with s being the normalized density $s = \ln(n/n_0)$, $s_0 \equiv -0.5\sigma_s^2$, and σ_s being the standard deviation of the distribution; the latter depends on the Mach number ($\mathcal{M}$) as (Krumholz & McKee, 2005)

$$\sigma_s^2 = \ln\left(1 + (\mathcal{M}/2)^2\right). \tag{2.34c}$$

To compute metal ion abundances and line emissions, we build two grids of CLOUDY models, i.e. with and without ionising radiation. Every grid is divided in seventeen bins of number density ($10^{-2} \leq n/\mathrm{cm}^{-3} \leq 10^{6.5}$), eight bins of metallicity ($10^{-3} \leq Z/\mathrm{Z}_\odot \leq 10^{0.5}$) and twelve bins of ISRF ($10^{-1} \leq G/\mathrm{G}_0 \leq 10^{4.5}$), for a total of 1632 distinct models per each grid. For the SED of the impinging radiation field on the slab of gas of interest in CLOUDY, we use a SED taken from STARBURST99 (Leitherer et al., 1999) with stellar age of 10 Myr and solar metallicity. The intensity of the radiation field is rescaled with the local G flux; if the simulated cell has an ionization parameter $U > 10^{-4}$ or if it contains young stars ($t_\star \leq 10$ Myr), we use the grid with ionising radiation. Otherwise, we use the intensity obtained computed without the ionising radiation. For each clump inside a cell of the simulation, given the input parameters (n, G, Z and N), we compute the line luminosity per unit area ($\mathscr{L}^{\mathrm{line}}_{\mathrm{clump}}$) and the corresponding ion mass ($\mathscr{M}^{\mathrm{ion}}_{\mathrm{clump}}$) by interpolating the values evaluated by CLOUDY grids. Then, to account for the cloud structure, we integrate the the clump distribution (eq.s 2.34) to obtain the total luminosity (L_i^{line}) and ion mass (M_i^{ion}) for the i-th cell as:

$$L_i^{\mathrm{line}} = \int \mathscr{L}^{\mathrm{line}}_{\mathrm{clump}} l_J^2 \mathrm{d}N_{\mathrm{clump}}\,, \tag{2.35a}$$

$$M_i^{\mathrm{ion}} = \int \mathscr{M}^{\mathrm{ion}}_{\mathrm{clump}} l_J^2 \mathrm{d}N_{\mathrm{clump}}\,. \tag{2.35b}$$

Given a field of view (FOV) and a line of sight (l.o.s), for optically thin lines (e.g. FIR lines such as [C II]) we can directly sum the contribution of all the gas cells in the field of view. For optically thick lines (e.g. C III] 1909Å) we should consider the radiative transfer through dust (see Behrens et al., 2019, for the additional efforts needed for Lyα).

2.3.4 Althæa and Freesia; general properties

For any galaxy in the SERRA suite, we have detailed information on structural properties of the ISM with a spatial resolution of 30 pc. Althæa and Freesia are two galaxies in this suite of simulations that are studied in more detail as galaxy dynamics laboratories in the following chapters.

In Figs. 2.9 and 2.10, a face-on representation of key properties (i.e. dark matter, gas and star surface density maps, H_2 and metallicity maps) of Althæa and Freesia are shown.

The maps for Althæa are shown at redshift $z = 6$. Althæa appears as a typical $z \geq 6$ LBG (Behrens et al., 2018, 2019), following the SFR-$M_\star$ relation observed at high-z (Jiang et al., 2016).

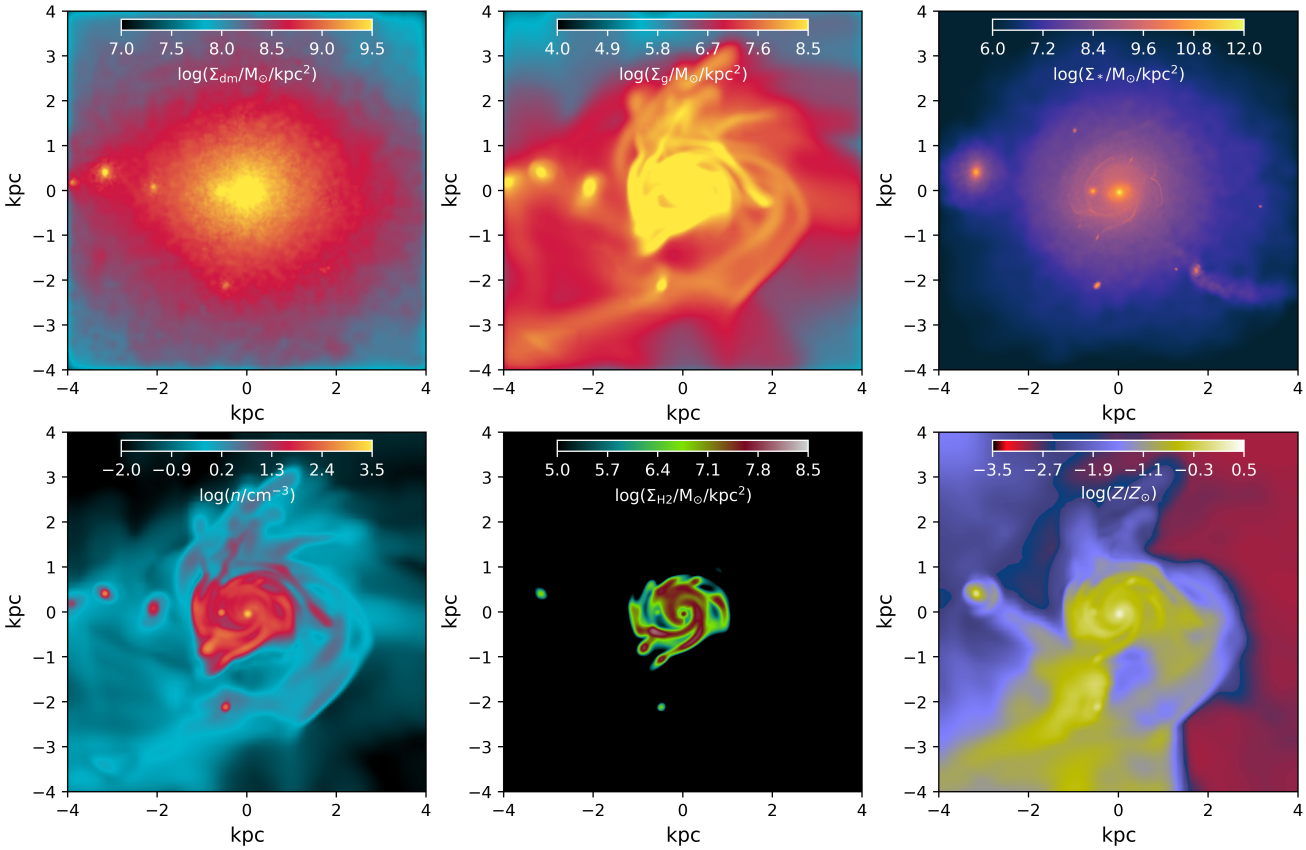

Figure 2.9: Portraits of Althæa at $z = 6$. The galaxy is seen face-on in a $\simeq 8\text{kpc}^2$ field of view. In the upper row, we plot the dark matter mass surface density ($\Sigma_{\rm dm}$), gas mass surface density ($\Sigma_{\rm g}$), and the stellar mass surface density($\Sigma_\star$). In the bottom row, we show the gas density (n), the molecular content ($\Sigma_{\rm H_2}$) and gas metallicity (Z).

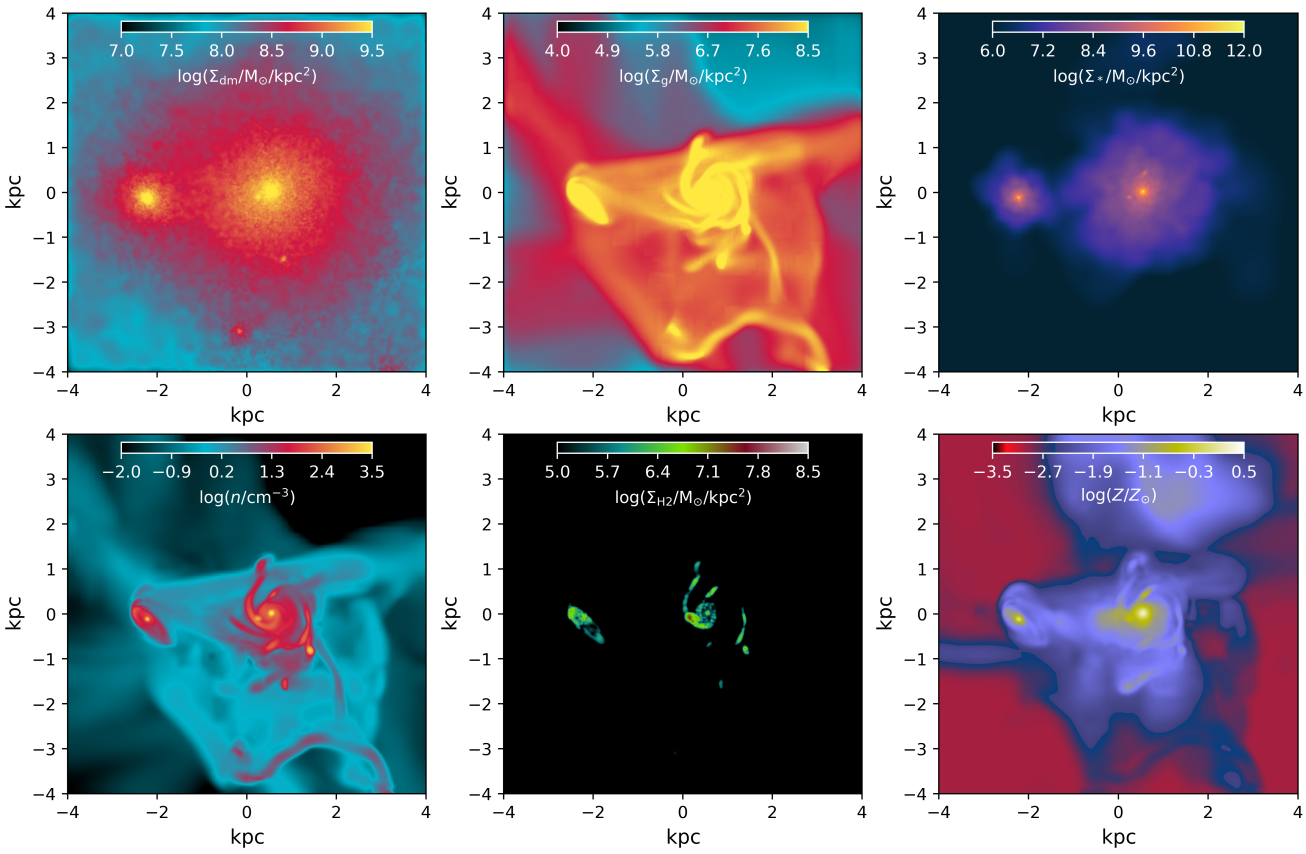

Figure 2.10: Portraits of Freesia at $z = 8$ when the galaxy has an age $t_\star \simeq 409\,\mathrm{Myr}$, $M_\star \simeq 4.2 \times 10^9 \mathrm{M}_\odot$ and $SFR \simeq 11.5 \mathrm{M}_\odot \mathrm{yr}^{-1}$. The galaxy is seen face-on in a $\simeq 8\mathrm{kpc}^2$ field of view. In the upper row, we plot the dark matter mass surface density (Σ_{dm}), gas mass surface density (Σ_{g}), and the stellar mass surface density($\Sigma_\star$). In the bottom row, we show the gas density (n), the molecular content ($\Sigma_{\mathrm{H_2}}$) and gas metallicity (Z).

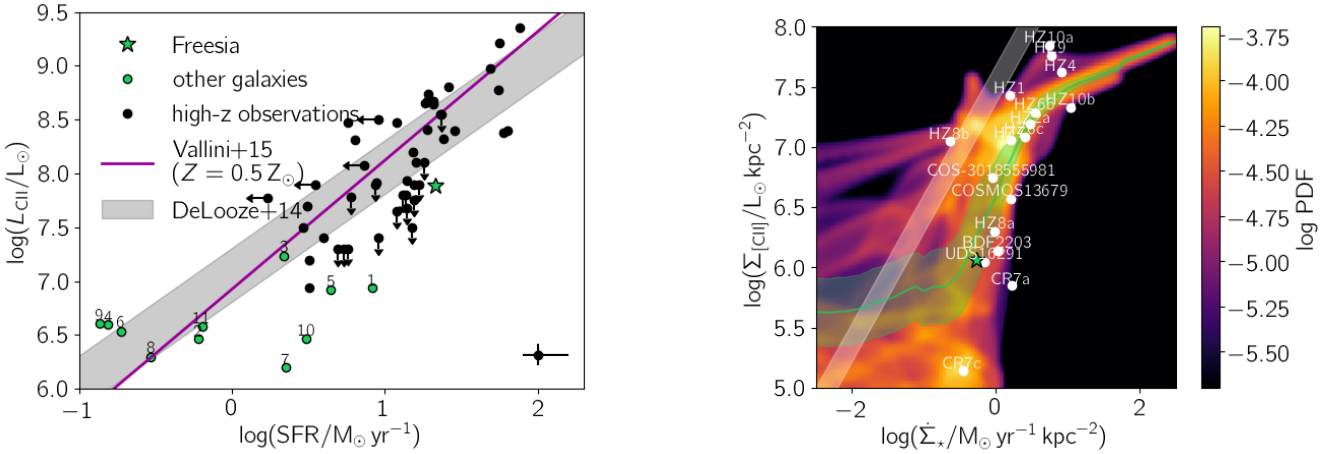

Figure 2.11: *Left Panel:* Integrated SFR-[C II] relation. Freesia is marked with a star and simulated galaxies are indicated with green circles. *Right Panel:* Resolved [C II]-SFR relation, i.e. the probability density function (PDF) in the $\Sigma_{CII} - \Sigma_{\rm SFR}$ plane of Freesia (Figure 10 and 13 in Pallottini et al. 2019).

Freesia is also a LBG galaxy. In Fig. 2.10, we show various maps of Freesia at $z = 8$. At this redshift, Freesia is hosted by a halo of mass $M_h \simeq 10^{11}{\rm M}_\odot$; its age is $t_\star \simeq 409\,{\rm Myr}$, it has a stellar mass $M_\star \simeq 4.2 \times 10^9{\rm M}_\odot$ and instantaneous $SFR \simeq 11.5{\rm M}_\odot{\rm yr}^{-1}$.

Freesia at this stage has two stellar components separated by $\simeq 2\,{\rm kpc}$, with the main galaxy containing about $\simeq 85\%$ of the total stellar mass and dominating the star formation rate (90%). Both components are highly concentrated, with effective radius of about $\sim 200\,{\rm pc}$ in both cases; they show stellar surface density peaks with $\Sigma_\star \simeq 5 \times 10^{11}{\rm M}_\odot/{\rm kpc}^2$, that are surrounded by a stellar halo with low surface density ($\Sigma_\star \simeq 10^7{\rm M}_\odot/{\rm kpc}^2$), that is likely due to the tidal interaction of the components. Freesia has a spiral structure with arms characterised by a gas density $10^2 \lesssim n/{\rm cm}^{-3} \lesssim 10^3$; the satellite reaches similar densities, but it has a more uniform disk structure because its lower mass prevents the development of arms. The only other dense ($n \simeq 10^2{\rm cm}^{-3}$) structure is likely an unstable filament located $\simeq 2.5\,{\rm kpc}$ north-west of Freesia. These three components are embedded in a lower density medium ($n \simeq 5\,{\rm cm}^{-3}$), with very low density ($\simeq 10^{-2}{\rm cm}^{-3}$) shock-heated patches of gas.

2.3.5 [CII]-SFR relation for simulated galaxies

As we mentioned in Sec. 1.2.3 and Sec. 2.2.2, there is a debate whether there is a relation between the [C II] luminosity of a galaxy and its star formation rate. Various theoretical attempts have been made to model the [C II] emission and interpret the observations at $z > 6$ (Vallini et al., 2013, 2015; Pallottini et al., 2017a; Olsen et al., 2017; Katz et al., 2019) using numerical simulations of galaxies. So far, the purpose of theoretical modelings was mostly to estimate the total [C II] luminosity of galaxies in the EoR and to understand the relative contribution from different ISM phases. These

theoretical works agree on the fact that most of the total [C II] luminosity arises from dense PDRs (Pallottini et al., 2017a) with a slight dependence on galaxy mass (Olsen et al., 2017). Still no clear consensus has been reached whether or not the local [C II] -SFR relation that is observed locally (De Looze et al., 2014) holds for $z > 6$ galaxies (cfr Carniani et al., 2018a). For instance while Vallini et al. 2015 and Pallottini et al. 2017a show that a deviation is present, Katz et al. 2019 show that for their suite of simulations at $z \sim 9$, the local relation holds.

We have studied this relation for our simulated galaxies. In Fig. 2.11, the integrated SFR-[C II] relation for Freesia and the other galaxies that are on average within (56.9 ± 21.6) kpc are shown. For a sample of 11 galaxies, we find that [C II] is increasing with SFR, however, the slope is shallower with respect to the local De Looze et al. 2014 relation: galaxies with lower star formation (SFR $\lesssim 1 M_\odot\,yr^{-1}$) lie above or on top of the local relation, while as we go to progressively high rates (SFR $\gtrsim 5 M_\odot\,yr^{-1}$) galaxies fall below the relation. However, the trend for the simulated galaxies is not clear, as the dispersion is large and the sample is limited. As noted in Carniani et al. 2018a, this trend is similar to what is observed at high-z: it is unclear whether the local De Looze et al. 2014 relation holds at high redshift because of the low statistical significance of the observed sample, and there is evidence that the dispersion is larger by a factor $\times 1.8$ with respect to the local [C II]-SFR. In particular, Freesia is within 2σ from the De Looze et al. 2014 relation, similarly to what is observed in high-z galaxies (Carniani et al., 2018a). Low metallicity alone cannot fully explain the tension from the local relation. The mean metallicity of the gas in Freesia and most of the other simulated galaxies is $Z = 0.5\,Z_\odot$. However, for $Z = 0.5\,Z_\odot$ the Vallini et al. 2015 model is consistent with the De Looze et al. 2014 relation.

Thanks to the high-resolution of our zoom-in simulations we can study the spatially resolved $\Sigma_{[C\ II]} - \Sigma_{SFR}$ relation in Freesia which can also test the analytical model described in Sec. 2.2.2. In the right panel of Fig. 2.11, the resolved relation is shown. We can see that $\Sigma_{[C\ II]}$ is increasing with Σ_{SFR} in Freesia: the slope is almost flat ($\lesssim 0.25$) for low ($\Sigma_{SFR} \lesssim 0.1 M_\odot yr^{-1}$) and high ($\Sigma_{SFR} \gtrsim 5 M_\odot yr^{-1}$) formation rates, while the trend is nearly linear for intermediate Σ_{SFR}. The scatter in the relation is decreasing with increasing Σ_{SFR}, because of the smaller spread in the metallicity of the gas as we go to progressively higher $\Sigma_{[C\ II]}$. The local $\Sigma_{[C\ II]}$-Σ_{SFR} is fitted with an almost linear slope. In this Fig., we see that most of the $\Sigma_{[C\ II]}$-Σ_{SFR} high-z data – obtained by integrating the various galaxy components and estimating their UV and IR sizes (see Carniani et al., 2018a, for details) – are nicely consistent with the average value extracted from Freesia, while they fall below the local relation. This is an indication that those galaxies are dominated by $\Sigma_{SFR} \gtrsim M_\odot yr^{-1} kpc^{-2}$, critical point where the local $\Sigma_{[C\ II]}$-Σ_{SFR} deviate from linear by saturating to an almost constant value (see Sec. 2.2.2).

Therefore, Freesia lies below the local [C II]-SFR relation as it is in a starburst phase. Spatial analysis reveals that patches of the galaxy that are above the resolved local relation (De Looze et al., 2014) are located below KS and vice-versa. Thus, the observed [C II]-SFR deficit can be primarily ascribed to negative stellar feedback during starburst phases, disrupting molecular clouds

around star formation sites as it was originally proposed in Vallini et al. 2015.

Chapter 3

Kinematics of $z \geq 6$ galaxies from [C II] line emission

The line profile provides information on the kinematics as well as structural properties of galaxies such as the presence of a disk and satellites. In this chapter, we explore different kinematical features of EoR galaxies and their connection with the assembly process as imprinted in the FIR line emission profiles. To this aim, we trace the evolution of "Althæa" (introduced in Sec. 2.3.4) from $z = 7$ to $z = 6$ through its [C II] emission maps and corresponding synthetic spectral line profiles. We use the results of the kinematics of simple analytical disk galaxy (described in Sec. 2.2.1) as our reference point for comparison. This chapter of the thesis is based on Kohandel et al. 2019.

3.1 Computing [CII] maps and spectra for Althæa

The first step is to compute the [C II] luminosity. Since we want to compare our results with the simple analytical disk (Sec. 2.2.1), we use the Dalgarno & McCray 1972b prescription for the [C II] line modeling (see Sec. 2.2.1 for the details). For that, we need n, n_H, n_e, T and Z as the inputs for the emission model (eq. 2.14) and CMB suppression (eq. 2.16). The first three parameters are computed by the simulation on-the-fly via the chemical network included in KROME. Temperature in RAMSES is defined from the thermal pressure and the gas density ($\rho = \mu m_H n$, where μ and m_H are the mean molecular weight and the hydrogen atom mass, respectively) by assuming an equation of state, i.e. $T = (\gamma - 1)\, P_{\rm k}/\rho$, with $\gamma = 5/3$ being the adiabatic index.

To derive the spectrum, in addition to the above mentioned quantities, we need to know the l.o.s. direction identified by $\hat{n}$, l.o.s velocity for each cell, namely $v_i = \vec{V}_i \cdot \hat{n}$, where $\vec{V}_i$ is the simulated velocity field of the galaxy and $\hat{n}$ the l.o.s. direction. Having these quantities, we model the contribution of each simulated i_{th} cell to the spectrum as a Gaussian function centred on v_i with a width $\sigma^i_{k,t}$ and an amplitude equal to the [C II] luminosity ($L^i_{\rm CII}$) of that cell. $\sigma^i_{k,t}$ is the

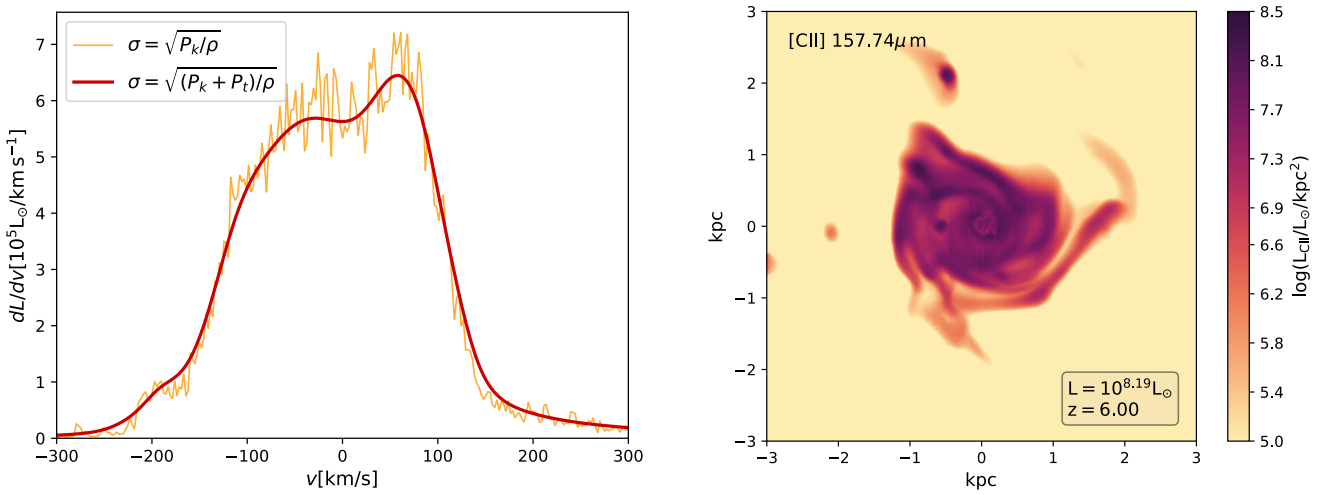

Figure 3.1: *Top panel*: Surface brightness of [C II] emission of Althæa (viewing face-on) at redshift $z = 6$. *Bottom panel*: The corresponding synthetic [C II] spectral profile. The spectrum either includes (red line) or does not include (yellow) turbulent broadening; in the latter case, only thermal broadening is taken into account. Turbulent motions smooth out the spectrum by erasing the spiky behaviour and decreasing the line intensity at the peak by 10%. The total spectrum shows two comparable peaks of emission with a relative difference of $< 15\%$ (Figure 3 in Kohandel et al. 2019).

broadening of the line for which we account for both the thermal and the turbulent motions as $\sigma^i_{k,t} = \sqrt{(P^i_k + P^i_t)/\rho_i}$ where P^i_t is the pressure due to the turbulent motions induced by the kinetic feedback in the simulation. For each velocity bin v_j we compute the integrated line spectrum $f_j = f_j(v_j)$ as

$$f_j = \sum_i \frac{L^i_{\rm CII}}{2\sqrt{\pi}\sigma^i_{k,t}} e^{-\left[(v_i - v_j)/\sqrt{2}\sigma^i_{k,t}\right]^2} \tag{3.1}$$

Having the spectrum as a function of the velocity bin, we define the mean spectral velocity as:

$$\langle v \rangle = \frac{\sum_j v_j f_j}{\sum_j f_j}, \tag{3.2}$$

which we use to centre the velocities in plotting the spectra. We compute the Full Width at Half Maximum (FWHM) of the line as the full width at which 68% of the light is contained; note that in calculating FWHM we do not consider values of f_j lower than 10 times the peak of the flux.

Note that throughout this work the [C II] maps are calculated by accounting for the emission of the gas centred on the simulated galaxy that is within a cube with a side equal to the FOV of the image. Unless noted otherwise, the spectra corresponding to a map are extracted from the same FOV.

We start by discussing the properties of [C II] emission coming from the face-on[1] view of Al-

[1]With face-on we mean that we orient the l.o.s. parallel to the eigenvector of the inertia tensor of the gas density distribution with the largest eigenvalue.

thæa at $z = 6$ in a rectangular FOV of size 7 kpc around the centre of the galaxy. In Fig. 3.1, we plot the l.o.s.-integrated surface brightness of the galaxy at this stage. The total [C II] luminosity is $L_{[CII]} = 10^{8.19} L_\odot$. The galaxy shows a relatively smooth disk-like structure, whose extent is ~ 2 kpc in [C II] emission. At this redshift, this translates to an angular size of 0.34 arcsec. For these early epochs, there is a clear hint of a broken spiral arm structure. The other interesting feature is the presence of bright clumps of size ≈ 100 pc within the disk.

Also shown in Fig. 3.1 is the corresponding synthetic face-on [C II] line spectrum; for comparison, we also present the spectrum in which only thermal broadening is taken into account. The main effect of the inclusion of turbulent motions, self-consistently derived from the simulation in each cell, is to make the line profile smoother by erasing the narrow spikes visible in the thermal-only broadened profile. As seen in the analytical model (Sec. 2.2.1), turbulent motions[2] can suppress characteristic features of the spectrum, such as the double-peak profile of a rotating disk. Note that the maximum of the rotational velocity of the galaxy is of order $\sim 190\,\mathrm{km\,s^{-1}}$ (see also in Fig. 3.5), while the level of turbulence for dense gas is of the order of $\sigma_t \simeq 30\,\mathrm{km\,s^{-1}}$ (Vallini et al., 2018); thus the effect of micro-turbulence is limited with respect to the range of turbulence explored in the analytical model (see Chap. 4 for further analysis of turbulence in the ISM of simulated galaxies). Accounting for turbulent motions in Althæa decreases the line intensity at the peak by 10%, as it was expected from the analytical model.

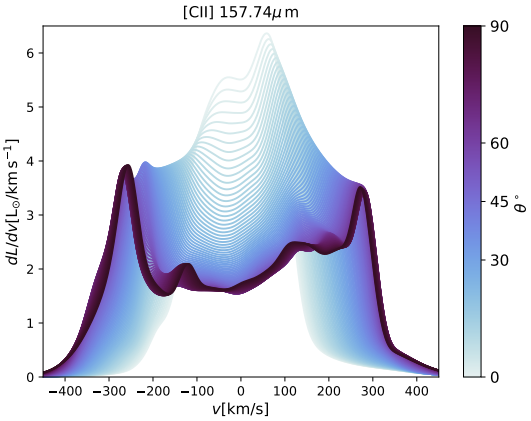

Figure 3.2: Synthetic spectra for Althæa at $z = 6$ (see also Fig. 3.1). Spectra are calculated for 100 inclinations between face-on ($\theta = 0°$) and edge-on ($\theta = 90°$) views. Changing the inclination clears the signature of the rotating disk from the spectral shape, i.e. the two comparable peaks at the edges. From face-on to edge-on the peak amplitude of the line decreases by a factor of ~ 1.6 (Figure 4 in Kohandel et al. 2019).

As pointed out in Sec. 2.2.1, a decreasing inclination can erase the signatures of a disk in the spectra, similar to what happens when increasing turbulent motions. To investigate the situation in our simulated galaxy, we extract [C II] spectra for 100 inclinations between the face-on and the edge-on view of Althæa disk at $z = 6$ and we plot the result in Fig. 3.2. Surprisingly, there are two comparable peaks in the spectrum when Althæa is seen edge-on. This confirms that the gas in the ISM of Althæa has already undergone ordered rotation at such a high redshift. As expected from

[2]Note that the turbulence is defined differently in the simulation and the analytical model. In the analytical disk, every motion but the circular ones are treated as turbulence, while in simulation, turbulence is present because of the kinetic feedback. To make an exact comparison, one should fit a disk model to the simulated galaxy and then define the turbulence as it is in the analytical model.

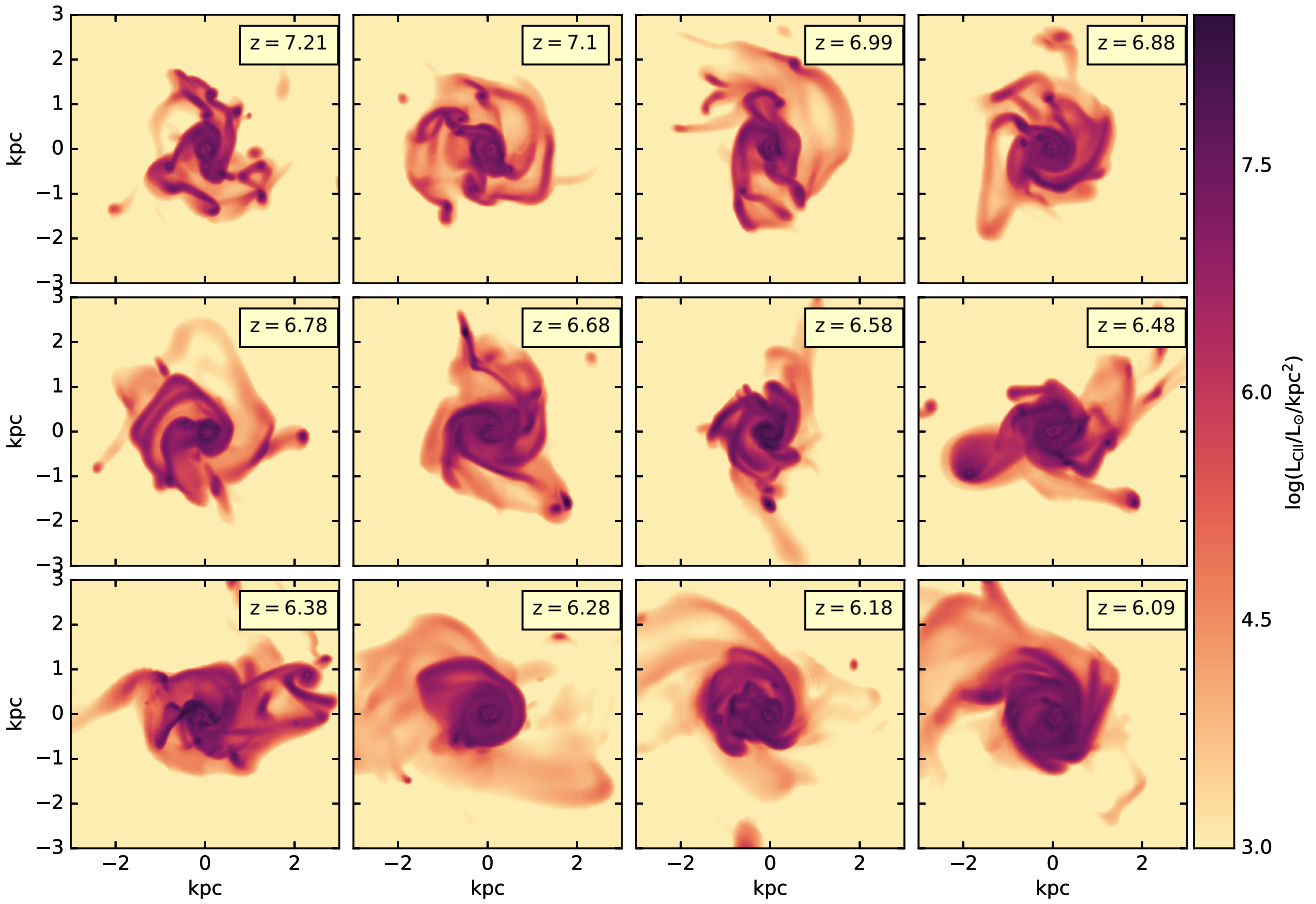

Figure 3.3: [C II] surface brightness of Althæa during its evolution in redshift range of $6.09 < z < 7$. Time is increasing from left to right, top to bottom. Neighbouring panels are separated by ~ 16 Myr (Figure 5 in Kohandel et al. 2019).

our analytical model (see Fig. 2.5), changing the inclination of the disk washes out the signature of the rotating disk from the spectral profile. Changing the inclination of the disk from $\theta = 0°$ to $\theta = 90°$, the peak amplitude of the line decreases by a factor of 1.6. With respect to the analytical disk, spectral profiles contain complicated structures which are due to the asymmetries and clumpy structure of the [C II] emitting gas. The degeneracy between inclination and turbulent motions is also present in the case of simulated disk but it is more complicated (explored in the analytical model, Fig. 2.5). Inclining the disk towards face-on not only masks the spectral signature of the disk but also affects the appearance or disappearance of various bumps and structures in the profile.

3.2 Galaxy evolution traced by [CII] line

With the tools in hand (emission maps and spectra), now we concentrate on studying the evolution of Althæa in a redshift range of $6.09 < z < 7$ (corresponding to a time span of 183 Myr) when

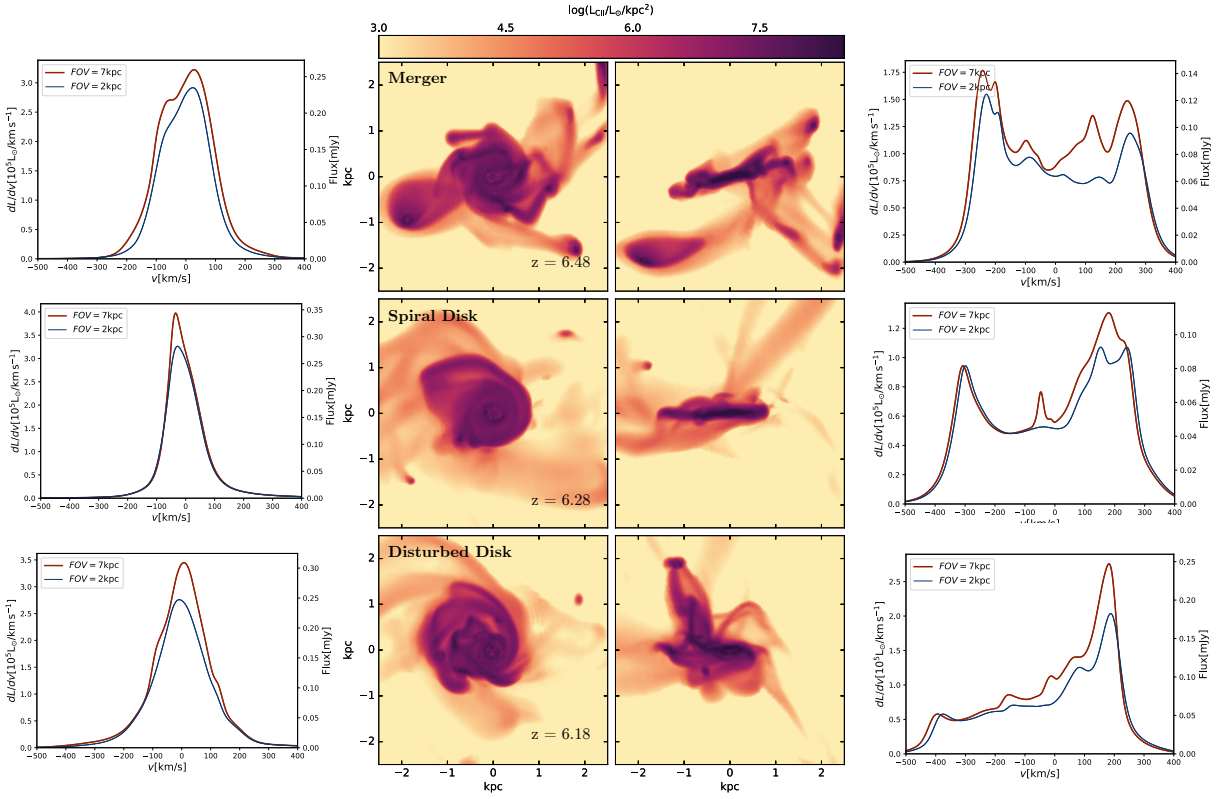

Figure 3.4: [C II] maps and spectra of three evolutionary stages of Althæa (Figure 6 in Kohandel et al. 2019). Left panel: [C II] spectra for the face-on inclinations taken from FOV = 7 kpc (red solid lines) and FOV = 2 kpc (blue solid lines). Middle panels: Face-on and edge-on emission maps for Althæa in different representative stages of evolution: Merger stage (top), Spiral Disk (centre), and Disturbed Disk (bottom). Right panel: [C II] spectra for the edge-on inclinations taken from FOV = 7 kpc (red solid lines) and FOV = 2 kpc (blue solid lines).

the system is in a very active assembling phase. In Fig. 3.3, we show the face-on emission maps of Althæa in that redshift range. The time-lapse among different panels is $\sim$ 16 Myr and the images are taken in a FOV of 7 kpc. At the earliest epochs, the galaxy is constituted by a small ($\approx$ 500 pc) disk surrounded by several emission knots of size $<$ 100 pc, which are feeding the central part through filaments. As time progresses, the disk grows in size and mass in an inside-out fashion, forming a compact core while acquiring mass from the satellites which are progressively disrupted and embedded in the disk. At $z = 6.48$, a merger event occurs, which is clearly seen in Fig. 3.3. The merger event dramatically perturbs the quasi-smooth disk structure, resulting in the very irregular and widespread emission seen at $z = 6.38$. However, the gravitational potential of the galaxy is able to restore the disk in less than 16 Myr.

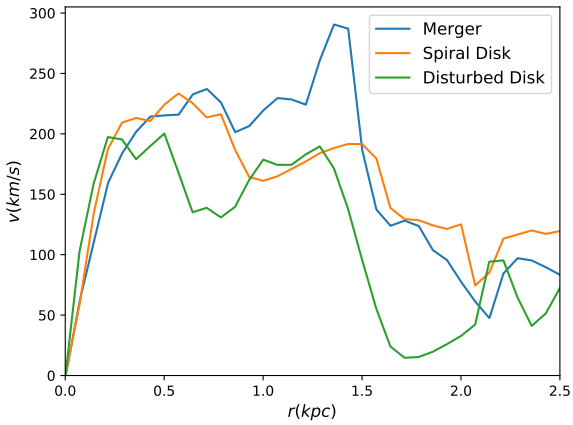

Figure 3.5: Velocity structure of Althæa in different evolutionary stages in the edge-on view (Figure 7 in Kohandel et al. 2019).

Among these stages, we select three particularly interesting stages for further analysis based on their [C II] emission morphology:

Merger: at $z = 6.48$, when Althæa experiences a merger event. The satellite in this stage has no stars but is hosted in a dark matter sub-halo that is about to merge with the galaxy. The total [C II] luminosity at this stage is $10^{7.87} L_\odot$.

Spiral Disk: at $z = 6.28$, the ISM of Althæa has relaxed into a disk that has a spiral arm on one side. The total [C II] luminosity at this stage is $10^{7.71} L_\odot$.

Disturbed Disk: this stage corresponds to $z = 6.18$ in which disk has been vertically disrupted. The total [C II] luminosity at this stage is $10^{7.86} L_\odot$.

In the two middle panels of Fig. 3.4, [C II] images for the face-on and edge-on views of the above-selected stages are shown. These stages are selected because they have distinct differences in morphology and structure which in principle can evoke differences in the spectral profile of the emission. Furthermore, we plot the l.o.s. velocity profiles of these stages in Fig. 3.5. These profiles are not monotonic and contain several bumps and peaks. This is an indication of the complex velocity structure of the gas. In the following, we compare these stages of the simulation with each other and also with the cases defined in our analytical model in terms of their spectral profile.

Recall from the analytical model that a double-peak profile is a signature of having a rotating disk in the system while a single peak Gaussian profile can be a sign of either a Disturbed Disk or a face-on view of a rotating disk (Sec. 2.2.1). We apply the spectra diagnostic to the face-on and

edge-on views of the above-defined stages. As visible in the [C II] images, multiple structures are present in the ISM of these systems, beyond the central 2 kpc. To distinguish between the central disk and the environment of the system, we extract the spectra for each of the stages in two FOV sizes, 7 kpc and 2 kpc. In the left panels of Fig. 3.4, these spectra for the face-on view of the stages are plotted, while in the right panels the spectra for the edge-on views are plotted.

The profile of the face-on view of all the stages contain a dominant single peak but they are different in comparison to Smooth Disk and Turbulent dominated Disk defined in the semi-analytical model.

The face-on profile of the Merger stage has a FWHM $= 167\,\mathrm{km\,s^{-1}}$ and the profile shows two merged peaks located at $v = -100\,\mathrm{km\,s^{-1}}$ and $v = 0\mathrm{km\,s^{-1}}$; the major peak is due to the central disk while the addition of [C II] from the starless satellite produces the secondary peak in the profile. The face-on view of the Spiral Disk with an asymmetric Gaussian shape has a FWHM $= 100\,\mathrm{km\,s^{-1}}$ and peak flux of ~ 0.35mJy. The asymmetry of the profile reflects the asymmetric kinematics of the [C II] emitting gas. Instead, the spectral profile of the Disturbed Disk in face-on view is semi-symmetric but it is wider (FWHM $= 143\,\mathrm{km\,s^{-1}}$) in the core because of the extra-planar flows perpendicular to the disk plane; such extra-planar flows can contribute to $\sim 10\%$ of the total signal, as it is analysed in Gallerani et al. (2018a).

In summary, the presence of a broken spiral arm, extra-planar flows and a merging satellite encode spectral signatures as asymmetric Gaussian peaks in the profile, broadening the core of the spectrum and a quite dominant peak very close to the disk's main peak in the face-on spectral profiles respectively.

We perform a similar comparison for the edge-on spectra. The situation for the edge-on profiles is more complicated because the spectra of the simulated stages are very structured. The edge-on profile of the Merger stage (with a peak of $\sim 0.14\,\mathrm{mJy}$) contains dominant asymmetric double-peaks (with a relative difference of $\sim 18\%$) because of the presence of the central rotating disk. Various bumps are present in the total spectrum and the most prominent one is due to the satellite: its magnitude is comparable to that of the horns of the disk, it is centred around $v = +100\,\mathrm{km\,s^{-1}}$ and has a velocity extension of $\sim 300\,\mathrm{km\,s^{-1}}$. Since this stage shows a clear hint of rotation in the spectrum, it implies that distinguishing systems with close mergers from a rotating system is very difficult using only spectra (Simons et al., 2019).

For the Spiral Disk, the total spectrum has a peak flux of 0.12 mJy and FWHM $\sim 479\,\mathrm{km\,s^{-1}}$; from the spectral shape, there is a clear hint of rotation because of the presence of double peaks in the two edges of the spectrum. The double peaks in the spectral profile are not symmetric as in the analytical model in Smooth Disk. This is because of the asymmetries seen in the disk of [C II] emitting gas (see the right panel of Fig. 3.4). In addition, there is a quite prominent bump in the core of the spectrum which was not present in the profiles of the analytical disk. The bumps in the spectrum are due to external gas (> 2 kpc) flowing into the disk. In this case, the contribution of the co-planar spiral arm to the edge-on spectrum becomes more prominent making

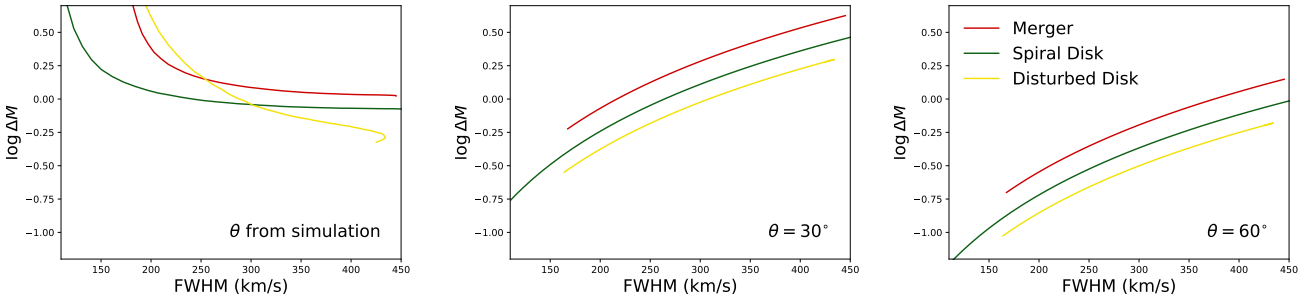

Figure 3.7: Analysis of the error in the dynamical mass determination using empirical estimates 3.5 (Figure 9 in Kohandel et al. 2019). The mass-error-function (ΔM, eq. 3.6) is plotted as a function of the FWHM for known inclination, as calculated in the simulation (left panel), and by assuming a fixed inclination of 30° (central panel) and 60° (right panel). Different lines indicate the three selected evolutionary stages (see Fig. 3.4).

the high-velocity tails.

As it is expected from the analytical model, the edge-on profile of the simulated Disturbed Disk does not have rotating double peaks. However, instead of having a smooth single Gaussian profile, there is an asymmetric Gaussian profile (centred on v = 200km s^{-1}) including multiple peaks in the long skewed tail. There is a relative difference of $\sim 80\%$ between the main peak of the spectrum and the lowest bump in the tail. The presence of extra-planar flows suppresses the blue part of the spectrum masking the signature of a rotating disk that was present in the Spiral Disk profile. Recall that the Disturbed Disk stage is just 16 Myr after the Spiral Disk stage in the evolution of Althæa.

The spectra for the simulated galaxy are very structured and complicated. To properly interpret the component analysis, it is required to apply full dynamical studies and extract the spectra for different velocity channels of the system.

3.3 Observational Implications

Investigating the evolution of Althæa, we have seen how the structural and kinematical differences result in various spectral profiles which depend on morphological properties, and inclination of the galaxy (Fig. 3.2). In this section, we analyse the implications of these results from an observational point of view.

For the synthetic spectra, we use the three different stages of Althæa discussed in Sec. 3.2. Our results are compared with observations of a sample of $5.2 < z < 7.1$ galaxies for which the spectra of [C II] line have been obtained with ALMA (Ouchi et al., 2013; Wang et al., 2013; Capak et al., 2015; Pentericci et al., 2016; Jones et al., 2017; Carniani et al., 2017). For reference, these objects are listed in Table 1.1, along with their redshift, total [C II] luminosity ($L_{\rm CII}$) and FWHM of the [C II] line.

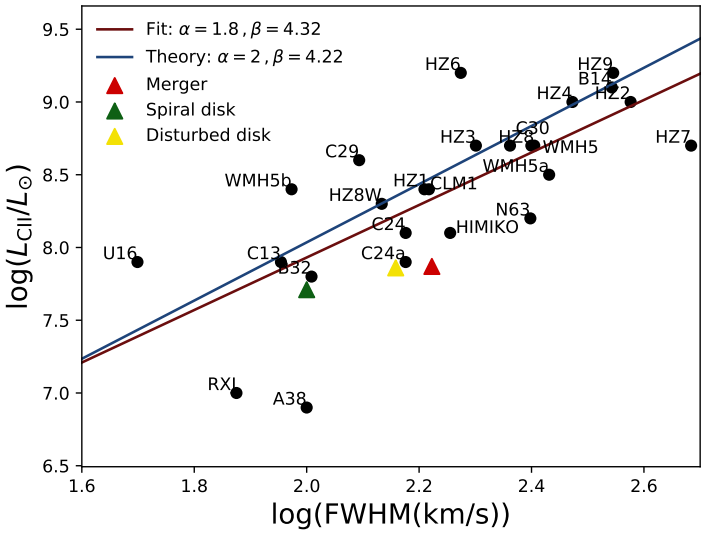

Figure 3.8: Correlation between $L_{\rm CII}$ and FWHM for the sample of observed high-z galaxies (black dots, Tab. 1.1). The red line indicates the fit to the data (functional form and parameters in eq.s 3.7). The blue line indicates the approximate relation given in eq. 3.10 assuming $R = 1\,$kpc and $\sin\theta = 0.5$ (Figure 10 in Kohandel et al. 2019).

3.3.1 Dynamical mass estimates

By assuming a rotating disk geometry (with radius R) for the [C II] emitting gas, the dynamical mass can be estimated as

$$M_{\rm dyn} = \frac{v_c^2 R}{G}\,. \tag{3.3}$$

From a [C II] spectrum obtained with a high signal to noise ratio and a good sampling of the velocity channels one can estimate v_c from the FWHM of the line using the following expression

$$\mathrm{FWHM} = \gamma v_c \sin\theta\,, \tag{3.4}$$

where γ is a factor of the order of unity that depends on geometry, line profile, and turbulence. Different values have been assumed in the literature for γ: for example, Capak et al. 2015 assumed $\gamma = 1.32$. Using eq.s 3.3 and 3.4, the general expression for the dynamical mass

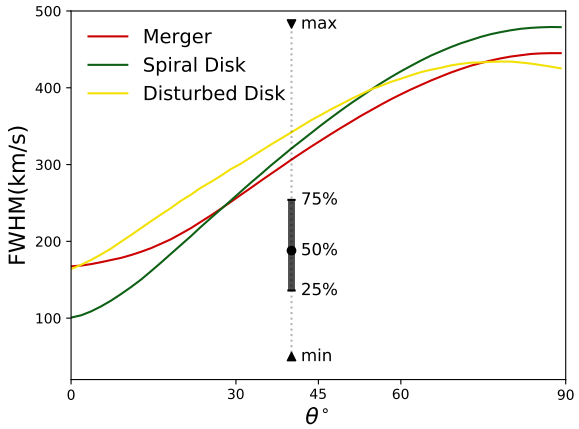

Figure 3.6: The FWHM of Althæa spectra as a function of inclination (Figure 8 in Kohandel et al. 2019). Each line corresponds to a different evolutionary stage (see Fig. 3.4). As a reference, we over-plot the statistical properties of the FWHM from observed in high-redshift galaxies (see Table 1.1).

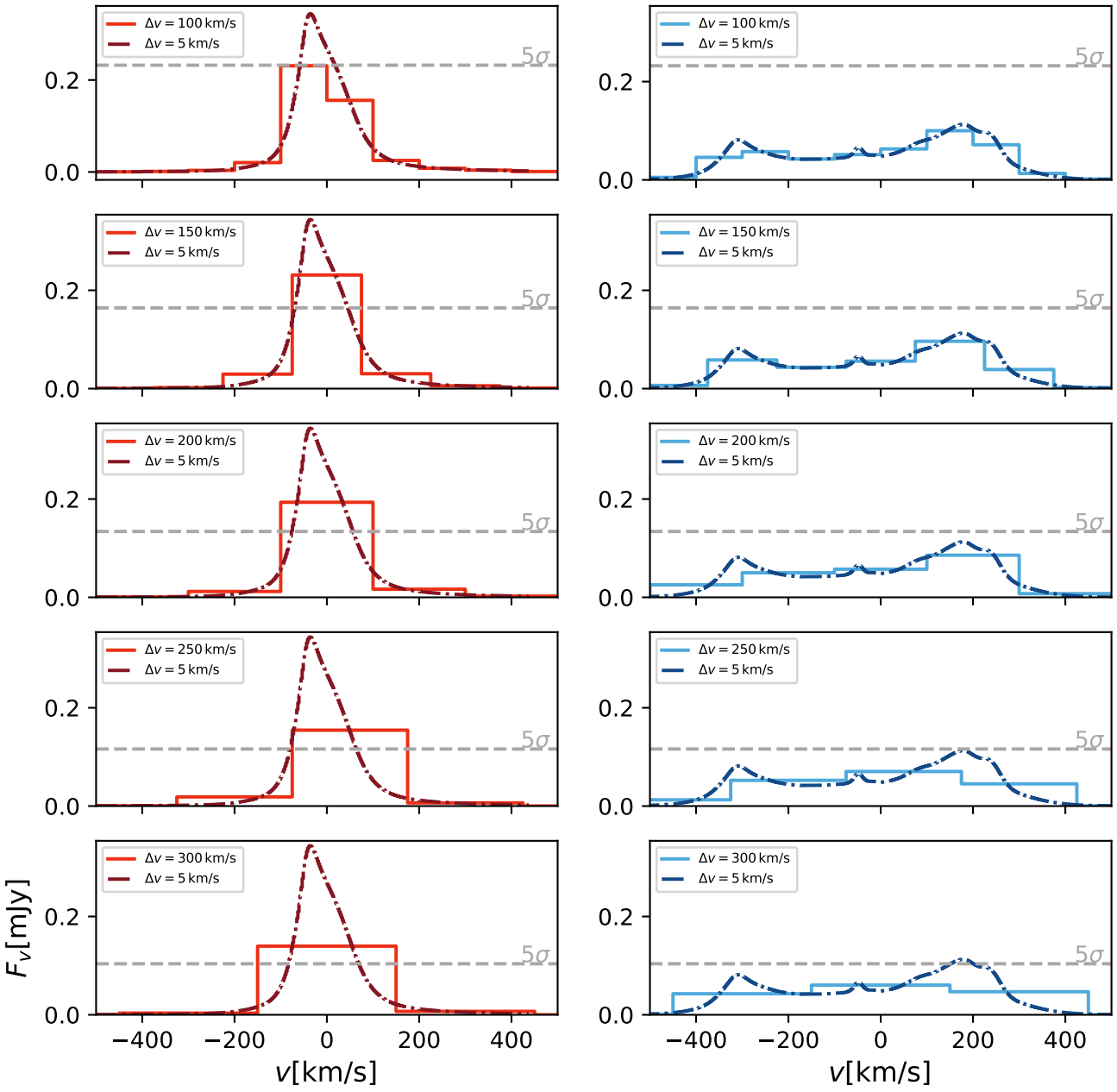

Figure 3.9: Comparison of the [C II] observability for face-on orientations (left panels) vs edge-on (right panels) ones when Althæa has $\log(L_{\rm CII}/{\rm L}_\odot) = 7.7$, at $z = 6.28$ (Spiral Disk). From top to bottom the spectrum is re-binned with an increasing channel width (Δv). As a reference, the $\Delta v = 5{\rm km\,s^{-1}}$ case is reported in all panels. The dashed horizontal line corresponds to 5σ noise level, which is calculated by assuming a 10 hours ALMA observation (Figure 11 in Kohandel et al. 2019).

is

$$\mathrm{M}_{\mathrm{dyn}}^{\mathrm{est}} = 2.35 \times 10^{9} \mathrm{M}_{\odot} \left(\frac{1}{\gamma^2 \sin^2 \theta} \right) \left(\frac{\mathrm{FWHM}}{100\,\mathrm{km\,s^{-1}}} \right)^2 \left(\frac{\mathrm{R}}{\mathrm{kpc}} \right) . \tag{3.5}$$

Before discussing the mass estimates, let us consider the FWHM of the spectra. We plot them as a function of inclination in Fig. 3.6. In general, the FWHM in Althæa is an increasing function of inclination and varies from a minimum of $100\,\mathrm{km\,s^{-1}}$ in the face-on case to a maximum of $480\,\mathrm{km\,s^{-1}}$ for the edge-on case. In the same Figure, we compare the simulated FWHM with the one inferred from observations of high-z galaxies (Tab. 1.1). The bulk of the observed spectra have a [C II] line FWHM around $180\,\mathrm{km\,s^{-1}}$ that is compatible with that found from Althæa seen face-on. Note that Althæa has a dynamical mass $M_{\mathrm{dyn}} \simeq 10^{10}\,\mathrm{M}_{\odot}$, while the dynamical masses of the observed galaxies range from $10^{9}\mathrm{M}_{\odot}$ to $10^{11}\mathrm{M}_{\odot}$ (Capak et al., 2015).

We are interested in assessing the reliability of the dynamical mass estimates obtained from eq. 3.5 as a function of [C II] line FWHM. The radius of the disk is computed from the [C II] image as $R \simeq r_{80}$, i.e. the effective radius of the system containing 80% of the total [C II] luminosity. For the three aforementioned stages of Althæa, $R \simeq 1\,\mathrm{kpc}$. It is convenient to define the "mass-error-function", i.e.

$$\Delta M \equiv M_{\mathrm{dyn}}^{\mathrm{est}} / M_{\mathrm{dyn}} \,, \tag{3.6}$$

that parametrises the error in the mass estimates using eq. 3.5, that depends on γ. We calculate γ from our simulation depending on the stage of the evolution. The value of γ for the Spiral Disk, Disturbed Disk and the merger stage is 1.78, 2.03 and 1.52, respectively.

In Fig. 3.7, we plot ΔM as a function of the FWHM for Althæa. In the left panel, estimates are performed by using the information on the inclination obtained from the simulation. The minimum of $\Delta M = 0.4$ is found for large FWHM ($\geq 350\,\mathrm{km\,s^{-1}}$). At low FWHM ΔM becomes very large as $M_{\mathrm{dyn}}^{\mathrm{est}} \propto 1/\sin^2\theta$. In all cases, we find $\Delta M > 1$ for low FWHM and $\Delta M < 1$ at high FWHM. This means that by using eq. 3.5 we tend to underestimate (overestimate) the dynamical mass at high (low) FWHM, or, equivalently, inclinations (see the left panel of Fig. 3.7).

It is interesting to calculate the mass-error-function for fixed inclinations, $\theta = 30°$ and $\theta = 60°$. These two values are generally assumed when θ cannot be directly determined from observations. This can happen when the spatial resolution does not allow us to constrain the inclination, as in Capak et al. 2015, that calculate the dynamical masses by assuming $\sin\theta = 0.45 - 1$. Results are shown in the central and right panels of Fig. 3.7. For $\theta = 60°$, $\Delta M < 1$ except for the high inclinations of the merger stage, while for $\theta = 30°$ the dynamical mass is typically overestimated, up to a factor $\simeq 4$. The error of the estimate is comparable with the one reported for the sample of Capak et al. 2015, where the authors concluded that at $z > 5$ the dynamical masses are typically a factor of ~ 3 greater than the stellar masses. This should be confronted with the analogous factor of $1.2 - 1.7$ measured at $z \sim 1 - 3$ (Förster Schreiber et al., 2009a).

The mass estimates eq. 3.5 is based on the assumption that the galaxy has a smooth disk. However, our simulations show that high-z galaxies have more complex dynamical structures which

result in correspondingly complex spectra. As observations are progressively becoming more precise, better modeling of kinematics and velocity structure of the galaxies is required (e.g. Di Teodoro & Fraternali, 2015).

3.3.2 Tully-Fisher relation for high-z galaxies

In Fig. 3.8, we plot the observed $L_{[\rm CII]}$ – FWHM relation for the high-z galaxy sample in Tab. 1.1. The best-fit to the data is

$$\log(L_{[\rm CII]}/L_\odot) = \alpha \log(\mathrm{FWHM}/\mathrm{km\,s^{-1}}) + \beta\,, \tag{3.7a}$$

with

$$\alpha = 1.80 \pm 0.35\,, \tag{3.7b}$$

$$\beta = 4.32 \pm 0.78\,. \tag{3.7c}$$

The Pearson coefficient is $\simeq 0.74$, suggesting a statistically reliable correlation between these two parameters. The three stages of Althæa (viewed face-on) are shown as triangles in this plot. They fall within 1σ from the best-fit curve.

Such relation resembles the Tully & Fisher 1977 relation. Its existence is not surprising because of the link between $L_{[\rm CII]}$ and the dynamical mass. As a rough estimate (see Pallottini et al. 2017a for an extensive discussion), we can assume a constant ratio between the total [C II] luminosity and the gas mass in a high-z galaxy; thus we can write

$$\kappa = \frac{L_{[\rm CII]}}{M_g} = \frac{L_{[\rm CII]}}{f_g M_b}\,, \tag{3.8}$$

where f_g is the gas fraction of the baryonic mass (M_b). Using eq. 3.5 and defining $f_{\rm DM} = M_{\rm DM}/M_b$ as the ratio between dark matter and baryonic mass, the relation between $L_{[\rm CII]}$ and the FWHM of the line reads as

$$L_{[\rm CII]} = \frac{\kappa R}{G}\left(\frac{f_g}{1+f_{\rm DM}}\right)\left(\frac{\mathrm{FWHM}}{\gamma \sin\theta}\right)^2\,. \tag{3.9}$$

Interestingly, this simple analytical expression is consistent with the empirical relation (eq. 3.7). It is convenient to express eq. 3.9 in terms of typical values found in high-z galaxies. Roughly, from our model we expect $\kappa = 0.1\mathrm{L_\odot/M_\odot}$ (eq. 2.14, see also Pallottini et al. 2017b), $\gamma \simeq 1.7$, $f_g \simeq 0.5$, and $f_{\rm DM} \simeq 0.5$; thus eq. 3.9 can be written as

$$L_{[\rm CII]} \simeq 5.4\times10^7 \mathrm{L_\odot}\left(\frac{1}{\sin^2\theta}\right)\left(\frac{\mathrm{FWHM}}{100\,\mathrm{km\,s^{-1}}}\right)^2\left(\frac{R}{\mathrm{kpc}}\right)\,. \tag{3.10}$$

Further, fixing $R = 1\,\mathrm{kpc}$ and $\sin\theta = 0.5$ we can express $\log L_{\rm CII}$ vs FWHM as in 3.7a with

parameters

$$\alpha = 2 \tag{3.11a}$$

$$\beta = 4.22 \tag{3.11b}$$

which is within 1σ from the fit (eq. 3.7). This predicted relation was later derived for ALPINE galaxies (Schaerer et al., 2020) with $\alpha = 2.24$ and $\beta = 3.21$.

As a final remark, we note that in Fig. 3.8, there is a lack of data in both the low FWHM-high $L_{[\mathrm{CII}]}$ and the high FWHM-low $L_{[\mathrm{CII}]}$ regions. While the first occurrence is physically motivated (it is unlikely that low mass galaxies have large luminosities), the second one might arise from an observational bias. In fact, as [C II] is optically thin, its luminosity is constant with inclination. As a consequence, as the FWHM increases, the peak flux might drop below the detection threshold. We investigate this issue in the next Section.

3.3.3 Observations of edge-on vs face-on galaxies

We now check the detectability of [C II] line for face-on and edge-one inclinations by performing mock ALMA observability simulations. We select the Spiral Disk evolutionary stage, i.e. when Althæa has luminosity $\log(L_{\mathrm{CII}}/\mathrm{L}_{\odot}) = 7.7$, similar to the one inferred for BD3299 (Maiolino et al., 2015; Carniani et al., 2017). As for BD3299 observation (Carniani et al., 2017), we assume a 10 hours integration time with ALMA. We consider the edge-on and face-on inclinations and we re-bin the spectra with channel width in the range $100 \leq \Delta v \leq 300$, i.e. the typical one used when searching for lines in normal star-forming galaxies (SFR $\lesssim 100\mathrm{M}_{\odot}/\mathrm{yr}$).

The results of such analysis are shown in Fig. 3.9 where we also plot the 5σ noise level for some selected values of Δv. The face-on case is detected at $> 5\sigma$ for all considered Δv, thus yielding a FWHM $\sim 100\,\mathrm{km\,s^{-1}}$ which is very similar to what is reported for BDF3299 in Carniani et al. 2017. However, the edge-on case with a larger intrinsic FWHM $= 479\,\mathrm{km\,s^{-1}}$ would be always undetected. Stated differently, the large l.o.s. velocities smear out the spectrum, making the detection more challenging if the galaxy is seen edge-on. This suggests that some of the non-detections reported at high-z might be due to inclination effects when the target is close to edge-on. Note that here we are assuming that no beam smearing effects are in place, which is equivalent to assuming that we marginally resolve the flux from the galaxy. This interpretation must be substantiated in future work with better quantifying channel noise and spatial correlations of the ALMA beam.

3.4 Summary

We have studied the structural and kinematical properties of galaxies in the Epoch of Reionization ($z \geq 6$) as traced by the spectral profile of the [C II] emission line. The emission is computed

from an analytical model accounting for gas cooling via the [C II] line (Dalgarno & McCray, 1972a; Wolfire et al., 1995; Vallini et al., 2013), and it includes CMB suppression of the line intensity (Da Cunha et al., 2013; Pallottini et al., 2015; Vallini et al., 2015).

First, we have applied our model to an idealised rotating disk galaxy, in order to investigate the effect of disk inclination (θ) and turbulent velocities (v_t) on the line profile. From this controlled environment, we have found that both large turbulent motions ($v_t/\bar{v}_c = \zeta > 0.5$, where $\bar{v}_c \simeq 75\,\mathrm{km\,s^{-1}}$ is the galaxy circular velocity) and inclination angles $\theta < 75°$ erase the double-peak line profile, expected from a rotating disk galaxy. In particular, we find that the peak flux of [C II] emission for face-on ($\theta = 0°$) can be a factor ~ 4 higher than in the edge-on view ($\theta = 90°$). Next, we have used zoom-in cosmological simulations of a prototypical Lyman break galaxy ("Althæa", Pallottini et al., 2017b) to analyse the [C II] emission properties during its evolution in the redshift range $6 \lesssim z \lesssim 7$. Information on velocities, thermal, and turbulent motions included in the simulation, enabled us to build the [C II] surface brightness maps of Althæa and the synthetic spectra. At $z = 6.0$, Althæa has a total [C II] luminosity $L_{[\mathrm{C\,II}]} = 10^{8.19} L_\odot$; this value accounts for a factor ~ 2 suppression due to the CMB (see Fig. 2.3). At this epoch and viewed face-on, the [C II] emission map shows a smooth, disk-like structure with an extent of $\sim 2\,\mathrm{kpc}$, on top of which are superimposed clumps with typical sizes of $\sim 100\,\mathrm{pc}$. From the analysis of the [C II] line profile, we find that the effect of turbulent motions is to smooth out the spectrum by broadening the thermal profiles and to decrease the peak line intensity by $\sim 10\%$. The degeneracy between turbulent motions and inclination is also present in the spectra of Althæa, which has a $\zeta \simeq 0.15$. The edge-on spectral profile of this stage is indicative of a rotating disk, i.e. it shows a double peak profile. Decreasing the inclination progressively washes out the disk signature from the profile and increases the peak flux by a factor of $\simeq 1.6$.

Studying the morphology of Althæa in the redshift range $6 \leq z \leq 7$, we have identified three main evolutionary stages with distinct spectral signatures: I) Merger, II) Spiral Disk, and III) Disturbed Disk. The irregular and choppy structure of the l.o.s. velocity profiles resulting from the simulations (see Fig. 3.5) translates into more structured [C II] line profiles with respect to the analytical model. Comparing the synthetic spectra for different stages of Althæa with the ones from the analytical model, we identify the spectral signatures of merger events, spiral arms and extra-planar flows in the respective stage both in the face-on and edge-on profiles. The main signatures are summarised as follows:

Merging Satellites: the face-on profile of the merger stage of Althæa has a peak flux of $\sim 0.27\,\mathrm{mJy}$, with a second peak in the blue part centred on $v = -100\,\mathrm{km\,s^{-1}}$. The major peak of the spectrum is due to the central disk, while the second peak is produced by the starless satellite. In the edge-on case, the spectrum shows an asymmetric double-peak along with multiple peaks in the core due to co-rotating clumps. The signature of the merging satellite is visible as a broad peak (with the spectral extent of $300\,\mathrm{km\,s^{-1}}$) in the red side of

the double peak profile (centred around $v = +100\,\mathrm{km\,s^{-1}}$).

Spiral arms manifest in the asymmetric Gaussian profile of the face-on spectrum of the Spiral Disk stage. In the edge-on view, the signature of spiral arms is contained in the asymmetry of the double-peak profile corresponding to the rotating disk.

Extra-planar flows: the [C II] spectrum for the face-on view of Disturbed Disk stage features a quasi-symmetric Gaussian profile which has a broader core and more prominent wings compared to the Spiral Disk. Instead, in the edge-on view, extra-planar flows tend to erase the blue peak of the line profile, hence masking the rotating disk characteristic feature.

Finally, we have discussed the observational implications of our analysis by comparing them to [C II] observations of high-z galaxies (see Tab. 1.1). The bulk of the observed spectra have FWHM $\sim 180\,\mathrm{km\,s^{-1}}$, that is compatible with face-on spectra of Althæa. Our key results are the following:

Dynamical mass estimates: we derived a generalised form of the dynamical mass vs. [C II]-line FWHM relation (eq. 3.5) which depends on the dynamical state of the galaxy. If precise information on the galaxy inclination is available, the returned mass estimate is accurate within a factor ~ 2. If the inclination is not constrained, the error increases up to a factor of $\simeq 4$. These errors are due to the fact that high-z galaxies have a complex dynamical structure and the assumption of a smooth disk used in the derivation of eq. 3.5 is not fully valid.

Tully-Fisher relation: we find a correlation between the $L_{[\mathrm{CII}]}$ and FWHM of the [C II] line by fitting the values for the sample of high-z galaxies, i.e. $L_{[\mathrm{CII}]} \propto (FWHM)^{1.80\pm0.35}$ (eq.s 3.7). This can be understood from simple physical arguments that are embedded in the relation given in eq. 3.9. By fixing the inclination and radius of the galaxy, we find that such approximate theoretical expression (eq. 3.10) is consistent with the empirical relation.

Inclination and detectability: we have performed mock ALMA simulations to check the detectability of [C II] line for face-on and edge-on views. We consider a fixed integration time (10 hr) and rebin the spectra of the Spiral Disk stage with channel width in the range of $100\,\mathrm{km\,s^{-1}} \leq \Delta v \leq 300\,\mathrm{km\,s^{-1}}$. When seen face-on, the galaxy is always detected at $> 5\sigma$; in the edge-on case, it remains undetected because the larger intrinsic FWHM pushes the peak flux below the detection limit. This suggests that some of the non-detections reported for high-z galaxies might be due to inclination effects.

Chapter 4

ISM velocity dispersion in early galaxies

In this chapter, we study the structure of spatially resolved, line-of-sight velocity dispersion for galaxies in the EoR traced by [C II] line emission at 158μm. Our laboratory is "Freesia", part of the SERRA suite (see Sec. 2.3.4). The analysis encompasses the redshift range $6 < z < 8$, when Freesia is in a very active assembling phase. This chapter of the thesis is based on Kohandel et al. 2020.

4.1 Bridging simulations and IFU observations

We want to extend these theoretical studies by modeling dynamical observables using state-of-the-art zoom-in simulations of galaxies in the EoR. The dynamical observables include the 2D spatially-resolved mean velocity and velocity dispersion maps derived from hyperspectral data cubes. To this aim, we bridge advanced zoom-in galaxy simulations to IFU-like observations (Sec. 4.1) by modeling the data cubes for [C II] line emission. For our dynamical studies, we choose three dynamically distinct evolutionary stages of "Freesia", i.e. Spiral Disk, Merger and Disturbed Disk (Sec. 4.2). Since the main focus of this chapter is to understand ISM velocity dispersion, in Sec. 4.3 we analyze spatially-resolved velocity dispersion maps extracted from [C II] data cubes for different dynamical stages, and then identify the physical drivers of the velocity dispersion. Finally, in Sec. 4.5, we investigate the relationships among different components of the velocity dispersion and star formation rates.

4.1.1 Hyperspectral data cubes

Interferometric observations like those obtained with ALMA, VLA, and LOFAR or Integral Field Units like SINFONI and MUSE yield multi-channel data cubes. These data cubes have two spatial dimensions (x and y) and one spectral dimension (λ). These data are sometimes called hyperspectral since they have an extremely high spectral resolution (e.g few thousand frequency channels in

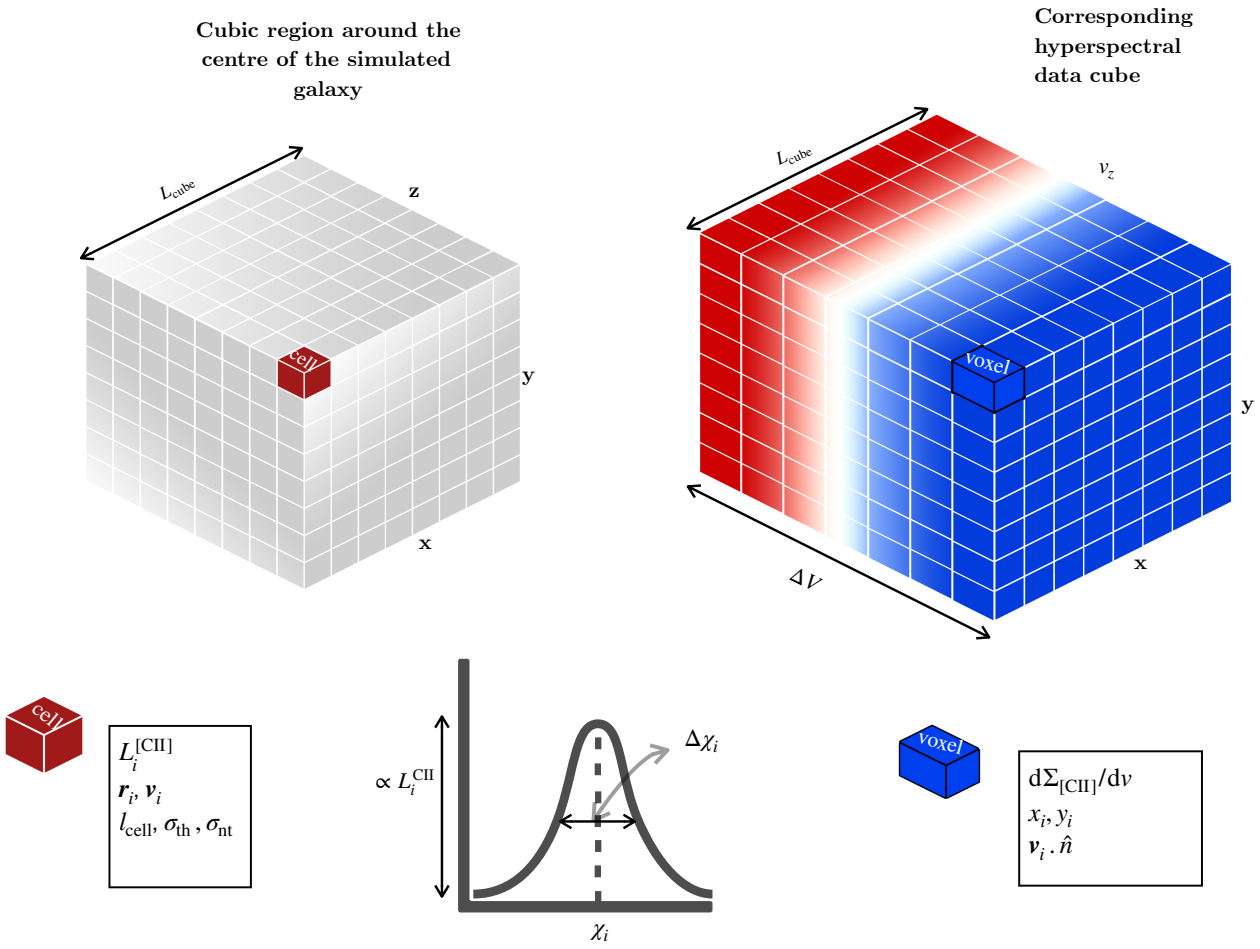

Figure 4.1: Sketch of the model used in this work to obtain hyperspectral data cubes from a simulation box (Figure 1 in Kohandel et al. 2020). Having the information on the [C II] luminosity ($L_i^{\rm CII}$), positions and velocities of the gas particles along with the cell size($l_{\rm cell}$), thermal ($\sigma_{\rm th}$) and non-thermal($\sigma_{\rm nt}$) line broadenings in a simulated cube, one can construct the hyperspectral data cubes with two spatial and one spectral dimensions. The mapping from the simulated box to the hyperspectral cube is done with three Gaussian filters in each dimension. The simulation box is represented as a uniformly binned space only for visualization purposes. See Sec. 4.1.1 for the details.

the case of ALMA). The frequency dimension of these data cubes which can be translated into a line-of-sight (l.o.s.) velocity information, allows the observer to study the dynamics of the galaxies.

To have a fair comparison between observations and simulations, we generate the Hyperspectral Data Cubes (hereafter HDC) for our simulated galaxies and extract dynamical observables (see Sec. 4.1.2). A sketch of the model is given in Fig. 4.1 and the process is detailed below.

First we extract a cubic region around the center of the galaxy with a side-length $L_{\rm cube}$ containing a number $N_{\rm cell}$ of AMR cells. For each gas cell we have information on its position ($\mathbf{r}_i$), velocity ($\mathbf{v}_i$), and [C II] luminosity ($L_i^{\rm [CII]}$, computed in post-processing using eq. 2.35a). Our HDC has two spatial and one velocity dimensions. Let us call z the l.o.s. direction, so that $v^z = \mathbf{v}\cdot\hat{\mathbf{z}}$ is the velocity component parallel to the l.o.s. and $x-y$ is the plane perpendicular to it. Then, the velocity-dependent [C II] surface brightness for each voxel of coordinates (x, y, v^z) can be modelled as follows

$$\frac{{\rm d}\Sigma_{\rm [CII]}}{{\rm d}v}(x,y,v^z) = \sum_{i=1}^{N_{\rm cell}} L_i^{\rm [CII]} K(x,x_i,\Delta x_i) K(y,y_i,\Delta x_i) K(v^z,v^z{}_i,\Delta v_i)\,, \tag{4.1a}$$

where

$$K(\chi,\chi_i,\Delta\chi_i) = \frac{1}{\Delta\chi_i\sqrt{2\pi}}\exp -\left(\frac{\chi-\chi_i}{\Delta\chi_i}\right)^2 \tag{4.1b}$$

represents the general Gaussian kernel[1] adopted for three dimensions (2 spatial + 1 velocity). The width of the Gaussian kernels ($\Delta\chi_i$) for spatial dimensions is $\Delta x_i = \Delta y_i = l_{\rm cell}$, with $l_{\rm cell}$ being the size of the considered cell. For the spectral dimension, $\Delta v_i = (\sigma_{\rm th}^2 + \sigma_{\rm nt}^2)^{1/2}$, where $\sigma_{\rm th}$ and $\sigma_{\rm nt}$ denote the thermal and non-thermal line broadening, respectively (see eq. 2.33).

4.1.2 Line spectrum and emission moment maps

Having the HDC, observables such as the line spectrum and various moments of the specific [C II] surface brightness ${\rm d}\Sigma_{\rm [CII]}/{\rm d}v$ can be obtained. It is useful to label n_x, n_y and n_v the number of bins in each dimension of the HDC, such that Δx, Δy, and Δv are the corresponding spatial and spectral resolutions. The integrated 1D line spectrum can be defined from the HDC as

$$\frac{{\rm d}L_{\rm [CII]}}{{\rm d}v}(v^z) = \sum_{l=1,m=1}^{n_x,n_y} \frac{{\rm d}\Sigma_{\rm [CII]}}{{\rm d}v}(x_l,y_m,v^z)\Delta x\,\Delta y\,. \tag{4.2}$$

The integrated surface brightness ($\Sigma_{\rm [CII]}$) as well as dynamical observables such as spatially resolved mean velocity ($\langle v\rangle$) and velocity dispersion ($\sigma_{\rm CII}$) maps are obtained from the velocity moments

[1] We have tested different kernels, finding no appreciable differences in the resulting observables.

Table 4.1: Properties of different evolutionary stages of Freesia depicted in Fig. 4.2. *Notes*: †: burstiness parameter defined in eq. 4.9, estimated with the total SFR and gas mass within $r_d = 1$ kpc; ‡: gas fraction defined as $f_g = \Sigma_g/(\Sigma_g + \Sigma_\star)$.

Stages	Short name	redshift	$M_\star$ $[10^9 M_\odot]$	M_g $[10^9 M_\odot]$	SFR $[M_\odot yr^{-1}]$	$L_{[CII]}$ $[10^8 L_\odot]$	v_c [km/s]	$k_s^\dagger$	$f_g^\ddagger$
Spiral Disk	SD	7.4	4.9	3.4	38.4	1.0	189	2.7	0.42
Merger	MG	8.0	4.0	3.0	29.5	0.7	173	2.6	0.43
Disturbed Disk	DD	6.5	10.5	3.6	85.4	1.6	246	5.6	0.26

of the HDC as follows

$$\Sigma_{[CII]}(x,y) = \sum_{j=1}^{n_v} \frac{d\Sigma_{[CII]}}{dv}(x,y,v_j^z)\Delta v\,, \tag{4.3a}$$

$$\langle v\rangle(x,y) = \frac{1}{\Sigma_{[CII]}(x,y)} \sum_{j=1}^{n_v} v_j^z \frac{d\Sigma_{[CII]}}{dv}(x,y,v_j^z)\Delta v\,, \tag{4.3b}$$

$$\sigma^2_{CII}(x,y) = \frac{1}{\Sigma_{[CII]}(x,y)} \sum_{j=1}^{n_v} \left(v_j^z - \langle v\rangle(x,y)\right)^2 \frac{d\Sigma_{[CII]}}{dv}(x,y,v_j^z)\Delta v\,. \tag{4.3c}$$

4.1.3 Numerical setup for the hyperspectral data cubes

The HDCs produced in the present analysis have the following setup. We select a cubic region centered on Freesia with side-length of $L_{cell} = 8$ kpc, which typically contains $N_{cell} \sim 10^7$ AMR gas cells; for both spatial dimensions we use $n_x = n_y = 256$. The l.o.s. velocities depend on the inclination of the galaxy; we use $n_v = 256$ bins to map a $(-400, +400)\,km\,s^{-1}$ velocity range, that is centered on the peak of the [C II] emission. Thus, the resulting HDCs have $N_{voxel} = 256^3$ voxels, with a spectral resolution of $\Delta v \simeq 3.1\,km\,s^{-1}$ and a spatial resolution of $\Delta x = \Delta y \simeq 31.2$ pc; the latter corresponds to an angular of $0.005''$ at $z = 6$. [2]

4.2 Identification of dynamical stages

We focus our analysis on three different dynamical stages during the evolution of Freesia in the redshift range of $6 < z < 8$. The stages are denominated "*Spiral Disk*" (SD), "*Merger*" (MG), and "*Disturbed Disk*" (DD). In Tab. 4.1, general properties of these stages are tabulated[3]. Among the stages, the gas mass of Freesia (M_g) varies within a factor $\lesssim 15\%$, while the star formation rate

[2] To speed up the computation of the HDCs, in eq. 4.1b we set the kernel to zero beyond 5 standard deviations away from the mean, i.e. $K(\chi, \chi_i, \Delta\chi_i) = 0$ when $|\chi - \chi_i| > 5\Delta\chi_i$.

[3] Since the stages are selected from the evolution of a single galaxy, they have different stellar masses as well as SFR. Alternatively, one could look at different galaxies with the same stellar masses and SFR, but different dynamical structures. This will be considered in future work.

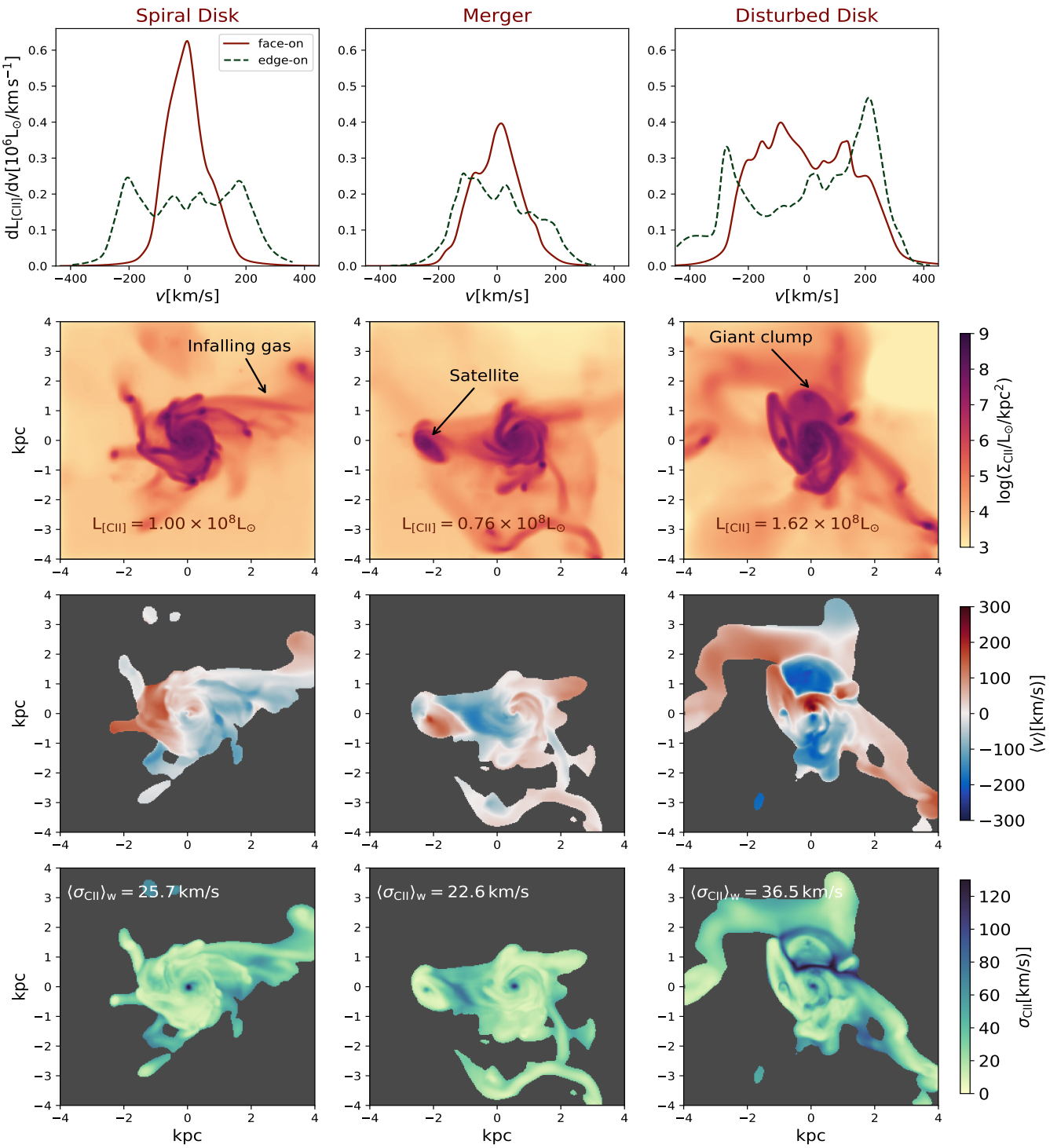

Figure 4.2: Observables derived from [C II] line hyperspectral data cubes for three stages of Freesia, Spiral Disk (SD, *left panels*), Merger (MG, *middle panels*) and Disturbed Disk (DD, *right panels*). From the top the plotted quantities are: 1D [C II] line spectra ($\mathrm{d}L_{[\mathrm{CII}]}/\mathrm{d}v$, *first row*), [C II] surface brightness ($\Sigma_{[\mathrm{CII}]}$, moment-0 map, *second row*), mean velocity ($\langle v \rangle$, moment-1 map, *third row*), and velocity dispersion ($\sigma_{[\mathrm{CII}]}$, moment-2 map *fourth row*). Spectra are extracted for face-on and edge-on views, maps are shown for the face-on view. In the surface brightness maps we report the total luminosity as an inset; on the velocity dispersion maps we quote $\langle \sigma \rangle_{\mathrm{w}}$, the [C II] luminosity weighted average of velocity dispersion. In the mean velocity and dispersion maps we gray out pixels with $\Sigma_{\mathrm{CII}} < 10^{4.5} L_{\odot}/\mathrm{kpc}^2$ (Figure 2 in Kohandel et al. 2020).

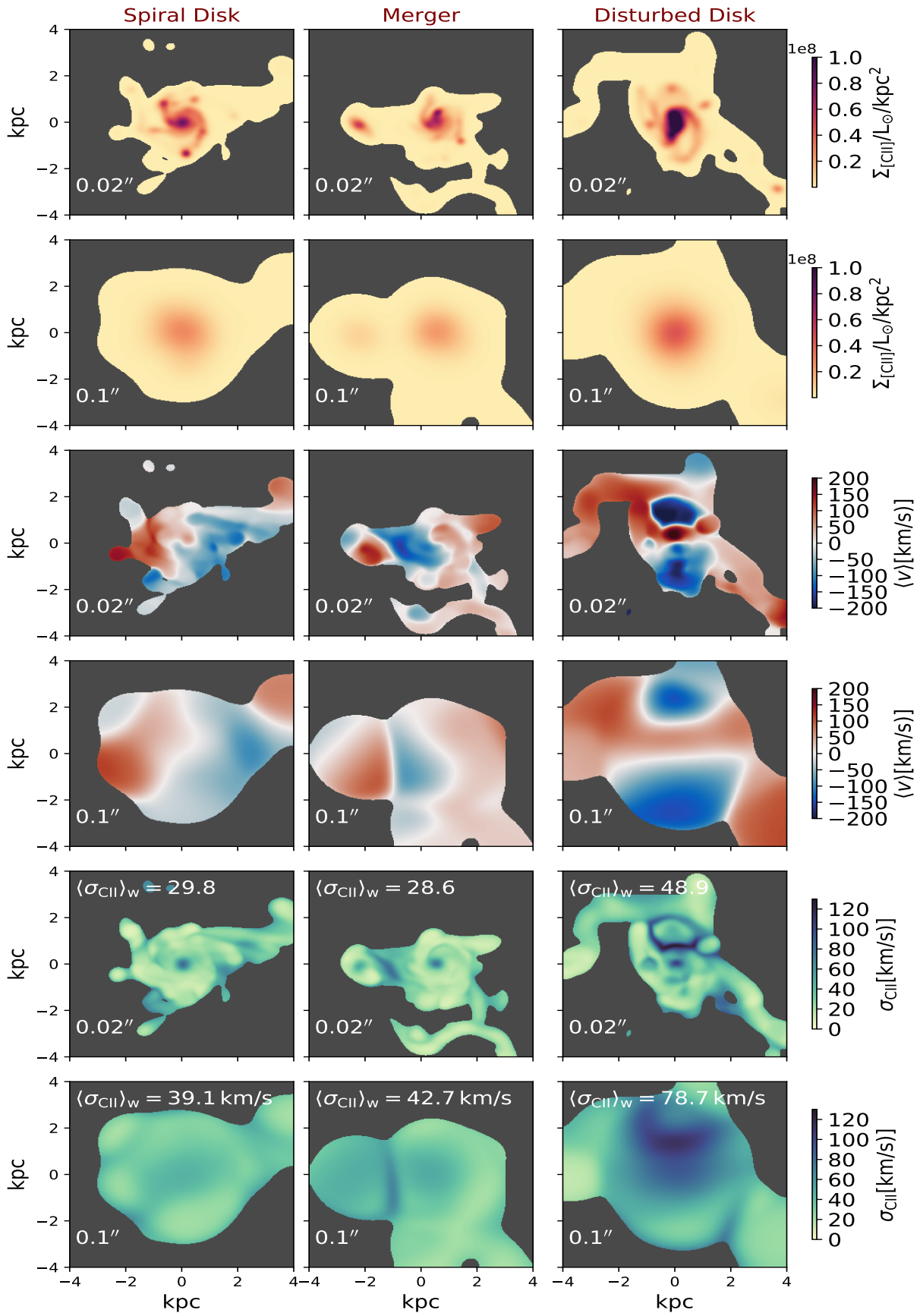

Figure 4.3: Moment maps of evolutionary stages of Freesia with angular resolution 0.02″ and 0.1″. Surface luminosities are in linear scale (Figure 3 in Kohandel et al. 2020). Notation as in Fig. 4.2.

Table 4.2: List of symbols used for the various components of the velocity dispersion.

Symbol	Description	Expression	Reference
$\sigma_{\rm th}$	Thermal velocity dispersion due to stellar feedback	$\sigma_{\rm th} = \sqrt{P_{\rm th}/\rho}$	eq. 2.33
$\sigma_{\rm nt}$	Non-thermal (turbulent) velocity dispersion due to stellar feedback	$\sigma_{\rm nt} = \sqrt{P_{\rm nt}/\rho}$	eq. 2.33
σ_{μ}	Total (small-scale) velocity dispersion due to stellar feedback	$\sigma_{\mu}^2 = \sigma_{\rm nt}^2 + \sigma_{\rm th}^2$	eq. 4.5
$\sigma_{\rm [CII]}$	Velocity dispersion derived from moment-2 of [C II] line emission	$\sigma_{\rm [CII]}^2 = \sigma_{\mu}^2 + \sigma_{\rm b}^2$	eq. 4.3c
$\sigma_{\rm b}$	Velocity dispersion due to bulk motions	$\sigma_{\rm b}^2 = \sigma_{\rm [CII]}^2 - \sigma_{\mu}^2$	eq. 4.6

(SFR) and stellar masses $M_\star$ have a variation by a factor $\lesssim 3$. In particular, DD stage has the highest star formation rate (SFR $\simeq 85.4\,{\rm M_\odot yr^{-1}}$) and stellar mass ($M_\star \simeq 10^{10}\,{\rm M_\odot}$) while the MG stage has the lowest values (SFR $\simeq 29.5\,{\rm M_\odot yr^{-1}}$, $M_\star \simeq 4\times10^9\,{\rm M_\odot}$). The total [C II] luminosity of all stages is similar and about $10^8 {\rm L_\odot}$, with the DD stage being the most luminous one. Overall, Freesia in these stages shows properties comparable to the bulk of the observed high-z galaxies, reported in Tab. 1.1.

The typical radius in all stages is $r_d = 1\,{\rm kpc}$, thus the circular velocity can be estimated via

$$v_{\rm c} = \sqrt{\frac{GM_{\rm dyn}}{r_d}}\,, \tag{4.4}$$

where $M_{\rm dyn} = M_{\rm g} + M_\star$ is the dynamical mass. Therefore, $v_{\rm c} = (189, 173, 246)\,{\rm km\,s^{-1}}$ for the (SD, MG, DD) stages, respectively.

Note that – similarly to Chap. 3 (Kohandel et al., 2019) – different stages are identified and labeled based on the morphology of the [C II] line surface brightness maps and the corresponding (total) spectra extracted for their face-on and edge-on views, as can be appreciated from Fig. 4.2, where we show moment maps as well as the corresponding integrated spectra.

We start by looking at the moment-0 (surface brightness) maps for the face-on view of the three stages (second row of Fig. 4.2). Morphologically, the three stages are clearly discernible. The SD stage features a rotating disk with a one-sided, extended tail due to infalling gas; the MG stage is produced by a satellite merging into the main galaxy; the DD stage resembles a very complex structure as a consequence of the presence of a nearby, giant star-forming clump of gas (size of about $\sim 0.5\,{\rm kpc}$) perturbing the main galaxy disk.

Rotating disks, mergers and disturbed disks have distinguishable spectral signatures in the [C II] spectra – particularly for inclinations close to edge-on, even at very high redshifts (Kohandel et al., 2019) (see Sec. 3.2). Looking at the edge-on spectra of the selected stages (first row of Fig. 4.2) we see that the SD stage shows a double-peak profile; instead, the signature of rotation in the spectra of the other two stages has been blurred by either the merging satellite (in MG stage) or the giant clump of gas hitting the disk (in DD stage). In each stage, the reported value of v_c (Tab. 4.1) is roughly consistent with the half-width of the corresponding edge-on spectra, as expected from rotation support.

As discussed in Sec. 4.1.2, a key dynamical quantity obtained from HDCs is the spatially

resolved mean velocity map, $\langle v \rangle$ (see eq. 4.3b), shown for the three stages in the third row of Fig. 4.2. The SD stage shows a well-formed velocity gradient in the central part of the system: this feature resembles a "spider diagram" pattern – i.e. a well-known signature of rotating spiral galaxies (Begeman, 1989) – that is indicative of the existence of a rotating disk. The MG stage has two distinct rotating components, one for the main galaxy and the other for its satellite. The DD stage has a very complex velocity structure due to the presence of the giant clump disturbing the disk. These results show that a single galaxy might undergo dramatic changes in the course of its evolution, mostly arising from the complexity and intermittency of the assembly processes. As velocity dispersion encodes a record of the associated kinetic energy deposition, it provides a unique diagnostic tool to understand the build-up of these early systems.

4.3 Characterising the velocity dispersion

In this Section, we first compute the velocity dispersion by analyzing moment-2 maps of the [C II] line data cubes for the considered evolutionary stages (Sec. 4.3.1). Then, in Sec. 4.4, we assess the role of (i) stellar feedback and (ii) bulk motions in driving the velocity dispersion.

4.3.1 Spatially resolved velocity dispersion maps

In the fourth row of Fig. 4.2, we plot moment-2 ($\sigma_{\rm CII}$) maps for the three evolutionary stages of Freesia. On each plot, the [C II] luminosity-weighted average velocity dispersion[4], i.e. $\langle \sigma_{\rm CII} \rangle_{\rm w}$, is reported which reduces the 2D maps to a single average value. As in the case of the $\langle v \rangle$ maps, the $\sigma_{\rm CII}$ maps are quite different, depending on the stage. Nevertheless, there are common features. All the stages show a $\sigma_{\rm CII}$ peak up to $\sim 130\,{\rm km\,s^{-1}}$ located at the galactic center; this is partially linked to the star formation activity, as we will see in Sec. 4.4.

Apart from the central peak, the SD stage (with $\langle \sigma_{\rm CII} \rangle_{\rm w} = 25.7\,{\rm km\,s^{-1}}$) has an almost uniform velocity dispersion map in the central 1 kpc region with a value of $\sim 15 - 20\,{\rm km\,s^{-1}}$ with enhanced values ($\sigma_{\rm CII}$ up to $70\,{\rm km\,s^{-1}}$) in the extended tail due to infalling gas.

The MG stage ($\langle \sigma_{\rm CII} \rangle_{\rm w} = 22.6\,{\rm km\,s^{-1}}$) looks similar in most of the disk region, but a second peak (at $\sim 50\,{\rm km\,s^{-1}}$) appears that corresponds to the center of the merging satellite. Moreover, $\sigma_{\rm CII}$ is boosted up to $\sim 80\,{\rm km\,s^{-1}}$ as a result of the bulk motions driven by the gravitational interaction between the main galaxy and the satellite (see Sec. 4.4.2).

Finally, the DD stage has the highest $\langle \sigma_{\rm CII} \rangle_{\rm w} = 36.5\,{\rm km\,s^{-1}}$) values, and has a complex velocity dispersion structure paralleling that of the $\langle v \rangle$ map. There are various arcs in the central 1 kpc scale of the disk; the region, 1 kpc north of the center, features a pronounced disturbance likely due to the very close encounter of the giant clump of gas with the disk; such very high $\sigma_{\rm CII}$ (up to $\sim 130\,{\rm km\,s^{-1}}$), the elongated region extends for about 1 kpc following the circumference of the disk.

[4] $\langle \sigma_{\rm CII} \rangle_{\rm w} \equiv \sum \sigma_{\rm CII} \Sigma_{\rm [CII]} / \sum \Sigma_{\rm [CII]}$

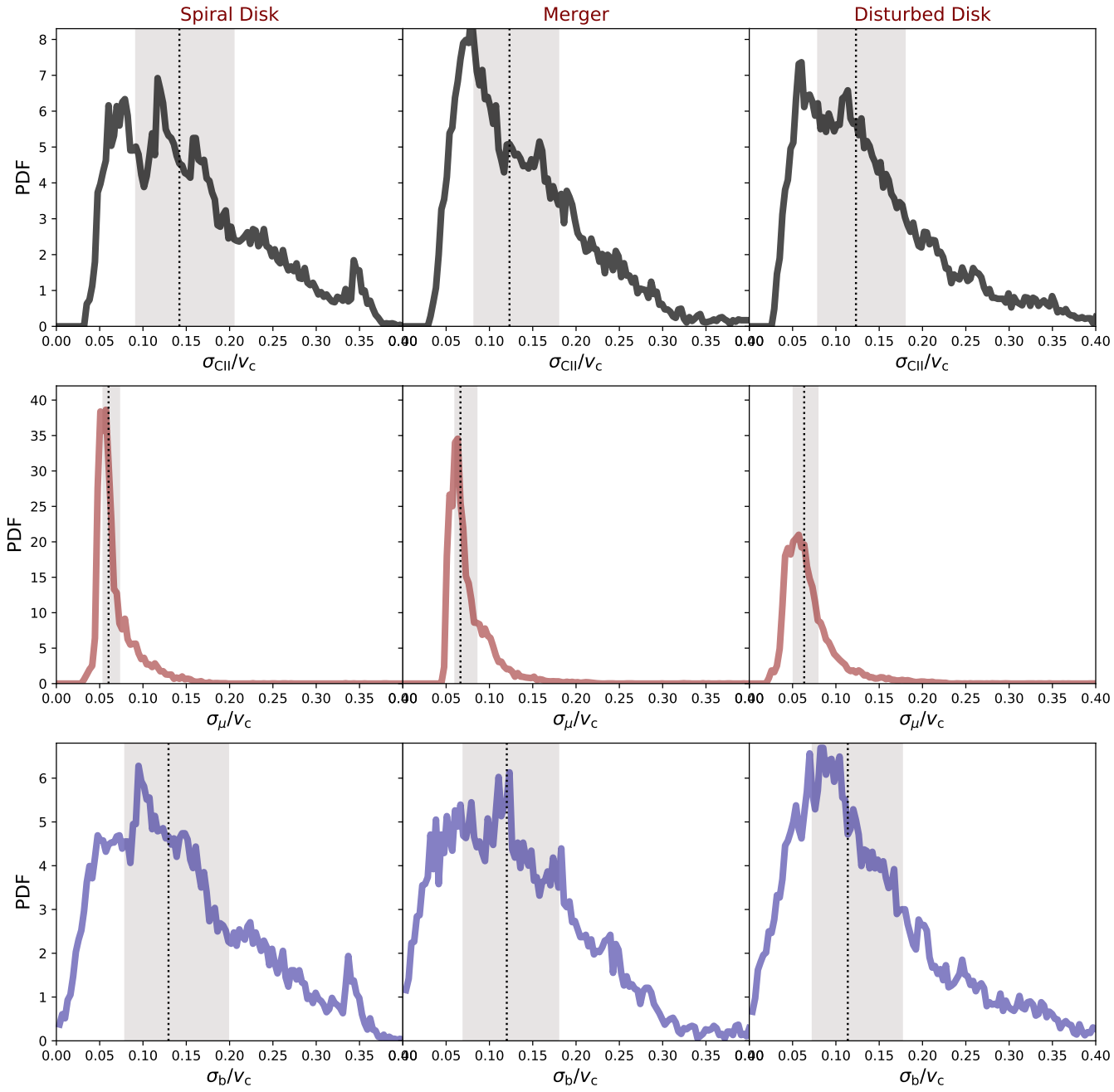

Figure 4.4: Probability distribution functions of the different velocity dispersion components for three evolutionary stages of Freesia. From top to bottom, we show the total velocity dispersion, $\sigma_{\rm [CII]} = (\sigma_{\mu}^2 + \sigma_{b}^2)^{1/2}$, from Fig. 4.2; small-scale velocity dispersion, σ_{μ}, due to stellar feedback from Fig. 4.5; the large-scale velocity dispersion, σ_{b}, due to bulk motions from Fig. 4.6. See Tab. 4.2 for a summary of the definitions. The vertical dotted line denotes the mean value; the gray-shaded area represents the width of the distribution which is the difference between 25th and 75th percentile of the distribution (Figure 4 in Kohandel et al. 2020).

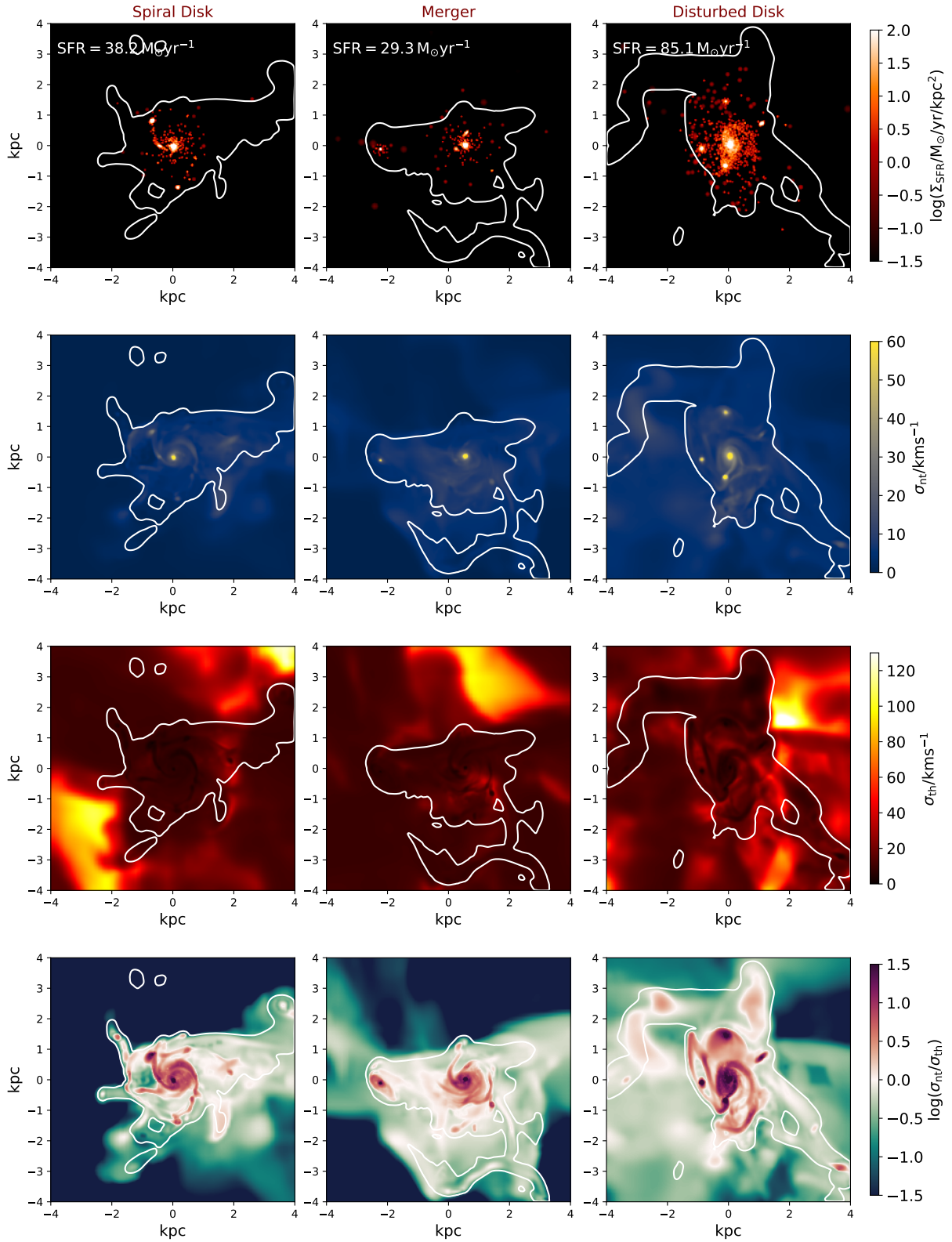

Figure 4.5: Star formation and stellar feedback in the different stages of Freesia. *Top row*: star formation rate density maps *Second*: the velocity dispersion due to non-thermal pressure (turbulence), *Third*: thermal line broadening. *Bottom*: the ratio between non-thermal and thermal line broadening. White contours correspond to the $\Sigma_{\rm CII} = 10^{4.5} L_\odot\,{\rm kpc}^{-2}$ cuts of Fig. 4.2 (Figure 5 in Kohandel et al. 2020).

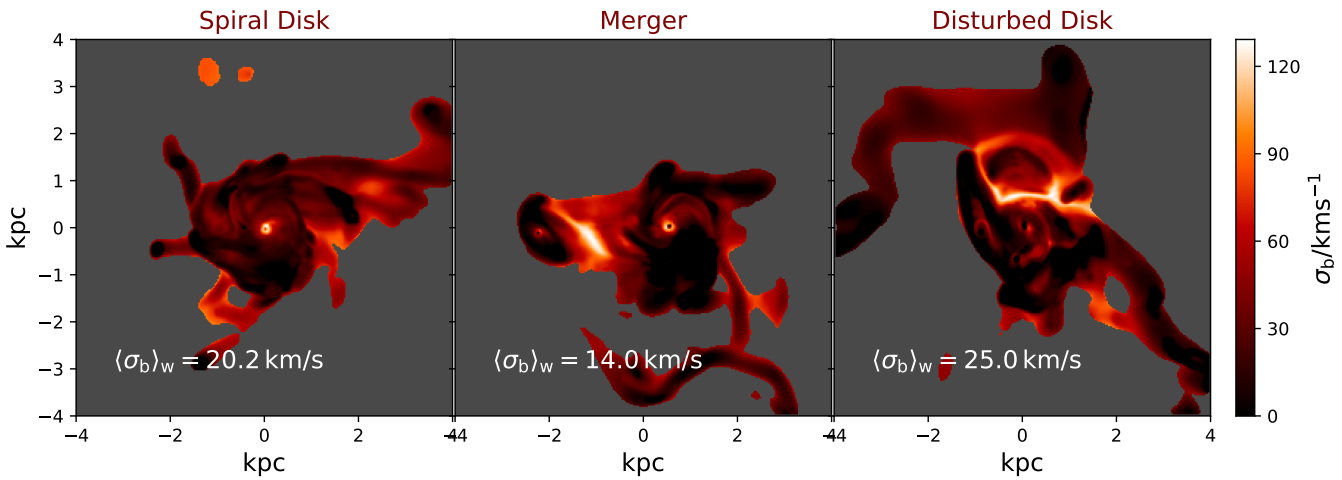

Figure 4.6: Maps of velocity dispersion due to gravitational interactions (eq. 4.6) for three stages of Freesia. Notation as in Fig. 4.2 (Figure 6 in Kohandel et al. 2020).

Such a feature in velocity dispersion maps is due to gravitational interactions of multi-component systems (in this case, the main galaxy and the giant gas clump), as we detail in Sec. 4.4.2.

To summarize, if we measure the level of ISM velocity dispersion via a luminosity-weighted average value as i.e. done in actual observations (e.g. Green et al. 2014), Freesia shows a moderate value around $\sim 23-38\,\mathrm{km\,s^{-1}}$. Note that these values are obtained for an angular resolution of $\sim 0.0005''$, which however impacts the conclusions, as we will see in Sec. 4.3.2.

Using the galaxy circular velocity and the average l.o.s velocity dispersion, we can define the rotational-to-dispersion support ratio, v_c/σ. Adopting $\sigma = \langle\sigma_{\rm CII}\rangle_w$ leads to a v_c/σ ratio of 7.4, 7.7 and 6.7 for the cold [C II] emitting gas in SD, MG and DD stage respectively. As a comparison, such ratio is ≈ 20 for the MW, and $3.5-6$ for intermediate redshift galaxies (Hodge et al., 2012; Swinbank et al., 2011). Thus, cold gas in EoR galaxies – unlike the MW but similarly to galaxies at comic noon – receives considerable support from random motions.

4.3.2 Beam smearing effects

We want to understand the effect of beam smearing on the resultant dynamical observables derived from the full resolution ($0.0005''$) [C II] line HDC. We mimic the beam smearing by performing a smoothing with a Gaussian kernel of 0.02 and 0.1 arcsecs. Then using eqs. 4.3, we obtain the low-resolution counterparts of Fig. 4.2. In Fig. 4.3, we show different moment maps of [C II] line for two angular resolutions (0.02 and 0.1 arcsecs) for the evolutionary stages of Freesia.

As expected, beam smearing affects the morphology of various moment maps. In the lowest resolution case, it is very challenging to derive morphological/structural properties like the presence of a disk, satellites, or clumps in each structure.

As shown in Fig. 4.3, $\langle\sigma_{\rm CII}\rangle_w$ *increases with decreasing angular resolution.* More precisely, at 0.02 arcsecs, it ranges between $28-50\,\mathrm{km\,s^{-1}}$ while at 0.1 arcsecs, it rises up to $40-80\,\mathrm{km\,s^{-1}}$. This

effect is more dramatic in the DD stage. With the lowest resolution, $\langle\sigma_{\rm CII}\rangle_{\rm w}$ is doubled compared to the high-resolution case (Fig. 4.2). This effect is more severe in the DD stage because, as we saw in Sec. 4.3.1, in the central $\sim 2\,$kpc part of the galaxy there are various arcs with large velocity dispersions $\lesssim 130\,{\rm km\,s^{-1}}$, substantially contributing to [C II] emission. When we perform the smoothing, the emission from these high dispersion arcs spreads over the disk (see the $\sigma_{\rm CII}$ DD map at 0.1 arcsec resolution). This yields a very large average velocity dispersion.

These results show that, when dealing with real observations, the beam smearing effect must be carefully accounted for when inferring the proper velocity dispersion of the system, particularly the interacting ones. For the rest of the chapter, we continue our analysis with the high-resolution cases (Fig. 4.2), unless otherwise stated.

4.4 Physical drivers of the velocity dispersion

To further investigate the structure of the observed velocity dispersion, it is convenient to build and analyze its 1-D probability distribution function (PDF). In the first row of Fig. 4.4, we plot the (normalized) PDFs of the distribution of $\sigma_{\rm CII}/v_{\rm c}$ for three evolutionary stages of Freesia. The three PDFs have similar shapes: they peak at $\sigma_{\rm CII}/v_{\rm c} < 0.1$ and have a high velocity dispersion tail. All the distributions have a similar width, i.e. the difference between 25th and 75th percentile, around 0.1. Regarding the shape of the distribution, while the MG stage shows a single sharp peak at the low $\sigma_{\rm CII}$ part of the distribution, the SD and DD stages have a multiple peak structure. In particular, the SD stage has an additional peak in the high velocity dispersion ($\sigma_{\rm CII}/v_{\rm c} \sim 0.35$) part of the distribution. To understand the physical origin of the main features in the PDF, it is necessary to quantify the individual contribution from different driving mechanisms to the observed velocity dispersion.

To identify the physical drivers of the observed velocity dispersion, $\sigma_{\rm CII}$, we start by investigating the effect of stellar feedback as a driver of velocity dispersion. Next, we turn to bulk motions sourced by gravitational interactions.

4.4.1 Stellar feedback

In Fig. 4.5 (first row), we plot Freesia's star formation rate density maps (eq. 2.32). For all of the stages, the SFR density is ($\Sigma_{\rm SFR} > 10^2\,{\rm M_\odot yr^{-1}kpc^{-2}}$) at the galaxy center. The SD stage with a total SFR of $38.2\,{\rm M_\odot yr^{-1}}$ has the smoothest $\Sigma_{\rm SFR}$ map, with most of the star formation occurring in the galactic disk. Interestingly, some bright star-forming regions are located along the spiral arms. The MG stage has the lowest total SFR ($29.3\,{\rm M_\odot yr^{-1}}$). Signs of recent star formation are seen both on the main galaxy and the satellite. The DD stage has the highest total SFR ($85.1\,{\rm M_\odot yr^{-1}}$), with various very bright star-forming sites along the spiral arms, as well as in the giant gas clump.

In Fig. 4.5, we plot the turbulent, i.e. $\sigma_{\rm nt}$, (second row), and thermal velocity dispersion, i.e. $\sigma_{\rm th}$, maps (third row) induced by stellar feedback for the evolutionary stages of Freesia. On these maps, we have overplotted contours inside which pixels have $\Sigma_{\rm CII} > 10^{4.5} L_{\odot}{\rm kpc}^{-2}$ (the same luminosity cut used in the mean velocity and velocity dispersion maps in Fig. 4.2). In Tab. 4.3, the [C II] luminosity weighted average values of the turbulent, $\langle\sigma_{\rm nt}\rangle_{\rm w}$, and thermal $\langle\sigma_{\rm th}\rangle_{\rm w}$ velocity dispersion are tabulated for the three evolutionary stages.

The $\sigma_{\rm nt}$ maps are almost flat but show high values at the galactic center ($\sigma_{\rm nt} = 100-140\,{\rm km\,s^{-1}}$ depending on the stage). The SD and MG stages have similar $\langle\sigma_{\rm nt}\rangle_{\rm w} \simeq 11\,{\rm km\,s^{-1}}$, while the DD stage has a slightly higher value ($\sim 18\,{\rm km\,s^{-1}}$). This behaviour was expected since the SD and MG stage have similar SFRs (see Tab. 4.1) while the MG stage has $\approx 3\times$ higher SFR ($\sim 85{\rm M_{\odot}yr^{-1}}$); it also has more star-forming sites with high SFR density compared to the other stages (see Fig. 4.5). Thus, the higher the star formation, the more turbulent the ISM becomes due to the collective kinetic energy deposition by SNe, stellar winds and radiation pressure.

Instead, looking at $\sigma_{\rm th}$ maps, we see some shock-heated extended regions with $\sigma_{\rm th} > 80\,{\rm km\,s^{-1}}$ in addition to smooth central ($< 1\,$kpc) parts with low dispersion values ($\sim 10\,{\rm km\,s^{-1}}$). Most of the shock-heated regions (for instance the south-west corner of the SD or a triangular region in the north of the MG stage map) are regions with very low [C II] line intensity ($\Sigma_{\rm [CII]} < 10^{4.5}\,{\rm L_{\odot}/kpc^2}$). In terms of average values, all the stages have similar $\langle\sigma_{\rm th}\rangle_{\rm w}$ ($\sim 10\,{\rm km\,s^{-1}}$; see Tab. 4.3).

In the bottom row of Fig. 4.5, we plot the ratio between the turbulent and thermal velocity dispersion as a proxy of the level of turbulence. The structure of the small-scale turbulence of the ISM of Freesia can be divided in three phases; sub-sonic ($\log(\sigma_{\rm nt}/\sigma_{\rm th}) \leq 0$), supersonic ($0 < \log(\sigma_{\rm nt}/\sigma_{\rm th}) < 1.5$) and hyper-sonic ($\log(\sigma_{\rm nt}/\sigma_{\rm th}) \geq 1.5$). In Freesia, the turbulence in most of the [C II] emitting gas is either supersonic (or even hypersonic). To quantify the total contribution of stellar feedback in $\sigma_{\rm CII}$, we introduce the small-scale velocity dispersion [5] (σ_{μ}) as

$$\sigma_{\mu} = \sqrt{\sigma_{\rm th}^2 + \sigma_{\rm nt}^2}\,. \tag{4.5}$$

In the middle row of Fig. 4.4, we show the PDFs of $\sigma_{\mu}/v_{\rm c}$. For all stages, the distribution can be fitted with a single Gaussian function apart from the tail of the distribution specially in the SD and MG stage. The excess in the high velocity dispersion tail of the distribution in these stages is due to pixels with hyper-sonic turbulence for which $\log(\sigma_{\rm nt}/\sigma_{\rm th}) \geq 1.5$ (see Fig. 4.5]). These high values of velocity dispersion will dissipate on time scales of $\lesssim 0.1$Myr (see eq. 2.30). The PDFs of $\sigma_{\mu}/v_{\rm c}$ with respect to $\sigma_{\rm CII}/v_{\rm c}$ (see first row of Fig. 4.4) are very narrow and confined. Most of the distribution of $\sigma_{\rm CII}/v_{\rm c}$ can not be fully described by σ_{μ} only. Therefore, stellar feedback alone is not sufficient to maintain the observed $\sigma_{\rm CII}$; bulk motions arising from gravitational forces are then required.

[5] Note that to compute the small-scale velocity dispersion we have just accounted for the pixels with $\Sigma_{\rm [CII]} > 10^{4.5}\,{\rm L_{\odot}/kpc^2}$

Table 4.3: [C II] luminosity weighted velocity dispersion values.

Stages	$\langle\sigma_{\rm CII}\rangle_{\rm w}$ [km s^{-1}]	$\langle\sigma_{\rm nt}\rangle_{\rm w}$ [km s^{-1}]	$\langle\sigma_{\rm th}\rangle_{\rm w}$ [km s^{-1}]	$\langle\sigma_{\rm b}\rangle_{\rm w}$ [km s^{-1}]
Spiral Disk (SD)	25.7	11.5	7.0	20.7
Merger (MG)	22.6	11.8	10.6	17.6
Disturbed Disk (DD)	36.5	18.4	10.5	27.8

4.4.2 Bulk motions

We define the bulk velocity dispersion as

$$\sigma_{\rm b} = \sqrt{\sigma^2_{\rm [CII]} - \sigma^2_{\mu}}\,. \tag{4.6}$$

One of the obvious sources of bulk motions is the rotational energy of the system. This can be directly subtracted out from the analysis if we consider, as done here, the face-on view of the galaxy. Other than rotation, the velocity dispersion can be increased by disordered, large-scale motions generated by gravitational interactions occurring in multi-component systems like Freesia.

For instance, the velocity enhancement mentioned earlier, and due to infalling gas (in the SD stage), merging satellites (MG), or close encounters with clumps (DD), fall in this category (see Fig. 4.2). These enhancements cannot be explained by the stellar feedback that we analyzed in the previous Section. In Fig. 4.6, we show $\sigma_{\rm b}$ maps for the three evolutionary stages of Freesia. In terms of average values, the DD stage has the highest $\langle\sigma_{\rm b}\rangle_{\rm w} \simeq 28\,{\rm km\,s^{-1}}$ value, whereas the MG stage only reaches $\simeq 18\,{\rm km\,s^{-1}}$. We also plot the $\sigma_{\rm b}/v_{\rm c}$ PDF in the bottom row of Fig. 4.4. By comparing the PDF of $\sigma_{\rm CII}/v_{\rm c}$ and $\sigma_{\rm b}/v_{\rm c}$, we conclude that the high velocity tail of the $\sigma_{\rm CII}$ distribution is largely produced by bulk motions such as gravitational interactions. Hence, gravity provides the dominant ($> 90\%$) contribution to kinetic energy observed in [C II].

A key difference between bulk motions and feedback-related turbulence is the dissipation time. Referring to eq. 2.30, the dissipation time scale for $\sigma_{\rm b}$ would be of the order of $l_{\rm b}/\sigma_b$, where $l_{\rm b}$ can be conservatively taken as the disk radius, or $l_b \approx 1{\rm kpc} = 100\,l_{\rm cell}$. Hence, the dissipation time of bulk motions is about 30-50 times longer than that of small-scale turbulence produced by energy injection from massive stars. In turn, this allows gravitationally-induced motions to dominate the overall kinetic energy budget of the galaxy.

4.5 Spatially resolved $\sigma_{\rm CII} - \Sigma_{\rm SFR}$ relation

Using the results in Sec. 4.4, we can study the local relation between the l.o.s velocity dispersion and star formation rate densities in Freesia. We compute the 2D distribution of different velocity

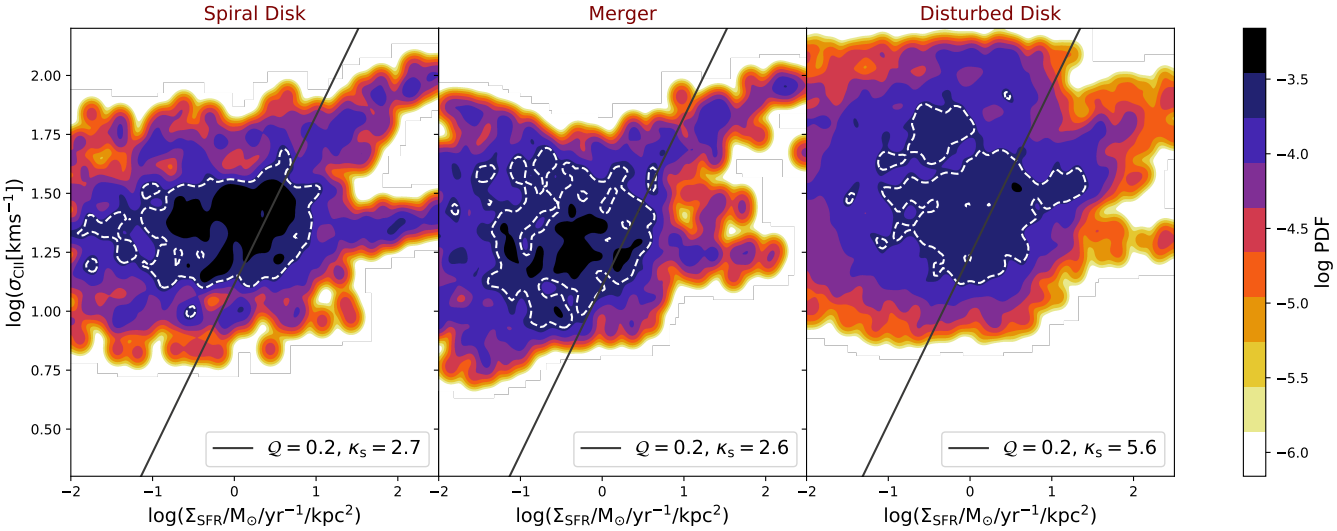

Figure 4.7: 2D PDFs of spatially resolved l.o.s velocity dispersion derived from [C II] data cubes ($\sigma_{\rm CII}$) and star formation rate densities for various stages of Freesia (Figure 7 in Kohandel et al. 2020). The white dashed contours show the region including 90% of the data. The solid lines indicate the analytical expression for $\sigma - \Sigma_{\rm SFR}$ relation (see eq. 4.10 and values given in Tab. 4.1).

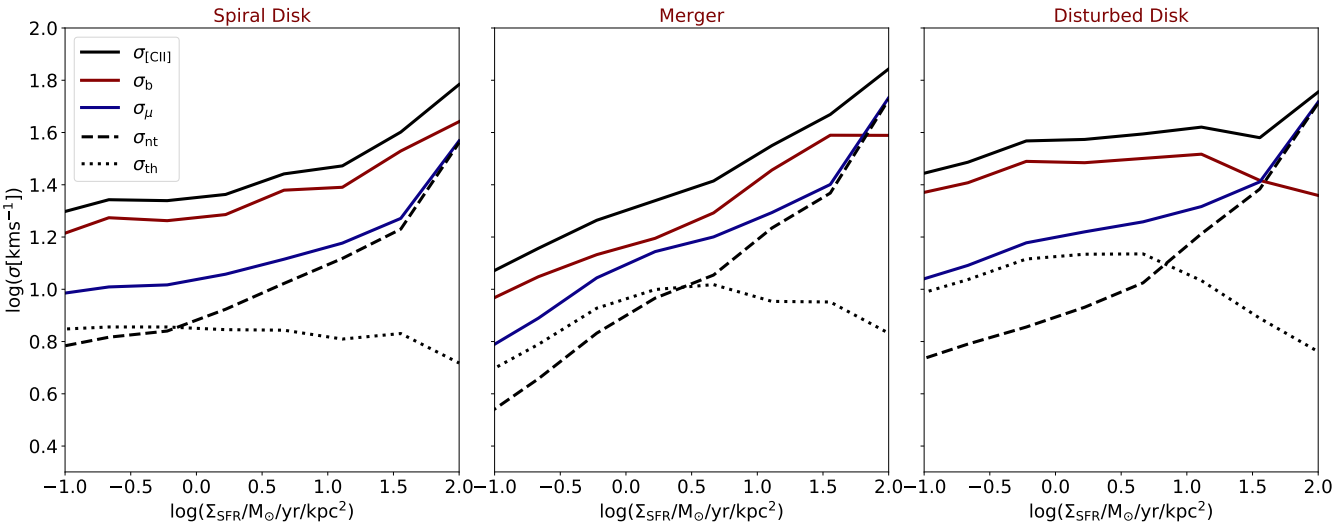

Figure 4.8: The average relation between different components (see internal label) of the total velocity dispersion, $\sigma_{\rm CII}$, and the star formation surface density $\Sigma_{\rm SFR}$. Each panel refers to a different evolutionary stage. The curves are obtained from the data shown in Fig. 4.7 by averaging the data in 10 bins of SFR density in the range $0.1 - 100\,{\rm M}_\odot{\rm yr}^{-1}{\rm kpc}^{-2}$ (Figure 8 in Kohandel et al. 2020).

dispersion components ($\sigma_{\rm CII}, \sigma_b, \sigma_\mu, \sigma_{\rm nt}\sigma_{\rm th}$) as a function of $\Sigma_{\rm SFR}$. In Fig. 4.7, we concentrate on the distribution of total $\sigma_{\rm CII}$ for the SD, MG and DD stage. We do not see a clear correlation between these quantities. It seems that $\sigma_{\rm CII}$ for all the stages is constant for a range of 4 dex of star formation rate densities.

To see the behaviour of other components of the velocity dispersion ($\sigma_{\rm CII}, \sigma_b, \sigma_\mu, \sigma_{\rm nt}\sigma_{\rm th}$), we obtain the average σ-$\Sigma_{\rm SFR}$ relation for each component by averaging the data in 10 bins of SFR density in the range $0.1 - 100\,{\rm M_\odot yr^{-1}kpc^{-2}}$. The results are shown in Fig. 4.6 for the usual three evolutionary stages.

First we concentrate on $\sigma_{\rm CII}$. For the SD and DD stages, $\sigma_{\rm CII}$ is almost independent on $\Sigma_{\rm SFR}$ over three orders of magnitude, apart from a slight increase (factor $\lesssim 1.5$) at the high-end of the star formation range. Such a result is in agreement with a recent theoretical work Orr et al. 2019a. These authors study the relation between gas velocity dispersion and star formation rate for Milky Way-like galaxies in FIRE-2 simulations (Hopkins et al., 2018). They find a relatively flat relation ($\sigma \sim 15 - 30\,{\rm km\,s^{-1}}$ in neutral gas) across 3 dexes in SFR; this is also in agreement with nearby galaxies observations (Zhou et al., 2017). Note that Orr et al. 2019a do not model emission lines to compute the l.o.s velocity dispersion. This might affect their conclusion as they are not directly computing the observed velocity dispersion, which can be affected by resolution issues (see Fig. 4.3).

For the MG stage, the situation is different. The dependence of $\sigma_{\rm CII}$ on $\Sigma_{\rm SFR}$ shows instead an increasing trend across the SFR range. This correlation might be partly caused by the fortuitous presence of a satellite with peculiar properties; The satellite has low $\sigma_{\rm CII}$, low SFR. Because of its large [C II] emission, it dominates the low SFR part of the relation decreasing the [C II]-weighted velocity dispersion and therefore $\sigma_{\rm CII}$ is biased-low.

The different contributions to $\sigma_{\rm CII}$ follow similar trends with star formation in the three stages: $\sigma_{\rm b}$ always dominates the relation for $\Sigma_{\rm SFR} \lesssim 10 - 30\ {\rm M_\odot yr^{-1}kpc^{-2}}$, i.e. bulk motions such as gravitational interactions are the main drivers of the velocity dispersion in moderate star-forming, high-redshift galaxies. At higher SFRs, stellar feedback becomes important and σ_μ catches up with bulk motions. The increase of σ_μ at high SFR is due to enhanced momentum injection by massive stars powering supersonic turbulence for which $\sigma_{\rm nt}/\sigma_{\rm th} > 3$. The contribution from supersonic regions to the total [C II] luminosity is $\approx 10\%$ for the SD and DD stages and $\approx 5\%$ for the MG stage. The thermal component, $\sigma_{\rm th}$ becomes larger than the turbulent term ($\sigma_{\rm nt}$) only at $\Sigma_{\rm SFR} \lesssim 5\ {\rm M_\odot yr^{-1}kpc^{-2}}$. In general, the feedback-related turbulent level in Freesia achieves an almost constant value of $\sigma_\mu \simeq 10 - 15\,{\rm km\,s^{-1}}$ independently of SFR. Such value is higher than the velocity dispersion typically observed in local molecular clouds, which is around $5 - 10\,{\rm km\,s^{-1}}$ (Bolatto et al., 2008). In summary, the ISM velocity dispersion in assembling, EoR galaxies appears to be dominated by the bulk motions component produced by gravitational interactions, such as accretion/merging events.

To gain some insight, it is instructive to compare our results with a simple physical model for

the $\sigma - \Sigma_{\rm SFR}$ relation. The Toomre parameter, $\mathcal{Q}$ (Toomre, 1964) for a galaxy with a total mass surface density $\Sigma = \Sigma_{\rm g} + \Sigma_\star$, l.o.s velocity dispersion σ, and epicyclic frequency $\kappa = a v_{\rm c}/r_d$, where $a = \sqrt{2}$ for galaxies with flat rotation curves (Inoue et al., 2016b; Leung et al., 2019) is given by

$$\mathcal{Q} = \frac{\sigma\kappa}{\pi G \Sigma} = \sqrt{2}\left(\frac{v_{\rm c}}{\sigma}\right)^{-1} \tag{4.7}$$

where G is the gravitational constant. The total mass surface density is computed from the data in Tab. 4.1 assuming as a reference radius, $r_d = 1$ kpc, for both gas and stars.

We introduce the gas fraction, $f_g = \Sigma_g/(\Sigma_\star + \Sigma_g)$; this is given in Tab. 4.1 for Freesia. Then assuming an average Toomre parameter $\mathcal{Q}$ for the galaxy, we can relate the l.o.s velocity dispersion to the gas surface density as

$$\sigma = \mathcal{Q}\sqrt{\frac{\pi G \Sigma_g r_d}{2 f_g}}. \tag{4.8}$$

To relate the gas surface densities to star formation rate surface densities, we assume a generalized KS relation (Heiderman et al., 2010; Pallottini et al., 2019; Ferrara et al., 2019)

$$\left(\frac{\Sigma_{\rm SFR}}{\rm M_\odot yr^{-1} kpc^{-2}}\right) = 10^{-12}\kappa_{\rm s}\left(\frac{\Sigma_{\rm g}}{\rm M_\odot kpc^{-2}}\right)^n, \tag{4.9}$$

with $n = 1.4$; $\kappa_{\rm s}$ is the burstiness parameter, given in Tab. 4.1, expressing deviations from the empirical local relation (Kennicutt, 1998). For starburst galaxies, $k_s > 1$. Hence, the relation between gas l.o.s velocity dispersion σ and star formation rate surface density $\Sigma_{\rm SFR}$ is

$$\sigma = 70\, A \left(\frac{\Sigma_{\rm SFR}}{\rm M_\odot yr^{-1} kpc^{-2}}\right)^{5/7}\left(\frac{r_d}{\rm kpc}\right)^{1/2} \rm km\, s^{-1}, \tag{4.10a}$$

where

$$A = \frac{1}{\sqrt{2}}\frac{\mathcal{Q}}{f_g^{1/2} k_s^{5/7}} \tag{4.10b}$$

which requires the information on the average $\mathcal{Q}$ parameter.

We calculate the average Toomre parameter for [C II] emitting gas in three stages of Freesia by using eq. 4.7 and $\sigma = \langle\sigma_{\rm CII}\rangle_{\rm w}$. We derive $\mathcal{Q} \simeq 0.2$ for all three stages, a value compatible, but slighlty lower, than typically deduced for intermediate redshift galaxies ($\mathcal{Q} \sim 0.5$ in Swinbank et al. 2011 and $\mathcal{Q} \sim 0.25$ in Hodge et al. 2012). Note that all the stages are in a starburst phase, with $\kappa_{\rm s}$ between 2.6 and 5.6, in an agreement with what inferred by Vallini et al. 2020 for COS-3018 – a $z \simeq 6.8$ redshift galaxy – from UV, CIII] and [CII] data (Carniani et al., 2018b; Smit et al., 2018; Laporte et al., 2017).

In Fig. 4.7, we overplot eq. 4.10 on top of simulations data for the three stages of Freesia. Although the simulated PDF of $\sigma_{\rm CII} - \Sigma_{\rm SFR}$ does not show a clear trend, 90% data inclusion regions lie on the derived average analytical expression for the SD and DD stages. The actual

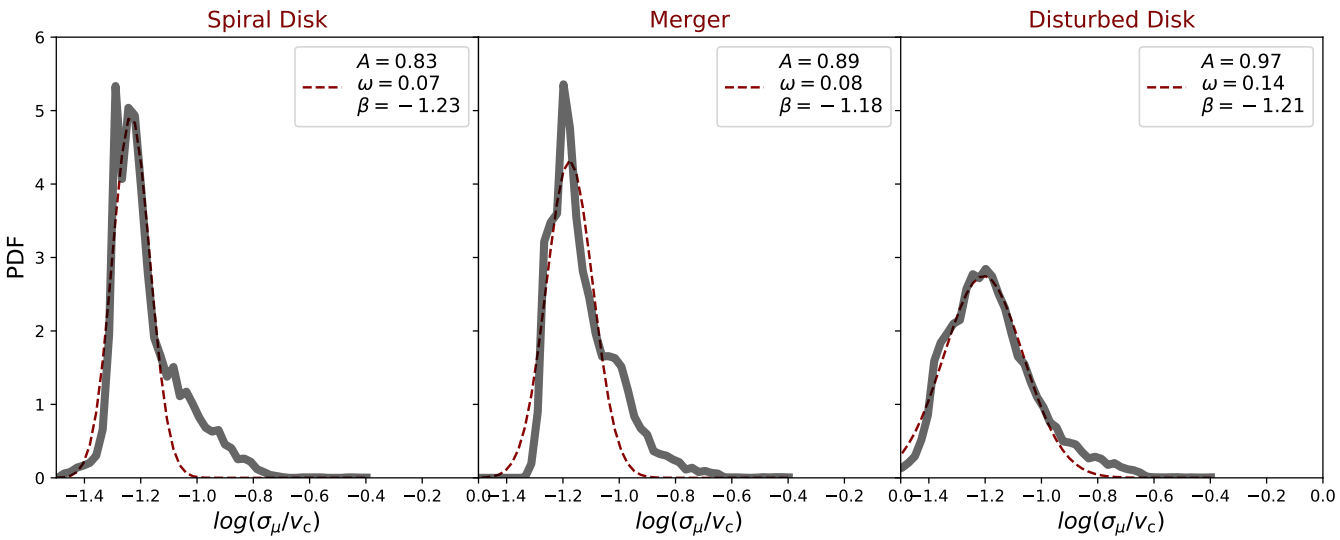

Figure 4.9: Probability distribution function of small-scale velocity dispersion for three stages of Freesia along with the fitted normal distribution (dashed line).

velocity dispersion in the MG stage is instead higher than predicted by the analytical relation; this is expected given the simplifying, thin disk assumptions on which the latter is based.

Although we have concluded that stellar feedback plays a sub-dominant role in determining the observed velocity dispersion, we should warn that the delay between star formation and the corresponding feedback can introduce complications in this picture (Orr et al., 2019b). In addition, the delay depends on the specific feedback process considered. For example, the delay time is $5-30$ Myr for supernova feedback, and $0-10$ Myr for ionizing radiation and winds from OB stars (Leitherer et al., 1999). However, the observed $\sigma - \Sigma_{\rm SFR}$ relation (Lehnert et al., 2013; Yu et al., 2019)) is obtained from star formation rates and the velocity dispersions measured at the same time. We have roughly accounted for this bias by including only stars younger than 30 Myr in the simulated SFR computation (see Sec. 2.3.1).

Small-scale velocity dispersion

In this section, we analyze the small-scale velocity dispersion (σ_μ) for three stages of Freesia. In Fig. 4.9, the PDFs of σ_μ/v_c in log-space are plotted for Freesia. We have fitted these profiles with a normal distribution

$$f(x) = \frac{A}{\sqrt{2\pi}\omega} \exp\left(-(x-\beta)^2/2\omega^2\right). \tag{4.11}$$

For all the three stages, we have been able to fit the overall distribution except for the tails. The tails are likely the result of recent starburst episodes for which turbulent energy has not yet had time to dissipate and reach a steady state. The fit parameters are reported in each plot. Among the stages, the PDF of the DD stage has a larger width which is due to the fact that the ISM is more turbulent in this stage and it has a broader thermal velocity distribution. In Fig. 4.10, the

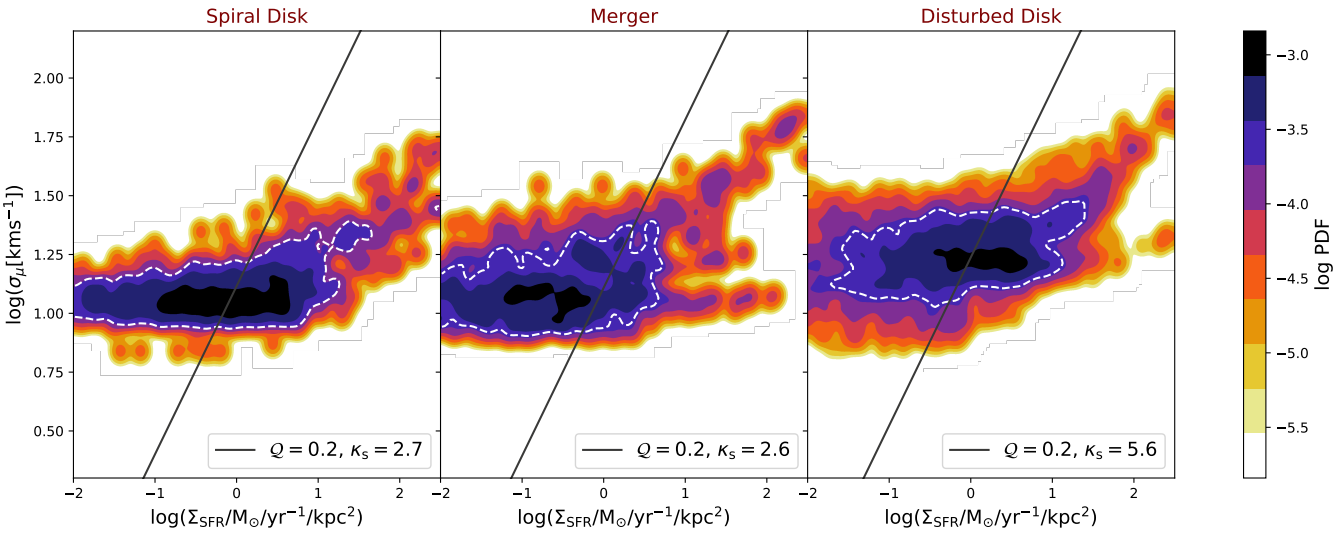

Figure 4.10: 2D PDFs of spatially resolved small-scale velocity dispersion and star formation rate densities for various stages of Freesia. The white dashed contours show the region including 90% of the data. The solid lines indicate the analytical expression for $\sigma - \Sigma_{\rm SFR}$ relation (see eq. 4.10 and values given in Tab. 4.1)

2D PDFs of spatially resolved σ_μ as a function of $\Sigma_{\rm SFR}$ for three evolutionary stages are shown. We see that σ_μ in all the stages is an almost constant independent of $\Sigma_{\rm SFR}$ over three orders of magnitude. The distribution of σ_μ is relatively narrow around the mean in all stages, with the DD one showing somewhat higher values. The 90% data inclusion regions in these distributions lie on the derived average analytical expressions (see eq. 4.10).

4.6 Summary

We have studied the structure of the spatially resolved line of sight velocity dispersion for galaxies in the EoR traced by [C II] line emission. Our laboratory is a galaxy in the SERRA suite of zoom-in simulations called "Freesia".

We have modelled [C II] emission Hyperspectral Data Cubes (HDC) for three evolutionary stages of Freesia: *Spiral Disk* (SD) at $z = 7.4$, *Merger* (MG) ($z = 8.0$), and *Disturbed Disk* (DD) ($z = 6.5$). These three stages correspond to well-defined, distinct dynamical states of the galaxy. SD is a rotating disk ($v_{\rm c} = 189\,{\rm km\,s^{-1}}$) with an extended, lopsided tail due to the in falling gas; the MG stage (with $v_{\rm c} = 173\,{\rm km\,s^{-1}}$) contains a satellite merging into the main galaxy; finally, the DD stage ($v_{\rm c} = 246\,{\rm km\,s^{-1}}$) is the most complex configuration due to the presence of a giant clump of gas (size about $\sim 0.5\,{\rm kpc}$) in the very vicinity of the main galaxy. The total [C II] luminosity of the stages is $\simeq 10^8\,L_\odot$. From the simulated HDC, we have built spatially resolved mean velocity $\langle v \rangle$, and velocity dispersion $\sigma_{\rm CII}$ maps for all the stages. Using $\sigma_{\rm CII}$ maps we have evaluated the level of velocity dispersion in the ISM of high-z galaxies and determined its physical drivers. We have studied the contribution of velocity dispersion due to bulk motions

($\sigma_{\rm b}$) and stellar feedback (σ_{μ}), the latter incorporating both turbulent ($\sigma_{\rm nt}$) and thermal ($\sigma_{\rm th}$) small-scale contributions. Finally, we have investigated the existence of a relationship between different components of velocity dispersion and the star formation rate. The main results of this work can be summarized as follows

- We have quantified the [C II] luminosity-weighted average velocity dispersion $\langle\sigma_{\rm CII}\rangle_{\rm w}$. At the full resolution of our simulation, which is equivalent to an angular resolution of $0.005''$, we find $\langle\sigma_{\rm CII}\rangle_{\rm w} = (25.7, 22.6, 36.5)\,{\rm km\,s^{-1}}$ for the (SD, MG, DD) stages, respectively. Hence, we conclude that Freesia has a moderate average velocity dispersion regardless of the stage.

- $\langle\sigma_{\rm CII}\rangle_{\rm w}$ is very sensitive to the angular resolution of the observations. Due to beam smearing effects, the average value increases at lower resolutions. This effect is more severe for actively interacting systems, exemplified by our DD stage. Observations with an angular resolution of $0.02''$ ($0.1''$), would infer an average velocity dispersion $16-34\%$ ($52-115\%$) larger than the actual one.

- We have calculated the rotational-to-dispersion support ratio as well as Toomre $\mathcal{Q}$ parameter using $\langle\sigma_{\rm CII}\rangle_{\rm w}$ for Freesia. We derive $v_{\rm c}/\sigma \simeq 7$ and $\mathcal{Q} \simeq 0.2$ suggesting that [C II] emitting cold gas in EoR galaxies – unlike the MW but similar to galaxies at cosmic noon – receives considerable support from random motions.

- Concerning the resolved $\sigma_{\rm CII} - \Sigma_{\rm SFR}$ relation, we find a relatively flat relation for $0.02 < \Sigma_{\rm SFR}/\,{\rm M_{\odot}yr^{-1}kpc^{-2}} < 30$. The majority of simulated data lies on the derived average analytical expression, i.e. $\sigma \propto \Sigma_{\rm SFR}^{5/7}$ for the SD and DD stages. However, in the MG stage, the actual velocity dispersion is somewhat higher than predicted by the analytical expression, due to the simplifying assumptions on which the latter is based.

- Stellar feedback yields a $\sigma_{\mu} \simeq 10-15\,{\rm km\,s^{-1}}$ almost independently from the total SFR, due to the balance between energy injection by massive stars, and the rapid dissipation of small-scale supersonic turbulence. However, the stellar feedback accounts only for $< 10\%$ of the total kinetic energy. We conclude that at high-redshift the velocity dispersion is dominated by bulk motions produced by gravitational interactions – such as accretion/merging events, that govern the build-up phase of EoR galaxies.

Chapter 5

Dynamically cold disks in the EoR

IFU observations of galaxies at $1 \leq z \leq 3$ (Genzel et al., 2006; Förster Schreiber et al., 2009b; Law et al., 2009; Stott et al., 2016; Förster Schreiber et al., 2018; Mieda et al., 2016; Mason et al., 2017) have revealed that although a remarkable number of galaxies around the cosmic noon resemble ordered, disk-like structures, they show significantly higher velocity dispersions ($\sim 50 - 100\,\mathrm{km\,s^{-1}}$) compared to local star-forming galaxies ($\sim 20 - 25\,\mathrm{km\,s^{-1}}$, Andersen et al. 2006; Epinat et al. 2010) suggesting that galaxies at high redshifts have more pressure support than the local galaxies. However, in the past couple of years, observing [C II] line in galaxies at $z > 4$ has revealed the existence of "dynamically cold disks" at high redshifts (Rizzo et al., 2020, 2021; Fraternali et al., 2021), meaning that they are rotation-dominated systems with a surprisingly large $V/\sigma \sim 10$ (see also Sec. 1.3.2).

It is very important to note that these two conclusions about the dynamical properties of high-z galaxies are based on two different emission lines i.e. the [C II] and Hα lines, which trace different phases of the ISM. Indeed, it is still debated whether neutral and ionized gas tracers can be used as reliable tracers of galaxy dynamics (Levy et al., 2018; Lelli et al., 2018). Typically, most numerical works as well as semi-analytic models (e.g. Dekel & Burkert, 2014; Zolotov et al., 2015; Pillepich et al., 2019) do not produce such cold disks at high redshifts (see also Sec. 5.3).

With the tools that we have developed in this Thesis so far, we are able now to address this recent puzzling issue in high-z galaxy dynamics studies. To this aim, we improve our previous analysis in two ways. On the one hand, we analyze a large sample of galaxies to be able to predict a general behavior regarding the dynamics of EoR galaxies. On the other hand, in addition to [C II] (which is the tracer of cold ISM), we model and analyze the $H\alpha$ line, a tracer of the ionized ISM, in order to provide an additional and complementary probe of the ISM of high-z galaxies. This step is crucial since – as stated before – $H\alpha$ has been used extensively in intermediate redshift dynamics studies and also because it will soon be available for EoR galaxies via JWST.

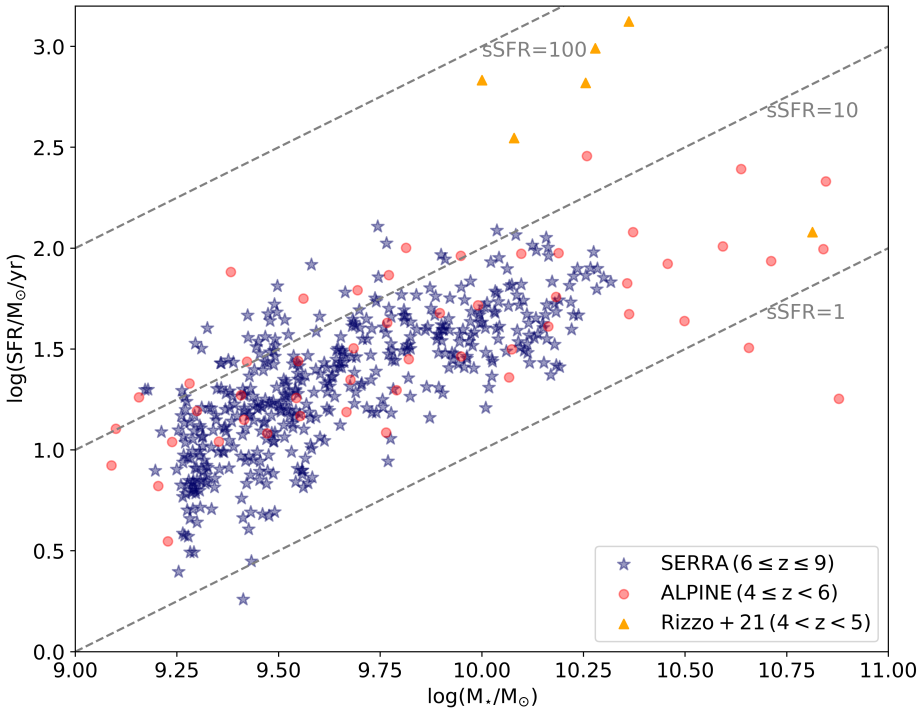

Figure 5.1: The SFR versus stellar mass of a sample of EoR galaxies from SERRA suit of simulations in comparison with ALPINE galaxies as well as dynamically cold galaxies analyzed by Rizzo et al. 2021 as candidates of high-z cold disks. The three dashed lines indicates constant value of sSFR $\simeq 1, 10, 100\,\mathrm{Gyr}^{-1}$.

5.1 Sample of simulated EoR galaxies

In this chapter, we focus on the analysis of a large sample of EoR galaxies (449 LBGs) from SERRA suite in the redshift range of $6 \leq z < 9$. This is a sub-sample of the SERRA galaxies which spans a SFR range of $2 - 130\,M_{\odot}\mathrm{yr}^{-1}$ and stellar mass range of $1.5 \times 10^{9} - 2.1 \times 10^{10} M_{\odot}$. In Fig. 5.1, the positions of simulated galaxies on $M_{\star}$-SFR plane are shown along with the data points from ALPINE survey as well as dynamically cold galaxies analyzed by Rizzo et al. 2021 as candidates of high-z cold disks. Our sample spreads a considerable range of observed high-z targets, but we are lacking very massive (i.e. $3 \times 10^{10} < M_{\star} < 10^{11}$) and highly star-forming (SFR$> 130 M_{\odot}\mathrm{yr}^{-1}$) galaxies, as very high mass galaxies are not present in SERRA. The bulk of the galaxies in our sample have a specific star formation rate $1\,\mathrm{Gyr}^{-1} <$ sSFR $\equiv$ SFR/M$_{\star} < 10\,\mathrm{Gyr}^{-1}$, i.e. extreme values with respect to local galaxies (sSFR $\simeq 0.1\,\mathrm{Gyr}^{-1}$), and higher than intermediate redshift targets (sSFR $\simeq 1\,\mathrm{Gyr}^{-1}$). Our sample is consistent with the data from ALPINE.

In Fig. 5.2, the gas fraction of SERRA galaxies with respect to other high-z galaxies are shown. Our galaxies have an average gas fraction of $\sim 20\%$ and only 7 galaxies have $f_g > 40\%$. These gas fractions are lower than what is usually observed for cosmic noon galaxies (Tacconi et al., 2010, 2013) where it is believed that gas accounts for $\sim 50 - 60\%$ of the baryonic mass as well as ALPINE galaxies (Dessauges-Zavadsky et al., 2020). This tension is present in almost all state-of-the-art

cosmological simulations, albeit in lower redshifts. Most simulations fail to reproduce such high gas fractions as late as $z \sim 2$, as star formation tends to consume most of the gas earlier. For example, the gas fraction in star-forming galaxies in the FIRE simulations (Feldmann et al., 2017) at intermediate redshifts is in average $\sim 20\%$. The same is true in the ILLUSTRIS (Genel et al., 2014) and ILLUSTRIS-TNG (Pillepich et al., 2019) simulations. It is debated that this discrepancy might be the reason for the failure of cosmological simulations in reproducing the long-lived giant clumps (with total masses of $10^{8-9} M_{\odot}$) which are observed in high-z star-forming galaxies. Fensch & Bournaud 2021 studied the difference in disk instability and evolution between galaxies with a medium ($\sim 20\%$) and high ($\sim 50\%$) gas fraction performing idealized disk simulations. Fensch & Bournaud 2021concluded that the giant clumps for models with a medium gas fraction are unbound while they are gravitationally bound in models with a high gas fraction. This is due to the fact that a higher gas fraction in a galaxy should make the disk more unstable (by lowering the Toomre 1964 $\mathcal{Q}$ parameter) and induce the formation of massive clumps (but see also Leung et al., 2020). The discrepancy between the observed gas fraction and the one from simulations can be due to different methods of inferring the gas content of galaxies. In high-z galaxy observations, the molecular masses are typically calculated using the luminosity of the CO($J = 1 - 0$) emission line and then converted to an H_2 mass via a $CO - H_2$ conversion factor α_{CO}. When the CO($J = 1 - 0$) is not available, higher rotational states are observed, and then converted to the ground state via an assumption about the CO excitation. It is suggested that this method tends to overestimate the gas fraction because of the usage of locally calibrated $CO - H_2$ conversion factors (Narayanan et al., 2012, e.g.). Since the detection of CO lines becomes challenging for $z > 4$, other line luminosities should be used for measuring the gas fraction of galaxies. The [C II] line has been used as an alternative since it is found to be correlated with the molecular gas (Zanella et al., 2018). The gas masses of the ALPINE galaxies in Fig. 5.2 are estimated with the Zanella et al. 2018 calibration:

$$\log(\frac{\mathrm{L_{CII}}}{\mathrm{L_{\odot}}}) = (-1.28 \pm 0.21) + (0.98 \pm 0.02)\log(\frac{\mathrm{M_{mol}^{CII}}}{\mathrm{M_{\odot}}})\,. \tag{5.1}$$

We obtain the molecular gas fraction for the sample of SERRA galaxies using this calibration and plot the results in Fig. 5.2. We find that Zanella et al. 2018 calibration tends to overestimate the gas fractions for our systems. The average value of gas fraction over the sample computed with this calibration is $\sim 45\%$ which is larger than two times the average gas fraction computed in the simulations (i.e. $\sim 20\%$). With this estimate, our simulated sample is overall consistent with the observed gas fractions. Therefore, this might be the reason for the discrepancy between the observed and theoretical gas fractions in high-z galaxies.

The gas fraction in a galaxy is an important parameter related to the gas velocity dispersion. We get back to this point in Sec. 5.3.

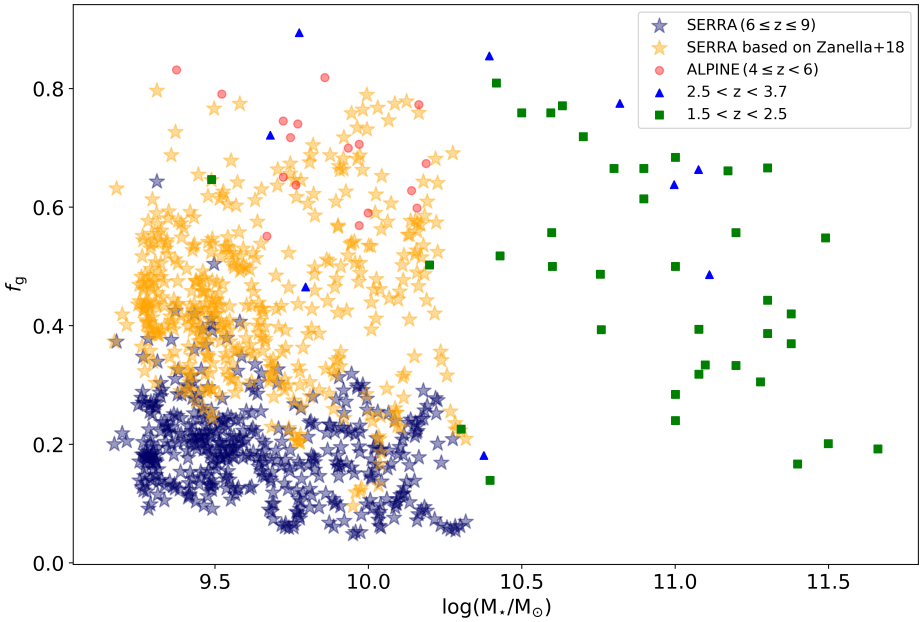

Figure 5.2: Position of SERRA galaxies on f_g-$M_\star$ plane in comparison with high-z galaxies in the literature from Dessauges-Zavadsky et al. 2020. For SERRA galaxies, we estimate the gas fraction by computing the gas mass in two ways: directly from the simulation (blue stars) and from the [C II] based Zanella et al. 2018 calibration (eq. 5.1, yellow stars).

5.2 Probing ISM with [C II] and Hα emission lines

Similar to Sec. 2.3.3, we model the [C II] line emission as a tracer of the cold and mainly neutral ISM for our sample of EoR galaxies. In addition, we choose $H\alpha$ emission as the tracer of ionized gas and model it in a similar fashion. Nebular line luminosities such as $L_{H\alpha}$ have been the primary measures of the SFRs in galaxies (Kennicutt, 1998) since Hα is directly a measure of the ionizing photons which are emitted by young stars. When computing the Hα line, we directly consider the intrinsic (unattenuated) emission; while Hα observations are typically de-reddened before performing the kinematic analysis, we skip this extra complication (first attenuating the HDCs, then de-reddening them).

We model the HDCs for both lines following the procedure described in Sec. 4.1.1. The FOV size used in this chapter is 2.5 kpc and all the galaxies are aligned face-on. For the sake of simplicity, spectral and spatial resolution are the same for the two lines.

5.2.1 Scaling relations

We start by analyzing the integrated properties of [C II] and $H\alpha$ line in our sample. In the left panel of Fig. 5.3, the position of our galaxy sample on $L_{\rm CII}$−SFR plane are plotted along with the fit provided by Schaerer et al. 2020 for ALPINE galaxies as well as the theoretical line predicted by Vallini et al. 2015 (assuming metallicity of $Z = 0.5$). In this Fig., galaxies are color-coded with the

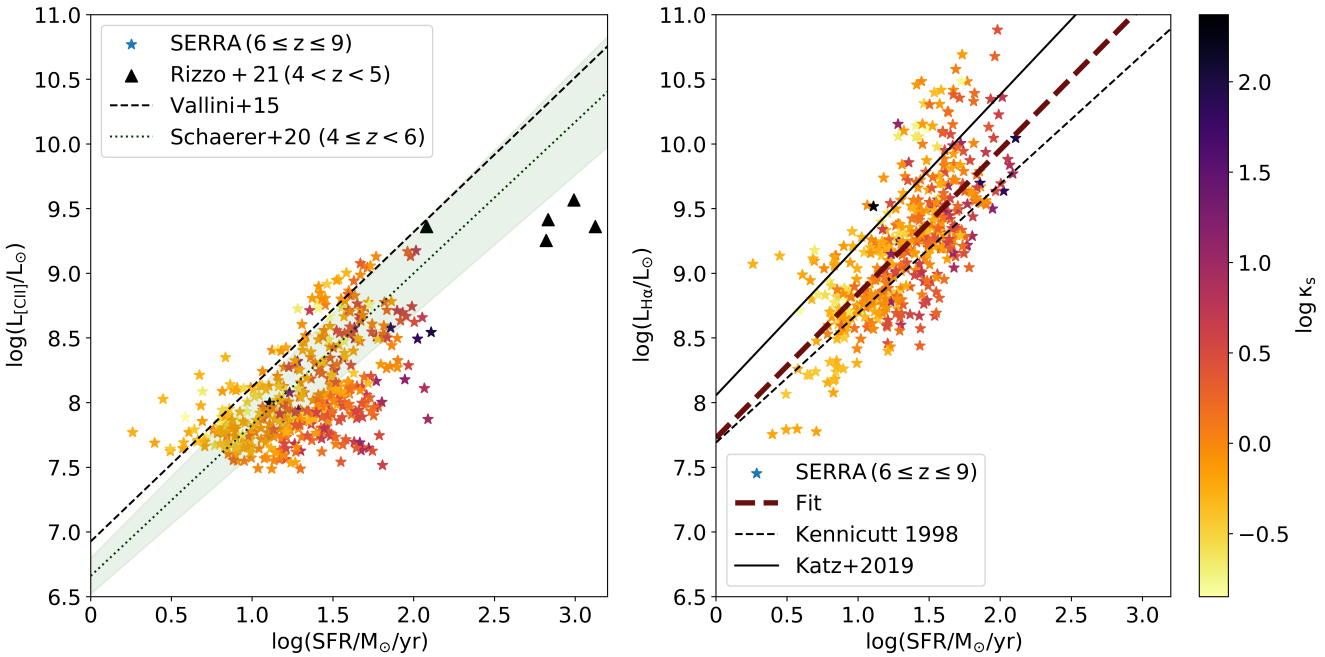

Figure 5.3: *Left panel:* The [CII]-SFR relation. Along with SERRA data in our sample, we report the fit given at $z = 4 - 6$ by ALPINE (Schaerer et al., 2020) and the results from analytical models (Vallini et al., 2015) as well as the data point from (Rizzo et al., 2021). *Right panel:* $L_{H\alpha} - \mathrm{SFR}$ relation. The dashed black line shows the fit from Kennicutt 1998, the solid black line is the fit provided by Katz et al. 2019 for simulated galaxies at $z \sim 10$ and the dark red dashed line is the fit to our data points.

value of burstiness parameter κ_s (see eq. 4.9 for the definition). The majority of galaxies in our sample can be either described by the local De Looze et al. 2014 relation or are within 2σ from the relation derived for ALPINE ($5 < z < 4$) galaxies (Schaerer et al., 2020), with a handful of them falling below both relations similar to what happens for observed $z \sim 6$ galaxies (Carniani et al., 2017). Typically, very starbursty galaxies ($\kappa_s \gg 1$) are falling below the relations. Additionally it is interesting to note that the trend for SERRA galaxies is consistent with what see in Fig. 2.11, albeit the limited number (about 10 galaxies) of data points in Pallottini et al. 2019.

In the right panel of Fig. 5.3 we show the intrinsic Hα luminosities as a function of SFR of SERRA galaxies color-coded with κ_s. We plot the same relation at $z \sim 10$ predicted by Katz et al. 2019 simulations, as well as the $L_{H\alpha}$-SFR calibration observed at $z = 0$ by Kennicutt 1998; the latter has been shifted to account for different assumptions on the IMF. To have a quantitative comparison, we fit our simulated galaxies to calibrate the Hα-SFR relation in the EoR, finding

$$\log(L_{\mathrm{H}\alpha}/L_\odot) = \alpha \log(\mathrm{SFR}/\mathrm{M}_\odot \mathrm{yr}^{-1}) + \beta\,, \tag{5.2a}$$

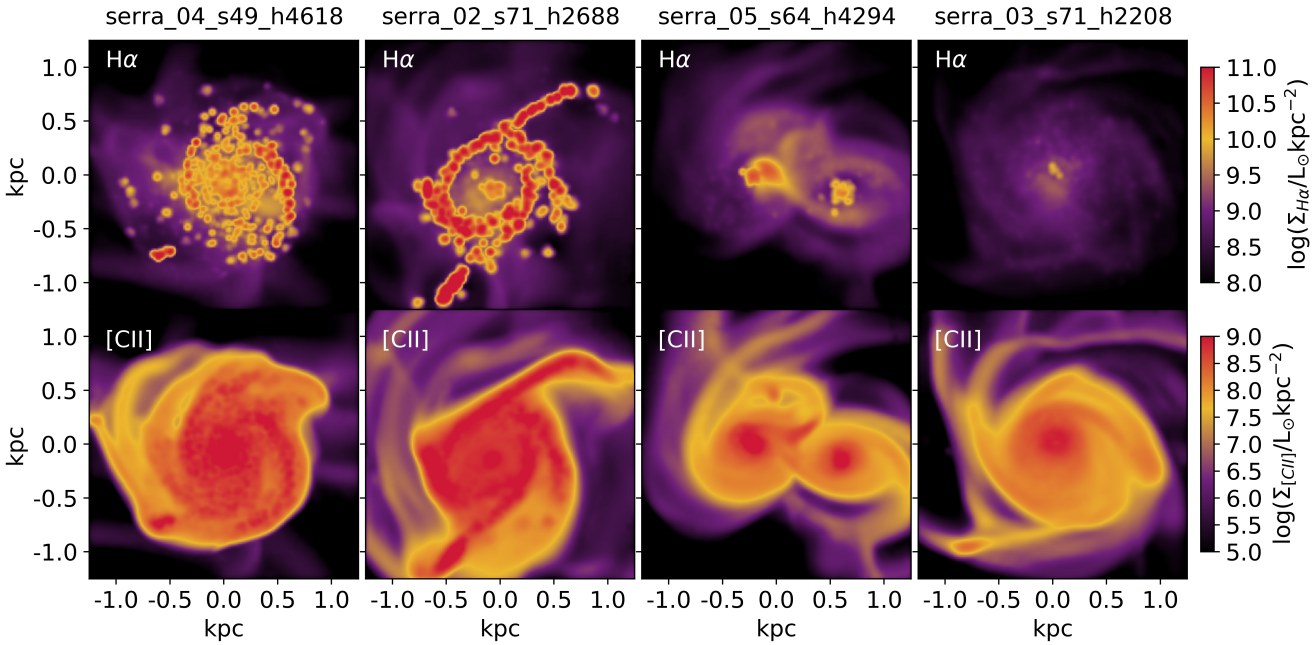

Figure 5.4: Hα and [C II] maps for four galaxies in our sample. Each row indicates one galaxy for which in the top panel the Hα map is shown while the bottom panel shows the [C II] map.

with

$$\alpha = 1.11 \pm 0.05\,, \tag{5.2b}$$

$$\beta = 7.73 \pm 0.07\,. \tag{5.2c}$$

Our fit lies between the Kennicutt (1998) calibration and the one from Katz et al. 2019. In particular, at higher SFRs, our simulated galaxies tend to have a higher $L_{\mathrm{H}\alpha}$ for a given SFR with respect to the local relation.

5.2.2 Spatially resolved ISM

Armed with the HDCs for both [C II] and Hα lines, we can produce images and kinematics observables from various ISM phases resolved down to $\simeq 10\,pc$ scales.

To illustrate how different lines trace different parts of the ISM, we select four galaxies in our sample with different morphological characteristics (disk, merger, etc[1]). This overview is shown in Fig. 5.4, where Hα and [C II] surface brightness maps ($\Sigma_{\mathrm{H}\alpha}$ and Σ_{CII}) are plotted. In general, [C II] maps are smoother, while Hα maps show more clumpy structures with the emission peaking on H II regions. We leave a complete morphological comparison between the two emission lines to future work.

[1]The selected galaxies have been chosen based also on the stellar morphology. See Appendix B for an extended sample.

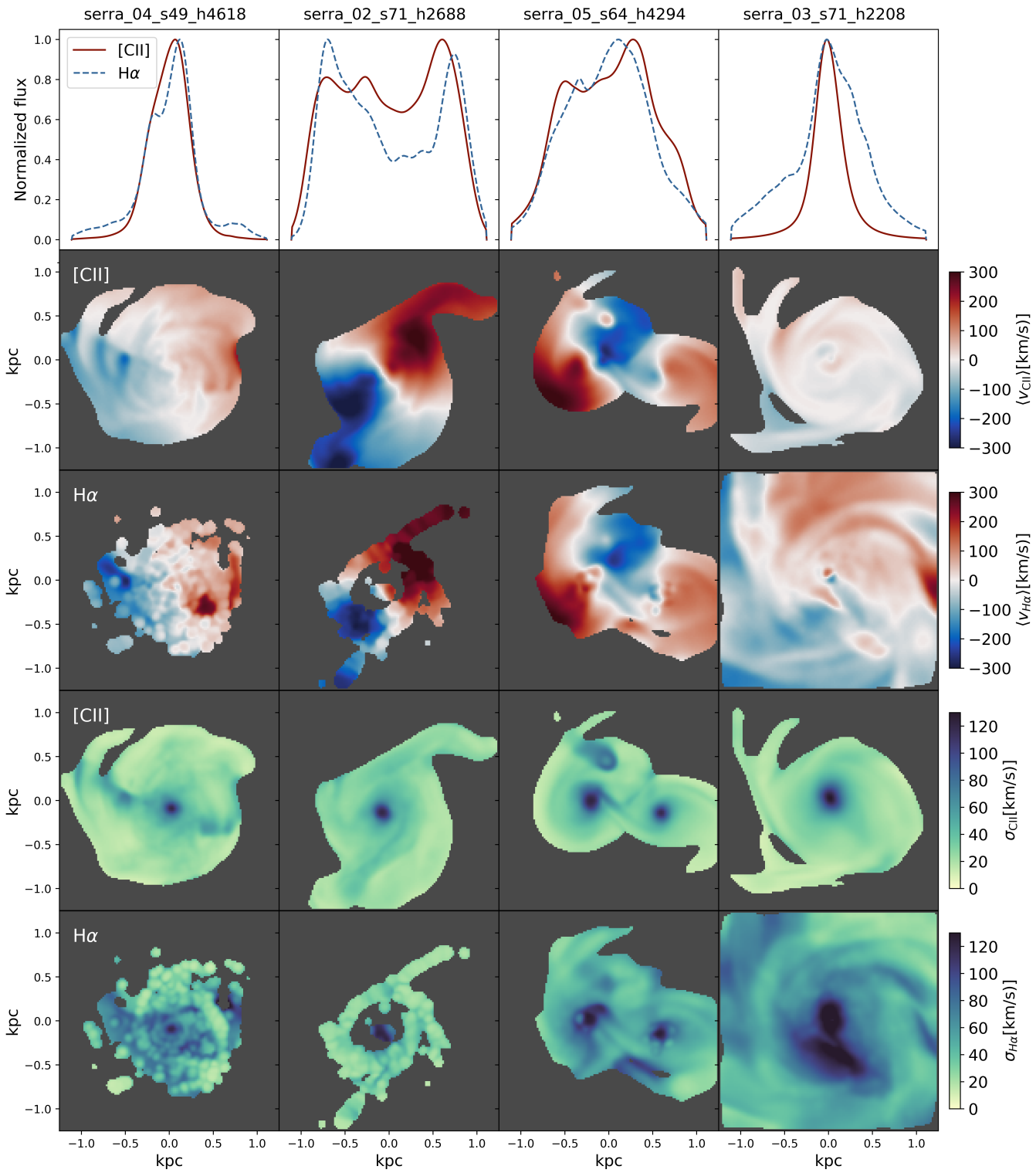

Figure 5.5: Dynamical observables derived from Hα and [C II] HDCs. *First row:* Normalised [C II] and Hα spectra for four galaxies in our sample. *Second and Third rows:* Mean velocity maps derived from [C II] and Hα line observations. *Fourth and Fifth rows:* CII and Hα velocity dispersion maps.

The corresponding kinematics observables for our selection are plotted in Fig. 5.5.

In the top panel, the spectra of [C II] and Hα are plotted for each galaxy. To appreciate the spectral differences, the spectra are normalized to the peak of the Hα line. The shape of [C II] and Hα spectra are quite similar in serra_02_s71_h4618 and serra_05_s64_h4294 while in serra_04_s49_h4618 and serra_03_s71_h2208 there is a clear difference; Hα spectrum in both galaxies has broader wings due to the outflowing gas. These broader wings are not present in the [C II] spectrum.

In other panels of Fig. 5.5, the moment-1 and moment-2 maps derived from [C II] and Hα HDCs are also shown (see Sec. 4.3 for the details). The morphological differences seen in Fig. 5.4 can be appreciated also in velocity maps. Qualitative differences can be appreciated also from the velocity maps. However, one needs to apply disk modeling to both cases for proper quantification. The same is true for the velocity dispersion map that in all cases peaks in the center of the galaxy regardless of the line. However, far from the center of galaxies, $\sigma_{H\alpha}$ maps show higher values compared to $\sigma_{\rm CII}$. This was expected because of I) different gas temperatures that each line is tracing and II) due to outflowing gas which are luminous in Hα but not in [C II]. Complete kinematics analysis of both [C II] and Hα would be very important for dynamics modelings of galaxies, in particular, it can be used to understand which emission line is a better tracer of galaxy dynamics. This is beyond the scope of this Thesis and we leave it for later work. For the purpose of this chapter, we need to consider the velocity dispersion maps to evaluate the average velocity dispersion of our galaxies. This enables us to understand whether the EoR galaxies are dynamically cold or hot systems.

5.3 Evolution of velocity dispersion across cosmic time

We utilize the spatially-resolved velocity dispersion maps of [C II] and Hα lines and attribute a single averaged velocity dispersion value (σ) for each galaxy corresponding to each line (see Sec. 4.3 for the details). In Fig. 5.6, the redshift evolution of σ is shown by using our sample of 449 galaxies. We find that the average velocity dispersion derived from [C II] line is $\sim 28.9 \pm 8.5\,{\rm km\,s^{-1}}$ while the one from the Hα line is $\sim 52.8 \pm 13.5\,{\rm km\,s^{-1}}$. Velocity dispersions computed from Hα line observations are higher than the ones computed from [C II] by a factor of ~ 1.7 which is due to the fact that Hα is tracing gas with a higher temperature than the one traced by [C II] and also because Hα is tracing the outflows which contribute to high-velocity tails in the line spectrum.

To evaluate the kinematics of the total gas, in Fig. 5.6 we also include the velocity dispersions that are computed by considering "theoretical" HDCs, i.e. where gas mass is adopted as the weight for each spaxel instead of the luminosity of a line. We find that the average velocity dispersion of the total gas is $\sim 39.0 \pm 11.4\,{\rm km\,s^{-1}}$ which is close to the value we get from the [C II] line. Regarding the evolution of the velocity dispersion, we do not find any obvious trend for any tracer in our sample. The reason for a flat velocity dispersion is partially due to the lack of evolution of

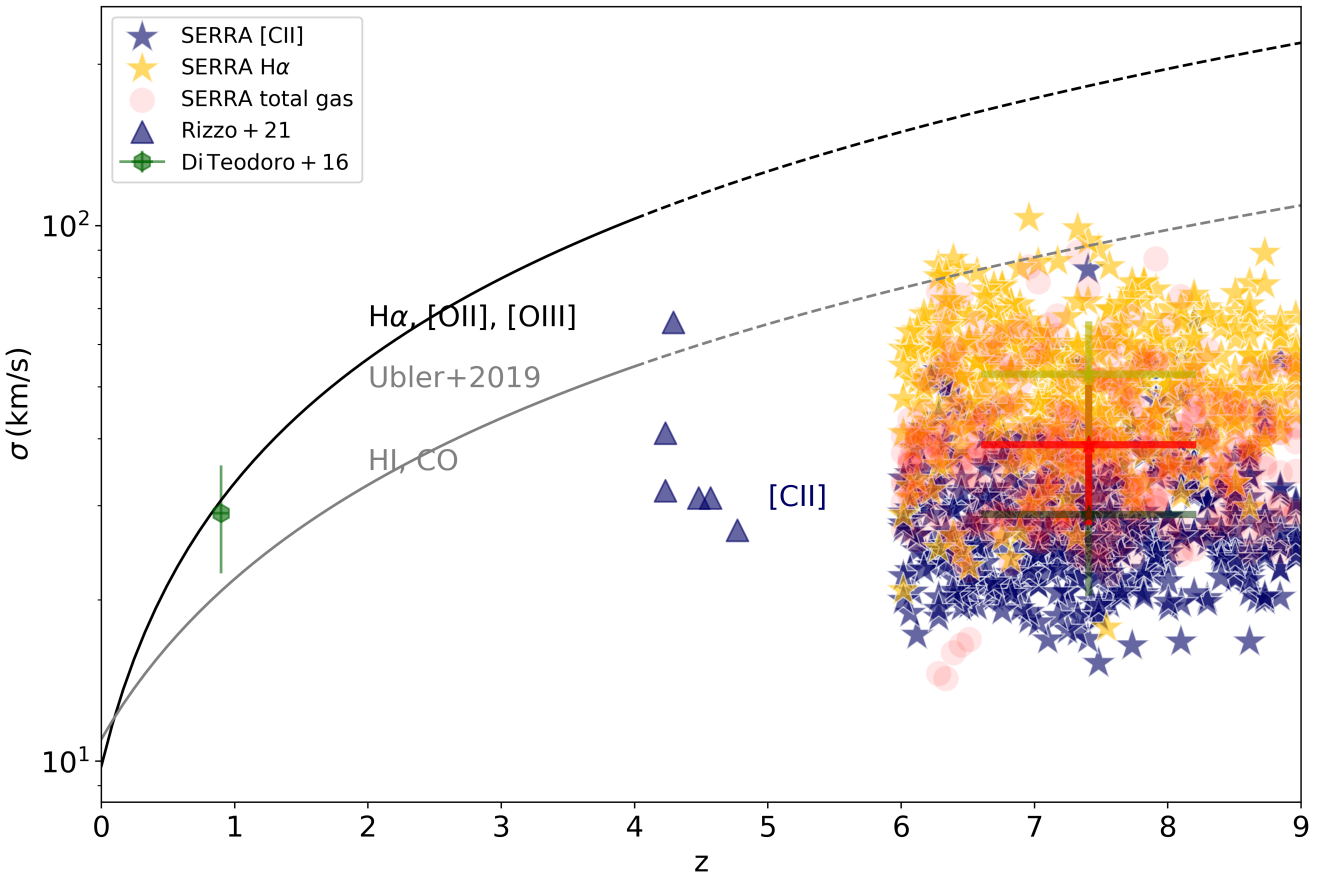

Figure 5.6: Location of galaxies in our sample on the velocity dispersion versus redshift plane. We include average velocity dispersion computed from [C II], Hα as well as the total gas. The green, yellow and red crosses indicate the average over the sample for each velocity dispersion component respectively. The green triangles are from $z > 4$ galaxies in Rizzo et al. 2021. The black solid and gray dotted lines show the best-fit relations to velocity dispersions measured from warm ionized tracers (Hα, [OII], [OIII]) and atomic (HI)/molecular (CO) tracers (Übler et al., 2019). The dot-dashed lines show the corresponding extrapolations up to $z \sim 9$.

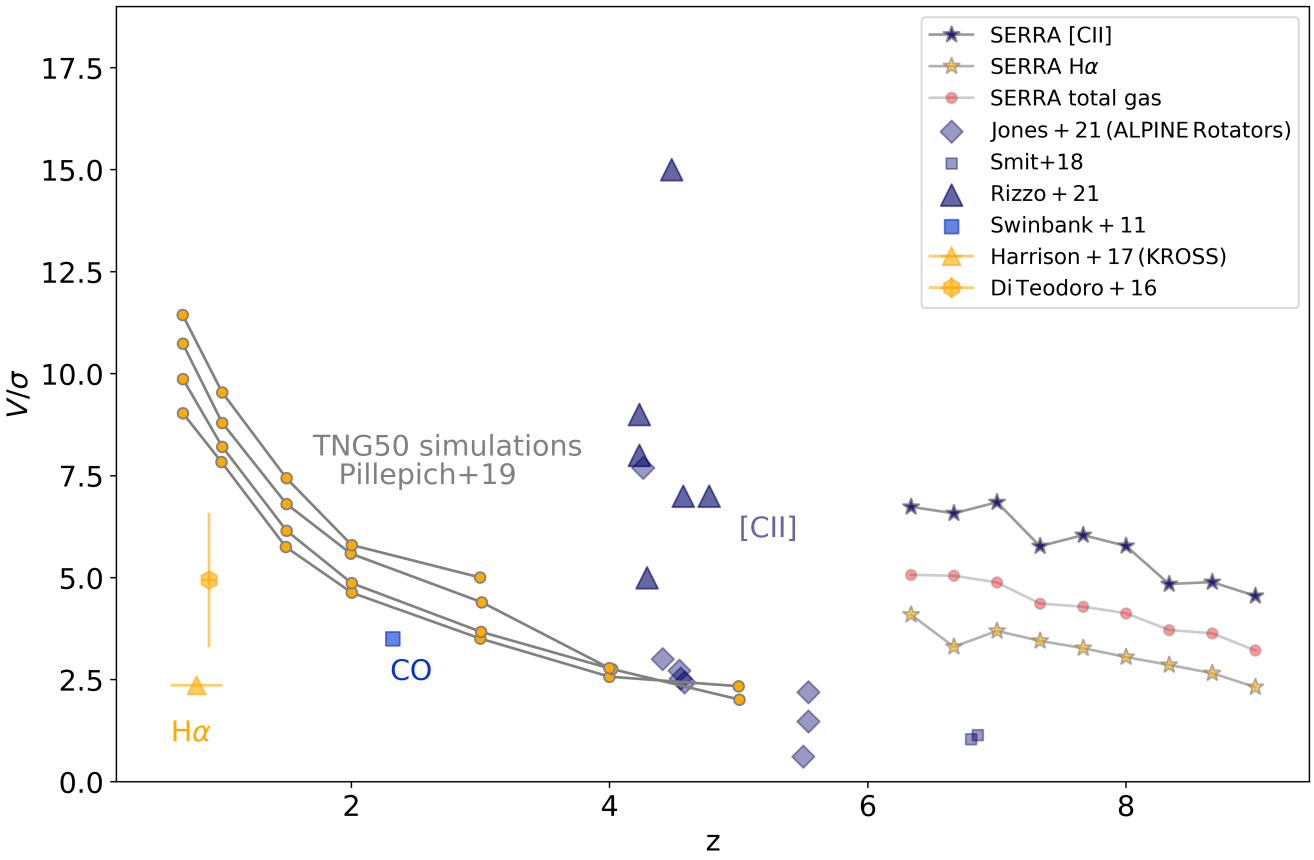

Figure 5.7: Evolution of V/σ with redshift in SERRA; The line with blue-filled star markers is derived from [C II] line, the one with red-filled circle markers is the total gas and the one with yellow-filled star markers is from Hα line. The lines with orange-filled circle markers are the results from TNG50 simulations (Pillepich et al., 2019).

the gas fraction in our sample (see Fig. 5.2); additionally the trend is blurred because of the large mass range of galaxies considered in our sample (see later Fig. 5.7).

To compare with observations, we include data points from Rizzo et al. 2021 and the empirical $\sigma - z$ relations found by Übler et al. 2019 for normal main-sequence galaxies up to $z \leq 3$ in Fig. 5.6. Similar to Rizzo et al. 2021, the extrapolation of these relations up to redshift 9 are plotted to be able to compare them with our simulations. In comparison with Rizzo et al. 2021 results, our galaxies have lower $\sigma_{\rm CII}$. This can be either due to the fact that our galaxies have lower mass compared to the $z > 4$ dusty star-forming galaxies or different procedures in which the velocity dispersion is computed. On the other hand, we find that the extrapolation of empirical relations from intermediate redshifts found by Übler et al. 2019 tends to overestimate the velocity dispersion by a factor of ~ 2 considering both[C II] and Hα.

Having the information on the velocity dispersion as well as the rotation velocities of our galaxy sample, we can study the rotational-to-dispersion support ratio (V/σ). In Fig. 5.7, the evolution of V/σ for SERRA galaxies is shown. The average rotational-to-dispersion support ratio for our

galaxy sample is $V/\sigma \sim 5.9 \pm 1.9$ when derived from [C II] observations and $V/\sigma \sim 3.24 \pm 1.4$ when derived from Hα observations. There is a clear trend with redshift for V/σ in all the tracers. The values quoted by Rizzo et al. 2021 for dynamically cold disks at $z > 4$ are similar to SERRA galaxies apart from SPT0113-46 which has a very large rotation velocity ($\sim 358\,\mathrm{km\,s^{-1}}$). In comparison with molecular gas observations of intermediate redshifts (e.g. galaxy kinematics with CO line: Swinbank et al., 2011), we find that SERRA galaxies have more rotation support. This can be due to either the overestimation of velocity dispersion in intermediate redshift galaxies associated with the beam smearing effect (see Sec. 4.3.2) or different galaxy populations in different studies. Regarding the ionized gas traced with Hα, we find that there is not a trend in terms of V/σ from intermediate redshift observations (Harrison et al., 2017; Di Teodoro et al., 2018) to the EoR galaxies in SERRA.

To compare with other simulations, the results from TNG50 simulations (Pillepich et al., 2019) are also plotted in Fig. 5.7. Similar to these simulations, V/σ is decreasing also in our galaxies when going to higher redshifts irrespective of the tracer that we are using. However, unlike the TNG50, our simulations predict the existence of dynamically cold disks at high-z down to the EoR when considering either [C II] or the total gas.

5.4 Summary

We have modeled the [C II] and Hα line HDCs for a large sample of EoR galaxies (449 LBGs) from SERRA suite in the redshift range of $6 \leq z < 9$ spanning a SFR range of $2 - 130\,M_{\odot}\mathrm{yr}^{-1}$ and a stellar mass range of $1.5 \times 10^{9} - 2.1 \times 10^{10} M_{\odot}$.

- Having the information on Hα luminosities and SFRs, we can predict the Hα-SFR relation in the EoR. We have found that our galaxies lie between the original calibration by Kennicutt 1998 and the one for $z \sim 10$ galaxy simulations by Katz et al. 2019.

- We have studied the evolution of [C II] and Hα velocity dispersion in our EoR galaxy sample. We find no redshift evolution in our sample. We find that the velocity dispersion measured from ([C II] , Hα, gas) is $\sigma = (28.9 \pm 8.5,\ 52.8 \pm 13.5,\ 39.0 \pm 11.4)$. Therefore, the dynamical stages of galaxies can be interpreted differently depending on the ISM tracer that we are using.

- We have studied the V/σ ratio for our galaxies and have concluded that our simulations unlike others do predict the existence of dynamically cold disks at high redshifts; as early as the EoR. This is true when we consider either [C II] or the total gas as the kinematics tracer.

Chapter 6

Conclusions and future prospects

In this Thesis, we have studied the structural and dynamical properties of star-forming galaxies belonging to the Epoch of Reionization (EoR) by utilizing analytical models as well as state-of-the-art hydrodynamical simulations of galaxies. Since our aim was to provide a solid benchmark and/or prediction for the upcoming observations, we have developed a framework in which a common cross-talk among observations and theoretical works is possible.

To address questions related to the dynamical and morphological properties of EoR galaxies, and the early formation of disks, first we have searched for specific signatures in the integrated spectral line profiles of galaxies. As our control environment, we have modeled the [C II] 158μm line emission and the corresponding integrated line profile for idealized rotating disk galaxies. From this analysis, disk inclination and gas turbulent motions were identified as the key parameters affecting the line profile.

Then, we have studied "Althæa", a highly-resolved (30 pc) simulated prototypical Lyman Break Galaxy (LBG), in the redshift range $z = 6 - 7$, when the galaxy is in a very active assembling phase. Based on morphology, we have selected three main dynamical stages: I) Merger, II) Spiral Disk, and III) Disturbed Disk. We have identified spectral signatures of merger events, spiral arms, and extra-planar flows in I), II), and III), respectively. Then, a generalized dynamical mass vs. [C II]-line FWHM relation was derived. We have shown that if precise information on the galaxy inclination is (not) available, the returned mass estimate is accurate within a factor 2 (4).

Equipped with the modeled line profiles for any arbitrary inclination of the simulated galaxy, we have performed ALMA simulations to check the detectability of [C II] line. We concluded that when seen face-on, Althæa is always detected at $> 5\sigma$ while in the edge-on case it remains undetected because the larger intrinsic FWHM pushes the line peak flux below the detection limit. This suggests that some of the reported non-detections might be due to inclination effects.

To study the energy support of EoR galaxies as well as their dynamical state, spatially resolved kinematics information is required. Therefore, we have extended our modeling scheme by fully bridging the zoom-in simulations of EoR galaxies and IFU observations such as ALMA. In

particular, we have modeled [C II] emission Hyperspectral Data Cubes (HDC). Our laboratory for this analysis was a simulated prototypical LBG, "Freesia", part of the SERRA suite. The analysis encompassed the evolution of Freesia in a redshift range of $6 < z < 8$. Velocity dispersion maps have been built for three dynamically distinct evolutionary stages (*Spiral Disk* at $z = 7.4$, *Merger* at $z = 8.0$, and *Disturbed Disk* at $z = 6.5$) using [C II] HDCs. We found that, at a high spatial resolution of $0.005''$ ($\simeq 30pc$), the luminosity-weighted average velocity dispersion is $\sigma_{\rm CII} \simeq 23 - 38\,{\rm km\,s^{-1}}$ with the highest value belonging to the highly-structured Disturbed Disk stage. Low-resolution observations tend to overestimate $\sigma_{\rm CII}$ values due to beam smearing effects that depend on the specific galaxy structure. For an angular resolution of $0.02''$ ($0.1''$), the average velocity dispersion is $16 - 34\%$ ($52 - 115\%$) larger than the actual one. The [C II] emitting gas in Freesia has a Toomre parameter $\mathcal{Q} \simeq 0.2$ and rotational-to-dispersion ratio of $v_{\rm c}/\sigma \simeq 7$ similar to that observed in $z = 2 - 3$ galaxies.

Regarding the energy source for the velocity dispersion, we found that the primary driver is due to gravitational processes, such as merging/accretion events, and energy input from stellar feedback is generally subdominant ($< 10\%$). Having information on the structure of pc-scale line-of-sight velocity dispersion, we have studied the resolved $\sigma_{\rm CII} - \Sigma_{\rm SFR}$ relation for three stages of Freesia. We found that the relation is relatively flat for $0.02 < \Sigma_{\rm SFR}/{\rm M_\odot yr^{-1}kpc^{-2}} < 30$, with the majority of data lying on the derived analytical relation $\sigma \propto \Sigma_{\rm SFR}^{5/7}$. At high SFR, the increased contribution from stellar feedback steepens the relation, and $\sigma_{\rm CII}$ rises slightly.

Finally, we have addressed one of the recent puzzling issues in high-z galaxy dynamics studies which is the existence of "dynamically cold disks" (i.e. rotation-dominated systems with a surprisingly large $V/\sigma \sim 10$) at high redshifts. To this aim, we have extended our previous analysis by including a sample of simulated EoR galaxies which contains 449 LBGs in a redshift range of $6 < z < 9$ spanning an SFR range of $2 - 130\,M_\odot{\rm yr^{-1}}$ and a stellar-mass range of $1.5 \times 10^9 - 2.1 \times 10^{10} M_\odot$. In addition to [C II] emission line (as a tracer of cold gas), the Hα emission line has been modeled as the tracer of ionized gas to have a complementary probe of the interstellar medium of high-z galaxies. Armed with the HDCs for both lines, we have studied the evolution of velocity dispersion observed by [C II] and Hα line in our EoR galaxy sample. The velocity dispersion derived from [C II] line is $\sim 27.5 \pm 8.7\,{\rm km\,s^{-1}}$ while the one from the Hα line is $\sim 52.7 \pm 12.0\,{\rm km\,s^{-1}}$. The average rotational-to-dispersion support ratio for the LBG sample is $V/\sigma \sim 5.9 \pm 1.9$ when derived from [C II] observations and $V/\sigma \sim 3.24 \pm 1.4$ from Hα observations. We have concluded that dynamical stages of galaxies can be interpreted differently depending on the ISM tracer that we are using. Considering the values for the cold gas traced by the [C II] line, our simulations unlike others do predict the existence of dynamically cold disks at high redshifts; as early as the EoR.

The tools that have been developed in this Thesis are very useful for a direct comparison of state-of-the-art cosmological simulations of galaxies with IFU like observations resolving galaxy properties in parsec scales. There are a range of applications for such tools both for observational

and theoretical purposes. From the observational point of view, the HDCs, as the most important data products of this Thesis, can be used in the process of applying for observing times on different instruments (such as ALMA and JWST). The modeled HDCs from simulations can be post-processed with the instruments' pipelines to have an exact estimation on the required observational set-up such as spatial/spectral resolution, S/N ratio, etc suitable. Moreover, they can be the base of a framework that can be regarded as a benchmark for the upcoming galaxy dynamics observations. All the kinematics modelings tools common in galaxy observations are either applied directly to HDCs or to their lower-dimensional products. One of the next projects is to find an optimal observational set-up for high-z galaxy observations such that one can perform reliable kinematics classification such as distinguishing between mergers and disk galaxies. This task will be performed by testing various existing kinematics modeling tools on the simulated HDCs. Another project aims at predicting the rotation curve and consequently the matter content of EoR galaxies. These predictions are crucial because in the near future instruments such as ALMA and JWST will unveil the internal properties of high-z galaxies.

As a different type of application, we are aiming to produce a large set of simulated HDCs suitable for performing machine learning and artificial intelligence techniques analysis to obtain a morphological and dynamical classification of high-z galaxies. These techniques represent a vital tool to tackle the complexity of high-redshift galaxy dynamics.

Appendix A

Clumpy morphology of early galaxies

This chapter is based on Zanella et al. (2021) in which we study the morphology of $z \sim 6$ galaxies by creating mock rest-frame ultraviolet, optical, and far-infrared observations of Althæa. In particular we compare two stages: in the first the galaxy appears as an undisturbed clumpy disk, in the second it is undergoing a merger. We investigate how the galaxy morphology differs in these two cases and what components are detected when considering different tracers (e.g. rest-frame UV and FIR emission).

A.1 Multi-wavelength mock maps

To compare the morphology and structural parameters of our simulated galaxies with actual $z \sim 5-7$ observations, the first step is to create synthetic continuum and emission line maps. In particular we aim at reproducing typical *HST* optical images (bands z', Y, J, and H), ALMA sub-millimeter continuum (Band 6) and emission line ([C II]) two-dimensional (2D) maps, as well as realistic near- and mid-infrared *JWST* observations.

First, starting from the simulated galaxy, we generated mock continuum and emission line images by using SKIRT (Camps & Baes, 2015) and CLOUDY (Ferland et al., 2017) respectively (Section A.1.1). Then we added observational artifacts to mimic typical UV and FIR high-redshift observations (Sections A.1.2).

A.1.1 Continuum and emission lines modeling

Continuum emission is generated by using SKIRT[1] (Baes & Camps, 2015; Camps & Baes, 2015), a Monte Carlo based code that computes the radiative transfer process in dusty media. The setup adopted here is similar to Behrens et al. (2018), and we summarize it as follows. The spatial distribution of the light sources is taken from the position of the stellar clusters in Althæa; for

[1] version 8.0, `http://www.skirt.ugent.be`

each cluster, we use its metallicity and age to compute the stellar SED, by adopting the Bruzual & Charlot (2003) models, and the same Kroupa (2001) IMF used in the simulation.

We use CLOUDY[2] (Ferland et al., 2017) to compute the line emission for [C II] and CO roto-vibrational transitions. For a fair comparison, we set the spatial resolution of the continuum and lines at 25 pc for both the clumpy disk and merger case, and we redshifted both of them to $z = 6$. In both snapshots the galactic disk is seen face-on.

A.1.2 Mimicking observational artefacts

To properly reproduce actual observations we also need to mimic the image broadening due to the limited spatial resolution (i.e. diffraction limit), the pixelization of the detectors, and the presence of noise that limits the depth of the data.

We reproduced the case of spatially-resolved observations of galaxies where a typical image quality of $0.5 - 1$ kpc, corresponding to $0.1" - 0.2"$ at $z \sim 6$, is reached (depending on the observing band, e.g. Grogin et al. 2011, Shibuya et al. 2019b). We also considered the ideal case of a galaxy observed with a resolution of ~ 0.25 kpc, corresponding to $\sim 0.05"$ at this redshift. Currently this resolution is beyond the diffraction limit of *HST* and is only achievable in moderately lensed sources (e.g. with magnification $\mu \gtrsim 10$, Knudsen et al. 2016, Bradač et al. 2017), or in the submillimeter with ALMA. However in the near future, the bluest *JWST*/NIRCam filters at wavelength $\lambda \lesssim 1.5\mu$m (corresponding to the *HST* ones considered in this chapter) will allow the community to achieve such a high spatial resolution also in the optical.

Throughout this chapter we will refer to the maps with $\sim 0.15"$ resolution as the "low-resolution" case and to the ones with $\sim 0.05"$ resolution as the "high-resolution" case.

We adopted the two following procedures to create mock maps in the optical and infrared (*HST*, *JWST*), and at sub-millimeter wavelengths (ALMA). To obtain the final *HST* and *JWST* images we smoothed the original-resolution maps with a Gaussian kernel. To account for the pixelization of the detector we resampled the smoothed maps to a pixel scale of $0.03"$ pixel^{-1} that can be achieved in *HST* imaging when dithering (e.g. Zanella et al. 2019). Adopting a larger pixel scale as in some studies (e.g. $0.06"$ pixel^{-1}, Brammer et al. 2012), does not affect our results. Finally, we have added random noise to reproduce the sensitivity of data taken in the commonly observed cosmological fields (e.g. CANDELS survey, Grogin et al. 2011). The 5σ limiting magnitude of our mock optical and infrared images is ~ 29 AB mag considering a point-source and an aperture with $\sim 0.25"$ radius. The original-resolution images as well as the mock maps obtained for our clumpy disk and merger are shown in Figures A.1 and A.2.

To reproduce the limited angular resolution, pixelization and noise of sub-millimeter images instead we used CASA[3], the observing simulator of ALMA (McMullin et al., 2007). We gave as

[2] C17.01 `https://www.nublado.org/`
[3] v5 `https://casa.nrao.edu/`

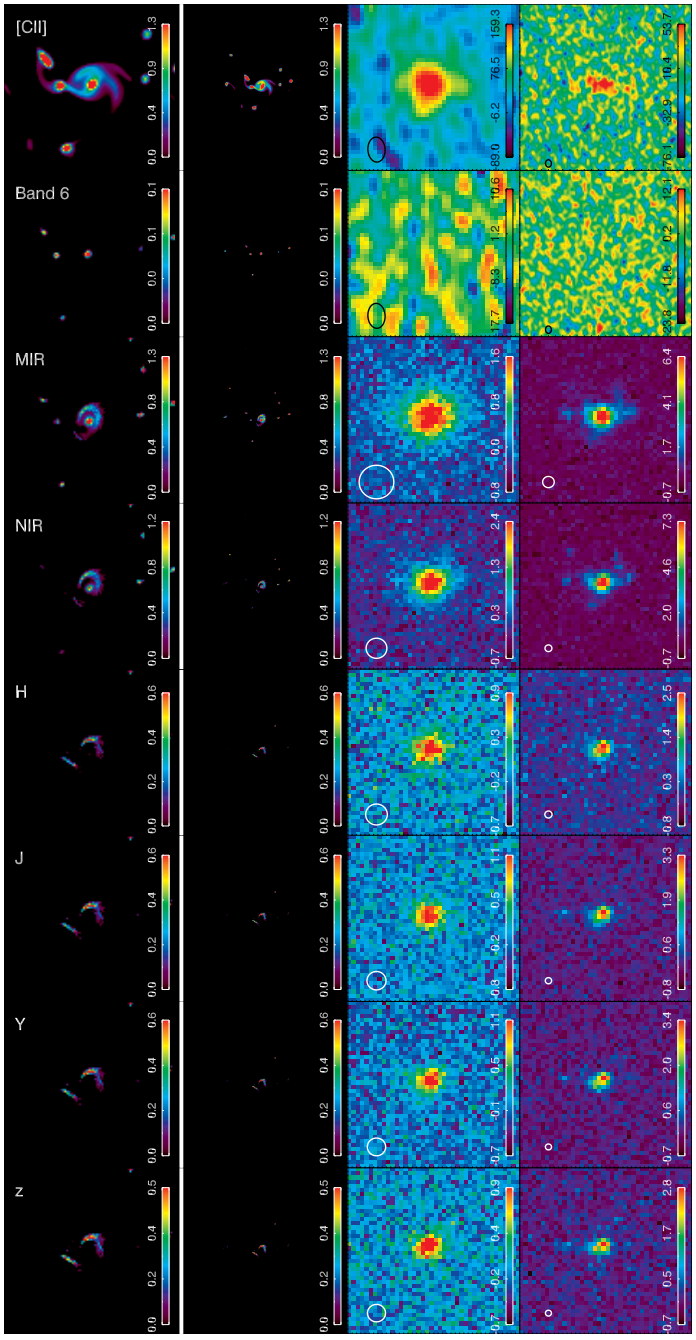

Figure A.1: Maps of Althæa in the clumpy disk stage. **From top to bottom:** different observing bands are shown. *HST*/ACS F850LP (*z'*), *HST*/WFC3 F105W (*Y*, F125W (*J*), F160W (*H*); *JWST*/NIRCam F444W (*NIR*), *JWST*/MIRI F770W (*MIR*); ALMA Band 6 continuum and the [CII] pseudo-narrow band emission line map. **From left to right:** maps with different spatial resolutions are shown, in particular the nominal resolution from the simulation (first two panels), the typical resolution of current observations ($\sim$ 0.15" - 0.2", third panel), and the higher resolution currently achievable with ALMA and/or in lensed systems ($\sim$ 0.05", considering a magnification factor $\mu \sim 10$, fourth panel). The stamps in the leftmost column have a size of 0.2" $\times$ 0.2" ($\sim 1.1 \times 1.1$ kpc at $z \sim 6$), whereas the other stamps have a size of 0.6" $\times$ 0.6" ($\sim 3.4 \times 3.4$ kpc at $z \sim 6$).

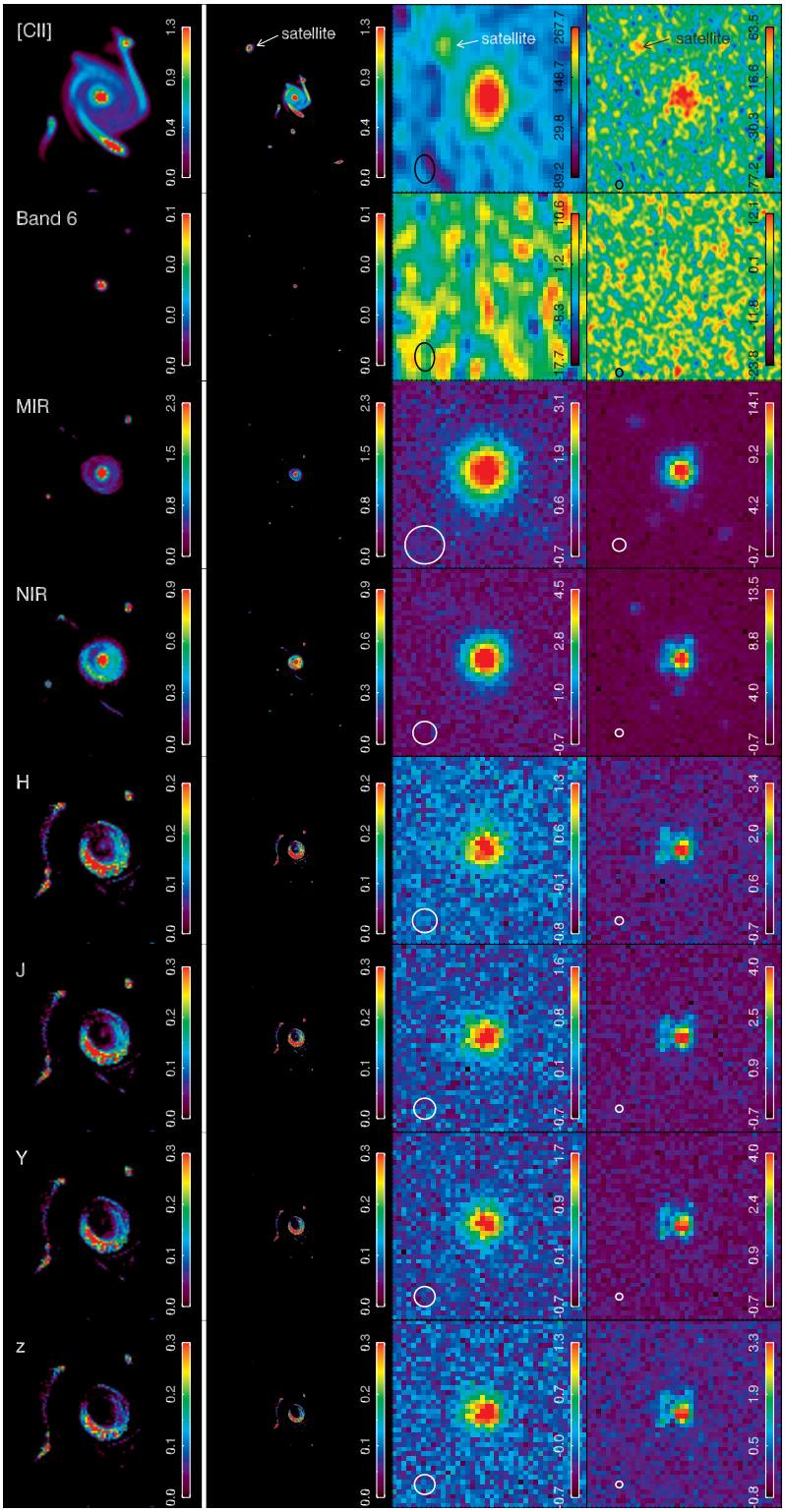

Figure A.2: Maps of Althæa in the merger stage. The color bars report the flux values in units of $10^{-3}\mu$Jy for the *HST* and *JWST* maps, and μJy beam^{-1} for the ALMA maps. The white and black circles in the bottom left corner of the maps indicate the spatial resolution of the observations (the full width at half maximum of the point spread function for the *HST* and *JWST* maps, the beam for the ALMA bands). Colors and symbols are as in Figure A.1.

input the original-resolution continuum and emission line models and generated *uv* data with the `simobserve` task. Since in this chapter we do not focus on the kinematical properties of galaxies, but rather on their morphology, we did not produce hyperspectral cubes (including spatial and velocity information). We directly fed CASA with the 2D [C II] models integrated over a line width of 100 km s^{-1}. We then imaged the simulated observations with the `simanalyze` task. We adopted different configurations, in order to achieve ~ 0.15" and ~ 0.05" angular resolutions. We set the observing time to 10 hours, as this is a typical integration time for high-redshift observations (e.g. Jones et al. 2017, Laporte et al. 2017, Carniani et al. 2018a). Imaging was performed using a Briggs weighting scheme (ROBUST = -0.5) which gives a good trade-off between resolution and sensitivity.

A.2 Results

A.2.1 Galaxy sizes

In Figure A.1 and A.2 we show the mock maps of our clumpy galaxy and merger. Our galaxies are clearly detected (S/N $\gtrsim 5$) in the optical and infrared bands, as well as in the [C II] emission line maps, irrespective of the resolution of the observations. Instead, they are undetectable in the sub-millimeter continuum maps (e.g. Band 6). This is consistent with literature results, where the continuum at ~ 158 μm is often undetected, even when the [C II] is observed with high S/N (Capak et al. 2015, Tamura et al. 2019, Bakx et al. 2020).

We fit the 2D light profile of the clumpy disk and merger using a Sérsic profile and determined the effective radius of the disks. We find that they both have $R_e \sim 300$ pc in the optical and infrared bands. The galaxies are marginally resolved or unresolved (especially in the *JWST*/MIRI band) in the low-resolution case, whereas they are resolved at high-resolution. The disk size estimate does not vary, within the uncertainties, when changing the angular resolution of the observations, indicating that the fits are robust when the sources are detected with S/N $\gtrsim 5$ at angular resolution < 0.15". The effective radius measured from the [C II] maps instead is systematically $\sim 1.5-2.5$ times larger than the optical one and ranges between 600 pc (for the merger) and 700 pc (for the clumpy disk).

The fact that [C II] sizes are systematically larger than the optical ones has been already reported (Carniani et al. 2017, Fujimoto et al. 2019, Ginolfi et al. 2020). Recently the ALPINE survey observed a sample of $z = 4-6$ galaxies and found, on a statistical basis, that the [C II] sizes are $\sim 2-3$ times larger than the rest-frame UV sizes measured in the z band, and $\sim 1.5-2$ times larger than the rest-frame optical sizes measured in the H band(Fujimoto et al., 2020). We find that the [C II] is systematically more extended than the rest-frame UV emitting regions, with [C II]-to-UV size ratios similar to those reported in the literature. We also find that the $R_{e,[CII]}/R_{e,z}$ ratio is $\sim 20-30\%$ smaller than the $R_{e,[CII]}/R_{e,H}$ ratio, in agreement with literature results.

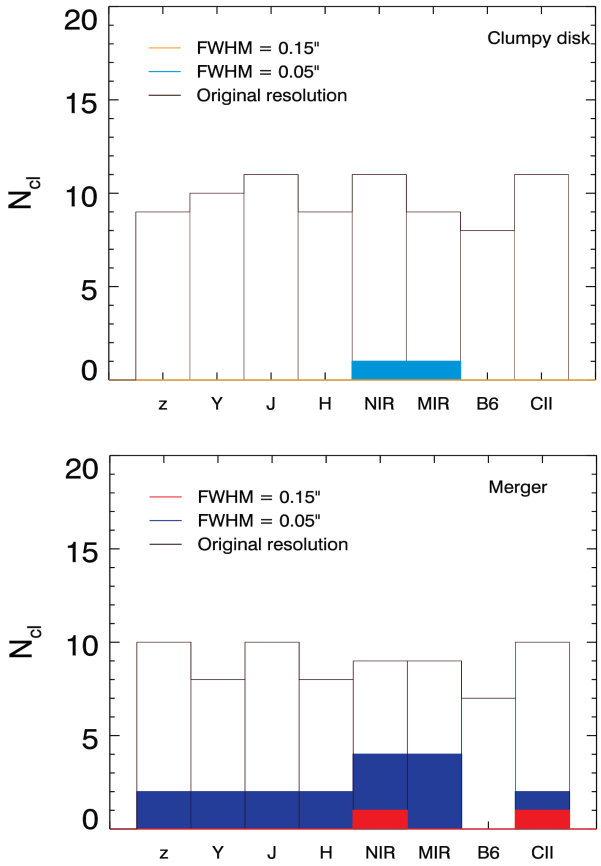

Figure A.3: Number of substructures found in different observing bands and with different spatial resolution. **Top:** clumpy galaxy case. **Bottom:** merger case. The number of substructures found in the simulations with original resolution (black empty histogram), mock observations with ~ 0.15" (red filled histogram), and ~ 0.05" (cyan and blue filled histogram) resolution are reported.

Our galaxies however seem to be more compact than those observed by Fujimoto et al. (2020), having both UV and [C II] effective radii a factor ~ 2.5 smaller than those reported in the literature. This might be due to the fact that the two stages of Althæa that we have analyzed were originally found at higher redshift, where galaxies are expected to have smaller sizes, at fixed stellar mass. More simulations are needed to understand the origin of this potential discrepancy with observations.

A.2.2 Galaxy clumpiness

We determine the number of clumps and satellites detected in the maps with the original resolution of the simulation (~ 25 pc) by using SEXTRACTOR (Bertin & Arnouts 1996). Both our clumpy disk and merger show a similar number of substructures, between 7 and 11 depending on the observing band. When we consider the low- and high-resolution galaxy maps (resolution ~ 0.15" and ~ 0.05" respectively), the number of detected substructures drastically decreases. The clumps that are closer to the galaxy nucleus are blended and cannot be detected against the galaxy disk. The

fainter and smaller clumps and satellites are instead undetected due to the lack of sensitivity and resolution of the mock observations. Only the substructures with high enough contrast against the galaxy disk or the background (e.g. those that are further away from the nucleus and/or brighter) can be detected.

We do not detect substructures in the low-resolution clumpy galaxy case, which appears as a smooth Sérsic disk. In the merger case we only detect one substructure in the near-infrared *JWST*/NIRCam band and in the [C II] map, but it does not appear at optical wavelengths. This is a merging satellite with stellar mass $M_\star = 1.3 \times 10^9$ $M_\odot$, molecular gas mass $M_{H2} = 0.4 \times 10^7$ $M_\odot$, and SFR = 10.8 $M_\odot$ yr^{-1}. Its projected galactocentric distance ($\sim$ 2.5 kpc) and high contrast allowed us to deblend it from the disk and detect it.

When considering the high-resolution case instead (resolution $\sim$ 0.05") more substructures appear. The clumpy disk shows one clump, detected in the near- and mid-infrared bands. The merger shows two substructures in the optical and [C II] maps, and five at near- and mid-infrared wavelengths. The stellar mass of these substructures ranges between $M_\star \simeq (0.3 - 2.5) \times 10^8 M_\odot$, their total gas mass $M_{\rm gas} \sim (1 - 4) \times 10^7 M_\odot$, and their SFR $\simeq 0.2 - 1.0$ $M_\odot$ yr^{-1}. The most massive one and the most distant from the galaxy nucleus is a satellite, whereas the innermost ones are clumps. We note however that even in our high-resolution cases, only the clumps that are laying in the outskirts of the disk are detectable, whereas the innermost ones have a too low contrast with the disk to be deblended and studied. We note however that the detection of clumps might be easier when targeting galaxies with larger effective radii than Althæa, as the contrast of the substructures with the galaxy disk is higher.

A.3 Summary

We have analyzed two stages of Althæa, a typical $z \simeq 6$ Lyman Break galaxy found in the SERRA zoom-in cosmological simulation suite. In the first snapshot Althæa appears as a clumpy disk, whereas in the second it is undergoing a merger with a small satellite (stellar mass ratio 1:8). We created mock optical (z', Y, J, and H *HST*-like), infrared (NIRCam/F444W and MIRI/F770W *JWST*-like) and sub-millimeter (Band 6 and [C II] ALMA-like) observations. We performed a 2D morphological analysis, considering maps with different angular resolutions (0.15" and 0.05"), and we deblended the emission of the galaxy disks from that of substructures (merging satellites or star-forming clumps). We found that:

- Our mock galaxies show [C II] effective radii $\sim 1.5 - 2.5$ times larger than the optical ones. This is consistent with recent findings from the literature (e.g. Carniani et al. 2018a, Fujimoto et al. 2020). We conclude that the observed [C II] halos arise from the joint effect of stellar outflows and carbon photoionization by the galaxy UV field, rather than from the emission of unresolved nearby satellites (Gallerani et al., 2018b; Pizzati et al., 2020).

- With a spatial resolution of ~ 0.15" we detect only one merging satellite at a distance of ~ 2.5 kpc from the galaxy nucleus. Star-forming clumps are instead embedded in the galaxy disk (distance $\lesssim 1$ kpc). We show that better resolution (~ 0.05") is required to detect these substructures at $z \sim 6$.

- Star-forming clumps found in our mock observations follow the local $L_{[C\ II]}$ – SFR_{UV} relation reported in the literature for galaxy disks, but sample the low-luminosity ($L_{[C\ II]} \lesssim 10^{7.5}$ $L_\odot$), low-SFR ($SFR_{UV} \lesssim 3$ $M_\odot$ yr^{-1}) tail of the distribution.

- Only clumps with low dust extinction ($A_V \simeq 0.1$) are detectable in the *HST*-like UV bands, whereas the dust-obscured ($A_V \sim 1$) and metal-rich ones are detected in [C II] maps. The *JWST* bands seem to be the most suitable ones to detect substructures thanks to their simultaneous sensitivity to both low-metallicity and dust-obscured regions that are bright at infrared wavelengths.

- By comparing the spatial extent, UV and [C II] luminosity, and separation of the substructures found in the multi-components systems reported in the literature at $z \sim 5-7$ (Carniani et al., 2018a), we conclude that current observations are likely detecting galaxies undergoing major mergers, rather than their internal star-forming clumps. Future telescopes (e.g. *JWST*, ELT) and instruments (e.g. VLT/MAVIS) with better sensitivity and spatial resolution will allow us to study star-forming clumps in $z \sim 6$ galaxies and quantify their contribution to the mass assembly of early galaxies.

Appendix B

SERRA galaxies probed by [C II] and Hα emission lines

The [C II] and Hα contours on the stellar maps of the extended sample of SERRA galaxies.

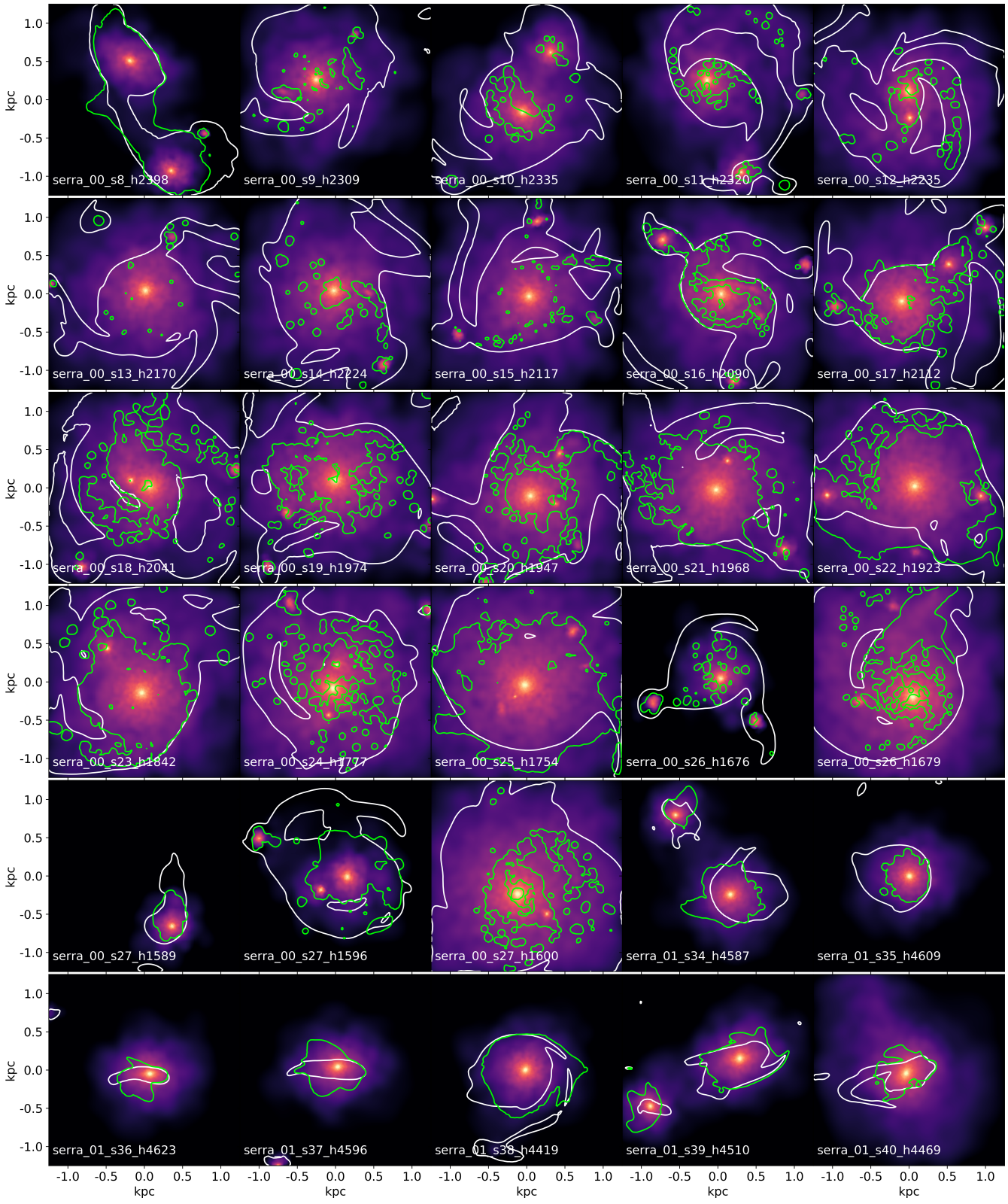
serra_00_s8_h2398
serra_00_s9_h2309
serra_00_s10_h2335
serra_00_s11_h2320
serra_00_s12_h2235
serra_00_s13_h2170
serra_00_s14_h2224
serra_00_s15_h2117
serra_00_s16_h2090
serra_00_s17_h2112
serra_00_s18_h2041
serra_00_s19_h1974
serra_00_s20_h1947
serra_00_s21_h1968
serra_00_s22_h1923
serra_00_s23_h1842
serra_00_s24_h1777
serra_00_s25_h1754
serra_00_s26_h1676
serra_00_s26_h1679
serra_00_s27_h1589
serra_00_s27_h1596
serra_00_s27_h1600
serra_01_s34_h4587
serra_01_s35_h4609
serra_01_s36_h4623
serra_01_s37_h4596
serra_01_s38_h4419
serra_01_s39_h4510
serra_01_s40_h4469
kpc
1.0
0.5
0.0
-0.5
-1.0

Figure B.1

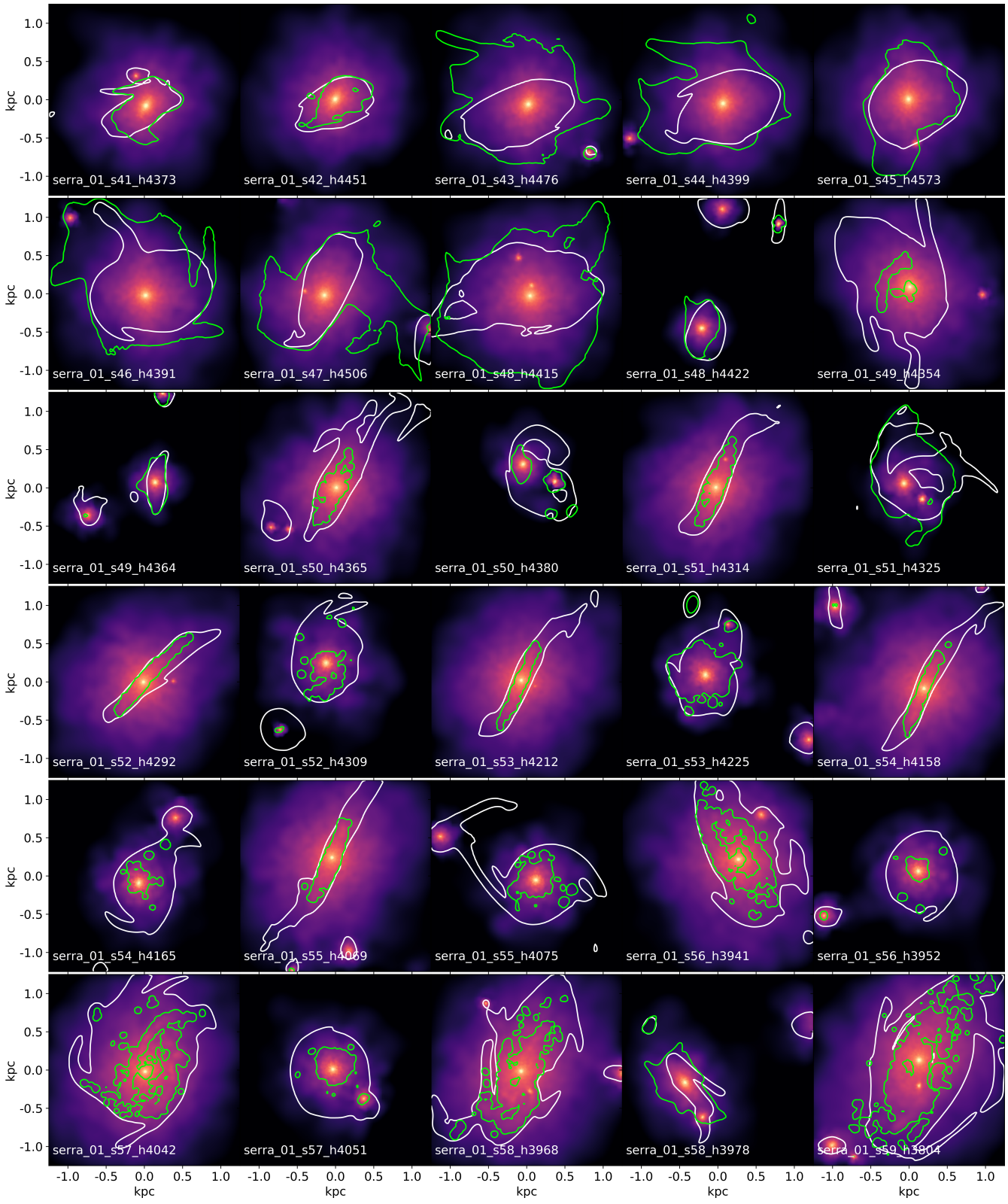
serra_01_s41_h4373
serra_01_s42_h4451
serra_01_s43_h4476
serra_01_s44_h4399
serra_01_s45_h4573
serra_01_s46_h4391
serra_01_s47_h4506
serra_01_s48_h4415
serra_01_s48_h4422
serra_01_s49_h4354
serra_01_s49_h4364
serra_01_s50_h4365
serra_01_s50_h4380
serra_01_s51_h4314
serra_01_s51_h4325
serra_01_s52_h4292
serra_01_s52_h4309
serra_01_s53_h4212
serra_01_s53_h4225
serra_01_s54_h4158
serra_01_s54_h4165
serra_01_s55_h4069
serra_01_s55_h4075
serra_01_s56_h3941
serra_01_s56_h3952
serra_01_s57_h4042
serra_01_s57_h4051
serra_01_s58_h3968
serra_01_s58_h3978
serra_01_s59_h3804
kpc
1.0
0.5
0.0
-0.5
-1.0

Figure B.2

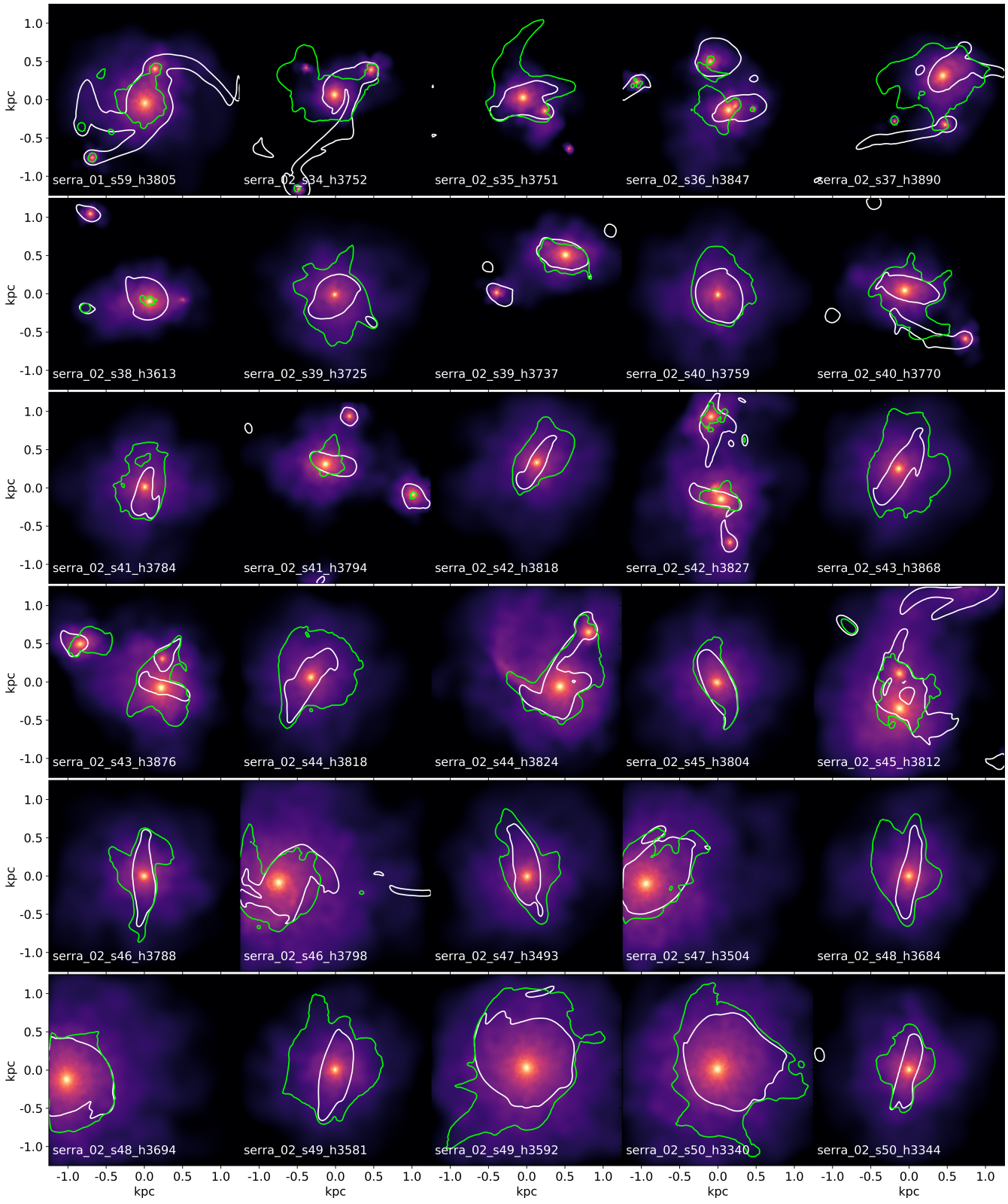
serra_01_s59_h3805
serra_02_s34_h3752
serra_02_s35_h3751
serra_02_s36_h3847
serra_02_s37_h3890
serra_02_s38_h3613
serra_02_s39_h3725
serra_02_s39_h3737
serra_02_s40_h3759
serra_02_s40_h3770
serra_02_s41_h3784
serra_02_s41_h3794
serra_02_s42_h3818
serra_02_s42_h3827
serra_02_s43_h3868
serra_02_s43_h3876
serra_02_s44_h3818
serra_02_s44_h3824
serra_02_s45_h3804
serra_02_s45_h3812
serra_02_s46_h3788
serra_02_s46_h3798
serra_02_s47_h3493
serra_02_s47_h3504
serra_02_s48_h3684
serra_02_s48_h3694
serra_02_s49_h3581
serra_02_s49_h3592
serra_02_s50_h3340
serra_02_s50_h3344
kpc
1.0
0.5
0.0
-0.5
-1.0

Figure B.3

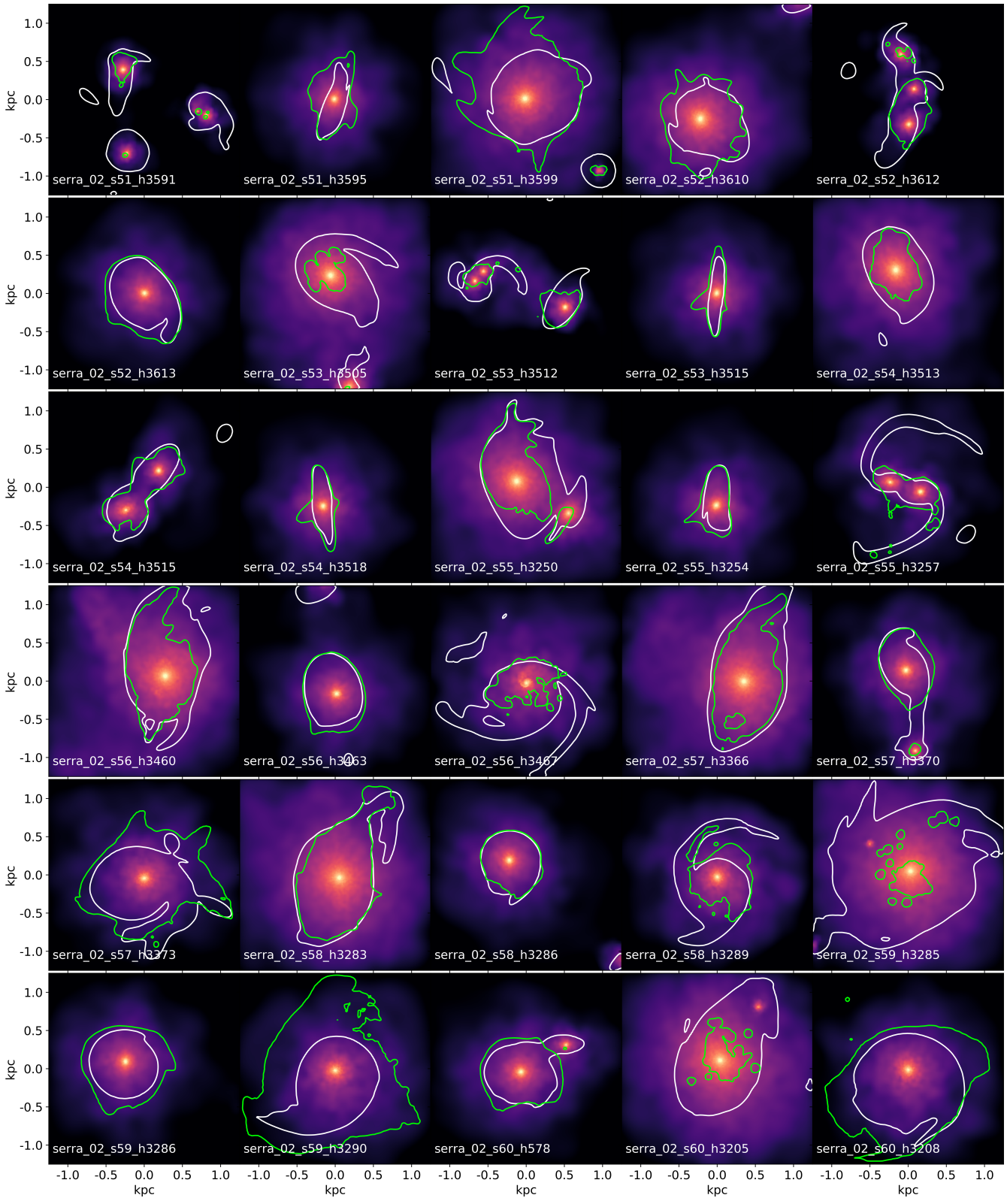
serra_02_s51_h3591
serra_02_s51_h3595
serra_02_s51_h3599
serra_02_s52_h3610
serra_02_s52_h3612
serra_02_s52_h3613
serra_02_s53_h3505
serra_02_s53_h3512
serra_02_s53_h3515
serra_02_s54_h3513
serra_02_s54_h3515
serra_02_s54_h3518
serra_02_s55_h3250
serra_02_s55_h3254
serra_02_s55_h3257
serra_02_s56_h3460
serra_02_s56_h3463
serra_02_s56_h3467
serra_02_s57_h3366
serra_02_s57_h3370
serra_02_s57_h3373
serra_02_s58_h3283
serra_02_s58_h3286
serra_02_s58_h3289
serra_02_s59_h3285
serra_02_s59_h3286
serra_02_s59_h3290
serra_02_s60_h578
serra_02_s60_h3205
serra_02_s60_h3208
kpc
1.0
0.5
0.0
-0.5
-1.0

Figure B.4

Bibliography

Agertz O., Kravtsov A. V., 2015, ApJ, 804, 18

Agertz O., Kravtsov A. V., Leitner S. N., Gnedin N. Y., 2013, ApJ, 770, 25

Andersen D. R., Bershady M. A., Sparke L. S., Gallagher John S. I., Wilcots E. M., van Driel W., Monnier-Ragaigne D., 2006, ApJS, 166, 505

Asplund M., Grevesse N., Sauval A. J., Scott P., 2009, ARA&A, 47, 481

Atek H., et al., 2015, ApJ, 814, 69

Aubert D., Teyssier R., 2008, MNRAS, 387, 295

Avila-Reese V., Zavala J., Firmani C., Hernández-Toledo H. M., 2008, AJ, 136, 1340

Baes M., Camps P., 2015, Astronomy and Computing, 12, 33

Bakx T. J. L. C., et al., 2020, MNRAS, 493, 4294

Bardeen J. M., Bond J. R., Kaiser N., Szalay A. S., 1986, ApJ, 304, 15

Barkana R., Loeb A., 2001, Phys. Rep., 349, 125

Begeman K. G., 1989, A&A, 223, 47

Behrens C., Pallottini A., Ferrara A., Gallerani S., Vallini L., 2018, MNRAS, 477, 552

Behrens C., Pallottini A., Ferrara A., Gallerani S., Vallini L., 2019, MNRAS, 486, 2197

Behroozi P. S., Wechsler R. H., Wu H.-Y., 2013, ApJ, 762, 109

Bell E. F., de Jong R. S., 2001, ApJ, 550, 212

Bertelli G., Bressan A., Chiosi C., Fagotto F., Nasi E., 1994, A&AS, 106, 275

Bertin E., Arnouts S., 1996, A&AS, 117, 393

Binney J., Tremaine S., 2008, Galactic Dynamics: Second Edition. Princeton University Press

Blanton M. R., Moustakas J., 2009, ARA&A, 47, 159

Bolatto A. D., Leroy A. K., Rosolowsky E., Walter F., Blitz L., 2008, The Astrophysical Journal, 686, 948

Bouwens R. J., Illingworth G. D., Franx M., Ford H., 2007, ApJ, 670, 928

Bouwens R. J., et al., 2010, ApJ, 725, 1587

Bouwens R. J., et al., 2011, Nature, 469, 504

Bouwens R. J., et al., 2015, ApJ, 803, 34

Bouwens R. J., et al., 2021, arXiv e-prints, p. arXiv:2106.13719

Bovino S., Grassi T., Capelo P. R., Schleicher D. R. G., Banerjee R., 2016, A&A, 590, A15

Bowler R. A. A., et al., 2014, MNRAS, 440, 2810

Bowler R. A. A., et al., 2015, MNRAS, 452, 1817

Bradač M., et al., 2017, ApJ, 836, L2

Brammer G. B., et al., 2012, ApJS, 200, 13

Bromm V., Coppi P. S., Larson R. B., 2002, in Gilfanov M., Sunyeav R., Churazov E., eds, Lighthouses of the Universe: The Most Luminous Celestial Objects and Their Use for Cosmology. p. 316 (arXiv:astro-ph/0110459), doi:10.1007/10856495_49

Bruzual G., Charlot S., 2003, MNRAS, 344, 1000

Bryan G. L., Norman M. L., 1998, ApJ, 495, 80

Burkert A., et al., 2016, ApJ, 826, 214

Burton W. B. E. B. G. G. R. P. D. . B. P., 1992, The galactic interstellar medium: Saas-Fee Advanced Course 21. Springer

Camps P., Baes M., 2015, Astronomy and Computing, 9, 20

Capak P. L., et al., 2015, Nature, 522, 455

Carniani S., et al., 2017, A&A, 605, A42

Carniani S., et al., 2018a, MNRAS, 478, 1170

Carniani S., Maiolino R., Smit R., Amorín R., 2018b, ApJ, 854, L7

Carroll S. M., Press W. H., Turner E. L., 1992, ARA&A, 30, 499

Ciardi B., Ferrara A., 2005, Space Sci. Rev., 116, 625

Conselice C. J., Bundy K., Ellis R. S., Brichmann J., Vogt N. P., Phillips A. C., 2005, ApJ, 628, 160

Courant R., Friedrichs K., Lewy H., 1928, Mathematische Annalen, 100, 32

Cresci G., et al., 2009, ApJ, 697, 115

Da Cunha E., et al., 2013, Astrophysical Journal, 766

Daddi E., et al., 2010, ApJ, 714, L118

Dalgarno A., McCray R. A., 1972a, ARA&A, 10, 375

Dalgarno A., McCray R. A., 1972b, Annual Review of Astronomy and Astrophysics, 10, 375

Dayal P., Ferrara A., 2018, preprint, (arXiv:1809.09136)

De Breuck C., et al., 2014, A&A, 565, A59

De Looze I., et al., 2014, A&A, 568, A62

Decataldo D., Ferrara A., Pallottini A., Gallerani S., Vallini L., 2017, MNRAS, 471, 4476

Decataldo D., Pallottini A., Ferrara A., Vallini L., Gallerani S., 2019, MNRAS, 487, 3377

Dekel A., Burkert A., 2014, MNRAS, 438, 1870

Dekel A., Sari R., Ceverino D., 2009, ApJ, 703, 785

Deparis N., Aubert D., Ocvirk P., Chardin J., Lewis J., 2019, A&A, 622, A142

Dessauges-Zavadsky M., et al., 2020, A&A, 643, A5

Di Teodoro E. M., Fraternali F., 2015, MNRAS, 451, 3021

Di Teodoro E. M., Fraternali F., Miller S. H., 2016, A&A, 594, A77

Di Teodoro E. M., et al., 2018, MNRAS, 476, 804

Dib S., Bell E., Burkert A., 2006, ApJ, 638, 797

Draine B. T., 1978, ApJS, 36, 595

Draine B. T., 2011, Physics of the Interstellar and Intergalactic Medium

Dunlop J. S., 2013, Observing the First Galaxies. p. 223, doi:10.1007/978-3-642-32362-1_5

Dutton A. A., 2012, MNRAS, 424, 3123

Einstein A., 1915, Sitzungsberichte der Königlich Preußischen Akademie der Wissenschaften (Berlin, pp 844–847

Elitzur M., Asensio Ramos A., Ceccarelli C., 2012, MNRAS, 422, 1394

Ellis R. S., et al., 2013, ApJ, 763, L7

Elmegreen B. G., Burkert A., 2010, ApJ, 712, 294

Elmegreen B. G., Elmegreen D. M., 2005, The Astrophysical Journal, 627, 632

Elmegreen D. M., Elmegreen B. G., 2017, ApJ, 851, L44

Epinat B., Amram P., Balkowski C., Marcelin M., 2010, MNRAS, 401, 2113

Epinat B., et al., 2012, A&A, 539, A92

Fan X., et al., 2006, AJ, 132, 117

Federrath C., Klessen R. S., 2013, ApJ, 763, 51

Feldmann R., Quataert E., Hopkins P. F., Faucher-Giguère C.-A., Kereš D., 2017, MNRAS, 470, 1050

Fensch J., Bournaud F., 2021, MNRAS, 505, 3579

Ferland G. J., et al., 2017, Rev. Mex. Astron. Astrofis., 53, 385

Ferrara A., 2008, Cosmological Feedbacks from the First Stars. pp 161–258, doi:10.1007/978-3-540-74163-3_2

Ferrara A., Vallini L., Pallottini A., Gallerani S., Carniani S., Kohandel M., Decataldo D., Behrens C., 2019, MNRAS, 489, 1

Field G. B., Goldsmith D. W., Habing H. J., 1969, in BAAS. p. 240

Fixsen D. J., 2009, ApJ, 707, 916

Förster Schreiber N. M., et al., 2009a, ApJ, 706, 1364

Förster Schreiber N. M., et al., 2009b, ApJ, 706, 1364

Förster Schreiber N. M., et al., 2018, ApJS, 238, 21

Fraternali F., Karim A., Magnelli B., Gómez-Guijarro C., Jiménez-Andrade E. F., Posses A. C., 2021, A&A, 647, A194

Freeman K. C., 1970, ApJ, 160, 811

Friedmann A., 1922, Zeitschrift fur Physik, 10, 377

Friedmann A., 1924, Zeitschrift fur Physik, 21, 326

Fujimoto S., et al., 2019, ApJ, 887, 107

Fujimoto S., et al., 2020, arXiv e-prints, p. arXiv:2003.00013

Gallerani S., Pallottini A., Feruglio C., Ferrara A., Maiolino R., Vallini L., Riechers D. A., Pavesi R., 2018a, MNRAS, 473, 1909

Gallerani S., Pallottini A., Feruglio C., Ferrara A., Maiolino R., Vallini L., Riechers D. A., Pavesi R., 2018b, MNRAS, 473, 1909

Galli D., Palla F., 1998, A&A, 335, 403

Genel S., et al., 2014, MNRAS, 445, 175

Genzel R., et al., 2006, Nature, 442, 786

Genzel R., et al., 2011, ApJ, 733, 101

Genzel R., et al., 2013, The Astrophysical Journal, 773, 68

Genzel R., et al., 2017, Nature, 543, 397

Georgi H., Glashow S. L., 1974, Phys. Rev. Lett., 32, 438

Gilmore G., Reid N., 1983, MNRAS, 202, 1025

Ginolfi M., et al., 2020, A&A, 633, A90

Girard M., et al., 2018, A&A, 613, A72

Glazebrook K., 2013, Publ. Astron. Soc. Australia, 30, e056

Gnedin N. Y., 2000, ApJ, 535, 530

Gnedin N. Y., Abel T., 2001, New Astron., 6, 437

Gnerucci A., et al., 2011, A&A, 528, A88

Goldsmith P. F., Langer W. D., Pineda J. L., Velusamy T., 2012, ApJS, 203, 13

Gong Y., Cooray A., Silva M., Santos M. G., Bock J., Bradford C. M., Zemcov M., 2012, ApJ, 745, 49

Gorti U., Hollenbach D., 2002, ApJ, 573, 215

Grassi T., Bovino S., Schleicher D. R. G., Prieto J., Seifried D., Simoncini E., Gianturco F. A., 2014, MNRAS, 439, 2386

Green A. W., et al., 2014, MNRAS, 437, 1070

Grogin N. A., et al., 2011, ApJS, 197, 35

Guillet T., Teyssier R., 2011, Journal of Computational Physics, 230, 4756

Gunn J. E., Peterson B. A., 1965, ApJ, 142, 1633

Habing H. J., 1968, Bull. Astron. Inst. Netherlands, 19, 421

Haffner L. M., et al., 2009, Reviews of Modern Physics, 81, 969

Hahn O., Abel T., 2011, MNRAS, 415, 2101

Haiman Z., Rees M. J., Loeb A., 1996, ApJ, 467, 522

Harikane Y., et al., 2019, arXiv e-prints, p. arXiv:1910.10927

Harrison C. M., et al., 2017, MNRAS, 467, 1965

Hashimoto T., et al., 2018, arXiv e-prints, p. arXiv:1806.00486

Hayward C. C., Hopkins P. F., 2017, MNRAS, 465, 1682

Heiderman A., Evans Neal J. I., Allen L. E., Huard T., Heyer M., 2010, ApJ, 723, 1019

Herrera-Camus R., et al., 2015, ApJ, 800, 1

Herrera-Camus R., et al., 2018, ApJ, 861, 95

Hirashita H., Ferrara A., 2002, MNRAS, 337, 921

Hodge J. A., Carilli C. L., Walter F., de Blok W. J. G., Riechers D., Daddi E., Lentati L., 2012, ApJ, 760, 11

Hodge J. A., Riechers D., Decarli R., Walter F., Carilli C. L., Daddi E., Dannerbauer H., 2014, The Astrophysical Journal, 798, L18

Hollenbach D. J., Tielens A. G. G. M., 1999, Rev. Mod. Phys., 71, 173

Hopkins P. F., Quataert E., Murray N., 2011, MNRAS, 417, 950

Hopkins P. F., Kereš D., Murray N., Hernquist L., Narayanan D., Hayward C. C., 2013, MNRAS, 433, 78

Hopkins P. F., et al., 2018, MNRAS, 480, 800

Hubble E., 1929, Proceedings of the National Academy of Science, 15, 168

Inoue A. K., et al., 2016a, Science, 352, 1559

Inoue S., Dekel A., Mandelker N., Ceverino D., Bournaud F., Primack J., 2016b, MNRAS, 456, 2052

Jeans J. H., 1902, Philosophical Transactions of the Royal Society of London Series A, 199, 1

Jiang L., et al., 2016, ApJ, 816, 16

Jones T. A., Swinbank A. M., Ellis R. S., Richard J., Stark D. P., 2010, MNRAS, 404, 1247

Jones G. C., Willott C. J., Carilli C. L., Ferrara A., Wang R., Wagg J., 2017, ApJ, 845, 175

Jones G. C., et al., 2020, MNRAS, 491, L18

Joung M. R., Mac Low M.-M., Bryan G. L., 2009, ApJ, 704, 137

Jura M., 1975, ApJ, 197, 575

Kapala M. J., et al., 2015, ApJ, 798, 24

Kashikawa N., et al., 2006, ApJ, 648, 7

Kashikawa N., et al., 2011, ApJ, 734, 119

Kassin S. A., et al., 2007, ApJ, 660, L35

Katz H., Kimm T., Sijacki D., Haehnelt M. G., 2017, MNRAS, 468, 4831

Katz H., et al., 2019, arXiv e-prints, p. arXiv:1901.01272

Keenan F. P., Lennon D. J., Johnson C. T., Kingston A. E., 1986, MNRAS, 220, 571

Kennicutt Jr. R. C., 1998, ApJ, 498, 541

Kim W.-T., Ostriker E. C., Stone J. M., 2003, ApJ, 599, 1157

Kleiner D., et al., 2019, MNRAS, 488, 5352

Klessen R. S., Hennebelle P., 2010, A&A, 520, A17

Knebe A., et al., 2013, MNRAS, 428, 2039

Knudsen K. K., Richard J., Kneib J.-P., Jauzac M., Clément B., Drouart G., Egami E., Lindroos L., 2016, MNRAS, 462, L6

Kohandel M., Pallottini A., Ferrara A., Zanella A., Behrens C., Carniani S., Gallerani S., Vallini L., 2019, MNRAS, 487, 3007

Kohandel M., Pallottini A., Ferrara A., Carniani S., Gallerani S., Vallini L., Zanella A., Behrens C., 2020, MNRAS, 499, 1250

Kroupa P., 2001, Monthly Notices of the Royal Astronomical Society, 322, 231

Krumholz M. R., Burkhart B., 2016, MNRAS, 458, 1671

Krumholz M. R., McKee C. F., 2005, ApJ, 630, 250

Krumholz M. R., Thompson T. A., 2012, ApJ, 760, 155

Lagache G., Cousin M., Chatzikos M., 2018, A&A, 609, A130

Lang P., et al., 2017, ApJ, 840, 92

Laporte N., et al., 2017, ApJ, 837, L21

Law D. R., Steidel C. C., Erb D. K., Larkin J. E., Pettini M., Shapley A. E., Wright S. A., 2009, ApJ, 697, 2057

Le Fèvre O., et al., 2020, A&A, 643, A1

Le Tiran L., Lehnert M. D., 2011, in Carignan C., Combes F., Freeman K. C., eds, IAU Symposium Vol. 277, Tracing the Ancestry of Galaxies. pp 150–153, doi:10.1017/S1743921311022666

Lehnert M. D., Le Tiran L., Nesvadba N. P. H., van Driel W., Boulanger F., Di Matteo P., 2013, A&A, 555, A72

Leitherer C., et al., 1999, ApJS, 123, 3

Lelli F., McGaugh S. S., Schombert J. M., 2016, ApJ, 816, L14

Lelli F., De Breuck C., Falkendal T., Fraternali F., Man A. W. S., Nesvadba N. P. H., Lehnert M. D., 2018, MNRAS, 479, 5440

Leung T. K. D., et al., 2019, ApJ, 871, 85

Leung T. K. D., Pallottini A., Ferrara A., Mac Low M.-M., 2020, ApJ, 895, 24

Levy R. C., et al., 2018, ApJ, 860, 92

Lifshitz E. M., 1946, Zhurnal Eksperimentalnoi i Teoreticheskoi Fiziki, 16, 587

Linde A. D., 1982, Physics Letters B, 116, 335

Livermore R. C., Finkelstein S. L., Lotz J. M., 2017, ApJ, 835, 113

Loiacono F., Talia M., Fraternali F., Cimatti A., Di Teodoro E. M., Caminha G. B., 2019, MNRAS, 489, 681

Luhman M. L., et al., 1998, ApJ, 504, L11

Luhman M. L., Satyapal S., Fischer J., Wolfire M. G., Sturm E., Dudley C. C., Lutz D., Genzel R., 2003, ApJ, 594, 758

Lupi A., 2019, MNRAS, 484, 1687

Lupi A., Pallottini A., Ferrara A., Bovino S., Carniani S., Vallini L., 2020, MNRAS,

Mac Low M.-M., 1999, ApJ, 524, 169

Madau P., Haardt F., Rees M. J., 1999, ApJ, 514, 648

Maiolino R., et al., 2015, MNRAS, 452, 54

Malhotra S., et al., 1997, ApJ, 491, L27

Marrone D. P., et al., 2018, Nature, 553, 51

Martizzi D., Faucher-Giguère C.-A., Quataert E., 2015, MNRAS, 450, 504

Mason C. A., et al., 2017, ApJ, 838, 14

Matthee J. J. A., et al., 2014, MNRAS, 440, 2375

Matthee J., Sobral D., Santos S., Röttgering H., Darvish B., Mobasher B., 2015, MNRAS, 451, 400

Matthee J., et al., 2017, ApJ, 851, 145

McGaugh S. S., 2012, AJ, 143, 40

McGaugh S. S., Schombert J. M., Bothun G. D., de Blok W. J. G., 2000, ApJ, 533, L99

McGreer I. D., Mesinger A., Fan X., 2011, MNRAS, 415, 3237

McMullin J. P., Waters B., Schiebel D., Young W., Golap K., 2007, in Shaw R. A., Hill F., Bell D. J., eds, Astronomical Society of the Pacific Conference Series Vol. 376, Astronomical Data Analysis Software and Systems XVI. p. 127

Meier D. L., 1976, ApJ, 207, 343

Mesinger A., 2016, Understanding the Epoch of Cosmic Reionization. Vol. 423, doi:10.1007/978-3-319-21957-8,

Mieda E., Wright S. A., Larkin J. E., Armus L., Juneau S., Salim S., Murray N., 2016, ApJ, 831, 78

Milosavljević M., Safranek-Shrader C., 2016, Star Formation for Predictive Primordial Galaxy Formation. p. 65, doi:10.1007/978-3-319-21957-8_3

Mo H., van den Bosch F. C., White S., 2010, Galaxy Formation and Evolution

Moiseev A. V., Tikhonov A. V., Klypin A., 2015, MNRAS, 449, 3568

Molina J., Ibar E., Swinbank A. M., Sobral D., Best P. N., Smail I., Escala A., Cirasuolo M., 2017, MNRAS, 466, 892

Murray N., 2011, ApJ, 729, 133

Narayanan D., Bothwell M., Davé R., 2012, MNRAS, 426, 1178

O'Shea B. W., Wise J. H., Xu H., Norman M. L., 2015, ApJ, 807, L12

Oesch P. A., et al., 2013, ApJ, 773, 75

Oesch P. A., et al., 2016, ApJ, 819, 129

Olsen K., Greve T. R., Narayanan D., Thompson R., Davé R., Niebla Rios L., Stawinski S., 2017, ApJ, 846, 105

Olsen K., et al., 2018, Galaxies, 6, 100

Orr M. E., et al., 2019a, arXiv e-prints, p. arXiv:1911.00020

Orr M. E., Hayward C. C., Hopkins P. F., 2019b, MNRAS, 486, 4724

Ostriker J. P., McKee C. F., 1988, Rev. Mod. Phys., 60, 1

Ostriker E. C., Shetty R., 2011, ApJ, 731, 41

Ouchi M., et al., 2005, ApJ, 620, L1

Ouchi M., et al., 2008, ApJS, 176, 301

Ouchi M., et al., 2010, ApJ, 723, 869

Ouchi M., et al., 2013, ApJ, 778, 102

Ouchi M., et al., 2018, PASJ, 70, S13

Padoan P., Nordlund Å., 2011, ApJ, 730, 40

Pallottini A., Ferrara A., Gallerani S., Salvadori S., D'Odorico V., 2014, MNRAS, 440, 2498

Pallottini A., Gallerani S., Ferrara A., Yue B., Vallini L., Maiolino R., Feruglio C., 2015, MNRAS, 453, 1898

Pallottini A., Ferrara A., Gallerani S., Vallini L., Maiolino R., Salvadori S., 2017a, MNRAS, 465, 2540

Pallottini A., Ferrara A., Bovino S., Vallini L., Gallerani S., Maiolino R., Salvadori S., 2017b, MNRAS, 471, 4128

Pallottini A., et al., 2019, MNRAS, 487, 1689

Pasetto S., et al., 2012, A&A, 547, A70

Pelliccia D., Tresse L., Epinat B., Ilbert O., Scoville N., Amram P., Lemaux B. C., Zamorani G., 2017, A&A, 599, A25

Pentericci L., et al., 2016, ApJ, 829, L11

Pierce M. J., Tully R. B., 1992, ApJ, 387, 47

Pillepich A., et al., 2019, MNRAS, 490, 3196

Piontek R. A., Ostriker E. C., 2004, ApJ, 601, 905

Pizagno J., et al., 2005, ApJ, 633, 844

Pizzati E., Ferrara A., Pallottini A., Gallerani S., Vallini L., Decataldo D., Fujimoto S., 2020, MNRAS, 495, 160

Planck Collaboration et al., 2014, A&A, 571, A16

Planck Collaboration et al., 2016, A&A, 596, A107

Popping G., van Kampen E., Decarli R., Spaans M., Somerville R. S., Trager S. C., 2016, MNRAS, 461, 93

Popping G., Narayanan D., Somerville R. S., Faisst A. L., Krumholz M. R., 2019, MNRAS, 482, 4906

Press W. H., Schechter P., 1974, ApJ, 187, 425

Price S. H., et al., 2016, ApJ, 819, 80

Puech M., et al., 2008, A&A, 484, 173

Reyes R., Mandelbaum R., Gunn J. E., Pizagno J., 2011, in American Astronomical Society Meeting Abstracts #217. p. 430.06

Rizzo F., Vegetti S., Powell D., Fraternali F., McKean J. P., Stacey H. R., White S. D. M., 2020, Nature, 584, 201

Rizzo F., Vegetti S., Fraternali F., Stacey H., Powell D., 2021, arXiv e-prints, p. arXiv:2102.05671

Rosdahl J., Teyssier R., 2015, MNRAS, 449, 4380

Rosdahl J., Blaizot J., Aubert D., Stranex T., Teyssier R., 2013, MNRAS, 436, 2188

Rubin V. C., Ford W. Kent J., D'Odorico S., 1970, ApJ, 160, 801

Rubin V. C., Ford W. K. J., Thonnard N., 1978, ApJ, 225, L107

Schaerer D., et al., 2020, A&A, 643, A3

Schmidt M., 1959, ApJ, 129, 243

Semenov V. A., Kravtsov A. V., Gnedin N. Y., 2016, ApJ, 826, 200

Shetty R., Ostriker E. C., 2012, ApJ, 754, 2

Shibuya T., Ouchi M., Harikane Y., Nakajima K., 2019a, ApJ, 871, 164

Shibuya T., Ouchi M., Harikane Y., Nakajima K., 2019b, ApJ, 871, 164

Simons R. C., et al., 2019, ApJ, 874, 59

Smit R., et al., 2014, ApJ, 784, 58

Smit R., et al., 2018, Nature, 553, 178

Smith B. D., Regan J. A., Downes T. P., Norman M. L., O'Shea B. W., Wise J. H., 2018, MNRAS, 480, 3762

Stacey G. J., Geis N., Genzel R., Lugten J. B., Poglitsch A., Sternberg A., Townes C. H., 1991, ApJ, 373, 423

Stark D. P., et al., 2015a, MNRAS, 450, 1846

Stark D. P., et al., 2015b, MNRAS, 454, 1393

Stark D. P., et al., 2017, MNRAS, 464, 469

Stecher T. P., Williams D. A., 1967, ApJ, 149, L29

Stott J. P., et al., 2016, MNRAS, 457, 1888

Straatman C. M. S., et al., 2017, ApJ, 839, 57

Suginohara M., Suginohara T., Spergel D. N., 1999, ApJ, 512, 547

Swinbank A. M., et al., 2011, ApJ, 742, 11

Swinbank A. M., Smail I., Sobral D., Theuns T., Best P. N., Geach J. E., 2012, ApJ, 760, 130

Swinbank A. M., et al., 2017, MNRAS, 467, 3140

Tacconi L. J., et al., 2010, Nature, 463, 781

Tacconi L. J., et al., 2013, ApJ, 768, 74

Tamura Y., et al., 2019, ApJ, 874, 27

Taniguchi Y., et al., 2005, PASJ, 57, 165

Teyssier R., 2002, A&A, 385, 337

Teyssier R., Pontzen A., Dubois Y., Read J. I., 2013, MNRAS, 429, 3068

Thompson T. A., Quataert E., Murray N., 2005, ApJ, 630, 167

Tielens A. G. G. M., 2010, The Physics and Chemistry of the Interstellar Medium

Toomre A., 1964, ApJ, 139, 1217

Trachternach C., de Blok W. J. G., McGaugh S. S., van der Hulst J. M., Dettmar R. J., 2009, A&A, 505, 577

Tully R. B., Fisher J. R., 1977, A&A, 500, 105

Übler H., et al., 2018, ApJ, 854, L24

Übler H., et al., 2019, ApJ, 880, 48

Vallini L., Gallerani S., Ferrara A., Baek S., 2013, MNRAS, 433, 1567

Vallini L., Gallerani S., Ferrara A., Pallottini A., Yue B., 2015, ApJ, 813, 36

Vallini L., Ferrara A., Pallottini A., Gallerani S., 2017, MNRAS, 467, 1300

Vallini L., Pallottini A., Ferrara A., Gallerani S., Sobacchi E., Behrens C., 2018, MNRAS, 473, 271

Vallini L., Ferrara A., Pallottini A., Carniani S., Gallerani S., 2020, MNRAS,

Wang R., et al., 2013, ApJ, 773, 44

Weaver R., McCray R., Castor J., Shapiro P., Moore R., 1977, ApJ, 218, 377

Weingartner J. C., Draine B. T., 2001, ApJ, 563, 842

Williams M. J., Bureau M., Cappellari M., 2010, MNRAS, 409, 1330

Willott C. J., Carilli C. L., Wagg J., Wang R., 2015, ApJ, 807, 180

Wisnioski E., et al., 2015, The Astrophysical Journal, 799, 209

Wisnioski E., et al., 2019, ApJ, 886, 124

Wolfire M. G., Hollenbach D., McKee C. F., Tielens A. G. G. M., Bakes E. L. O., 1995, ApJ, 443, 152

Wolfire M. G., McKee C. F., Hollenbach D., Tielens A. G. G. M., 2003, ApJ, 587, 278

Wolfire M. G., Hollenbach D., McKee C. F., 2010, ApJ, 716, 1191

Yang C.-C., Krumholz M., 2012, ApJ, 758, 48

Yu X., et al., 2019, MNRAS, 486, 4463

Zanella A., et al., 2018, MNRAS, 481, 1976

Zanella A., et al., 2019, MNRAS, 489, 2792

Zanella A., Pallottini A., Ferrara A., Gallerani S., Carniani S., Kohandel M., Behrens C., 2021, MNRAS, 500, 118

Zaritsky D., et al., 2014, AJ, 147, 134

Zhou L., et al., 2017, MNRAS, 470, 4573

Zolotov A., et al., 2015, MNRAS, 450, 2327

van der Kruit P. C., Freeman K. C., 2011, ARA&A, 49, 301

List of Figures

List of Tables

Acronyms

ALMA Atacama Large Millimeter/Submillmeter Array. 13

AMR Adaptive Mesh Refinement. 42

BB Big Bang. 3

CMB Cosmic Microwave Background radiation. 4

CNM Cold Neutral Medium. 28

DM Dark Matter. 2

FOV Field of View. 49

FRW Friedman Robertson Walker. 2

FWHM Full width at half maximum. 54

GMC Giant Molecular Clouds. 10

GR General Relativity. 1

HIM Hot Ionized Medium. 28

HMF Halo Mass Funciton. 8

HST Hubble Space Telescope. 11

IFU Integral Field Unit. 17

IGM intergalactic medium. 9

JWST James Webb Space Telescope. 13

KS Kennicutt–Schmidt. 15

l.o.s Line of Sight. 49

LAE Lyman Alpha Emitters. 11

LBG Lyman Break Galaxies. 11

LTE local thermal equilibrium. 32

MC Molecular Clound. 28

MW Milky Way. 22

PDR Photodissociation Region. 28

REBELS Reionization Era Bright Emission Line Survey. 13

SED Spectral Energy Distribution. 11, 44

SFG Star Forming Galaxy. 12

SN Supernovae. 24

UV Ultraviolet raidation. 5

VLT Very Large Telescope. 11

WIM Warm Ionized Medium. 28

WNM Warm Neutral Medium. 28